Third Generation SUSY Searches at CMS

Florent Lacroix[1] on behalf of the CMS collaboration

[1]University of California Riverside, CA 92521, U.S.A.

DOI: http://dx.doi.org/10.3204/DESY-PROC-2014-04/191

In this talk, the latest results from CMS on searches for stop and sbottom squarks are presented. Searches for direct squark production and indirect production through gluino cascades in a variety of decay channels are reviewed. The results are based on 20/fb of data collected during the 8 TeV LHC run.

1 Introduction

Supersymmetry (SUSY) is a popular extension of the standard model (SM), offering an additional symmetry of nature between fermions and bosons. A new supersymmetric partener particle (sparticle) is proposed for each SM particle, providing an elegant mechanism to mitigate the hierarchiy problem. The symmetry is not exact, as no sparticles have been observed experimentally; however the stabilising features of SUSY can survive if sparticles are not too much heavier than their SM partners. The third generation in particular offers scope to search for SUSY because of the relatively large mass of the top quark. The mass difference between the stop quark and its SUSY partener the top squark must be small to provide a "natural" solution to the hierarchy problem, and similarly for the bottom quark and the sbottom squark. They may be accessible at the TeV scale, and pair produced at the LHC.

This paper presents the latest results of the searches performed with the CMS detector [1] looking for direct and indirect production of the third generation squarks in a variety of decay channels. The results are based on the data collected during the 2012 8 TeV LHC run.

2 Direct top squark production

Light (stop1) and heavy (stop2) stop squarks can be directly pair produced at the LHC via gluon fusion or quark annihilation and are investigated in CMS by a broad search program.

2.1 Light stop results

Several analyses have been performed in CMS to search for the direct production of a pair of light stop, assuming that the stop decays to a top quark and a neutralino: a fully hadronic search using a top tagger [2], an inclusive analysis based on the razor variables [3], a fully hadronic analysis using the MT2 variable [4] and an analysis looking to the single-lepton final state [5]. The razor and single-lepton results have been combined in a recent publication [6].

If the mass difference between the stop squark and the lighest supersymmetric particle (LSP) is very small, the stop decays to a charm quark and the LSP through loop. In this case the charm jets are expected to be relatively soft and hidden by the low energy QCD background events or too soft for the CMS detector to identify. However these events can be detected if they are accompanied by initial state radiation (ISR). Provided final state particles are invisible, such events contain a high pt jet and missing transverse energy. A monojet analysis have been designed to search for these events [7].

No significant deviations from the standard model predictions have been observed in all these analyses. Results are interpreted as exclusion limits on Simplified Model Spectra and are presented in Figure 1.

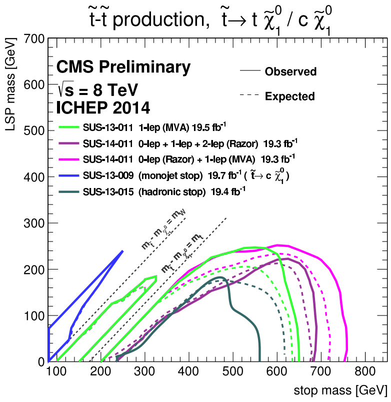

Figure 1: Expected and observed limit curves for stop pair production, assuming 100% branching fraction of the stop decay mode to a top quark and a neutralino or, in case of a highly compressed spectrum, the stop decay mode to a charm quark and a neutralino.

The stop squark can also decay into a chargino and a b-jet, with the chargino decaying into a W boson and a neutralino. This model has been studied in the reference [5] where the limits obtained are shown for different mass relations for the chargino, neutralino and stop squark. The sensitivity is dependent on assumptions made on the chargino polarization and the left/right handedness of the coupling. An other interpretation with chargino is presented in the reference [6], assuming a mass difference of 5 GeV between the chargino and the neutralino, resulting in a decay with a virtual W.

2.2 Heavy stop results

Several analyses are looking to heavy stop pair production. In this case the stop2 decays to stop1 and either a Higgs boson or a Z boson. The resuls of the single-lepton+2 opposite charge leptons analysis [8], the same-sign dileptons analysis [9] and the 3-leptons analysis [10] have been combined and are presented in the reference [11]. The limits obtained for Higgs only and Z only decays are presented in Figure 2, but mixed branching ratio scenario results are also avialable in the reference [11].

2.3 Other direct stop searches

Some R-parity violating models have also been investigated by CMS, with a search for anomalous production of events with three or more isolated leptons and at least one b-jet produced [12].

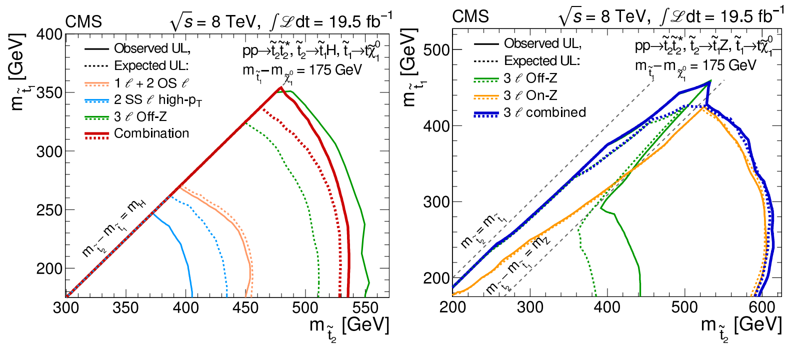

Figure 2: Observed (expected) exclusion contours, which are indicated by the solid (dashed) curves for the contributing channels. The excluded region in the m(stop1) and m(stop2) parameter space is obtained assuming that the stop2 decays to stop1 and a Higgs boson in the left plot and assuming a decay to stop1 and Z boson in the right plot.

There is also a program of gauge mediated susy breaking scenarios using diphoton Higgs decays [13] and three leptons events [10].

3 Direct sbottom production

Instead of a pair of stop squarks, a pair of sbottom squarks can be produced in LHC collisions. Three decays of the sbottom squarks have been investigated:

- b quark and a neutralino;
- top quark and a chargino, with the chargino decaying in a W boson and a neutralino;
- b quark and a neutralino 2, with the neutralino 2 decaying in a Z boson and a neutralino 1.

The first model has been investigated by a dedicated sbottom search [14] and with the inclusive MT2 analysis [4]. A multilepton search [15], the same-sign dilepton search [9] and the three leptons search [10] have been used to search for the second model with a chargino. The third model has been investigated by the three leptons search [10], assuming a mass difference between the neutralinos of 110 GeV. In this case the neutralino 2 is indeed decaying only to a Z boson and the LSP, the decay with a Higgs boson being forbidden.

4 Gluino mediated production

Stop and sbottom are also searched in gluino mediated processes, looking for deviation in specific final states that can be produced if an intermidiate third generation squark has been involved in the process. They have been investigated in models where the stop/sbottom squarks are produced off-shell, in which case the third generation squarks existence is probed indirectly.

The first simplified model considered (T1bbbb) is when the pair produced gluinos decay to two b jets and a neutralino. This leads to a purely hadronic final state and has been investigated by the razor analysis [6], the met+ht analysis [16], the alphaT analysis [17] and the MT2 analysis [4].

The other simplified model considered (T1tttt) is when the gluinos decay to two top quark and a neutralino. All the lepton multiplicities in the final state are investigated by different analyses: 0-lepton analyses [4, 6, 16, 17], 1-lepton analyses [18], 2-leptons analyses [9, 19] and 3-leptons analyses [10, 15].

The results of these two models are presented in Figure 3.

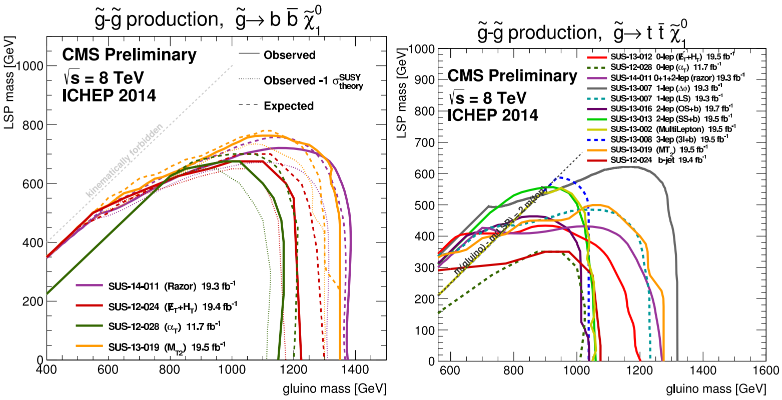

Figure 3: Expected and observed limit curves in the (LSP mass, gluino mass) plane for the T1bbbb (left) and T1tttt (right) simplified models.

The mixed branching ratios scenarios (T1tbbb, T1ttbb and T1tttb) have also been studied with the razor analysis [6]. The limits obtained for mixed branching ratios lie within the T1bbbb and the T1tttt contours. So the limit obtained with the razor analysis for the model where both gluinos decay to top quarks can be considered as a conservative branching ratio independent limit.

The gluino mediated stop and sbottom squarks production has also been investigated when the stop/sbottom are produced on-shell. On-shell stop squark in gluino decay are investigated by the single-lepton search [18], the same-sign dilepton search [20] and the three lepton search [10]. Two analyses interpret their results in term of on-shell sbottom squark: the same-sign dilepton search [20] and the three lepton search [10].

5 Conclusion

The CMS program to discover third generation SUSY is wide and rich, covering many topologies and final states. So far no significant hint of SUSY particle has been observed, putting the naturalness of the SM Higgs under severe pressure. However the missing corners need to be explored, in particular with the future data taken with a higher energy in the centre of mass.

References

[1] S. Chatrchyan *et al.* [CMS Collaboration], "The CMS experiment at the CERN LHC," JINST **3**, S08004 (2008).

[2] CMS Collaboration [CMS Collaboration], "Search for top squarks in multijet events with large missing momentum in proton-proton collisions at 8 TeV," CMS-PAS-SUS-13-015.

[3] CMS Collaboration [CMS Collaboration], "Search for supersymmetry using razor variables in events with b-jets in pp collisions at 8 TeV," CMS-PAS-SUS-13-004.

[4] CMS Collaboration [CMS Collaboration], "Search for supersymmetry in hadronic final states using MT2 with the CMS detector at sqrt(s) = 8 TeV," CMS-PAS-SUS-13-019.

[5] S. Chatrchyan *et al.* [CMS Collaboration], "Search for top-squark pair production in the single-lepton final state in pp collisions at $\sqrt{s}$ = 8 TeV," Eur. Phys. J. C **73**, 2677 (2013) [arXiv:1308.1586 [hep-ex]].

[6] CMS Collaboration [CMS Collaboration], "Exclusion limits on gluino and top-squark pair production in natural SUSY scenarios with inclusive razor and exclusive single-lepton searches at 8 TeV.," CMS-PAS-SUS-14-011.

[7] CMS Collaboration [CMS Collaboration], "Search for top squarks decaying to a charm quark and a neutralino in events with a jet and missing transverse momentum," CMS-PAS-SUS-13-009.

[8] CMS Collaboration [CMS Collaboration], "higgs from stop decay (h to bb)," CMS-PAS-SUS-13-021.

[9] CMS Collaboration [CMS Collaboration], "Search for new physics in events with same-sign dileptons and jets in pp collisions at 8 TeV," CMS-PAS-SUS-13-013.

[10] CMS Collaboration [CMS Collaboration], "Search for supersymmetry in pp collisions at sqrt(s) = 8 TeV in events with three leptons and at least one b-tagged jet," CMS-PAS-SUS-13-008.

[11] V. Khachatryan *et al.* [CMS Collaboration], "Search for top-squark pairs decaying into Higgs or Z bosons in pp collisions at $\sqrt{s}$=8 TeV," Phys. Lett. B **736**, 371 (2014) [arXiv:1405.3886 [hep-ex]].

[12] S. Chatrchyan *et al.* [CMS Collaboration], "Search for top squarks in R-parity-violating supersymmetry using three or more leptons and b-tagged jets," Phys. Rev. Lett. **111**, no. 22, 221801 (2013) [arXiv:1306.6643 [hep-ex]].

[13] S. Chatrchyan *et al.* [CMS Collaboration], "Search for top squark and higgsino production using diphoton Higgs boson decays," Phys. Rev. Lett. **112**, 161802 (2014) [arXiv:1312.3310 [hep-ex]].

[14] CMS Collaboration [CMS Collaboration], "Search for direct production of bottom squark pairs," CMS-PAS-SUS-13-018.

[15] S. Chatrchyan *et al.* [CMS Collaboration], "Search for anomalous production of events with three or more leptons in pp collisions at sqrt(s) = 8 TeV," Phys. Rev. D **90**, 032006 (2014) [arXiv:1404.5801 [hep-ex]].

[16] S. Chatrchyan *et al.* [CMS Collaboration], "Search for gluino mediated bottom- and top-squark production in multijet final states in pp collisions at 8 TeV," Phys. Lett. B **725**, 243 (2013) [arXiv:1305.2390 [hep-ex]].

[17] S. Chatrchyan *et al.* [CMS Collaboration], "Search for supersymmetry in hadronic final states with missing transverse energy using the variables α_T and b-quark multiplicity in pp collisions at $\sqrt{s}$ = 8 TeV," Eur. Phys. J. C **73**, 2568 (2013) [arXiv:1303.2985 [hep-ex]].

[18] S. Chatrchyan *et al.* [CMS Collaboration], "Search for supersymmetry in pp collisions at $\sqrt{s}$=8 TeV in events with a single lepton, large jet multiplicity, and multiple b jets," Phys. Lett. B **733**, 328 (2014) [arXiv:1311.4937 [hep-ex]].

[19] CMS Collaboration [CMS Collaboration], "Search for supersymmetry in pp collisions at sqrt(s) = 8 Tev in events with two opposite sign leptons, large number of jets, b-tagged jets, and large missing transverse energy.," CMS-PAS-SUS-13-016.

[20] S. Chatrchyan *et al.* [CMS Collaboration], "Search for new physics in events with same-sign dileptons and jets in pp collisions at $\sqrt{s}$ = 8 TeV," JHEP **1401**, 163 (2014) [arXiv:1311.6736, arXiv:1311.6736 [hep-ex]].

Search for Higgs Bosons Beyond the Standard Model with the CMS Detector

Matthias Schröder on behalf of the CMS Collaboration
DESY, Notketraße 85, 22607 Hamburg, Germany

DOI: http://dx.doi.org/10.3204/DESY-PROC-2014-04/190

After a Higgs boson with a mass near 125 GeV has been discovered, it is still unclear whether this is the Higgs boson predicted by the standard model (SM). Various models with extended Higgs sectors are being considered, such as the minimal supersymmetric extensions of the SM. Recent results of searches for non-SM Higgs bosons with the CMS detector are presented, which are based on pp collision data collected at centre-of-mass energies of 7 and 8 TeV corresponding to integrated luminosities of about 5 and 20 fb^{-1}.

While the recently discovered Higgs boson with a mass near 125 GeV [1] is consistent with the standard model (SM) expectations, non-SM couplings are only excluded up to branching ratios of $\approx 30\%$ with the current data [2]. Furthermore, numerous BSM models predict extended Higgs sectors. The minimal supersymmetric extension (MSSM) [3], for example, requires two complex Higgs doublets, one of which couples to the u-type and one to the d-type fermions. After electroweak symmetry breaking, five physical states remain: a light and a heavy CP-even boson h and H, an CP-odd boson A, all of which are neutral and collectively denoted Φ, and two charged bosons $\mathrm{H}^{\pm}$. At tree level, the MSSM Higgs sector is completely defined by two parameters, conventionally chosen as the mass m_{A} of the CP-odd boson and the ratio $\tan\beta$ of the vacuum expectation values of the two doublets.

In this article, recent results of direct searches both for additional Higgs bosons and for non-SM decays of the 125 GeV boson conducted by the CMS experiment [4] at the LHC are reviewed: a search for a heavy neutral Higgs boson $\Phi \to \tau\tau$, for a light charged Higgs boson $\mathrm{H}^{+} \to \mathrm{c\bar{s}}$, and for lepton-flavour violating Higgs boson decays $\mathrm{H} \to \mu\tau$. The analyses are performed with 4.9 and 19.7 fb^{-1} of data collected at centre-of-mass energies $\sqrt{s}$ of 7 and 8 TeV, respectively. A particle-flow algorithm [5] is used to reconstruct the individual particles in the events, from which hadronically decaying taus τ_{h}, the missing transverse momentum $\not{E}_{\mathrm{T}}$, and jets are clustered. Jets initiated by b-quarks are identified (b-tagged) with a likelihood discriminant combining track-based lifetime and secondary-vertex information [6].

1 Searches for heavy neutral Higgs bosons

At the LHC, the neutral MSSM Higgs bosons Φ are expected to be predominantly produced either in gluon-gluon fusion or in b-quark associated production. For larger values of $\tan\beta$, the latter mode dominates, and at the same time, the branching fraction ($\mathcal{B}$) to τ leptons is also enhanced relative to the SM over the whole m_{A} range. CMS has performed a search for $\Phi \to \tau\tau$ using the full 25 fb^{-1} of the 7 and 8 TeV data and considering five $\tau\tau$ final-states, $\mathrm{e}\tau_{\mathrm{h}}$, $\mathrm{e}\mu$, $\mu\tau_{\mathrm{h}}$,

$\mu\mu$, and $\tau_h\tau_h$ [7]. Events are collected using a combination of e, μ, and τ_h triggers, whose criteria varied during the data-taking periods. Offline, events are further selected requiring two oppositely charged, well isolated leptons. Additional channel-dependent selection criteria are applied to suppress contributions from SM background processes; for example, in the $\mu\tau_h$ channel the transverse mass of the μ and the $\not{E}_T$ is required to be less than 30 GeV to reject W+jets events. Moreover, the selected events are split into two categories of either 0 or ≥ 1 b-tagged jets to enhance the sensitivity to the different production modes.

The invariant mass $m_{\tau\tau}$ of the di-τ system is reconstructed from the leptons and $\not{E}_T$ in the event using a maximum-likelihood technique based on a model of the τ-decay phase-space and the $\not{E}_T$ resolution, which results into a relative mass resolution of typically 20% at 90 GeV. The $m_{\tau\tau}$ distribution observed in the $\mu\tau_h$ 0-b-tag channel is shown in Fig. 1 (left). The dominant SM background contribution arises from $Z \to \tau\tau$ events and is determined from data with an embedding technique, where the muons in $Z \to \mu\mu$ events are replaced by simulated τ-decay products. Further important backgrounds are due to W+jets and QCD-multijet events with jets mis-identified as τ_h and μ and are estimated from signal-depleted control regions in data.

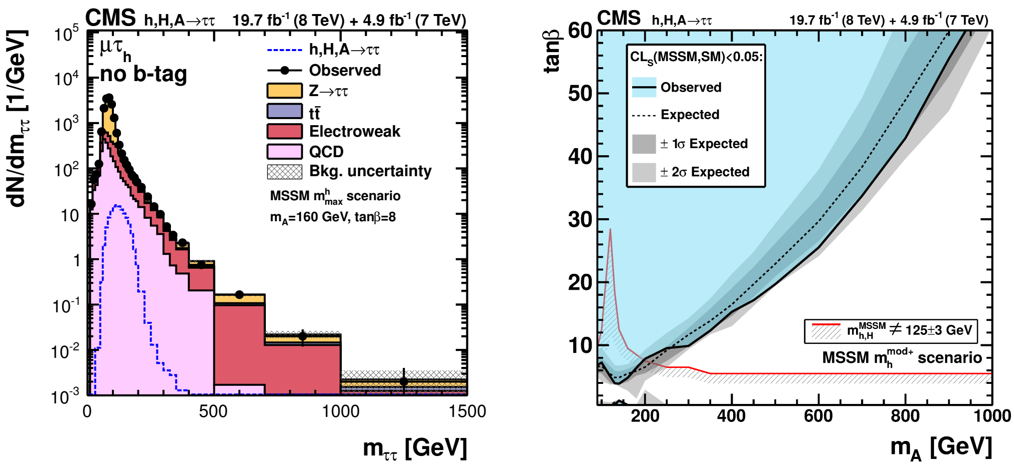

Figure 1: $m_{\tau\tau}$ distribution in the $\mu\tau_h$ 0-b-tag channel (*left*) and 95% C. L. exclusion limits on the MSSM parameters m_A and $\tan\beta$ (area above the black lines is excluded) in the m_h^{mod+} scenario (*right*); the region above the red line is compatible with a 125 GeV Higgs boson.

In all channels, the observed data agree well with the SM-only expectation. Thus, model-independent upper limits are derived on the resonance production rate $\sigma \times \mathcal{B}(\Phi \to \tau\tau)$. The results are also interpreted as constraints on the MSSM parameters, expressed as limits at 95% confidence level (C. L.) in $(\tan\beta, m_A)$ space assuming the other MSSM parameters to be fixed at certain benchmark values. In all cases, the signal hypothesis is tested against a background plus SM-Higgs hypothesis, thus taking into account the Higgs boson at 125 GeV. Likewise, the MSSM interpretation is not only performed in the traditionally used m_h^{max} benchmark scenario but also in several other recently proposed scenarios [8] that are compatible with either h or H having a mass of 125 GeV in most parts of the parameter space. This is not the case in the m_h^{max} scenario, which is therefore disfavoured by data. The sensitivity in the m_h^{mod+} scenario [8], for example, reaches up to $m_A = 1$ TeV and down to $\tan\beta = 5$ at low m_A, cf. Fig. 1 (right).

2 Search for light charged Higgs bosons

If the charged Higgs boson H^+ predicted by the MSSM is lighter than the mass difference of the t- and b-quarks, t quarks can decay as $t \rightarrow \mathrm{H}^+\mathrm{b}$, and if $\tan\beta < 1$, the H^+ decays predominantly to a $\mathrm{c\bar{s}}$-quark pair (charge conjugation is implied). CMS has performed a search for light H^+ bosons in $\mathrm{t\bar{t}} \rightarrow \mathrm{H}^+(\rightarrow \mathrm{c\bar{s}})\mathrm{bW}^-(\rightarrow \mu\nu)\mathrm{b}$ events in $19.7\,\mathrm{fb}^{-1}$ of data at $\sqrt{s} = 8\,\mathrm{TeV}$ [9].

Events are collected triggering on an isolated μ with $p_\mathrm{T} > 24\,\mathrm{GeV}$. Offline, exactly one μ is required to suppress contributions from Z+jets and $\mathrm{t\bar{t}}$ events. Furthermore, four central jets with $p_\mathrm{T} > 30\,\mathrm{GeV}$, two of which are b-tagged, and $\not{E}_\mathrm{T} > 20\,\mathrm{GeV}$ are required. After this selection, the expected SM contributions arise almost exclusively from $\mathrm{t\bar{t}}$ events in the semi-leptonic decay channel. Assuming that the $\mathrm{t\bar{t}}$ production cross-section remains un-altered, a signal would manifest in the invariant dijet-mass distribution of the two non-b-tagged jets as a deficit of events at the W mass and an excess at the H^+ mass compared to the SM expectation due to the additional decay-channel. The mass resolution is significantly improved using a kinematic fit to reconstruct the $\mathrm{t\bar{t}}$ event, where the t-quark mass is constraint to $172.5\,\mathrm{GeV}$.

Since no significant deviation is observed, model-independent upper limits at 95% C. L. on $\mathcal{B}(\mathrm{t} \rightarrow \mathrm{H}^+\mathrm{b})$ are derived assuming $\mathcal{B}(\mathrm{H}^+ \rightarrow \mathrm{c\bar{s}}) = 100\%$, cf. Fig. 2 (left). The limits range from 2 to 7% for H^+ masses between 90 and 160 GeV.

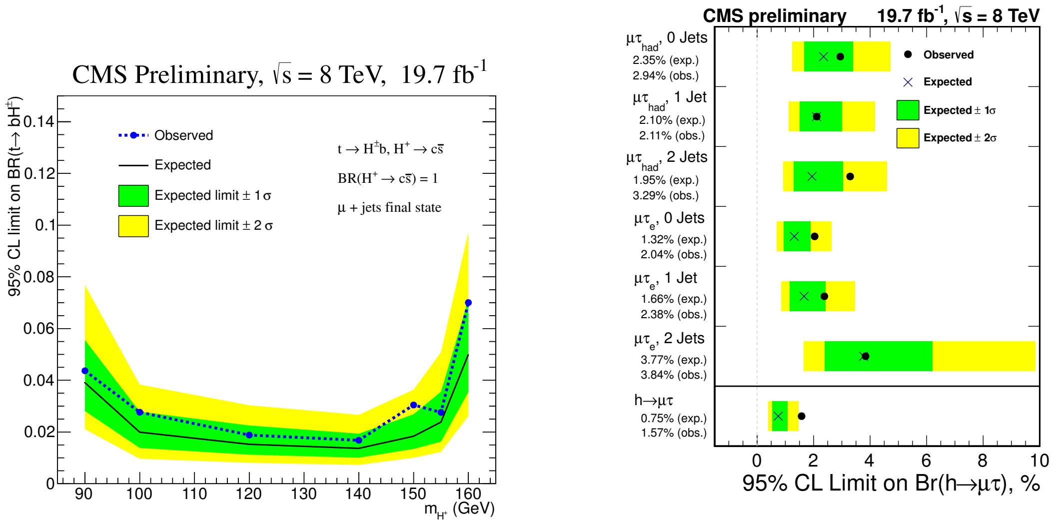

Figure 2: Upper limits at 95% C. L. on $\mathcal{B}(\mathrm{t} \rightarrow \mathrm{H}^+\mathrm{b})$ assuming $\mathcal{B}(\mathrm{H}^+ \rightarrow \mathrm{c\bar{s}}) = 100\%$ (*left*) and on $\mathcal{B}(\mathrm{H} \rightarrow \mu\tau)$ in the different channels and their combination (*right*).

3 Search for lepton-flavour violating Higgs boson decays

While lepton-flavour violating (LFV) Higgs boson decays are not allowed in the SM, they can occur naturally in various BSM models such as composite-Higgs and Randall-Sundrum models. CMS has performed the first direct search for LFV decays $\mathrm{H} \rightarrow \mu\tau$ of the 125 GeV Higgs boson in the $\mu\tau_\mathrm{e}$ and $\mu\tau_\mathrm{h}$ final states using $19.7\,\mathrm{fb}^{-1}$ of 8 TeV data [10].

Events are collected triggering on an isolated μ and e with p_T above 17 and 8 GeV, respectively, in the $\mu\tau_e$ channel and an isolated μ with $p_T > 17$ GeV in the $\mu\tau_h$ channel. Offline, the leptons are required to have opposite charge, and events are further divided into jet-multiplicity categories to enhance the sensitivity to different production modes. Further selection criteria to suppress SM contributions exploit that the μ in signal events stems promptly from the LFV decay and thus tends to have larger p_T than in SM $H \to \tau_\mu \tau_{e/h}$ events for example. An important residual background arises from $Z \to \tau\tau$ and is estimated from data using the aforementioned embedding technique. Depending on the channel, further main backgrounds are due to W+jets, QCD-multijet, and $t\bar{t}$ events, in which jets are mis-reconstructed as leptons or τ_h and which are determined from control regions in data using estimates of the mis-reconstruction rate. The invariant $\mu\tau$ mass is approximated from the μ, the visible τ decay products τ_{vis}, and the $\not{E}_T$ component along τ_{vis}, which is assumed to be collinear to the ν due to the high boost of the τ.

No significant excess of events above the SM expectation is observed in the mass distributions. The combined upper limit at 95% C. L. on the LFV $\mathcal{B}(H \to \mu\tau)$ is (0.75 ± 0.38)% expected and 1.57% observed, cf. Fig. 2 (right). Interpreted as signal, it corresponds to $\mathcal{B}(H \to \mu\tau) = (0.89^{+0.40}_{-0.37})$%, i. e. a significance of 2.5 standard deviations. The limit is also translated into constraints on $\mu\tau$ Yukawa couplings, improving earlier results from indirect measurements by an order of magnitude.

4 Conclusions

CMS has performed a wide variety of searches both for non-SM properties of the 125 GeV Higgs boson and for additional Higgs bosons. In this article, searches for heavy neutral and for light charged Higgs bosons as well as for lepton-flavour violating decays have been discussed, which have been performed with up to 25 fb^{-1} of 7 and 8 TeV data. No significant deviation from the SM is observed, and the results are used to derive valuable constraints on the BSM-Higgs parameter space, which mostly exclude for example the low-m_A region of the MSSM.

References

[1] CMS Collaboration. Observation of a new boson with mass near 125 GeV in pp collisions at $\sqrt{s} = 7$ and 8 TeV. *JHEP*, 1306:081, 2013.

[2] CMS Collaboration. Precise determination of the Higgs boson mass and studies of the compatibility of its couplings with the standard model. CMS Physics Analysis Summary CMS-PAS-HIG-14-009, CERN, 2014.

[3] H.P. Nilles. Supersymmetry, supergravity and particle physics. *Physics Reports*, 110(1-2):1–162, 1984.

[4] CMS Collaboration. The CMS experiment at the CERN LHC. *JINST*, 3:S08004, 2008.

[5] CMS Collaboration. Particle-flow event reconstruction in CMS and performance for jets, taus, and MET. CMS Physics Analysis Summary CMS-PAS-PFT-09-001, CERN, 2009.

[6] CMS Collaboration. Performance of b tagging at $\sqrt{s} = 8$ TeV in multijet, $t\bar{t}$ and boosted topology events. CMS Physics Analysis Summary CMS-PAS-BTV-13-001, CERN, 2013.

[7] CMS Collaboration. Search for neutral MSSM Higgs bosons decaying to a pair of tau leptons in pp collisions. CMS Physics Analysis Summary CMS-PAS-HIG-13-021, CERN, 2014.

[8] M. S. Carena et al. MSSM Higgs Boson Searches at the LHC: Benchmark Scenarios after the Discovery of a Higgs-like Particle. *Eur.Phys.J.*, C73:2552, 2013.

[9] CMS Collaboration. Search for a light charged Higgs boson in the $H^+ \to c\bar{s}$ channel at CMS. CMS Physics Analysis Summary CMS-PAS-HIG-13-035, CERN, 2014.

[10] CMS Collaboration. Search for Lepton Flavour Violating Decays of the Higgs Boson. CMS Physics Analysis Summary CMS-PAS-HIG-14-005, CERN, 2014.

Search for Dark Matter at CMS

Kerstin Hoepfner on behalf of the CMS collaboration

RWTH Aachen University, Otto-Blumenthal-Str., 52074 Aachen, Germany

DOI: http://dx.doi.org/10.3204/DESY-PROC-2014-04/193

The latest results from CMS searches for dark matter are presented based on 20/fb of pp collision data collected at $\sqrt{s}$= 8 TeV at the LHC. Analyses are performed in several final states, including a single jet/photon/W-boson or a single top quark as well as production in association with $t\bar{t}$-pairs. No indication of dark matter was found so far and exclusion limits on the DM-nucleon scattering cross section are set using an effective field approach.

1 The dark matter model

Indications for the existence of dark matter (DM) are one of the strongest hints for physics beyond the SM. Many experiments seek their detection and understanding of their nature. Candidates particles for dark matter occur in many theoretical models. They may also be pair produced in pp collisions at the LHC and directly be searched for without specific theoretical assumptions. Up to now, such production has been described by an effective field theory (EFT) without modeling a specific messenger, assuming a contact interaction between Standard Model (SM) particles and DM. This approach allows to probe different models, while being specific enough to make predictions. The EFT description is valid as long as the messenger mass M is larger than the energy and momentum transfer in the partonic collision. Then two characterizing parameters fully determine the interaction, the scale of the effective interaction $\Lambda = M/\sqrt{(g_{DM} g_{SM})}$ and the mass of the dark matter candidate M_χ. Different assumptions for the coupling with DM are possible, such as vector, scalar and axial-vector coupling.

Weakly interaction DM particles would not yield a detectable signal in the detector and rather contribute to missing transverse energy (MET) which can also be created by neutrinos or other weakly interacting particles. Therefore, their detection has to be based on additional particles - the emission of a single photon or a single jet as initial-state or final-state radiation or through a recoiling particle, such as a W- or a Z-boson. The CMS experiment [1] has performed such searches using the full 2012 pp dataset at $\sqrt{s}$=8 TeV.

2 The mono-X search channels

The pioneering search for pair-produced DM at hadronic colliders exploits the single jet + MET final state [2]. It is challenged by the trigger and high QCD background. Single-jet trigger thresholds would be far too high, therefore the trigger either uses MET above 120 GeV or a jet+MET combination with jet transverse momentum p_T >80 GeV and MET>105 GeV. To suppress instrumental and beam-related backgrounds, events are rejected if less than 20% of

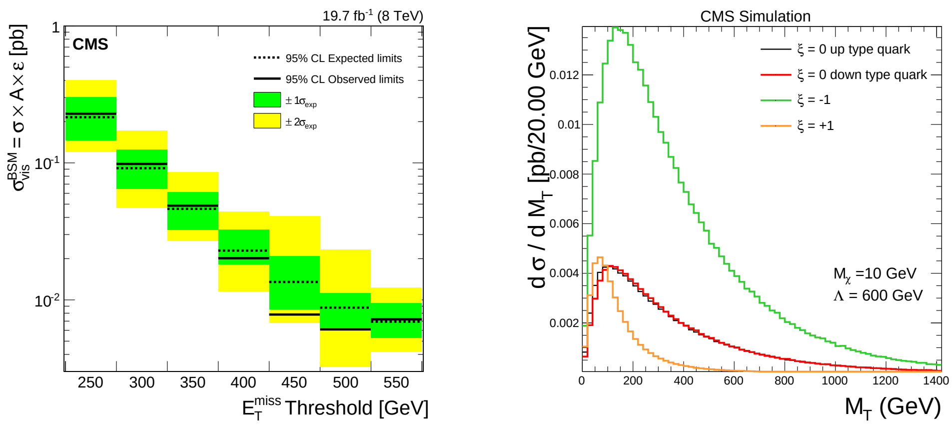

Figure 1: Left: The monojet analysis searches the MET distribution after all selections in seven bins. Shown are the model-independent observed and expected 95% C.L. upper limits on the visible cross section times acceptance times efficiency ($\sigma \times A \times \epsilon$) for non-SM production of events. Right: The mono-W channel could disentangle potentially different couplings to up- and down-type quarks, described by the parameter ξ. The resulting cross section and M_T shape would differ strongly.

the energy of the highest p_T jet is carried by charged hadrons or more than 70% of this energy is carried by either neutral hadrons or photons. The most energetic jet is required to have $p_T >$ 110 GeV within $|\eta| < 2.4$. A second jet is only allowed if nearby, in order to suppress QCD dijet events. The dominant backgrounds after all selection steps are due to Z($\nu\nu$) and W+jet events, estimated from data samples of Z($\mu\mu$) andW($\mu\nu$) events. The analysis is performed in seven regions of MET (see Fig. 1-left). Upper limits on the cross section × acceptance × efficiency ($\sigma \times A \times \epsilon$) are placed ranging from 2 pb for MET>250 GeV to 10^{-2}pb for MET>500 GeV.

The same $\sqrt{s}$=8 TeV dataset was used for searches with a single photon [3] instead. Events are triggered with either a single photon or a photon+MET cross trigger with offline thresholds of MET>140 GeV and p_T^γ >145 GeV. A tight photon ID rejects fakes. Events with either a single lepton or hadronic activity are being vetoed. The dominant irreducible backgrounds after selection are due to $Z(\to \nu\nu) + \gamma$ and $W(\to \ell\nu) + \gamma$ along with fake photon backgrounds. Searching in six bins of p_T^γ shows that data are compatible with the SM expectation and 90% C.L. limits are set on Λ using effective operators in the EFT approach. The resulting DM-nucleon cross section limits are depicted in Fig. 2-left.

The monolepton channel [4] – where DM recoils against a W-boson which subsequently decays to an electron(muon) and corresponding neutrino – is special as it allows to disentangle possibly different couplings to the up- or the down-type quark. Their relative coupling strength is parametrized by the factor ξ with the considered values of 0, +1, -1, following ref.[5]. The factor ξ could modify either the up or down-type quark couplings with the resulting M_T distributions shown in Fig. 1-right. The coupling changes the total cross section and the shape of the spectrum which in turn impacts the sensitivity. While the very high end of the transverse mass spectrum is nearly background free, at lower masses the small signal has to be separated from background.

In the monolepton search, candidate events with at least one high transverse momentum lepton are selected using single electron(muon) triggers with offline p_T >100(45) GeV. The lepton reconstruction is optimized for high momenta. The main observable is the transverse mass (M_T) of the lepton-MET spectrum. The main background $W \to \ell\nu$ is described with an M_T-binned k-factor for higher order QCD and electroweak corrections. Other backgrounds are Z/DY, ttbar, multi-jet QCD and di-boson processes, all are derived from simulation using NLO cross sections (except QCD). In order to suppress backgrounds, events exhibiting a back-to-back kinematics are selected. The three cases of ξ with related cross sections yield three limits on λ which subsequently are translated to limits of the DM-nucleon cross section (see Fig. 2-right).

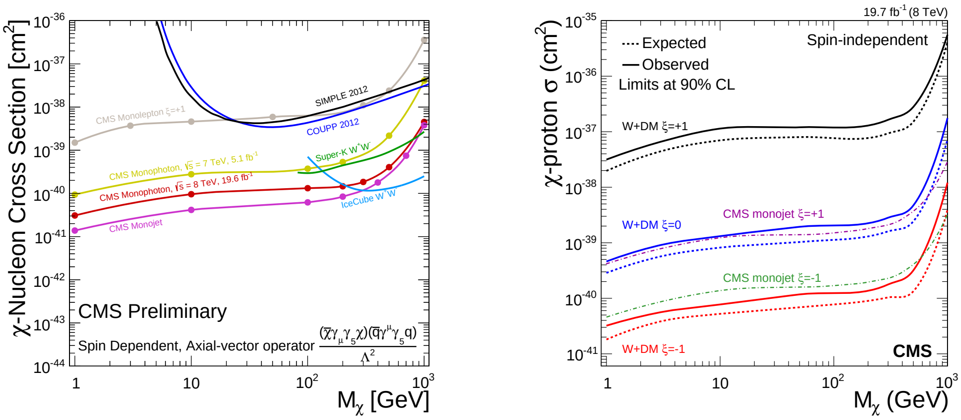

Figure 2: Dark matter nucleon exclusion limits with EFT assumption for different channels addressing the spin dependent (axial-vector) coupling (left) and spin independent (vector) coupling (right).

3 Using top quarks

Unlike the previously discussed vector and axial-vector couplings which are simply proportional to Λ^{-2}, scalar couplings do contain a mass term (m_q/Λ^3 for D1 and m_q/Λ^2 for C1). Such searches are therefore performed best with top quarks. A single DM particle could be produced along with a top-quark in the s- or t-channel [6] or DM pairs in association with top-quark pairs [7, 8]. All channels require large MET due to DM, with thresholds of 320 GeV and 350 GeV for the monotop and top-pair channel, respectively. Depending on the W decay originating from $t \to Wb$, the final state contains several jets or jets plus leptons.

The fully hadronic channel is used in the monotop search [6], thus yielding three final state jets of which one has to be b-tagged and the two leading ones exhibit p_T >60 GeV. No isolated electron or muon should be present. Along with the MET requirement this selection removes about 4/5 of the background. The main remaining backgrounds are $t\bar{t}$ (with the leptonic decay of the W and undetected lepton) and V+jets while QCD multi-jet and diboson events are largely suppressed by the b-tag. The invariant mass of the three leading jets in selected events with one b-tag is depicted in Fig. 3-left. Data are compared to the simulated backgrounds and a

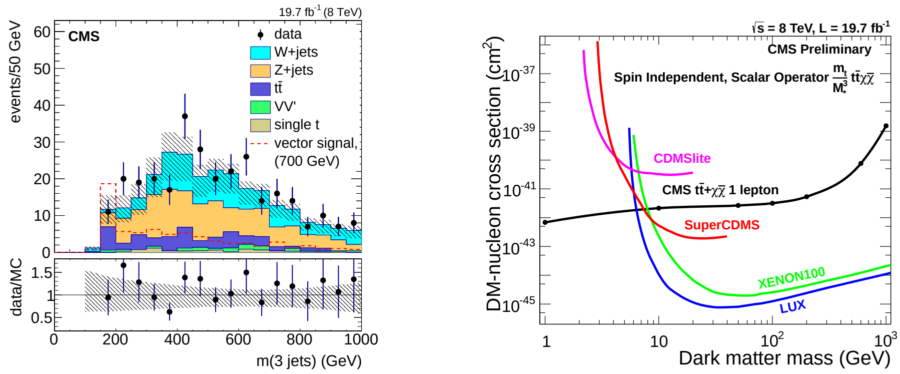

Figure 3: Left: The invariant mass of the three leading jets in selected events with one b-tag in the monotop DM search. Measured data points are compared to the simulated backgrounds (stacked histograms) and one of the signal models (solid line) scaled to 19.7/fb. The shaded area represents systematic uncertainties. Right: The 90% C.L. upper limits on the dark matter-nucleon spin-independent scattering cross sections for the scalar operator considered in the ttbar analysis, compared to results from selected direct detection experiments.

signal model. In the full 8 TeV data sample, no deviation from the SM expectation is observed and DM masses below 655(327) GeV are excluded at 95% C.L. for vector(scalar) couplings.

Assuming DM may be pair-produced in association with top-quarks, searches are performed in the dilepton $\ell\ell bb + MET$ [7] and the semi-leptonic $\ell jjjb + MET$ final state [8]. Events are selected with one lepton + ≥3 jets + ≥1 b-jet along with the MET requirement. Both W-bosons are reconstructed via M_T. According to its final state, the dilepton search rather selects events with 2 leptons + ≥2 jets and applies cuts on the scalar sum of leptons and jets, and lepton opening angle. The main background for both analyses is $t\bar{t}$. Signal efficiencies are about 1-2% but the background is also very low. Using the EFT description from above with the characteristic parameters Λ and M_χ, values of Λ <120(90) GeV are excluded in the semi-leptonic(dileptonic) channel for M_χ <100 GeV. Combining both results, the excluded DM-nucleon cross sections are shown in Fig. 3-right for a scalar operator where other channels rarely set limits due to their low sensitivity.

4 Summary

Several analyses based on the full 2012 data sample search for pair-produced DM in pp collisions at the LHC but found no significant indication of such signals. Based on an effective field approach for the SM-DM interaction, limits on the DM-nucleon scattering cross section are being set for different types of interaction (vector, axial-vector and scalar).

References

[1] CMS Collaboration, The CMS experiment at the CERN LHC, JINST 3, S08004 (2008).

[2] CMS Collaboration, Search for dark matter, extra dimensions, and unparticles in monojet events in proton-proton collisions at $\sqrt{s} = 8$ TeV, $[arXiv : 1408.3583[hep-ex]]$, CMS-PAS-EXO-12-048

[3] CMS Collaboration, Search for Dark Matter and Large Extra Dimensions in the photon + Missing Transverse Energy final state in pp Collisions at $\sqrt{s} = 8$ TeV in the CMS Experiment with 19.6 fb^{-1} of data, CMS-PAS-EXO-12-047

[4] CMS Collaboration, Search for physics beyond the standard model in final states with a lepton and missing transverse energy in proton-proton collisions at $\sqrt{s} = 8$ TeV, $[arXiv : 1408.2745[hep-ex]]$, CMS-PAS-EXO-12-060, CMS-PAS-EXO-13-004

[5] Yang Bai Tim M.P. Tait, Searches with Mono-Leptons, Phys.Lett. B723 (2013), $[arXiv : 1208.4361[hep-ph]]$, doi 10.1016/j.physletb.2013.05.057

[6] CMS Collaboration, Search for monotop signatures in proton-proton collisions at sqrt(s) = 8 TeV, $[arXiv : 1410.1149[hep-ex]]$, CMS-PAS-B2G-12-022

[7] CMS Collaboration, Search for the Production of Dark Matter in Association with Top Quark Pairs in the Di-lepton Final State in pp collisions at $\sqrt{s}$=8 TeV, CMS-PAS-B2G-13-004

[8] CMS Collaboration, Search for the Production of Dark Matter in Association with Top Quark Pairs in the Single-lepton Final State in pp collisions at $\sqrt{s} = 8$ TeV, CMS-PAS-B2G-14-004

Search for heavy Resonances in Two-Particle Final States with Leptons, Jets and Photons at CMS

Andreas Güth[1] on behalf of the CMS collaboration

[1]III. Physikalisches Institut A, RWTH Aachen University, Aachen, Germany

DOI: http://dx.doi.org/10.3204/DESY-PROC-2014-04/185

At the LHC, the production of heavy resonances decaying into a pair of particles can be probed at unprecedented centre-of-mass energies. Two-particle resonances are predicted in a variety of BSM models and can be searched for in a largely model-independent fashion. Results from searches for resonances in final states with leptons, jets and photons based on the full dataset of 20 fb^{-1} taken by the CMS detector in 2012 in proton-proton collisions at a centre-of-mass energy of 8 TeV are presented. They are interpreted in terms of various theories of BSM physics ranging from generic heavy resonances such as the Z' to excited quarks or Randall-Sundrum gravitons. In the absence of a significant deviation from the expected SM background, 95% CL limits are set on model parameters of the theories under study.

1 Introduction

Searches for heavy resonances constitute an important part of the effort devoted to the test of beyond the Standard Model (BSM) physics carried out by the CMS collaboration at the LHC [1]. This note can only present an excerpt of the full program and is therefore restricted to three exemplary analyses with singly produced resonances which decay into a pair of reconstructed objects. The common feature of these searches is the distinct signal shape of the resonance on top of smoothly falling backgrounds. This leads to shape-based searches which are robust against deviations in the background spectrum in the region of high invariant mass of the two-object system.

2 Dilepton resonances

The search for narrow dilepton resonances in the dimuon and dielectron final states [2] focuses on the mass range above $M_{\ell\ell} = 200$ GeV, well above the Z peak. The interpretation of the results is carried out in terms of different spin-1 Z' signal models. With an invariant mass resolution of about 1% in the dielectron channel above $M_{ee} = 500$ GeV and 4% ($M_{\mu\mu} = 1$ TeV) to 9% ($M_{\mu\mu} = 3$ TeV) in the dimuon channel, the CMS detector is well-suited for the task of finding TeV-scale dilepton resonances. The selection of dimuon events is based on a dataset satisfying a single-muon trigger requirement with a central muon within $|\eta| < 2.1$ and $p_T > 40$ GeV. Two isolated muons, which satisfy identification criteria optimized for the efficient selection of

muons at high p_T, with $p_T > 45$ GeV and $|\eta| < 2.4$ have to be present in the event. The two selected muons are required to carry opposite electric charge, originate from the same vertex and have an opening angle smaller than $\pi - 0.02$ radians, where the latter requirement rejects background from cosmic muons. The invariant mass distribution of selected muon pairs in data is compared to the expectation from SM backgrounds in Fig. 1. Over the entire mass range, the background is dominated by the irreducible $Z/\gamma^* \to \ell\ell$ process. In the search region above $M_{\mu\mu} = 200$ GeV, the Drell-Yan contribution amounts to 80% of the expected background with $t\bar{t}$ and diboson production dominating the remaining 20%.
Dielectron events are selected based on a double-electron trigger asking for two clusters in the electromagnetic calorimeter (ECAL) with $E_T > 33$ GeV. Events containing two isolated electrons with $E_T > 35$ GeV are split into two categories for further analysis: a dielectron sample with both electrons in the central part of the ECAL with $|\eta| < 1.44$ and one with a central electron and the second electron in the ECAL endcap with $1.56 < |\eta| < 2.5$. These subsets of the dielectron candidates differ in background composition and invariant mass resolution.

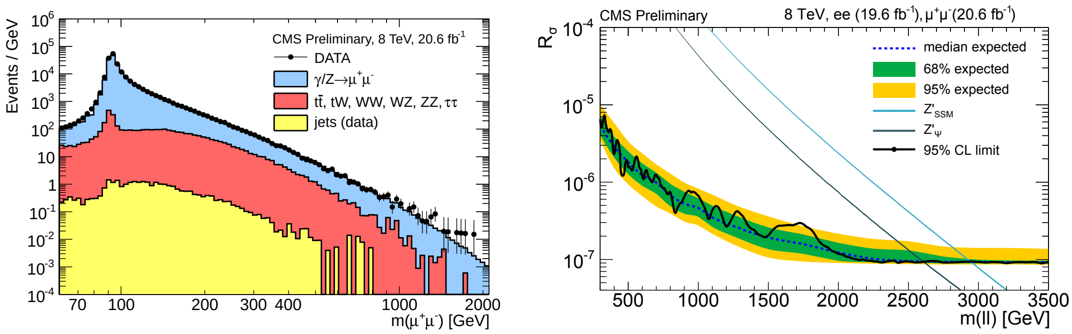

Figure 1: Left: Invariant mass distribution of selected muon pairs. Right: 95% confidence level limits on the cross section ratio R_σ as a function of signal mass.

No significant excess is observed in either dilepton channel and limits on two Z' models are set: a sequential SM Z'_{SSM} and a Z'_ψ expected in certain grand unified theories. In order to reduce the impact of systematic uncertainties on the results, limits are determined on the cross section ratio R_σ between the spin-1 Z' signal and the SM Drell-Yan cross section (including the branching ratios), rather than on the signal cross section. The cross sections in the ratio are evaluated in the mass range $0.6\ M_{Z'} - 1.4\ M_{Z'}$ and $60 - 120$ GeV for the signal and SM Drell-Yan processes, respectively. A Bayesian limit setting procedure using an unbinned likelihood with a uniform prior for the signal cross section is used to derive lower limits on the signal mass at 95% confidence level (CL). Combination of the dimuon channel and the two dielectron channels yields lower limits on the Z' mass of 2960 GeV and 2600 GeV for the Z'_{SSM} and Z'_ψ signals, respectively. The limits on R_σ are shown in Fig. 1.

3 Dijet resonances

At a hadron collider such as the LHC, searches for resonance production in the dijet final state [3] probe a variety of BSM models. At a signal mass of 1 TeV, the signal cross sections for the different resonance models considered (Table 1) cover a wide range from the pb regime in case of weakly coupling models such as the Z'_{SSM} up to several nb for string resonances. The models further differ in the type of jets in the final state (qq, qg, gg or a combination).

This leads to different resonance shapes depending on the signal under study, with larger low-mass tails in final states containing gluon jets. The statistical interpretation is therefore carried out with different signal shapes, depending on the final state.
The jet reconstruction starts from the particle-flow (PF) CMS event reconstruction and builds jets using the anti-k$_T$ algorithm with jet parameter $R = 0.5$ (AK5 jets). Among the jets with $p_T > 30$ GeV and $|\eta| < 2.5$, the two leading jets are selected and two "wide jets" are formed around them by adding the Lorentz vectors of all other jets within $\Delta R = \sqrt{(\Delta\eta)^2 + (\Delta\phi)^2} = 1.1$. The two wide jets then form the dijet system used in the analysis with invariant mass M_{jj}. This approach reduces the sensitivity to gluon radiation off the two partons from the resonance decay. The event selection is performed on a dataset obtained from a combination of two triggers selecting events with the scalar sum of the jet transverse momenta above $H_T = 650$ GeV or with $M_{jj} > 750$ GeV, respectively. The selection of two wide jets is performed as described above and they both have to fall within $|\eta| < 2.5$. Requiring a small pseudorapidity gap of $|\Delta\eta_{jj}| < 1.3$ reduces the SM dijet background. Events with $M_{jj} < 890$ GeV are rejected. The resulting dijet mass spectrum is depicted in Fig. 2 and compared to the expectation.

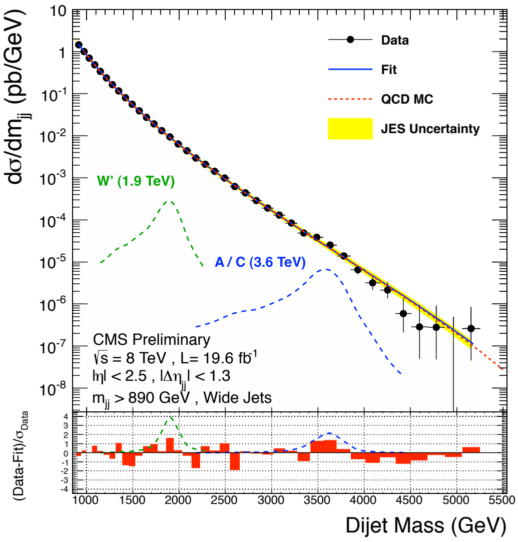

Figure 2: Invariant mass distribution of selected wide jet pairs. Signal distributions are shown for W' and axigluon/coloron signals.

In the absence of a significant excess, upper limits are set on the product of signal cross section, branching ratio, and acceptance for the various resonance models. The 95% CL upper limits are obtained from a Bayesian approach with uniform prior for the signal cross section and derived for the three different combination of jet types, qq, qg, and gg, all of which come with different resonance shapes. The observed limits on the cross section for signals with qq final state are stronger than for those with gg final state by a factor 2 to 3. The corresponding excluded ranges of the resonance mass for different signal models are given in Table 1 and reach up to 5 TeV in case of string resonances. Searches for dijet resonances have also been performed by the CMS collaboration with b-tagged jets [4] and W/Z-tagged jets [5].

Model	Final State	Obs. Mass Excl. [TeV]
String Resonance	qg	[1.20 , 5.08]
Excited Quark	qg	[1.20 , 3.50]
E_6 Diquark	qq	[1.20 , 4.75]
Axigluon/Coloron	q$\bar{q}$	[1.20 , 3.60]+ [3.90 , 4.08]
Color Octet Scalar	gg	[1.20 , 2.79]
W' Boson	q$\bar{q}$	[1.20 , 2.29]
Z' Boson	q$\bar{q}$	[1.20 , 1.68]
RS Graviton	q$\bar{q}$+gg	[1.20 , 1.58]

Table 1: Excluded resonance mass ranges at 95% CL for the different signal models.

4 Photon+jet resonances

The search for resonances in the photon+jet invariant mass spectrum [6] is motivated by theories of quark compositeness at an energy scale Λ involving excited quark states q^*. The production of the excited quark via quark-gluon fusion and the decay into the photon+quark final state involve strong and electromagnetic gauge couplings with a coupling modifier f as a free parameter. A combination of spin-1/2, mass degenerate excitations of the first generation quarks $q^* = (u^*, d^*)$ is used as the signal model.

Photon+jet pairs are selected from a dataset that has been collected with a single-photon trigger with $E_T > 150$ GeV. The presence of at least one isolated photon with $p_T > 170$ GeV in the central part of the ECAL with $|\eta| < 1.44$ is requested. Selected AK5 jet candidates have to be separated in $\eta - \phi$ space by $\Delta R > 0.5$ from the selected photon. The leading jet with $p_T > 170$ GeV and $|\eta| < 3$ is chosen. The dominant backgrounds in this search, QCD photon+jet production and dijet events with a jet misidentified as a photon, are produced predominantly via t-channel diagrams. These contributions are reduced by requiring $|\Delta\eta_{\gamma j}| < 2.0$ and a back-to-back topology $|\Delta\phi_{\gamma j}| > 1.5$. The invariant mass $M_{\gamma j}$ has to exceed 560 GeV. After selection, the expected background composition is dominated by SM photon+jet production, which contributes 80.5%, followed by dijet events with 18.5% and electroweak backgrounds with 1%. The invariant mass resolution ranges from 4.5% at $M_{\gamma j} = 1$ TeV to 3% at $M_{\gamma j} = 3$ TeV. The observed invariant mass distribution exhibits no significant deviation from the background expectation, and bounds in the two-parameter space of coupling modifier f and the excited quark mass M_{q^*} at 95% CL are obtained, as shown in Fig. 3. For the choice $f = 1$ and $\Lambda = M_{q^*}$, excited quarks are excluded at 95% CL in the mass range 0.7 TeV $< M_{q^*} <$ 3.5 TeV.

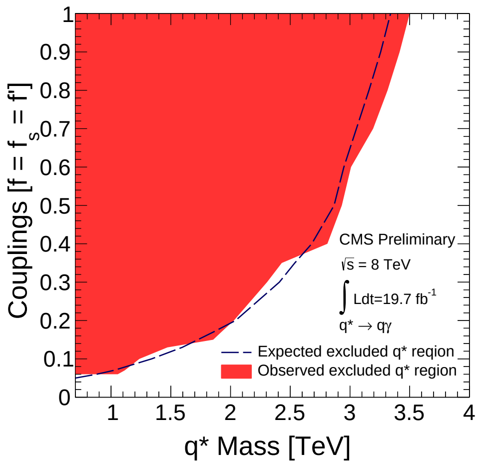

Figure 3: 95% CL bounds in the two-parameter space of coupling modifier f and M_{q^*}, assuming $\Lambda = M_{q^*}$.

References

[1] CMS collaboration, *The CMS experiment at the CERN LHC*, JINST **3** S08004 (2008).

[2] CMS collaboration, *Search for Narrow Resonances in Dilepton Mass Spectra in pp Collisions at $\sqrt{s}$= 8 TeV*, CMS Physics Analysis Summary **CMS-PAS-EXO-12-061** (2013).

[3] CMS collaboration, *Search for Narrow Resonances using the Dijet Mass Spectrum with 19.6 fb^{-1} of pp Collisions at $\sqrt{s}$=8 TeV*, CMS Physics Analysis Summary **CMS-PAS-EXO-12-059** (2013).

[4] CMS collaboration, *Search for Heavy Resonances Decaying into $b\bar{b}$ and bg Final States in pp Collisions at $\sqrt{s}$ = 8 TeV*, CMS Physics Analysis Summary **CMS-PAS-EXO-12-023** (2013).

[5] CMS collaboration, *Search for massive resonances in dijet systems containing jets tagged as W or Z boson decays in pp collisions at $\sqrt{s}$ = 8 TeV*, JHEP **08** 173 (2014).

[6] CMS collaboration, *Search for excited quarks in the γ+jet final state in proton-proton collisions at $\sqrt{s}$ = 8 TeV*, arXiv:hep-ex/1406.5171 (2014).

Constraints on new phenomena through Higgs coupling measurements with the ATLAS detector

Camilla Maiani[1] on behalf of the ATLAS Collaboration

[1]DSM/IRFU (Institut de Recherches sur les Lois Fondamentales de l'Univers), CEA Saclay (Commissariat à l'Energie Atomique et aux Energies Alternatives), Gif-sur-Yvette, France

DOI: http://dx.doi.org/10.3204/DESY-PROC-2014-04/229

The ATLAS experiment at the Large Hadron Collider has measured the couplings of the newly found Higgs boson to other particles using about 25 fb^{-1} of proton-proton collision data at 7 and 8 TeV center-of-mass energy. These measurements have been used to contrain the parameters on new physics phenomena. In this document a short review of such studies is presented. No deviations from the Standard Model are observed. Perspectives at the High-Luminosity LHC are also discussed.

1 Introduction

The ATLAS [1] and CMS [2] Collaborations at the Large Hadron Collider (LHC) announced the discovery of a new particle in the summer of 2012 [3, 4]. The measurements of the new-found particle's mass [5, 6], coupling parameters [5, 6] and spin-parity [7, 8, 9] are compatible, within experimental uncertainties, with those of a Standard Model (SM) Higgs boson. The question remains open whether the Higgs sector is extended, and a whole family of Higgs-like bosons exists at higher mass, as predicted by many Beyond the SM (BSM) theories. At ATLAS, some BSM are tested by performing both direct searches for new particles, and indirectly by using the Higgs boson coupling measurements to put constraints. In this report, a short review of some of the indirect searches performed is described, a full discussion can be found in Ref. [10]. Perspectives at the High-Luminosity (HL) LHC [11], are also discussed.

2 Methodology and statistical treatment

The analyses presented use the full data sample collected by ATLAS during the first run of the LHC in 2011 and 2012, corresponding to about 25 fb^{-1} of proton-proton collision data at 7 and 8 TeV center-of-mass energy. The measurements of the Higgs boson couplings to bosons and fermions in all studied channels are considered: $h \to \gamma\gamma$, $h \to ZZ^\star \to 4\ell$, $h \to WW^\star \to \ell\nu\ell'\nu'$, $h \to \tau\tau$ and $h \to b\bar{b}$. The direct search for $Zh \to \ell\ell +$ invisible is also considered in the studies presented in Sec. 5. Relying on the Higgs coupling measurements confidence intervals are set on the BSM parameters based on a profile likelihood ratio test [12], following the method described in Ref. [13, 14]. The likelihood function used is defined as the product of the likelihood functions in each channel, and depend on the parameters of interest, such as the signal strength, the Higgs boson mass m_h or the couplings. Experimental and theoretical systematic uncertainties are introduced in the likelihood by means of nuisance parameters. In each decay channel, the likelihood describes the optimal observable for signal to background separation; in the $h \to \gamma\gamma$ case, for example, the discriminant observable is the di-photon invariant mass. The signal shape is extracted from Monte Carlo (MC), whereas the background shape comes from either MC or data driven estimates.

3 Two-Higgs-doublet model

A simple extension of the SM is a class of models named Two-Higgs-Doublet Models (2HDMs) [15]. These models predict the existence of an additional Higgs doublet: one neutral CP-even boson H, one neutral CP-odd boson A, and two charged bosons $H^{\pm}$. Different couplings to vector bosons and fermions are tested [10]. Limits are set on the $(\cos(\beta - \alpha), \tan(\beta))$ plane and are found to be consistent with the SM expectations for all the coupling configurations tested. In Fig. 1, limits obtained in one case considered are shown.

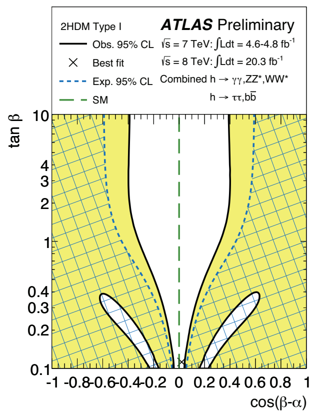

Figure 1: Regions of the $(\cos(\beta - \alpha), \tan(\beta))$ plane for a coupling configuration of 2HDMs excluded by fits to the measured rates of the Higgs boson production and decays. The cross marks the best fit value, the light shaded and hashed regions indicate the observed and expected 95% confidence level exclusions. [10]

4 Simplified minimal supersymmetric model

Supersymmetry [16] was introduced to solve the hierarchy problem, and provides Weakly Interacting Massive Particles (WIMPs) that are good candidates for dark matter. In this study, limits have been set, within the simplified Minimal SuperSymmetric Model (MSSM) formalism, in the (m_A, $\tan(\beta)$) plane. Results are shown in Fig. 2 (left). The observed (expected) lower limit at 95% Confidence Level (CL) on m_A is 400 GeV (280 GeV) for $2 \leq \tan(\beta) \leq 10$. Everything is consistent with the SM, although there is still a large unexplored region for $\tan(\beta) > 1$.

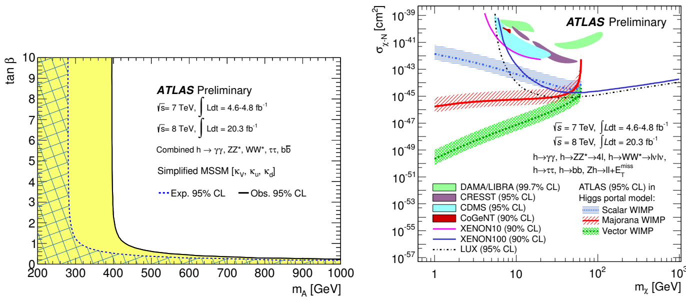

Figure 2: Left: regions of the $(\mathrm{m_A}, \tan(\beta))$ plane excluded in a simplified MSSM model via fits to the Higgs boson production and decay rates. The light shaded and hashed regions indicate the observed and expected 95% CL exclusions respectively. [10] Right: ATLAS 95% CL upper limit on the WIMP-nucleon scattering cross section in a Higgs portal model as a function of the dark matter candidate's mass for different spin configurations. Excluded and allowed regions from direct detection experiments are also shown. [10]

5 Higgs portal to dark matter

In the "Higgs portal to dark matter" models [17, 18] a WIMP is introduced as a dark matter candidate, that interacts very weakly with all SM particles except the Higgs boson. From the Higgs boson coupling measurements, and from direct searches of $Zh \to \ell\ell +$invisible, the upper limit at 95% CL on the Branching Ratio of the Higgs boson to invisible final states ($\mathrm{BR_{inv}}$) is found to be $\mathrm{BR_{inv}} < 0.37$, where the expectation is 0.39. The upper limit is then transformed into constraints on the coupling of the WIMP to the Higgs boson as a function of its mass [18] to allow for comparison with direct searches for dark matter [19]. The results are shown in Fig. 2 (right) for different spin configurations of the WIMP. The ATLAS experiment results dominate in a broad region at low mass.

6 Perspectives at HL LHC

The LHC is expected to be brought to the high luminosity phase in 2023. Five to ten times the nominal luminosity will be reached in the HL-LHC collisions, and about 3000 fb^{-1} of proton-proton data will be collected by 2030 at 14 TeV of center-of-mass energy. Experimental precisions of 1.5% and 3% are expected on the couplings of the Higgs boson to vector bosons and fermions respectively. In the Higgs portal to dark matter studies expected limits on $\mathrm{BR_{inv}}$ will be set at the level of 8 to 16% in direct $Zh \to \ell\ell +$ invisible searches, and of 12 to 15% in indirect searches from coupling measurements.

7 Summary

The data collected during the first phase of the operation at the LHC have been used to extract a first measurement of the Higgs boson couplings. Such measurements allow to perform indirect searches for new physics at high energy. The results presented show an impressive consistency with the SM, and allow to set limits on the parameters of the BSM models studied.

Acknowledgements

This report was supported by the European Research Council, Grant Agreement N^o 279170 DIBOSON.

References

[1] ATLAS Collaboration, JINST **3** S08003 (2008).

[2] CMS Collaboration, CMS-TDR-008-1/2 (2006).

[3] ATLAS Collaboration, Phys. Lett. **B 716** 1 (2012), [arXiv:1207.7214].

[4] CMS Collaboration, Phys. Lett. **B 716** 30 (2012), [arXiv:1207.7235].

[5] ATLAS Collaboration, Phys. Lett. **B 726** 88 (2013), [arXiv:1307.1427].

[6] CMS Collaboration, CMS-PAS-HIG-13-005 (2013).

[7] ATLAS Collaboration, Phys. Lett. **B 726** 120 (2013), [arXiv:1307.1432].

[8] CMS Collaboration, Phys. Rev. Lett. **110** 081803 (2013), [arXiv:1212.6639].

[9] CMS Collaboration, [arXiv:1312.5353].

[10] ATLAS Collaboration, ATLAS-CONF-2014-010 (2014), http://cds.cern.ch/record/1670531/files/ATLAS-CONF-2014-010.pdf.

[11] ATLAS Collaboration, ATL-PHYS-PUB-2013-015 (2013), https://cds.cern.ch/record/1611189/files/ATL-PHYS-PUB-2013-015.pdf.

[12] G. Cowan *et al.*, Eur. Phys. J. **C 71** 1554 (2011).

[13] ATLAS Collaboration, Phys. Rev. **D 86** 032003 (2012).

[14] ATLAS and CMS Collaborations, ATL-PHYS-PUB-2011-011 CERN-CMS-NOTE-2011-005 (2011), https://cds.cern.ch/record/1375842/files/ATL-PHYS-PUB-2011-011.pdf.

[15] LHC Higgs Cross Section Working Group, [arXiv:1307.1347]; T. Lee, Phys. Rev. **D 8** 1226 (1973); J. F. Gunion and H. E. Haber, Phys. Rev. **D 67** 075019 (2003), [arXiv:hep-ph/0207010]; G. Branco *et al.*, Phys. Rept. **516** 1 (2012), [arXiv:1106.0034].

[16] H. Miyazawa, Prog. Theor. Phys. **36** no. 6 1266 (1966); P. Ramond, Phys. Rev. **D 3** 2415 (1971); Y. Golfand and E. Likhtman, JETP Lett. **13** 323 (1971); A. Neveu and J. Schwarz, Nucl. Phys. **B 31** 86 (1971); A. Neveu and J. Schwarz, Phys. Rev. **D 4** 1109 (1971); J.-L. Gervais and B. Sakita, Nucl. Phys. **B 34** 632 (1971); D. Volkov and V. Akulov, Phys. Lett. **B 46** 109 (1973); J. Wess and B. Zumino, Phys. Lett. **B 49** 52 (1974); J. Wess and B. Zumino, Nucl. Phys. **B 70** 39 (1974).

[17] ATLAS Collaboration, [arXiv:1402.3244]; B. Parr and F. Wilczek, [arXiv:hep-ph/0605188]; S. Kanemura *et al.*, Phys. Rev. **D 82** 055026 (2010), [arXiv:1005.5651]; P. J. Fox *et al.*, Phys. Rev. **D 85** 056011 (2012), [arXiv:1109.4398]; L. Lopez-Honorez *et al.*, Phys. Lett. **B 716** 179 (2012), [arXiv:1203.2064]; ATLAS Collaboration, Phys. Rev. Lett. **112** 041802 (2014), [arXiv:1309.4017].

[18] A. Djouadi *et al.*, Phys. Lett. **B 709** 65 (2012), [arXiv:1112.3299].

[19] XENON10 Collaboration, Phys. Rev. Lett. **107** 051301 (2011), [arXiv:1104.3088]; XENON100 Collaboration, Phys. Rev. Lett. **109** 181301 (2012), [arXiv:1207.5988]; P. Belli *et al.*, Phys. Rev. **D 84** 055014 (2011), [arXiv:1106.4667]; G. Angloher *et al.*, Eur. Phys. J. **C 72** 1971 (2012), [arXiv:1109.0702]; CDMS Collaboration, Phys. Rev. Lett. **111** (2013), [arXiv:1304.4279]; CoGeNT Collaboration, Phys. Rev. Lett. **107** 141301 (2011), [arXiv:1106.0650]; LUX Collaboration, [arXiv:1310.8214].

Searches for dark matter and extra dimensions with the ATLAS detector

Christophe Clément[1] on behalf of the ATLAS Collaboration

[1]Stockholm University, Fysikum, 106 91 Stockholm, Sweden

DOI: http://dx.doi.org/10.3204/DESY-PROC-2014-??/204

This paper presents the results of different approaches to finding evidence for dark matter with the ATLAS experiment at LHC. These include searches for events with large missing transverse momentum and a single jet, photon or W/Z boson. Searches for hidden sectors in events with long-lived particles resulting in displaced hadronic vertices or lepton-jet signatures are also reported. Finally, studies sensitive to the presence of extra spatial dimensions are described, as for example classical and quantum black holes and other non-resonant phenomena. Results from $\sqrt{s} = 8$ TeV ATLAS data taking are presented.

1 Dark Matter

The origin of dark matter is one of the outstanding questions in contemporary physics. Collider experiments such as ATLAS are sensitive to the pair production of so-called Weakly Interacting Massive Particles (WIMPs) in association with an initial state radiation jet, photon or W/Z, $p+p \to \chi\chi + X$, where χ denotes the WIMP and X is either a jet, photon or W/Z. The χ pair escapes the detector undetected, leading to a signature of missing transverse energy ($E_{\mathrm{T}}^{\mathrm{miss}}$). The remaining signal characteristics are determined by the nature of X.

In the case of hadronically decaying W/Z [1], the two daughter quarks are boosted and yield a large cone jet. The large jet is reconstructed using the Cambridge-Aachen algorithm [2] of size $\Delta R = 1.2$, with transverse momentum $p_{\mathrm{T}} > 250$ GeV and $|\eta| < 1.2$. It is required that two anti-k_T jets of size $\Delta R = 0.4$ are also found inside the fat jet and that the momentum is fairly distributed between them as expected from W/Z decays, this is ensured by $\sqrt{y} = \frac{\min(p_{\mathrm{T1}},p_{\mathrm{T2}})\Delta R_{\mathrm{jj}}}{m_{\mathrm{jet}}} > 0.4$, where m_{jet} is the invariant mass of the two small jets, and p_{T1}, p_{T2} are their momenta and ΔR_{jj} is the inter-jet distance. Finally for consistency with a W/Z decay, it is required $50 < m_{\mathrm{jet}} < 120$ GeV. A veto is applied against leptons, photons and light jets. Two signal regions are defined with $E_{\mathrm{T}}^{\mathrm{miss}} > 350$ and 500 GeV.

In the case of leptonically decaying W [3], a single electron (muon) with $p_{\mathrm{T}} > 125$ GeV (45 GeV) is required. The same lepton-dependent selection cut value is applied on the $E_{\mathrm{T}}^{\mathrm{miss}}$. The final discriminating variable is the transverse mass $m_{\mathrm{T}} = \sqrt{2p_{\mathrm{T}}E_{\mathrm{T}}^{\mathrm{miss}}(1-\cos\phi_{\ell\nu})}$, where $\phi_{\ell\nu}$ is the distance in the azimuthal angle ϕ between the charged lepton and the direction of $E_{\mathrm{T}}^{\mathrm{miss}}$. Several signal regions are used with different thresholds on m_{T} but start to be sensitive to new physics at $m_{\mathrm{T}} > 252$ GeV.

If the associated boson is Z decaying into two charged leptons [4], the identification of the final state relies on the presence of two same flavour leptons denoted ℓ (electrons or muons), with $p_{\mathrm{T}} > 20$ GeV and such that their invariant mass is within 10 GeV of the Z-boson mass, and $|\eta|$ of the dilepton system is required to be within 2.5. The dilepton system is required to balance $E_{\mathrm{T}}^{\mathrm{miss}}$ in both direction and magnitude, with $\Delta\phi(E_{\mathrm{T}}^{\mathrm{miss}}, p_{\mathrm{T},\ell\ell}) > 2.5$, where $p_{\mathrm{T},\ell\ell}$ is the transverse momentum of the dilepton system, and $|E_{\mathrm{T}}^{\mathrm{miss}} - p_{\mathrm{T},\ell\ell}| < 0.5$. Several signal regions are defined by a final selection on the $E_{\mathrm{T}}^{\mathrm{miss}}$ which ranges from 150 to 450 GeV.

The results from ATLAS dark matter searches are translated into upper limits on the WIMP-nucleon cross section as function of the WIMP mass (m_χ) in Fig. 1 using an effective field theory approach [5], in the case of spin-independent (left panel) and spin-dependent interactions (right panel).

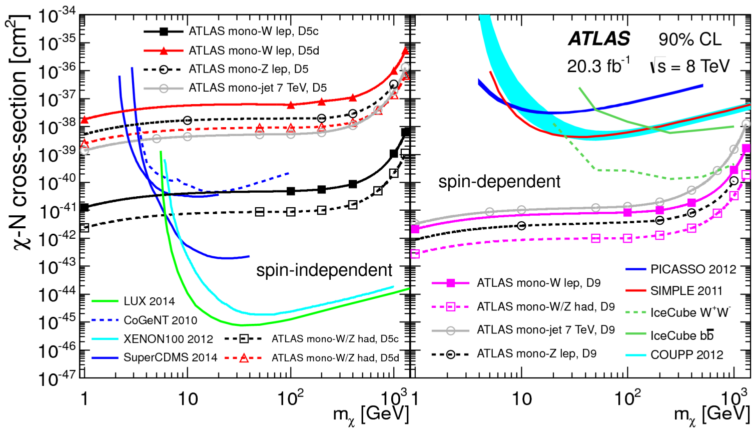

Figure 1: Summary of ATLAS upper limits on WIMP-nucleon cross section for spin-independent (spin-dependent) interactions on the left (right) panel.

2 Hidden Valley

A number of extensions of the Standard Model of particle physics (SM) involve a hidden sector that is weakly coupled to the SM, via a heavy communicator scalar particle, Φ_{HS} of mass m_Φ [6]. In the model considered here the Φ_{HS} couples to mass in the same manner as the Higgs. A confining gauge in the Hidden Sector leads to the existence of so-called valley-hadrons and include long-lived valley-pions denoted here π_v. Using a dedicated trigger that looks at the ratio of energy in the hadron calorimeter (E_{H}) to that in the electromagnetic calorimeter (E_{EM}), the ATLAS experiment looks for π_v decaying into SM hadrons deep in the electromagnetic calorimeter or inside the hadronic calorimeter [7]. The signal is searched for by selecting collisions which present two hadronic jets with $E_{\mathrm{H}}/E_{\mathrm{EM}} > 1.2$ and p_{T} of the leading jet greater than 60 GeV, and no tracks close to the jet. Standard model backgrounds are reduced by requiring $E_{\mathrm{T}}^{\mathrm{miss}}$ <50 GeV. Figure 2 shows the resulting exclusion limits on the proper decay length of the π_v as function of its mass $m_{\pi v}$ and m_Φ.

3 Black Holes

Black holes relevant to particle physics are predicted in models with n extra dimensions. While SM particles are confined to the usual 3+1 dimensions, gravity is permitted to propagate to the extra dimensions. In this class of models the fundamental gravity scale M_{D} is given by $M_{\mathrm{D}}^{2+n} = M_{\mathrm{Planck}}^2 R^{-n}/8\pi$, where M_{Planck} is the usual Planck mass and R is the size of the extra dimensions. The fundamental gravity scale M_{D} could potentially be as small as a few TeV and thus requires investigation at LHC. Two types of black holes are investigated, quantum black holes (QBH), semi-classical black holes (BH).

The QBH are relevant when the black holes are produced close to their production threshold M_{th}. In this regime the QBH decays into two high p_{T} particles, including lepton+quark final states that violate baryon and lepton numbers. The signal region [8] is defined by the presence of a single electron or muon with $p_{\mathrm{T}} > 130$ GeV and a jet. The final discriminating variable is the invariant mass of the lepton-jet system $M(\ell, jet)$ required to be larger than $0.9M_{\mathrm{th}}$ in the electron channel and larger than $([0.95 - 0.05 \times M_{\mathrm{th}}]/1\mathrm{TeV}) \times M_{\mathrm{th}}$ in the muon channel.

The semi-classical approximation of thermal black holes where the BH loses mass and angular momentum via Hawking radiation is valid if $M_{\mathrm{th}} >> M_{\mathrm{D}}$, the BH decays to a high particle multiplicity, high p_{T} particle final state including both leptons and hadrons. The signal region [9] is defined by requiring at least one electron or muon with $p_{\mathrm{T}} > 100$ GeV and at least two more particles with $p_{\mathrm{T}} > 100$ GeV. The final discriminating variable is the scalar sum of the p_{T} of all particles with $p_{\mathrm{T}} > 60$ GeV, including both leptons and jets, and denoted $\sum p_{\mathrm{T}}$. The signal region is defined by $\sum p_{\mathrm{T}} > 2000$ GeV.

Figure 3 presents a selection of the ATLAS exclusion limits on QBH (left) and semi-classical black holes (right). In the case of QBH, production thresholds of up to 5.5 TeV are excluded. In the case the semi-classical black holes n =2 to 6 extra dimensions have been investigated, two models have been considered for black hole production and decay using CHARYBDIS [10] and BLACKMAX [11]. Both rotating and non-rotating black holes have been considered. In all cases production thresholds below 5−6 TeV are excluded for M_{D} between 1.5−4 TeV.

Acknowledgments

The author would like to acknowledge support from the Swedish Research Council and Stockholm University Natural Science Faculty.

MC sample m_Φ, $m_{\pi v}$ [GeV]	excluded range 30% BR $\Phi_{\mathrm{HS}} \to \pi_{\mathrm{v}}\pi_{\mathrm{v}}$ [m]	excluded range 10% BR $\Phi_{\mathrm{HS}} \to \pi_{\mathrm{v}}\pi_{\mathrm{v}}$ [m]
126, 10	0.10 - 4.38	0.13 - 2.30
126, 25	0.27 - 10.01	0.37 - 5.12
126, 40	0.54 - 12.11	0.86 - 5.62

Figure 2: ATLAS excluded range at 95% CL for the proper decay length of the π_v for different masses $m_{\pi v}$ and m_Φ and values of the branching ratio (BR) of $\Phi_{\mathrm{HS}} \to \pi_v\pi_v$.

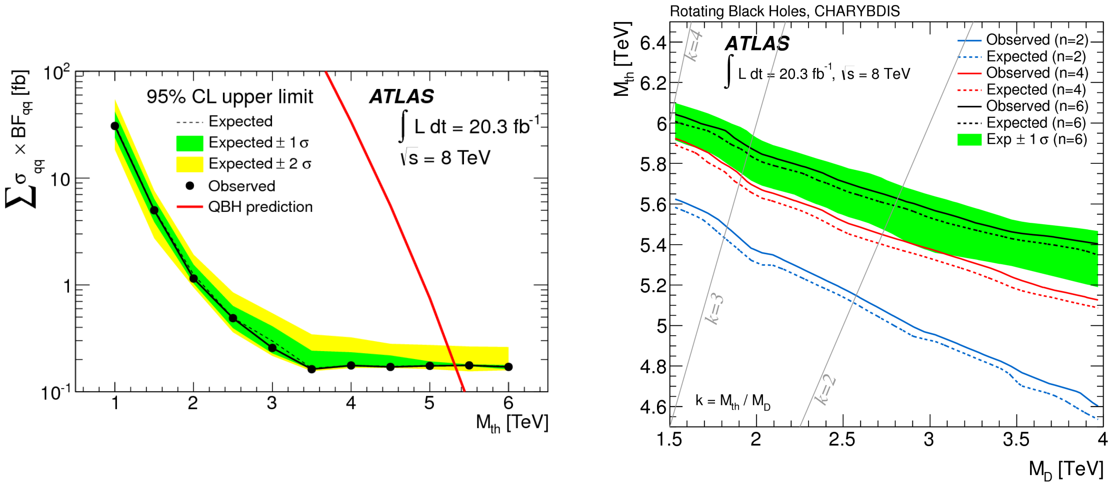

Figure 3: Left: ATLAS upper limit at 95% CL on the total quantum black hole production cross section given by the sum over all quark-quark production channels times the branching ratio of each channel into the quark+lepton final state, as function of the production threshold $M_{\rm th}$. Right: ATLAS excluded region in the case of semi-classical black holes, in the plane $M_{\rm D}, M_{\rm th}$, reproduced here in the scenario of rotating black holes simulated with CHARYBDIS.

References

[1] ATLAS Collaboration, Phys. Rev. Lett. 112, 041802 (2014).
[2] Y. L. Dokshitzer et *al.*, J. High Energy Phys. 08 (1997).
[3] ATLAS Collaboration, J. High Energy Phys. 09, 037 (2014).
[4] ATLAS Collaboration, Phys. Rev. D 90, 012004 (2014).
[5] J. Goodman et *al.*, Phys.Rev. D 82, (2011).
[6] M. J. Strassler and K. M. Zurek, Phys. Lett. B 651, 374379 (2007).
[7] ATLAS Collaboration, Public Conference Result, ATLAS-CONF-2014-041 (2014).
[8] ATLAS Collaboration, J. High Energy Phys. 08, 103 (2014).
[9] ATLAS Collaboration, Phys. Rev. Lett. 112, 091804 (2014).
[10] J. A. Frost et al., J. High Energy Phys. 10, 014 (2009).
[11] D.-C. Dai et *al.*, Phys. Rev. D 77, 076007 (2008).

Search for New Physics with Top quarks in ATLAS at 8 TeV ($t\bar{b}$, $t\bar{t}$, vector-like quarks)

David Calvet on behalf of the ATLAS Collaboration

LPC Clermont-Ferrand, BP80026, 63171 Aubière cedex, France

DOI: http://dx.doi.org/10.3204/DESY-PROC-2014-04/206

This contribution presents results from searches for new resonances (W', Z', g_{KK}), decaying to a top-antibottom pair or a top-antitop pair, including the use of boosted top quark reconstruction techniques. Results from the search for vector-like quarks (focusing on the decay channels $T \to Zt$ and $B \to Zb$) are also presented. These searches use the data sample recorded in 2012 at $\sqrt{s} = 8$ TeV centre-of-mass energy by the ATLAS experiment at the LHC. Data are in good agreement with the Standard Model predictions, therefore limits are derived on the production of these new processes.

1 Introduction

The Standard Model (SM) of particle physics is a tremendous success, in particular with the recent discovery at LHC of a new scalar boson that is compatible with the one predicted by the Brout-Englert-Higgs mechanism. However, several aspects indicate that the SM cannot be the ultimate theory and many extensions[1] have been proposed in the past. Most of them predict the existence of new heavy particles, usually coupled preferentially to the top quark due to its very high mass. Among these new particles, this contribution will focus on W' decaying to $t\bar{b}$, new $t\bar{t}$ resonances (Z' and g_{KK}) and vector-like quarks (VLQ), with the ATLAS [1] detector.

2 $W' \to t\bar{b}$

In the SM, the W boson couples only to left-handed fermions. It is therefore natural to search for a partner of the W that would couple to right-handed fermions, the W'_R. Moreover, some theories beyond the SM (BSM), including extra-dimensions or technicolor, predict the existence of a heavier partner of the standard W, still coupling to left-handed fermions, the W'_L. In this contribution, the W' is supposed to decay mainly to $t\bar{b}$ (or $\bar{t}b$), with an unknown coupling constant g', and the analysis presented here [2] is designed for the reconstruction of the hadronic decay of the top quark. The main target of this analysis is a very heavy W' (from 1.5 to 3 TeV), thus ensuring the decay products are highly boosted.

The selected events must have been triggered by the presence of at least 700 GeV of transverse energy in the calorimeters. Events are not accepted if a high quality electron or muon is present. Each event must contain exactly one b- and one top-quark candidate. The b-quark candidate is a small-R (R=0.4) b-tagged jet with $p_T > 350$ GeV. Being highly boosted, the

[1] In this contribution, only non-SUSY extensions of the SM are considered.

top-quark candidate must be reconstructed as a single large-R (R=1.0) jet with $p_T > 350$ GeV. Both jets must be well separated[2] ($\Delta R > 2.0$). The events are then splitted in two categories: the *one b-tag* category and the *two b-tag* category. In the latter one, a small-R b-tagged jet must be present inside the top-quark candidate.

The background is composed of 99% multijet events in the one b-tag category and of 88% multijet events and 11% $t\bar{t}$ events in the two b-tag category. The multijet background is estimated from data using control regions while the $t\bar{t}$ background is estimated from Monte Carlo (MC) simulation. Figure 1 shows the distributions of the mass of the two jets (m_{tb}) observed in the data for the two categories. The result of background-only fits to these spectra are also shown and exhibits no excess with respect to the SM production. Therefore, 95% confidence level (C.L.) upper limits on the production cross-sections times BR($W' \to t\bar{b}$) are derived as a function of the W' mass, and range from 0.16 pb to 0.33 pb for the W'_L, and from 0.10 pb to 0.21 pb for the W'_R. Assuming $g' = g_{\rm SM}$, these limits can be translated to a lower limit of 1.68 TeV (1.63 TeV expected) for the mass of the W'_L and 1.76 TeV (1.85 TeV expected) for the mass of the W'_R. Removing this assumption, limits can be set in the $(g' - m_{W'})$ plane as can be seen in Fig. 2.

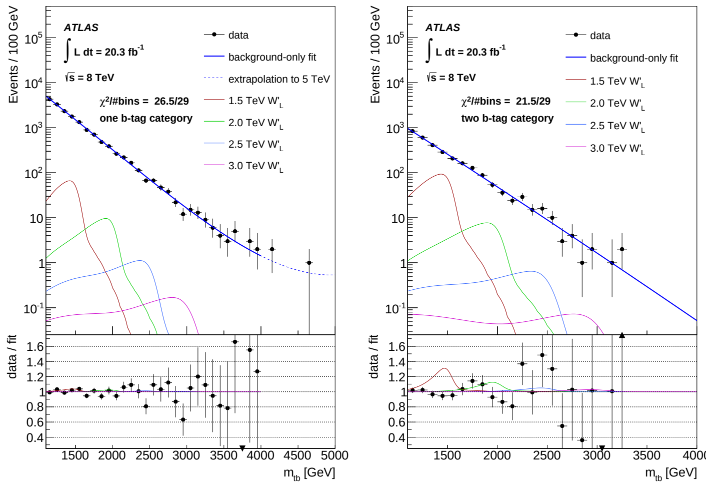

Figure 1: m_{tb} distributions in data in the one b-tag (left) and two b-tag (right) categories. Background-only fits are shown and the bottom plots show the ratio of the data and the fit. Potential W'_L signal shapes with $g'_L = g_{\rm SM}$ are also overlaid.

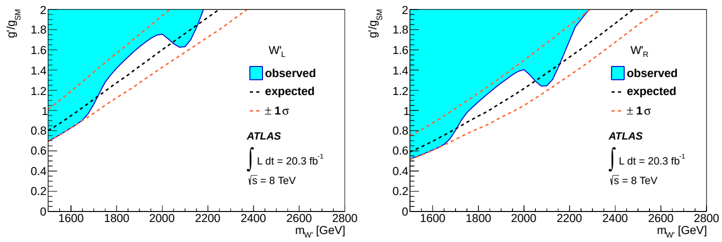

Figure 2: Observed and expected 95% C.L. limits on the ratio of coupling $g'_L/g_{\rm SM}$ ($g'_R/g_{\rm SM}$) of the W'_L (W'_R) model as a function of the W' mass.

3 $g_{KK}/Z' \to t\bar{t}$

New bosons that could decay to $t\bar{t}$ are predicted by several BSM models. In the analysis [3] described in this contribution, two benchmark models are tested: a narrow leptophobic Z' and a Kaluza-Klein (KK) excitation of the gluon in the Randall-Sundrum model.

[2] $\Delta R = \sqrt{\Delta\eta^2 + \Delta\phi^2}$

The selected events must have been triggered by the presence of one electron or muon and each event must contain at least one b-tagged jet. The events are then splitted in two categories: the *resolved* and the *boosted* ones. In the resolved category, the $t\bar{t}$ system is reconstructed using the lepton, the missing transverse momentum and three or four small-R jets. In the boosted category, the top quark that decays leptonically is reconstructed using the lepton, the missing transverse momentum and one small-R jet, while the hadronically decaying top is reconstructed as one high-mass large-R jet.

Figure 3 shows the distribution of the mass of the reconstructed $t\bar{t}$ system observed in data, compared to the SM prediction. No significant excess is observed, therefore 95% C.L. upper limits on the production cross section of new bosons are set. For the Z', these limits can be translated to a lower limit on its mass of 1.8 TeV, while for the KK gluon, the limit on the mass is 2.0 TeV. These results have been obtained with 70% of the statistics available, a refined analysis on the full dataset is being performed.

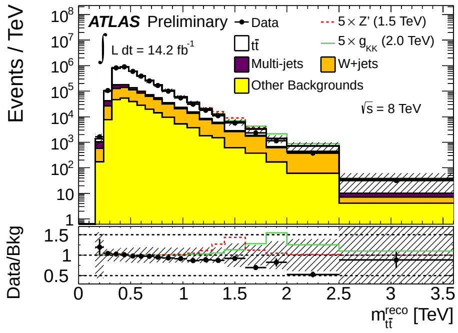

Figure 3: The $t\bar{t}$ invariant mass spectrum, summing the spectra from the resolved and boosted categories.

4 Vector-like quarks

The simple implementation of a fourth generation of quarks is now excluded by the LHC data. Vector-like quarks, predicted by various BSM models, including composite Higgs, are not ordinary quarks because their left- and right-handed components have the same weak isospin. Thanks to this property, such new quarks are still allowed by the current data. In the analysis [4] described in this contribution, the new T (with charge +2/3) and B quarks (with charge -1/3) are searched for, both in the pair and single production processes, concentrating on the $T \to Zt$ and $B \to Zb$ decays, but also including the decays $T \to Wb/Ht$ and $B \to Wt/Hb$.

The selected events must have been triggered by the presence of one electron or muon. Each event must contain at least two central jets ($|\eta| < 2.5$) and an opposite-sign same-flavour pair of electrons or muons that is compatible with the mass of the Z boson and with a p_T above 150 GeV. The events are then splitted in two categories: the *dilepton* category when no additional lepton (e or μ) is present, and the *trilepton* category when at least a third lepton is present. The number of b-tagged jets must be at least one in the trilepton category and at least two in the dilepton category. For the selection of the pair production signal, the scalar sum of the p_T of the jets must also be at least 600 GeV in the dilepton category. For the single production, the presence of at least one forward jet ($2.5 < |\eta| < 4.5$) is required in both categories. Background processes are dominated by Z+jets, WZ and $t\bar{t} + Z$ and are estimated from simulated samples. For the Z+jets samples, a reweighting is applied, determined from a fit of the Z p_T spectrum observed in data in the zero b-tag control region. After selection of the dilepton events, the spectra of the mass of the $Z - b$ system (m_{Zb}) observed in data are compared to the expected ones, both for the pair production selection and for the single production. Similarly, for the trilepton events, the spectra of the scalar sum of the p_T of the jets and the leptons (H_T) are examined. All observed spectra are compatible with the expectations, thus 95% C.L. upper limits on the T and B production cross sections are set.

For the pair production, these limits can be translated to lower limits on the mass of the new quarks assuming some specific values of the decay branching ratios. In the case of $SU(2)$ singlets, these limits are 685 GeV for the B and 655 GeV for the T. If the new quarks are members of $SU(2)$ doublets, the limits are 755 GeV for the B and 735 GeV for the T. Without any assumption on the branching ratios, lower limits on the masses can be set for any configuration, as shown in Figure 4: the best sensitivity is achieved in the lower-left corner, where the branching ratio to Zb/t is 1.

For the single production, the upper limits on the production cross sections are shown in Figure 5 as a function of the new quark mass. As for the pair production, the limits on the T single production are obtained combining the dilepton and trilepton categories, while the limits on the B single production are obtained only with the dilepton events, the trilepton ones being insensitive to this signal.

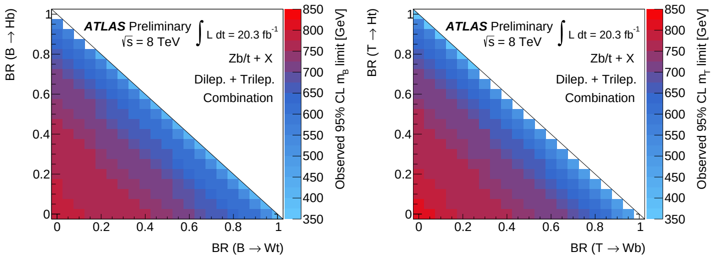

Figure 4: Observed 95% C.L. lower limits on the mass of the B (left) and the T (right) quark as a function of the branching ratios, assuming the pair production hypothesis.

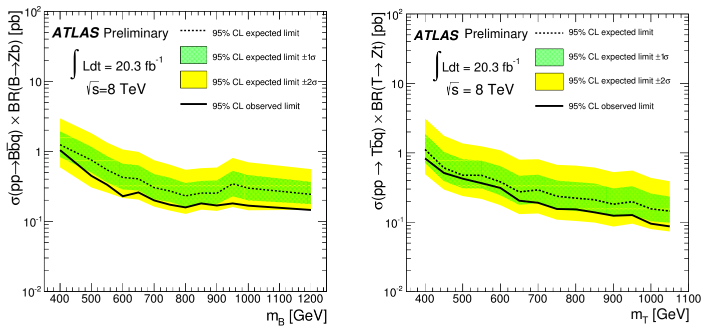

Figure 5: Expected and observed 95% C.L. upper limits on the single production cross section times the branching ratio as a function of the B (left) and the T (right) quark mass.

5 Conclusion

Many analyses are performed by the ATLAS Collaboration searching for non-SUSY new bosons or new fermions with top quarks. In this contribution, only the most recent results have been presented for the W' decaying to $t\bar{b}$, new $t\bar{t}$ resonances and vector-like quarks. The W' search presented here is focusing on high mass W' (above 1.5 TeV), leading to highly boosted top quarks, and the candidates are reconstructed in a fully hadronic mode. The $t\bar{t}$ resonances search combines the resolved and boosted topologies and constrains the Z' and g_{KK} productions. The VLQ search that was presented is designed for the decays $T \to Zt$ and $B \to Zb$ with the Z boson decaying to electrons or muons. None of these analyses exhibit any deviation from the SM prediction, therefore various limits have been derived.

References

[1] ATLAS Collab., JINST 3 S08003 (2008), doi:10.1088/1748-0221/3/08/S08003.

[2] ATLAS Collab., arXiv:1408.0886 [hep-ex].

[3] ATLAS Collab., ATLAS-CONF-2013-052, `https://cds.cern.ch/record/1547568`.

[4] ATLAS Collab., ATLAS-CONF-2014-036, `https://cds.cern.ch/record/1735195`.

Searches for direct pair production of third generation squarks with the ATLAS detector

Giulio Usai[1] on behalf of the ATLAS collaboration

[1]University of Texas at Arlington Arlington, USA

DOI: http://dx.doi.org/10.3204/DESY-PROC-2014-04/208

Naturalness arguments for weak-scale supersymmetry favour supersymmetric partners of the third generation quarks with masses not too far from those of their Standard Model counterparts. Top or bottom squarks with masses less than a few hundred GeV can also give rise to direct pair production rates at the LHC that can be observed in the data sample recorded by the ATLAS detector. This note presents recent ATLAS results from searches for direct stop and sbottom pair production.

1 Introduction

Supersymmetry (SUSY) [1, 9] is an extension of the Standard Model (SM) which can resolve the hierarchy problem by introducing supersymmetric partners to the known fermions and bosons. The dominant contributions for the radiative corrections to the Higgs mass are loop diagrams with top quarks. These can be canceled (naturally) if the supersymmetric partner of the top quark (stop) has a mass below the TeV range. A light bottom squark is also likely because the partners of the left-handed top and bottom squarks share the same mass term in the SUSY-breaking Lagrangian. In R-parity conserving supersymmetric models, the SUSY particles are produced in pairs and the lightest supersymmetric particle (LSP) is stable. In many models the LSP is the lightest neutralino, $\tilde{\chi}_1^0$, which is only weakly interacting and provides a candidate particle to address the dark matter problem.

In these proceedings, a summary of ATLAS searches for third generation squarks is presented. All the searches are based on the 2012 dataset of p p collisions at $\sqrt{s} = 8$ TeV representing about 20 fb^{-1} of integrated luminosity.

2 The ATLAS detector

The ATLAS detector [10] consists of an inner detector (ID) operating in a 2 T superconducting solenoid, a calorimeter system and a muon spectrometer with a toroidal magnetic field. The ID tracking system includes a silicon pixel detector, a silicon microstrip detector (SCT), and a transition radiation tracker (TRT). It provides tracking information for charged particles in a pseudo-rapidity range $|\eta| < 2.5$ and allows identification of jets originating from b-hadron decays. The ID is surrounded by high-granularity liquid-argon (LAr) sampling electromagnetic calorimeters. An iron/scintillator tile calorimeter provides hadronic energy measurements in the central pseudo-rapidity range ($|\eta| < 1.7$). In the forward regions ($1.5 < |\eta| < 4.9$), it is complemented by two end-cap calorimeters using LAr as the active material and copper or tungsten as an absorber. The muon spectrometer (MS) surrounds the calorimeters and consists of three large superconducting eight-coil toroids, a system of tracking chambers, and detectors for triggering.

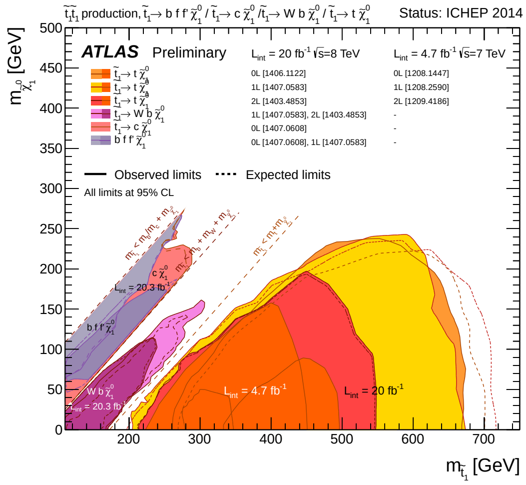

Figure 1: Summary of top squark pair production searches. Exclusion limits at 95% CL are shown in the stop-neutralino mass plane.

3 Top squark searches

The decay of the top squark depends on the mass splitting between the stop and its possible decay products, leading to very different topologies depending on the mass spectrum. For a heavy stop, the dominant decays would be $\tilde{t_1} \to t\tilde{\chi}_1^0$ (kinematically allowed if $\mathrm{m}(\tilde{t_1}) > \mathrm{m(t)} + \mathrm{m}(\tilde{\chi}_1^0)$) and $\tilde{t_1} \to b\tilde{\chi}_1^{\pm}$ which is allowed if $\mathrm{m}(\ \tilde{t_1}) > \mathrm{m(b)} + \mathrm{m}(\ \tilde{\chi}_1^{\pm})$.

If the $\tilde{t_1} \to t\tilde{\chi}_1^0$ decay is kinematically forbidden, the stop could have a three-body decay $\tilde{t_1} \to bW\tilde{\chi}_1^0$ via an off-shell top and if the mass difference between the stop and the lightest neutralino is smaller than the sum of the W boson and b-quark masses, eventually the decay can proceed with an off-shell W or with a loop decay to a charm quark and the lightest neutralino $\tilde{t_1} \to c\tilde{\chi}_1^0$.

The searches for a heavy stop decay are designed based on the decay of the W boson in the top or chargino decay modes, leading to topologies with zero, one or two leptons.

Searches for stop decay in the fully hadronic channel [11] require up to six jets (two of which b-tagged) and show a very good sensitivity at high stop masses. This is reached using large radius ($\Delta R = 1.2$) re-clustering techniques that become very efficient in boosted topologies.

The semi-leptonic analyses [12] make use of shape fits in the E_T^{miss} and m_T variables to distinguish a potential stop signal from the $t\bar{t}$ background showing good sensitivity for high and medium stop masses. The shape-fit techniques push the sensitivity toward the kinematic limit for the stop decay though top. Here the kinematic properties of the signal closely resemble the

$t\bar{t}$ pairs production making this region very challenging. (Stop pairs production cross-section is typically a few percent of the top pairs production and LSPs are very soft).

The fully leptonic final state analyses [13] target both $\tilde{t}_1 \rightarrow b\tilde{\chi}_1^{\pm}$ and $\tilde{t}_1 \rightarrow t\tilde{\chi}_1^0$ decays, making use of a generalization of the transverse mass variable (m_{T2}) as a discriminator between signal and background.

Two other analyses target the very small Δm values, using charm-tagging jets techniques and the monojet selections [14]. These analyses show good sensitivity in this very challenging region up to the kinematic limit. Both these approaches use ISR or FSR to select boosted stops and explore the very compressed decay spectra.

4 Bottom squark searches

The direct production of bottom squarks is targeted by complementary analyses, which are sensitive to different decay modes. A fully hadronic final state search [15] selects events with two b-jets and large E_T^{miss}, and is sensitive to the $\tilde{b}_1 \rightarrow b\tilde{\chi}_1^0$ decay mode. Selection with large values of invariant and cotransverse mass of the two b-jets is sensitive to large values of $\Delta m(\tilde{b}_1, \tilde{\chi}_1^0)$, while the sensitivity to small values of the mass difference is achieved by looking for events with a hard jet produced by initial or final state radiation. We require an untagged leading jet. The observed number of events is in agreement with the SM expectations for both selections. The resulting limits in the sbottom, neutralino mass plane are shown in Fig. 2.

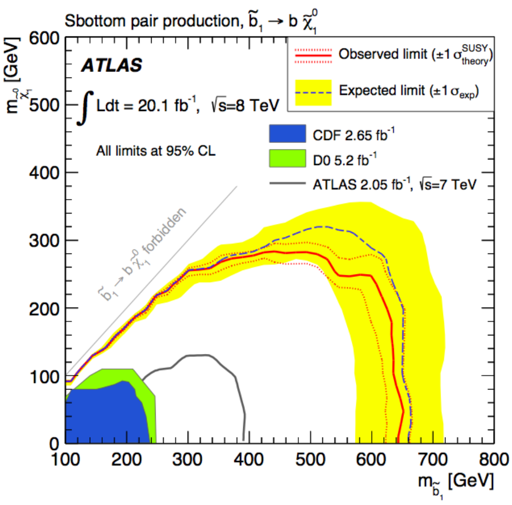

Figure 2: Expected and observed exclusion limits at 95% CL in the $\tilde{b}_1$ $\tilde{\chi}_1^0$ mass plane for the sbottom pair production scenario considered.

A search in events with two same-sign leptons [16] is sensitive to the $\tilde{b}_1 \rightarrow t\tilde{\chi}_1^{\pm} \rightarrow tW\tilde{\chi}_1^0$ decay mode and places exclusion limits on the $\tilde{b}_1$ $\tilde{\chi}_1^{\pm}$ mass plane for fixed neutralino mass values. A search with three b-jets [17] in the final state places limits on models with $\tilde{b}_1 \rightarrow b\tilde{\chi}_2^0 \rightarrow bh\tilde{\chi}_1^0$ where h is the CP-even Higgs boson.

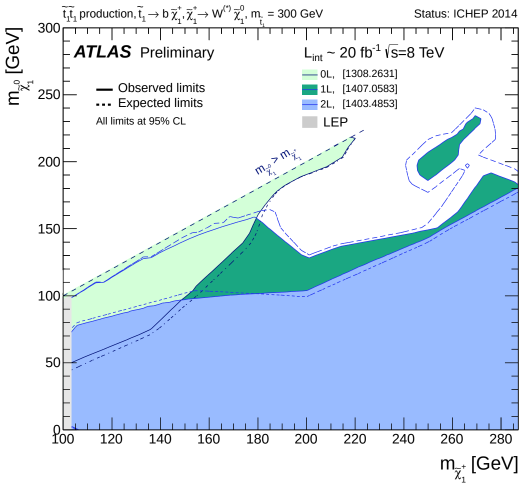

Figure 3: Summary of top squark pair production searches. Exclusion limits at 95% CL are shown in the chargino-neutralino mass plane for stop of 300 GeV.

5 Summary

ATLAS has a number of dedicated searches sensitive to direct production of third-generation squarks. These proceedings give a short reference to these searches, with emphasis on new results.

No significant excesses over the SM expectations are observed, and exclusion limits are set on squark masses. Figure 1 summarizes the exclusion limits obtained by ATLAS as a function of the stop and neutralino masses for simplified models with different stop decays. Under the many assumptions used on these models, stop masses up to about 700 GeV are excluded for a massless neutralino, while for massive neutralinos of 250-300 GeV, stop sensitivity falls to 450-500 GeV. Many important holes are still present close to the various kinematic limits, as illustrated in Figure 3 in the chargino-neutralino mass plane.

References

[1] H. Miyazawa, Prog. Theor. Phys. 36 (6), 1266 (1966)

[2] R. Ramond, Phys. Rev. D3, 2415 (1971)

[3] Y. Golfand, E. Likhtman, JETP Lett. 13, 323 (1971)

[4] A. Neveu, J. Schwarz, Nucl. Phys. B31, 86 (1971)

[5] A. Neveu, J. Schwarz, Phys. Rev. D4, 1109 (1971)

[6] J. Gervais, B. Sakita, Nucl. Phys. B34, 632 (1971)

[7] D. Volkov, V. Akulov, Phys. Lett. B46, 109 (1973)

[8] J. Wess, B. Zumino, Phys. Lett. B49, 52 (1974)

[9] J. Wess, B. Zumino, Nucl. Phys. B70, 39 (1974)

[10] ATLAS Collaboration, JINST 3, S08003 (2008)

[11] ATLAS Collaboration, JHEP 09, (2014) 015

[12] ATLAS Collaboration, submitted to JHEP (arXiv:1407.0583)
[13] ATLAS Collaboration, JHEP 06, (2014) 124
[14] ATLAS Collaboration, Phys. Rev. D. 90, 052008 (2014)
[15] ATLAS Collaboration, JHEP 10, (2013) 189
[16] ATLAS Collaboration, JHEP 06, (2014) 035
[17] ATLAS Collaboration, submitted to JHEP (arXiv:1407.0600)

Chapter 11

Flavour physics - CKM and beyond

New physics searches with b-hadrons at the ATLAS experiment

Lidia Smirnova on behalf of the ATLAS Collaboration

Lomonosov Moscow State University, Faculty of Physics,
119991, Moscow, GSP-1, Leninskie gory 1-2, Russia

DOI: http://dx.doi.org/10.3204/DESY-PROC-2014-04/216

Flavour changing neutral currents and precision measurements of CP violation are investigated by the ATLAS experiment as probes to new physics beyond the standard model. This talk presents the most recent results on the search for the rare decay $B_s^0 \to \mu^+\mu^-$, as well as the latest update on the study of the various angular amplitudes contributing to flavour tagged $B_s^0 \to J/\psi(\mu^+\mu^-)\phi(K^+K^-)$ decays. The latter analysis measures the CP-violating phase ϕ_s, as well as the average B_s meson lifetime Γ_s and the decay width difference $\Delta\Gamma_s$.

1 Introduction

The searches with b-hadrons can present indirect evidence for new physics and show the size of new effects. They are complementary to direct searches. The talk presents the most recent results on the search for the rare decay $B_s^0 \to \mu^+\mu^-$ [1] and the latest update on the study of the various angular amplitudes contributing to flavour tagged $B_s^0 \to J/\psi(\mu^+\mu^-)\phi(K^+K^-)$ decays [2]. Both results are based on the integrated luminosity of 4.9 fb^{-1}, collected in 2011 for pp data at $\sqrt{s} = 7$ TeV.

2 Search for $B_s^0 \to \mu^+\mu^-$ rare decay

The decay $B_s^0 \to \mu^+\mu^-$ is highly suppressed in the standard model (SM) and therefore is of particular interest in the search for new physics. The existence of new hypothetical particles may change the branching fraction for this decay and, thus, demonstrate the presence of new physics. The SM predicts the branching fraction for the $B_s^0 \to \mu^+\mu^-$ decay to be $(3.23 \pm 0.27) \cdot 10^{-9}$ [3]. The CMS and LHCb common results with all RUN-1 collected data show evidence for $\mathscr{B}(B_s^0 \to \mu^+\mu^-) = (2.9 \pm 0.7) \cdot 10^{-9}$ [4, 5, 6]. The ATLAS [7] experiment sets the upper limit $\mathscr{B}(B_s^0 \to \mu^+\mu^-) < 2.2 \cdot 10^{-8}$ at 95% C.L. with half of the integrated 2011 luminosity (2.4 fb^{-1}) [8].

A new analysis was performed with the data in the di-muon invariant mass region from 5066 to 5666 MeV removed from the analysis until the procedures for event selection, as well as for the signal and limit extractions were completely defined.

The $B_s^0 \to \mu^+\mu^-$ branching fraction is measured with respect to the prominent reference decay $B^\pm \to J/\psi K^\pm$. The branching fraction can be written as $\mathscr{B}(B_s^0 \to \mu^+\mu^-) = N_{\mu^+\mu^-} \times \text{SES}$, where single-event sensitivity SES $= \frac{\mathscr{B}(B^{\pm}\to J/\psi K^{\pm})}{N_{J/\psi K^{\pm}}} \cdot \frac{f_u}{f_s} \cdot R_{A_\epsilon}$, $N_{\mu^+\mu^-}$ and $N_{J/\psi K^{\pm}}$ are the event numbers of the corresponding decays, $\frac{f_u}{f_s}$ is relative b-quark hadronisation probability of $B^{\pm}$ and B_s^0, taken from previous measurements, and R_{A_ϵ} is the acceptance and efficiency ratio for the two decays. A limit on $\mathscr{B}(B_s^0 \to \mu^+\mu^-)$ is derived by assuming $\mathscr{B}(B^0 \to \mu^+\mu^-)$ to be negligible.

Monte Carlo simulated event samples were adjusted by an iterative re-weighting procedure with re-weighting based on simulation, followed by a data driven re-weighting. This procedure uses the comparison of MC events to the sample of $B^{\pm} \to J/\psi K^{\pm}$ events in collision data. Only candidates with odd event numbers are used in the re-weighting procedure, while the remaining sample is used for the yield measurement. The weights are cross-checked on the $B_s^0 \to J/\psi\phi$ control channel.

Only events containing candidates for $B_s^0 \to \mu^+\mu^-$ and $B^{\pm} \to J/\psi K^{\pm}$ are retained for this analysis. The sidebands for signal events are [4766, 5066] and [5666, 5966] MeV. For the reference channel, the signal region is [5180, 5380] MeV and sidebands are [4930, 5130] and [5430, 5630] MeV. After preselection, approximately $3.9 \cdot 10^5$ $B_s^0 \to \mu^+\mu^-$ and $2.5 \cdot 10^5$ $B^{\pm} \to J/\psi K^{\pm}$ candidates are obtained in the signal regions.

Two categories of background are considered: a continuum with smooth dependence on the di-muon invariant mass, and various sources of resonant contributions, most of which come from the $B_{(s)}^0 \to h^+h'^-$ decays (with h being a kaon or pion) when both daughters are misidentified as muons in the detector. The combinatorial background from $b\bar{b} \to \mu^+\mu^- X$ decays provides a reasonable description for event variables, used for background suppression, in sidebands. The contribution of the resonant background is estimated from MC.

The Boosted Decision Tree (BDT) algorithm was found to be the best performing discrimination between the signal and background events. It uses 13 variables. Distributions from $B^{\pm} \to J/\psi K^{\pm}$ events simulated with MC are compared to data after the side-band background subtraction for all discriminating variables and variables used in the preselection. The optimisation procedure aims at selecting the best performing BDTs and obtaining the final selection cuts in the BDT output variable q and in the invariant mass window Δm. The signal region is defined as $\pm\Delta m$ centred around a mass of 5366.33 MeV. The optimization is performed by maximizing the estimator $P = \frac{\epsilon}{1+\sqrt{B}}$, where ϵ is the signal efficiency and B is the number background events selected. The 2-dimensional optimization on the BDT output requirement and the signal region width is performed on the signal MC sample and the odd-numbered data events from sidebands. The optimization gives a maximum P value of 0.0145 with BDT output > 0.118 and $|\Delta m| < 121$ MeV.

The branching fraction for the reference channel is calculated as a product of $\mathscr{B}(B^{\pm} \to J/\psi K^{\pm}) = (1.016 \pm 0.033) \cdot 10^{-3}$ and $\mathscr{B}(J/\psi \to \mu^+\mu^-) = (5.93 \pm 0.06)\%$. The ratio $\frac{f_u}{f_s}$ is taken from $\frac{f_s}{f_d} = 0.256 \pm 0.020$ using $\frac{f_d}{f_u} = 1$. The ratio R_{A_ϵ} is evaluated using MC samples and found to be $0.267 \pm 1.8\% \pm 6.9\%$. The reference channel yield $N_{J/\psi K^{\pm}}$ is determined from a multi-dimensional unbinned extended maximum likelihood fit to the distribution of the invariant-mass of the $\mu^+\mu^- K^{\pm}$ system and its event-by-event uncertainty. The combined result for $N_{J/\psi K^{\pm}}$ gives 15214 even-numbered events with an uncertainty $\pm 1.1\%$ (stat.) and $\pm 2.4\%$ (syst.). The SES value is obtained as $(2.07 \pm 0.26) \cdot 10^{-9}$.

To extract the upper limit on the $\mathscr{B}(B_s^0 \to \mu^+\mu^-)$ the standard implementation of the CLs method in ATLAS is used. Before unblinding the signal region, the expected number of background events in this region is found to be 6.75. After unblinding, 6 events are counted in the signal region and used in CLs analysis. The observed CLs as a function of $\mathscr{B}(B_s^0 \to \mu^+\mu^-)$ is shown in Fig. 1a. The observed limit is $\mathscr{B}(B_s^0 \to \mu^+\mu^-) < 1.5(1.2) \cdot 10^{-8}$ at 95% (90%) CL.

3 CP violation parameter ϕ_s and $\Delta\Gamma_s$ from angular amplitudes of $B_s^0 \to J/\psi\phi$ decay

New phenomena beyond SM may alter CP violation in B-decays. A channel $B_s^0 \to J/\psi\phi$ is expected to be sensitive to new physics contributions. CP violation in this channel occurs due to interference between direct decays and decays with B_s^0—$\bar{B}_s^0$ mixing, characterized by Δm_s of heavy (B_H) and light (B_L) mass eigenstates, and is measured by the weak phase ϕ_s. It is small in SM: the predicted value is $\phi_s = -0.0368 \pm 0.0018$ rad [9]. The width difference $\Delta\Gamma_s = \Gamma_H - \Gamma_L$ is not expected to be significantly affected by new physics and is useful for the SM prediction test. The average decay width is $\Gamma_s = (\Gamma_H + \Gamma_L)/2$.

Previous ATLAS measurement of ϕ_s, Γ_s and $\Delta\Gamma_s$ from fully reconstructed decays $B_s^0 \to J/\psi(\mu^+\mu^-)\phi(K^+K^-)$ with only statistical CP states separation with 4.9 fb^{-1} is published in [10]. The results are updated with the flavour tagged time-dependent angular analysis [2].

The determination of the initial flavor of neutral B-mesons can be inferred from the B-meson that is produced from another b-quark in the event. The calibration of the method is performed in events containing the decays $B^\pm \to J/\psi K^\pm$.

Several methods are available to infer the flavor of the opposite-side b-quark. First, the measured charge of a muon from semileptonic decay of the B-meson provides a strong separation power and it can be enhanced by considering a weighted sum of the charge q_i of the tracks in the cone ΔR around muon:

$$Q_\mu = \frac{\sum_i^{N_{\rm tr}} q_i \cdot (p_T^i)^k}{\sum_i^{N_{\rm tr}} (p_T^i)^k},$$

where $k = 1.1$, number of tracks $N_{\rm tr}$ includes tracks with $p_T > 0.5$ GeV and $|\eta| < 2.5$, $\Delta R = 0.5$. If no muon is present, a b-tagged jet is required in the event, which is seeded from calorimeter clusters with an energy threshold of 10 GeV and a minimum b-tag weight of -0.5. The jet is reconstructed using the anti-k_t algorithm with a cone size 0.6. The jet charge $Q_{\rm jet}$ is defined similar to Q_μ, where the sum is over the tracks associated with the jet. In both cases, the tracks associated with the signal decay products are excluded from the sum.

Candidates for $B_s^0 \to J/\psi\phi$ decays are selected by following requirements: no displaced vertex or time cuts applied in the trigger or offline; J/ψ mass window adapted separately for barrel and endcap regions; ϕ mass window of 22 MeV; kaons $p_T > 1$ GeV; B-vertex fit quality χ^2/d.o.f. < 3. In total, 131k B_s^0 candidates within $5.15 < m(B_s^0) < 5.65$ GeV are used in the fit.

An unbinned maximum likelihood fit is performed on the selected events to extract the parameters of the $B_s^0 \to J/\psi(\mu^+\mu^-)\phi(K^+K^-)$ decay. The fit uses reconstructed mass and proper time with the uncertainties, the tag probability and the transversity angles $\Omega(\theta_T, \psi_T, \phi_T)$, defined in the rest frames of $J/\psi(\theta_T, \phi_T)$ and $\phi(\psi_T)$. The likelihood function includes the combination of signal and background probability density functions. The full simultaneous maximum likelihood fit contains 25 free parameters. The number of signal B_s^0 mesons extracted from the fit is 22670 ± 150. The solution with $\Delta\Gamma_s > 0$ is considered.

The results for physics parameters are

$$\phi_s = 0.12 \pm 0.25\,(\text{stat.}) \pm 0.05\,(\text{syst.})\,\text{rad},$$

$$\Delta\Gamma_s = 0.053 \pm 0.021\,(\text{stat.}) \pm 0.010\,(\text{syst.})\,\text{ps}^{-1},$$
$$\Gamma_s = 0.667 \pm 0.007\,(\text{stat.}) \pm 0.004\,(\text{syst.})\,\text{ps}^{-1},$$
$$|A_{\parallel}(0)|^2 = 0.220 \pm 0.008\,(\text{stat.}) \pm 0.009\,(\text{syst.}),$$
$$|A_0(0)|^2 = 0.529 \pm 0.006\,(\text{stat.}) \pm 0.012\,(\text{syst.}),$$
$$\delta_{\perp} = 3.89 \pm 0.47\,(\text{stat.}) \pm 0.11\,(\text{syst.})\,\text{rad}.$$

The values are consistent with those obtained in the untagged analysis [10] and reduce the statistical uncertainty on ϕ_s by 40%. The fit demonstrates sensitivity to the strong phase $\delta_{\perp}$. Likelihood contours in the $\phi_s - \Delta\Gamma_s$ plane are presented in Fig. 1b. The results are consistent with the values predicted in the standard model.

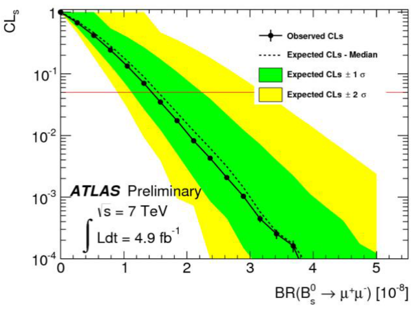

(a)

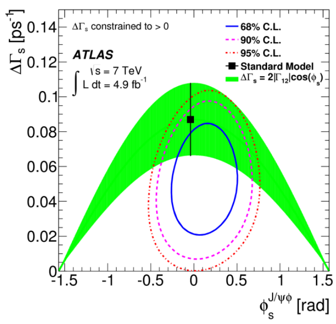

(b)

Figure 1: (a) Observed CL$_s$ as a function of $\mathscr{B}(B_s^0 \to \mu^+\mu^-)$. (b) Likelihood contours in the $\phi_s - \Delta\Gamma_s$ plane.

4 Conclusions

ATLAS results from the full 2011 data for pp collisions at 7 TeV ($4.9\,\text{fb}^{-1}$) are obtained for new physics searches in the rare decay $B_s^0 \to \mu^+\mu^-$ selection and $B_s^0 \to J/\psi\phi$ decay parameters measurement. The flavour tagged time dependent angular analysis is used for $B_s^0 \to J/\psi\phi$ improving on the previous ATLAS measurement without tagging. All results are consistent with the predictions of the standard model.

References

[1] ATLAS Collaboration, ATLAS-CONF-2013-076, `https://cds.cern.ch/record/1562934`
[2] ATLAS Collaboration, Phys. Rev. D 90 (2014) 052007
[3] Buras et al., Eur.Phys.J. **C72** (2012) 2172
[4] CMS Collaboration, Phys. Rev. Lett. 111 (2013) 101804
[5] LHCb Collaboration, Phys. Rev. Lett. 111 (2013) 101805
[6] CMS and LHCb Collaborations, CMS-PAS-BPH-13-007, `https://cds.cern.ch/record/1564324`
[7] ATLAS Collaboration, JINST **3**, S008003 (2008)
[8] ATLAS Collaboration, Phys. Lett. B 713 (2012) 387
[9] UTfit collab., M.Bona et al., Phys.Rev.Lett. 97 (2006) 151803
[10] ATLAS Collaboration, JHEP 12 (2012) 072

The New Muon $g-2$ Experiment at Fermilab

David Kawall[1] on behalf of the E989 Collaboration

[1]Department of Physics, University of Massachusetts Amherst, MA 01003, USA

DOI: http://dx.doi.org/10.3204/DESY-PROC-2014-04/132

Experiment E989 is under preparation at Fermilab, intending to measure the anomalous magnetic moment of the muon $g_\mu - 2$ to an accuracy of 140 ppb, a fourfold improvement over the Brookhaven E821 result. The latter differs by more than 3 standard deviations from Standard Model predictions, perhaps hinting at new physics and motivating a more sensitive comparison. The techniques of the new experiment to reduce experimental statistical uncertainties by a factor four and systematics by a factor three will be described.

1 Introduction and current status of the muon $g-2$ value

The magnetic moment of a fundamental particle is given by $\vec{\mu} = g(e\hbar/2m)\vec{S}/\hbar$, where $\vec{S}$ is the spin operator and $g = 2$ was predicted by Dirac for point-like spin 1/2 particles such as the electron or muon. This leading order prediction of the Standard Model (SM) is perturbed by radiative corrections. These couple the fields of virtual particles to the muon, leading to additional contributions so g_μ deviates from 2. The sum of all such corrections is characterized by the anomalous magnetic moment $a_\mu \equiv \frac{1}{2}(g_\mu - 2)$.

The largest contribution to a_μ comes from the Schwinger term, which involves the exchange of an additional virtual photon and contributes a_μ(QED, Leading-Order)$=\alpha_{\mathrm{QED}}/2\pi \approx 1.16 \times 10^{-3}$. The Schwinger term contribution to the electron a_e was confirmed experimentally by Kusch and Foley in 1947.

The modern SM prediction for a_μ includes QED contributions calculated to order α^5_{QED} [1], weak interaction contributions calculated to 2 loops [2], and hadronic contributions. The latter are usually described in terms of a leading-order (LO) hadronic vacuum polarization (HadVP) and higher-order HadVP, where the LO HadVP is best determined from a dispersion relation and measurements of e^+e^- scattering into hadronic final states made by BABAR, KLOE, CMD2, and SND (see [3, 4] for details and references). The hadronic light-by-light contribution (Had-LBL) is determined from the "Glasgow Consensus" and is discussed in [5].

Abundant hadronic decay data of τ from LEP and CLEO can be used with isospin breaking corrections and the assumption of CVC to evaluate the LO HadVP contribution to a_μ. Since the τ data just has the isovector part of the contribution, the isoscalar part from e^+e^- scattering must be introduced by hand, so e^+e^- and τ evaluations of LO HadVP are not fully independent. Early τ-based evaluations were different from those based on e^+e^- scattering. Recently it has been shown that after properly accounting for $\gamma - \rho$ mixing the results are consistent [6].

The SM prediction is compared with the experimental result from Brookhaven E821 [7] in Table 1, where a 3.6 σ difference is observed. Using a different evaluation of the LO HadVP contribution, $(6949.1 \pm 42.7) \times 10^{-11}$, from [8], reduces the discrepancy to 3.3 σ.

There is great interest in this discrepancy since the Standard Model is incomplete, and many models of physics beyond the Standard Model, such as supersymmetry (SUSY), predict new particles which contribute to the muon anomaly and naturally cause such a discrepancy. For instance, given a mass scale Λ, the SUSY contribution in terms of $\tan\beta$ and the SUSY μ-parameter is [9] (see Fig. 1):

$$a_\mu(\mathrm{SUSY}) \approx \mathrm{sign}(\mu) \times 130 \times 10^{-11} \times \tan\beta \times \left(\frac{100\ \mathrm{GeV}}{\Lambda}\right)^2 .$$

Thus a_μ measurements are potentially sensitive to SUSY interactions at the TeV scale. Technicolor models and models with extra spatial dimensions also predict contributions to a_μ. The muon anomaly is sensitive to new physics in a manner which is unique and complementary to other searches for new physics. It is more sensitive to new physics than the electron anomaly by a factor $(m_\mu/m_e)^2 \approx 43{,}000$. Anomaly contributions come from interactions which are CP- and flavor-conserving, chirality-flipping, and which appear in loops. This complements LHC searches for new physics since those observables are typically chirality-conserving. Further, the $\tan\beta$ parameter and $\mathrm{sign}(\mu)$ parameter which are important in many SUSY models are difficult to measure at the LHC, and determined better by a precision $g-2$ measurement [9]. Lower energy precision tests such as electric dipole moment (EDM) searches are sensitive to CP-violating interactions, and searches such as $\mu \to e$ conversion are flavor-violating. Muon $g-2$ is primarily sensitive to leptonic couplings so it complements precision s and B physics experiments that search for the hadronic couplings of new physics.

Whether the discrepancy between theory and experiment for a_μ is an indication of new physics can only be resolved by reducing the uncertainties. New precision measurements and analysis of e^+e^- scattering data from BESIII, Novosibirsk, and Frascati, and lattice QCD calculations of LO HadVP [10] should reduce the theoretical uncertainties. The discrepancy also motivates the new high rate, next generation $g_\mu - 2$ experiment E989 at Fermilab [11].

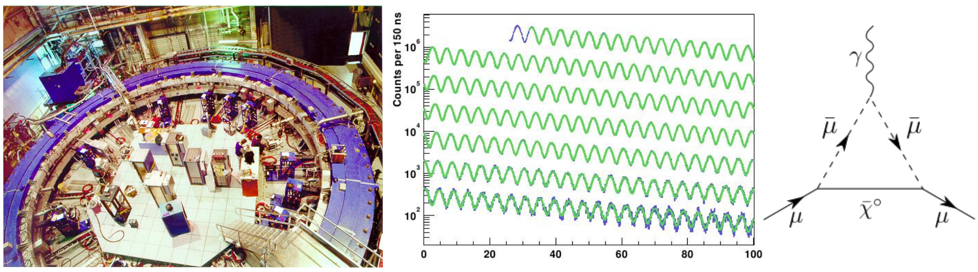

Figure 1: Left: The BNL E821 storage ring. Center: The BNL E821 "wiggle" plot showing the anomalous precession ω_a. Right: A one-loop SUSY contribution to a_μ from a smuon and chargino loop.

2 Overview of experimental technique

The experiment E989 will inject polarized muons through a superconducting inflector into a 7.1 m radius magnetic storage ring with electric quadrupoles for vertical focusing and scraping

Source		Contribution	Uncertainty
a_μ(QED)	=	116 584 718.951	$\pm$ 0.080 (α^5)
a_μ(HadVP; LO)	=	6 923	$\pm$ 42 (Exp)
a_μ(HadVP; HO)	=	-98.4	$\pm$ 0.6 (Exp) $\pm$ 0.4 (Rad)
a_μ(Had-LBL)	=	105	$\pm$ 26
a_μ(Weak; 1 loop)	=	194.8	
a_μ(Weak; 2 loop)	=	-41.2	$\pm$ 1 (Had) $\pm$ 2$\rightarrow$ 0 (Higgs)
a_μ(SM Theory)	=	116 591 802	$\pm$ 49 $\times 10^{-11}$ (0.42 ppm)
a_μ(E821 Expt.)	=	116 592 089	$\pm$ 63 $\times 10^{-11}$ (0.54 ppm)
Δ(Expt.-Theory)	=	287	$\pm$ 80 $\times 10^{-11}$ (3.6 σ)

Table 1: Standard model prediction from M. Davier *et al.* [4] for a_μ in units of 10^{-11}, and the experimental result from BNL E821 [7].

(essentially a Penning trap, see Fig. 1) [7, 11]. A magnetic kicker is pulsed on during the first turn, resulting in $\approx 10^4$ muons on a stable orbit per fill. While stored, the muon spin vector precession frequency ω_S is faster than the momentum vector cyclotron frequency ω_C. The difference frequency ω_a is proportional to a_μ:

$$\vec{\omega}_a = \vec{\omega}_S - \vec{\omega}_C = -\frac{e}{m}\left[a_\mu \vec{B} - \left(a_\mu - \left(\frac{mc}{p}\right)^2\right)\frac{\vec{\beta}\times\vec{E}}{c}\right], \quad (1)$$

where $B = 1.45$T is the storage ring magnet field, and $\vec{E}$ is the electric field from the electrostatic quadrupoles. The electric field dependence cancels by using muons at the magic momentum $p_{\rm magic} = m_\mu c/\sqrt{a_\mu} \approx 3.094$ GeV/c, $\gamma \approx 29.3$.

To extract a_μ from Eq. 1, experiment FNAL E989 is required to measure two quantities precisely (i) the anomalous muon spin frequency precession frequency $\omega_a \approx 2\pi \times 229$ kHz and (ii) the magnetic field $\vec{B}$ averaged over the muon distribution in the ring. The magnetic field is measured using pulsed NMR [12, 13] and expressed in terms of the Larmor precession frequency a free proton would exhibit in the same field, $\omega_p \approx 2\pi \times 61.79$ MHz, using the relation $\hbar\omega_p = 2\mu_p B$.

The anomalous precession frequency ω_a is measured by detecting positrons from the decay of stored μ^+. Parity violation in this weak decay leads to a correlation between the positron emission direction and the muon spin direction. The lab frame positron energy is given approximately in terms of the rest frame energy E^* and rest frame angle between muon spin and positron direction θ^* by $E_{\rm lab} \approx \gamma E^*(1+\cos\theta^*)$. Detecting decay e^+ above 1.9 GeV corresponds to to a cut on θ^* and allows the reconstruction of the muon spin direction as a function of time. The resulting positron spectrum $N(t) \approx N_0 e^{-t/(\gamma\tau)}[1 + A\cos(\omega_a t + \phi)]$ from BNL E821 is seen in Fig. 1. Corrections are applied for muons not at the magic momentum, and for the pitching motion from vertical betatron oscillations.

The positron energies and arrival times will be determined by 24 calorimeters in the interior of the storage ring. The calorimeters have a 6×9 array of PbF_2 Čerenkov crystals with attached SiPMs read by 12 bit ADCs digitizing at 800 MSPS. Timing resolution is better than 100 ps, and spatial/temporal separation resolves e^+ arriving >5 ns apart. Gain stability over a fill of 0.1% requires a precision laser calibration system and mV SiPM bias stability. Information about the muon spatial and momentum distribution in the ring will come from fiber beam monitors, a fast-rotation analysis [7], and from several sets of straw tracking chambers. The latter will also be used for an improved limit on the electric dipole of the muon. The systematics on the extraction of ω_a will be held to 70 ppb.

A significant, 20-fold improvement in detected positrons comes from several advantages of FNAL over BNL. First a more intense muon beam will be injected into the ring at a rate of about 12 Hz versus < 0.5 Hz at BNL. Unlike BNL, the muon beam will be free of pion contamination due the much longer decay line used - this yields much smaller backgrounds and allows the detectors to remain on during muon injection. Other improvements in the overall efficiency lead to an expected statistical precision of 100 ppb.

The magnetic field measurement will be improved by upgrades to the NMR measurement system, improved NMR probes and procedures, coupled with a more homogeneous and stable storage ring magnetic field, in part from an experimental hall with $\pm 1°$C stability. The goal is a field measurement with an accuracy on the equivalent precession frequency of a free proton weighted by the muon distribution $\tilde{\omega}_p$ to 70 ppb.

3 Summary

The E989 experiment is under construction at Fermilab, intending to measure the anomalous magnetic moment of the muon a_μ to an accuracy of 140 ppb. Comparison of the experimental result with theoretical predictions yields a precise check of the Standard Model, with sensitivity to new physics. The first stored muons are expected around 2017.

Acknowledgments

This work was supported by the U.S Department of Energy Grant DE-FG02-88ER40115.

References

[1] T. Aoyama, M. Hayakawa, T. Kinoshita, and M. Nio, Phys. Rev. Lett. **109**, 111808 (2012).

[2] A. Czarnecki and W.J. Marciano, "Electromagnetic Dipole Moments and New Physics," in *Lepton Dipole Moments*, ed. by B.L. Roberts and W. Marciano, World Scientific, Singapore, pp.11-68, (2010).

[3] M. Davier, "Hadronic Vacuum Polarization and Lepton Anomalous Magnetic Moments," in *Lepton Dipole Moments*, ed. by B.L. Roberts and W.J. Marciano, World Scientific, Singapore, 2010, p. 273.

[4] M. Davier, A. Hoecker, B. Malaescu, and Z. Zhang, *Eur. Phys. J.* **C**71, 1515 (2011), erratum *Eur. Phys. J.* **C**72, 1874 (2012).

[5] J. Prades, E. de Rafael, and A. Vainshtein, "The Hadronic Light-by-Light Scattering Contribution to the Muon and Electron Anomalous Magnetic Dipole Moments," in *Lepton Dipole Moments*, ed. by B.L.Roberts and W.Marciano, World Scientific, Singapore, 2010, pp. 303–318; and arXiv:0901.0306v1 [hep-ph].

[6] F. Jegerlehner and R. Szafron, Eur. Phys. J. **C71**, 1632 (2011).

[7] G.W. Bennett et al. (BNL E821 Muon g-2 Collaboration), *Phys. Rev. D* **73**, 072003 (2006).

[8] K. Hagiwara et al., *J. Phys. G: Nucl. Part. Phys.* **38**, 085003 (2011).

[9] A. Czarnecki and W.J. Marciano, Phys. Rev. D**64**, 013014 (2001).

[10] C. Aubin and T. Blum, *Nucl. Phys. Proc. Suppl.* **181**, 251 (2006).

[11] The proposal to DOE can be found at http://gm2.fnal.gov

[12] R. Prigl *et al.*, Nucl. Instrum. Methods A **374**, 118 (1996).

[13] X. Fei, V.W. Hughes and R. Prigl, Nucl. Instrum. Methods A **394**, 349 (1997).

Measurements of CP Violation and Mixing in Charm Decays at LHCb

Michael Alexander on behalf of the LHCb collaboration
University of Glasgow, University Avenue, Glasgow, UK, G12 8QQ

DOI: http://dx.doi.org/10.3204/DESY-PROC-2014-04/244

During run I, the LHCb experiment at the LHC, CERN, collected 1.0 fb^{-1} of pp collisions at $\sqrt{s} = 7\,\text{TeV}$ and 2.0 fb^{-1} at $\sqrt{s} = 8\,\text{TeV}$, yielding the world's largest sample of decays of charmed hadrons. This sample is used to search for direct and indirect *CP* violation in charm and to measure D^0 mixing parameters. Recent measurements from several complementary decay modes are presented.

1 Introduction

The LHCb detector is a forward-arm spectrometer, with pseudo-rapidity coverage $2 < \eta < 5$, specifically designed for high precision measurements of decays of b and c hadrons [1]. During run I, the experiment collected 1.0 fb^{-1} of pp collisions at $\sqrt{s} = 7\,\text{TeV}$ and 2.0 fb^{-1} at $\sqrt{s} = 8\,\text{TeV}$, yielding the world's largest sample of decays of charmed hadrons. This allows *CP* violation and mixing in charm to be studied with unprecedented precision in many complementary decay modes. The Standard Model (SM) predicts *CP* asymmetries to be $\mathcal{O}(10^{-3})$ or less in charm interactions [2, 3]; observation of significantly larger *CP* violating effects could indicate new physics.

For a decay $\text{D} \to f$ and its *CP* conjugate $\bar{\text{D}} \to \bar{f}$, with amplitudes A_f and $\bar{A}_{\bar{f}}$ respectively, direct *CP* violation is quantified by $A_d = (|A_f|^2 - |\bar{A}_{\bar{f}}|^2)/(|A_f|^2 + |\bar{A}_{\bar{f}}|^2)$. For D^0 mesons, the mass eigenstates $|\text{D}_{1,2}\rangle$, with masses $m_{1,2}$ and widths $\Gamma_{1,2}$, are defined in terms of the flavour eigenstates, $|\text{D}^0\rangle$ and $|\bar{\text{D}}^0\rangle$, as $|\text{D}_{1,2}\rangle = p|\text{D}^0\rangle \pm q|\bar{\text{D}}^0\rangle$, with p and q complex, satisfying $|p|^2 + |q|^2 = 1$. The rate of mixing is quantified by $x \equiv 2(m_2 - m_1)/(\Gamma_1 + \Gamma_2)$ and $y \equiv (\Gamma_2 - \Gamma_1)/(\Gamma_1 + \Gamma_2)$. *CP* violation in mixing is quantified by $A_m \equiv (|q/p|^2 - |p/q|^2)/(|q/p|^2 + |p/q|^2)$ and the interference between mixing and decay (when $f = \bar{f}$) by $\lambda_f \equiv q\bar{A}_f/pA_f = |q\bar{A}_f/pA_f|\, e^{i\phi}$.

The flavour of the D^0 meson at production is determined using either $\text{D}^{*+} \to \text{D}^0\pi_s^+$ decays, where the charge of the "soft pion", π_s, track gives the D^0 flavour, or $\text{B} \to \text{D}^0\mu^- X$ decays, where the charge of the μ track gives the D^0 flavour.

2 Multi-body D decays

Multi-body D decays are sensitive to *CP* violation due to the interference of different resonances across the multi-body phase space. In $\text{D}^0 \to \text{K}^+\text{K}^-\pi^+\pi^-$ decays, triple products of final state particle momenta in the D^0 rest frame, defined as $C_T \equiv \vec{p}_{\text{K}^+} \cdot (\vec{p}_{\pi^+} \times \vec{p}_{\pi^-})$ and

$\bar{C}_T \equiv \vec{p}_{K^-} \cdot (\vec{p}_{\pi^-} \times \vec{p}_{\pi^+})$ for D^0 and $\bar{D}^0$ mesons respectively, are odd under T. The decay rate asymmetries

$$A_T \equiv (\Gamma(C_T > 0) - \Gamma(C_T < 0))/(\Gamma(C_T > 0) + \Gamma(C_T < 0)),$$
$$\bar{A}_T \equiv (\Gamma(-\bar{C}_T > 0) - \Gamma(-\bar{C}_T < 0))/(\Gamma(-\bar{C}_T > 0) + \Gamma(-\bar{C}_T < 0)),$$

are thus sensitive to *CP* violation. However, final state interactions introduce significant asymmetries, and so the difference $a_{CP}^{T\text{-odd}} \equiv \frac{1}{2}(A_T - \bar{A}_T)$ is used to access the asymmetry of the D^0 meson. The observable $a_{CP}^{T\text{-odd}}$ is by definition insensitive to production and detection asymmetries, so is very robust against systematic uncertainties.

Using 3 fb^{-1} of data, the phase space integrated measurements are found to be [4]

$$A_T = (-7.18 \pm 0.41(\text{stat}) \pm 0.13(\text{syst}))\%,$$
$$\bar{A}_T = (-7.55 \pm 0.41(\text{stat}) \pm 0.12(\text{syst}))\%,$$
$$a_{CP}^{T\text{-odd}} = (0.18 \pm 0.29(\text{stat}) \pm 0.04(\text{syst}))\%.$$

This shows no evidence of *CP* violation but achieves a significant improvement in precision over the previous world average of $a_{CP}^{T\text{-odd}} = (0.11 \pm 0.67)$[5].

The same measurements are also performed in 32 bins of Cabibbo-Maksimowicz phase space variables, defined as the invariant mass squared of the $\pi^+\pi^-$ (K^+K^-) pair, $m^2_{\pi^+\pi^-}$ ($m^2_{K^+K^-}$); the cosine of the angle of the π^+ (K^+) with respect to the direction opposite to the D^0 momentum in the $\pi^+\pi^-$ (K^+K^-) rest frame, $\cos(\theta_\pi)$ ($\cos(\theta_K)$); and the angle between the K^+K^- and $\pi^+\pi^-$ planes in the D^0 rest frame, ϕ. The asymmetries are extracted in each bin of phase space and $a_{CP}^{T\text{-odd}}$ calculated. A χ^2 test for consistency across the phase space is performed, yielding a p-value of 74 %. Similarly, binning in the decay time of the D^0 candidates and performing the same test gives sensitivity to indirect *CP* violation. This yields a p-value of 72 %, so there is no evidence for direct or indirect *CP* violation.

A complementary method for studying *CP* violation in multi-body D meson decays is to examine *CP* asymmetries across the multi-body phase space directly. Signal yields are obtained in bins of the multi-body phase space, and the test statistic $S^i_{CP} \equiv (N_i(D^0) - \alpha N_i(\bar{D}^0))/\sqrt{\alpha(N_i(D^0) + N_i(\bar{D}^0))}$, calculated in each bin i, where $\alpha \equiv N(D^0)/N(\bar{D}^0)$ cancels any global production and detection asymmetries. A χ^2 test for consistency with zero *CP* violation is performed using $\chi^2 = \Sigma_i {S^i_{CP}}^2$ and $N_{bins} - 1$ degrees of freedom. This analysis has been performed on $D^0 \to K^+K^-\pi^+\pi^-$ and $D^0 \to \pi^+\pi^-\pi^+\pi^-$ candidates, using 1 fb^{-1} of data, for which the nominal binning scheme yields a *p*-value of 9.1 % (41 %) for $D^0 \to K^+K^-\pi^+\pi^-$ ($D^0 \to \pi^+\pi^-\pi^+\pi^-$) [6]. The decay $D^+ \to \pi^-\pi^+\pi^+$ has also been studied in this way, using 1 fb^{-1} of data [7]. Various binning schema are used, as well as an unbinned method to measure *CP* asymmetries, all of which yield p-values of more than 20 %. Thus, no evidence for *CP* violation is found in these decay modes.

3 *CP* violation in $D^\pm_{(s)} \to K^0_S h^\pm$

The singly-Cabibbo-suppressed (SCS) decays $D^\pm \to K^0_S K^\pm$ and $D^\pm_s \to K^0_S \pi^\pm$ offer a means of measuring direct *CP* violation with high precision. The *CP* asymmetry is defined as

$\mathcal{A}_{CP}^{D_{(s)}^{\pm}\to K_S^0 h^{\pm}} \equiv (\Gamma(D_{(s)}^{+}\to K_S^0 h^{+}) - \Gamma(D_{(s)}^{-}\to K_S^0 h^{-}))/(\Gamma(D_{(s)}^{+}\to K_S^0 h^{+}) + \Gamma(D_{(s)}^{-}\to K_S^0 h^{-}))$, while the measured asymmetry is

$$\begin{aligned}\mathcal{A}_{\text{meas}}^{D_{(s)}^{\pm}\to K_S^0 h^{\pm}} &\equiv (N_{\text{sig}}^{D_{(s)}^{+}\to K_S^0 h^{+}} - N_{\text{sig}}^{D_{(s)}^{-}\to K_S^0 h^{-}})/(N_{\text{sig}}^{D_{(s)}^{+}\to K_S^0 h^{+}} + N_{\text{sig}}^{D_{(s)}^{-}\to K_S^0 h^{-}}) \\ &\simeq \mathcal{A}_{CP}^{D_{(s)}^{\pm}\to K_S^0 h^{\pm}} + \mathcal{A}_{\text{prod}}^{D_{(s)}^{\pm}} + \mathcal{A}_{\text{det}}^{h^{\pm}} + \mathcal{A}_{K_S^0}.\end{aligned}$$

Here N_{sig} is the number of signal candidates of the given decay, $\mathcal{A}_{\text{prod}}^{D_{(s)}^{\pm}}$ is the production asymmetry of the $D_{(s)}^{\pm}$ meson, $\mathcal{A}_{\text{det}}^{h^{\pm}}$ is the detection asymmetry of the $h^{\pm}$ meson, and $\mathcal{A}_{K_S^0}$ is the combined detection and *CP* asymmetry of the K_S^0 meson. Assuming negligible *CP* violation in the Cabibbo-favoured (CF) decays $D_s^{\pm}\to K_S^0 K^{\pm}$, $D^{\pm}\to K_S^0\pi^{\pm}$ and $D_s^{\pm}\to \phi\pi^{\pm}$, the production and detection asymmetries cancel in the double difference

$$\begin{aligned}\mathcal{A}_{CP}^{DD} &\equiv \left[\mathcal{A}_{\text{meas}}^{D_s^{\pm}\to K_S^0\pi^{\pm}} - \mathcal{A}_{\text{meas}}^{D_s^{\pm}\to K_S^0 K^{\pm}}\right] - \left[\mathcal{A}_{\text{meas}}^{D^{\pm}\to K_S^0\pi^{\pm}} - \mathcal{A}_{\text{meas}}^{D^{\pm}\to K_S^0 K^{\pm}}\right] - 2\mathcal{A}_{K_S^0}, \\ &= \mathcal{A}_{CP}^{D^{\pm}\to K_S^0 K^{\pm}} + \mathcal{A}_{CP}^{D_s^{\pm}\to K_S^0\pi^{\pm}},\end{aligned}$$

while the K_S^0 asymmetry is calculable, so the sum of the *CP* asymmetries can be measured. Similarly the individual *CP* asymmetries can be accessed using

$$\begin{aligned}\mathcal{A}_{CP}^{D^{\pm}\to K_S^0 K^{\pm}} &= \left[\mathcal{A}_{\text{meas}}^{D^{\pm}\to K_S^0 K^{\pm}} - \mathcal{A}_{\text{meas}}^{D_s^{\pm}\to K_S^0 K^{\pm}}\right] - \left[\mathcal{A}_{\text{meas}}^{D^{\pm}\to K_S^0\pi^{\pm}} - \mathcal{A}_{\text{meas}}^{D_s^{\pm}\to \phi\pi^{\pm}}\right] - \mathcal{A}_{K_S^0}, \\ \mathcal{A}_{CP}^{D_s^{\pm}\to K_S^0\pi^{\pm}} &= \mathcal{A}_{\text{meas}}^{D_s^{\pm}\to K_S^0\pi^{\pm}} - \mathcal{A}_{\text{meas}}^{D_s^{\pm}\to \phi\pi^{\pm}} - \mathcal{A}_{K_S^0}.\end{aligned}$$

Using 3 fb^{-1} of data the results thus obtained are [8]

$$\begin{aligned}\mathcal{A}_{CP}^{D^{\pm}\to K_S^0 K^{\pm}} + \mathcal{A}_{CP}^{D_s^{\pm}\to K_S^0\pi^{\pm}} &= (+0.41 \pm 0.49(\text{stat}) \pm 0.26(\text{syst}))\%, \\ \mathcal{A}_{CP}^{D^{\pm}\to K_S^0 K^{\pm}} &= (+0.03 \pm 0.17(\text{stat}) \pm 0.14(\text{syst}))\%, \\ \mathcal{A}_{CP}^{D_s^{\pm}\to K_S^0\pi^{\pm}} &= (+0.38 \pm 0.46(\text{stat}) \pm 0.17(\text{syst}))\%.\end{aligned}$$

These are the most precise measurements of their kind to date and show no evidence of *CP* violation.

4 Mixing and *CP* violation in $D^0\to h^+h^{(\prime)-}$ decays

Decays of $D^0\to h^+h^{(\prime)-}$ provide a means of measuring direct and indirect *CP* violation, as well as mixing, in the D^0 system. The measured *CP* asymmetry in $D^0\to K^+K^-$ and $D^0\to\pi^+\pi^-$ decays, flavour tagged using $B\to D^0\mu^- X$ decays, is $\mathcal{A}_{\text{meas}}^{D^0\to h^+h^-} = \mathcal{A}_{CP}^{D^0\to h^+h^-} + \mathcal{A}_{\text{det}}^{\mu^{\pm}} + \mathcal{A}_{\text{prod}}^{B}$. The $\pi^+\pi^-$ and K^+K^- final states are *CP* eigenstates, so have no detection asymmetry. Defining $\Delta\mathcal{A}_{CP} \equiv \mathcal{A}_{\text{meas}}^{D^0\to K^+K^-} - \mathcal{A}_{\text{meas}}^{D^0\to\pi^+\pi^-} = \mathcal{A}_{CP}^{D^0\to K^+K^-} - \mathcal{A}_{CP}^{D^0\to\pi^+\pi^-}$, the nuisance asymmetries cancel. Similarly to the analysis described in Sec. 3, CF decays can be used to cancel nuisance asymmetries as $\mathcal{A}_{CP}^{D^0\to K^+K^-} = \mathcal{A}_{\text{meas}}^{D^0\to K^+K^-} - \mathcal{A}_{\text{meas}}^{D^0\to K^-\pi^+} + \mathcal{A}_{\text{det}}^{K^{\mp}\pi^{\pm}}$, and $\mathcal{A}_{\text{det}}^{K^{\mp}\pi^{\pm}}$ can be calculated using the asymmetries of $D^+\to K^-\pi^+\pi^+$ and $D^+\to K_S^0\pi^+$ decays, and the known $\mathcal{A}_{K_S^0}$. The asymmetry $\mathcal{A}_{CP}^{D^0\to\pi^+\pi^-}$ can then be determined using $\mathcal{A}_{CP}^{D^0\to\pi^+\pi^-} = \mathcal{A}_{CP}^{D^0\to K^+K^-} - \Delta\mathcal{A}_{CP}$.

Using 3 fb^{-1} of data yields [9]

$$\begin{aligned}\Delta\mathcal{A}_{CP} &= (+0.14 \pm 0.16(\text{stat}) \pm 0.08(\text{syst}))\%,\\ \mathcal{A}_{CP}^{\mathrm{D}^0\to\mathrm{K}^+\mathrm{K}^-} &= (-0.06 \pm 0.15(\text{stat}) \pm 0.10(\text{syst}))\%,\\ \mathcal{A}_{CP}^{\mathrm{D}^0\to\pi^+\pi^-} &= (-0.20 \pm 0.19(\text{stat}) \pm 0.10(\text{syst}))\%.\end{aligned}$$

Indirect *CP* violation in $\mathrm{D}^0 \to \mathrm{K}^+\mathrm{K}^-$ and $\mathrm{D}^0 \to \pi^+\pi^-$ decays can be measured using

$$A_\Gamma \equiv \frac{\hat{\Gamma}(\mathrm{D}^0 \to f) - \hat{\Gamma}(\bar{\mathrm{D}}^0 \to f)}{\hat{\Gamma}(\mathrm{D}^0 \to f) + \hat{\Gamma}(\bar{\mathrm{D}}^0 \to f)} \approx \eta_{CP}\left[\frac{1}{2}(A_m + A_d)y\cos\phi - x\sin\phi\right].$$

Here, $\hat{\Gamma}$ is the inverse of the effective lifetime of the decay and η_{CP} is the *CP* eigenvalue of f. The effective lifetimes are measured directly using a data-driven, per-candidate correction for the selection efficiency on 1 fb^{-1} of data, yielding [10]

$$\begin{aligned}A_\Gamma(\pi\pi) &= (+0.033 \pm 0.106(\text{stat}) \pm 0.014(\text{syst}))\%,\\ A_\Gamma(\mathrm{KK}) &= (-0.035 \pm 0.062(\text{stat}) \pm 0.012(\text{syst}))\%.\end{aligned}$$

Thus, no evidence for direct or indirect *CP* violation in $\mathrm{D}^0 \to \mathrm{h}^+\mathrm{h}^-$ decays is found.

Mixing in the D^0 system is measured using the ratio of the decay rates of “wrong sign” DCS $\mathrm{D}^0 \to \mathrm{K}^+\pi^-$ to “right sign” CF $\mathrm{D}^0 \to \mathrm{K}^-\pi^+$ as a function of D^0 decay time, as

$$R(t) = \frac{N_{WS}(t)}{N_{RS}(t)} = R_D + \sqrt{R_D}y't + \frac{x'^2 + y'^2}{4}t^2,$$

where $R_D = \left|\frac{A_{DCS}}{A_{CF}}\right|^2$, $x' = x\cos(\delta) + y\sin(\delta)$, $y' = -x\sin(\delta) + y\cos(\delta)$, and $\delta = \arg\left(\frac{A_{DCS}}{A_{CF}}\right)$. Using 3 fb^{-1} of data yields [11]

$$x'^2 = (5.5 \pm 4.9) \times 10^{-5}, y' = (4.8 \pm 1.0) \times 10^{-3}, R_D = (3.568 \pm 0.066) \times 10^{-3}.$$

Allowing for *CP* violation yields:

$$A_D \equiv (R_D(\mathrm{D}^0) - R_D(\bar{\mathrm{D}}^0))/(R_D(\mathrm{D}^0) - R_D(\bar{\mathrm{D}}^0)) = (-0.7 \pm 1.9)\%,$$

$$0.75 < |q/p| < 1.24, (68.3\ \%\ \text{CL}).$$

These are the most precise measurements of mixing in the D^0 system and of *CP* violation in $\mathrm{D}^0 \to \mathrm{K}^+\pi^-$ decays to date.

5 Conclusions

There is a rich programme of charm physics studies at the LHCb experiment, with many complementary measurements already performed using some or all the 3 fb^{-1} of data collected during run I. No evidence for *CP* violation has been found, though constraints of $\mathcal{O}(10^{-3})$ have been achieved in many decay modes. Mixing in the D^0 system has also been measured to unprecedented precision. With run II shortly to begin, and the LHCb upgrade in the near future, there are great prospects for future measurements with precisions of $\mathcal{O}(10^{-4})$, which will tightly constrain, or potentially discover, new physics.

References

[1] The LHCb collaboration. The LHCb Detector at the LHC. *JINST*, 3(S08005), 2008.

[2] Joachim Brod, Alexander L. Kagan, and Jure Zupan. Size of direct CP violation in singly Cabibbo-suppressed D decays. *Phys.Rev.*, D86:014023, 2012.

[3] M. Bobrowski, A. Lenz, J. Riedl, and J. Rohrwild. How Large Can the SM Contribution to CP Violation in $D^0 - \bar{D}^0$ Mixing Be? *JHEP*, 1003:009, 2010.

[4] The LHCb collaboration. Search for CP violation using T-odd correlations in $D^0 \to K^+K^-\pi^+\pi^-$ decays. *JHEP*, 1410:5, 2014.

[5] The Heavy Flavor Averaging Group. `http://www.slac.stanford.edu/xorg/hfag/`, August 2014.

[6] The LHCb collaboration. Model-independent search for CP violation in $D^0 \to K^-K^+\pi^-\pi^+$ and $D^0 \to \pi^-\pi^+\pi^+\pi^-$ decays. *Phys.Lett.*, B726:623–633, 2013.

[7] The LHCb collaboration. Search for CP violation in the decay $D^+ \to \pi^-\pi^+\pi^+$. *Phys.Lett.*, B728:585–595, 2014.

[8] The LHCb collaboration. Search for CP violation in $D^\pm \to K^0_S K^\pm$ and $D^\pm_s \to K^0_S \pi^\pm$ decays. *JHEP*, 1410:25, 2014.

[9] The LHCb collaboration. Measurement of CP asymmetry in $D^0 \to K^-K^+$ and $D^0 \to \pi^-\pi^+$ decays. *JHEP*, 1407:041, 2014.

[10] The LHCb collaboration. Measurements of indirect CP asymmetries in $D^0 \to K^-K^+$ and $D^0 \to \pi^-\pi^+$ decays. *Phys.Rev.Lett.*, 112(4):041801, 2014.

[11] The LHCb collaboration. Measurement of D^0-$\bar{D}^0$ mixing parameters and search for CP violation using $D^0 \to K^+\pi^-$ decays. *Phys.Rev.Lett.*, 111:251801, 2013.

Perspective Study of Charmonium and Exotics above $D\bar{D}$ Threshold

M. Yu. Barabanov, A. S. Vodopyanov

Joint Institute for Nuclear Research, Joliot-Curie 6, Dubna, Moscow region Russia 141980

DOI: http://dx.doi.org/10.3204/DESY-PROC-2014-04/11

The spectroscopy of exotic states with hidden charm is discussed. Together with charmonium it is a good testing tool for theories of strong interactions including QCD in both perturbative and non-perturbative regime, lattice QCD, potential models and phenomenological models. An elaborated analysis of exotics spectrum is given, and attempts to interpret recent experimental data in the above $D\bar{D}$ threshold region are considered. Experimental data from different collaborations (BES, BaBar, Belle, LHCb) are analyzed with special attention given to new states with hidden charm which were discovered recently. Some of these states can be interpreted as higher-lying charmonium states and tetraquarks with hidden charm. It has been shown that charge/neutral tetraquarks must have their neutral/charge partners with mass values differ by few MeV. This hypothesis coincides with that proposed by Maiani and Polosa. But much more data on different decay modes are needed before firmer conclusions can be made. These data can be derived directly from the experiments using the high quality antiproton beam with momentum up to 15 GeV/c and proton-proton collisions with momentum up to 26 GeV/c.

1 Introduction

The study of strong interactions and hadron matter in the process of antiproton-proton annihilation and proton-proton collisions seems to be a challenge nowadays. One of the main goals of contemporary physics is to search for new exotic forms of matter, which must manifest in the existence of charmed hybrids and multiquark states such as meson molecules and tetraquarks [1, 2]. The researches of spectrum of charmed hybrids $c\bar{c}g$ and tetraquarks with hidden charm ($cq\bar{c}\bar{q}'$, and q and $q' = u,\ d,\ s$) together with the charmonioum spectrum are promising to understand the dynamics of quark interactions at small distances. It is a good testing tool for the theories of strong interactions: QCD in both perturbative and non-perturbative regimes, QCD inspired potential models, phenomenological models, non-relativistic QCD and LQCD.

Charmed hybrids $c\bar{c}g$ represent themselves as the states with an excited gluonic degree of freedom. These states are described by different models and calculation schemes (LQCD, bag model, flux tube model) [1, 2]. All model predictions and calculations agree that the mass of the lowest-lying charmonium hybrids is between 3.9 and 4.6 GeV/c^2 and that the state with $J^{PC} = 1^{-+}$ has the lowest mass. Until now, discussions have been focused only around the lowest-lying charmonium hybrids. Four of these states $J^{PC} = 2^{-+},\ 1^{-+},\ 1^{--},\ 0^{-+}$ correspond to a $c\bar{c}$ pair with $J^{PC} = 0^{-+}$ or 1^{--}, coupled to a gluon in the lightest mode with $J^{PC} = 1^{+-}$. The other four states $J^{PC} = 2^{+-},\ 1^{+-},\ 1^{++},\ 0^{+-}$ with the gluon mode

$J^{PC} = 1^{-+}$ are, probably, a bit heavier. The expected mass splitting between the states 1^{-+} and 0^{+-} is about 150 - 250 MeV. Three of these eight charmonium hybrids have spin-exotic quantum numbers $1^{-+},\ 0^{+-},\ 2^{+-}$, so mixing effects with nearby $c\bar{c}$ states are excluded for them thus making their experimental identification especially easy. The next possible hybrid states with quantum numbers $2^{++},\ 2^{+-},\ 1^{++},\ 1^{+-},\ 0^{+-},\ 0^{++}$ correspond to $c\bar{c}$ pairs with quantum numbers $J^{PC} = 1^{+-}$ or $J^{PC} = (0,1,2)^{++}$ coupled to a gluon in the lightest mode with $J^{PC} = 1^{+-}$. The states with quantum numbers $2^{--},\ 2^{-+},\ 1^{--},\ 1^{-+},\ 0^{-+},\ 0^{--}$ correspond to pair $c\bar{c}$ with quantum numbers $J^{PC} = 1^{+-}$ or $J^{PC} = (0,1,2)^{++}$ coupled to a gluon mode with $J^{PC} = 1^{-+}$. One can find a possibility of the existence of hybrid state with exotic quantum numbers $J^{PC} = 0^{--}$. The most interesting and promising decay channels of charmed hybrids are as follows: $\bar{p}p \to \tilde{\eta}_{c0,1,2}(0^{-+},\ 1^{-+},\ 2^{-+})\eta \to \chi_{c0,1,2}(\eta, \pi\pi; \ldots)$; $\bar{p}p \to \tilde{h}_{c0,1,2}(0^{+-},\ 1^{+-},\ 2^{+-})\eta \to \chi_{c0,1,2}(\eta, \pi\pi; \ldots)$; $\bar{p}p \to \tilde{\Psi}(1^{--},\ 2^{--}) \to J/\psi(\eta, \omega, \pi\pi; \ldots)$; $\bar{p}p \to \tilde{\eta}_{c0,1,2}, \tilde{h}_{c0,1,2}, \tilde{\chi}_{c1}(0^{-+},\ 1^{-+},\ 2^{-+},\ 0^{+-},\ 1^{+-},\ 2^{+-},\ 1^{++},\ 2^{++})\eta \to D\bar{D}_J^*\eta$.

Two generic types of multiquark states have been described in the literature [3, 4, 5]. The first one, the molecular state, is comprised of two charmed mesons bound together to form a molecule. These states are by nature loosely bound. Molecular states bound through two mechanisms: quark/colour exchange interactions at short distances and pion exchange at a large distance. Since the mesons inside the molecule are weakly bound, they tend to decay as if they are free. The second type is a tightly bound four-quark state, so called tetraquark that is predicted to have properties that are different from those of a molecular state. In the model of Maiani [4, 5], for example, the tetraquark is described as a diquark-diantiquark structure in which the quarks group into the colour-triplet scalar and vector clusters and the interactions are dominated by a simple spin-spin interaction. Here, strong decays are expected to proceed via rearrangement processes followed by dissociation that gives rise, for example, to such decays as: $p\bar{p} \to X \to J/\psi\ \rho \to J/\psi\ \pi\pi$; $p\bar{p} \to X \to J/\psi\ \omega \to J/\psi\ \pi\pi\pi$; $p\bar{p} \to X \to \chi_{cJ}\pi$; $p\bar{p} \to X \to D\bar{D}^* \to D\bar{D}\gamma$; $p\bar{p} \to X \to D\bar{D}^* \to D\bar{D}\eta$. A prediction that distinguishes tetraquarks containing a $c\bar{c}$ pair from conventional charmonia is possible existence of multiplets which include members with non-zero charge $cu\bar{c}\bar{d}$, strangeness $cd\bar{c}\bar{s}$, or both $cu\bar{c}\bar{s}$.

2 Calculation of exotics spectrum

For this purpose we have fulfilled the elaborated analysis of the spectrum of charmed hybrids and tetraquarks with the hidden charm in the mass region above $D\bar{D}$ threshold. The analysis of spectrum of charmonium [6, 7] was carried out earlier. Different decay modes of charmed hybrids and tetraquarks such as decays into charmonium and light mesons and decays into $D\bar{D}_J^*$ and $D\bar{D}^*$ pairs, were, in particular, analyzed. A special attention was given to the new states with the hidden charm discovered recently [2, 3, 4, 5]. The experimental data from different collaborations like Belle, BaBar, LHCb, BES were carefully analyzed. Using the combined approach based on the quarkonium potential model and confinement model [8, 9], more than twenty charmed hybrids are expected to exist in the discussed mass region (see Figs. 1, 2).

Charmed hybrids with exotic quantum numbers are marked with dark colour and charmed hybrids with nonexotic quantum numbers – with light colour. The results of calculations for hybrids are in good agreement with the well accepted picture that the quartet $1^{--},\ (0,1,2)^{-+}$ is lower in mass than $1^{++},\ (0,1,2)^{+-}$. The mass splitting between the states 1^{-+} and 0^{+-} is about 200 MeV/c^2. More than twenty tetraquarks with hidden charm (see Fig. 3) are expected to exist in the mass region above $D\bar{D}$ threshold.

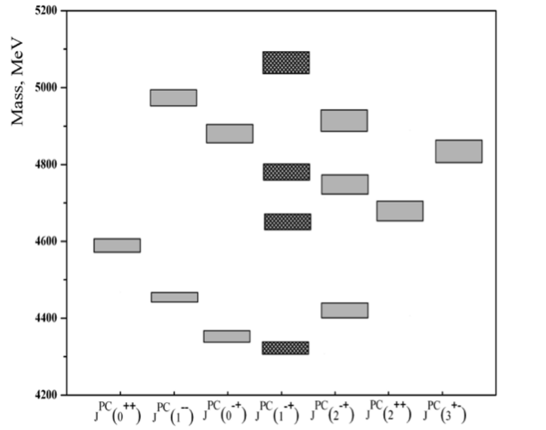

Figure 1: The spectrum of charmed hybrids with quantum numbers $J^{PC} = 3^{+-},\ 2^{++},\ 2^{-+},\ 1^{-+},\ 1^{--},\ 0^{-+},\ 0^{++}$.

The black-white boxes correspond to the recently revealed XYZ states with the hidden charm that may be interpreted as tetraquarks. White boxes correspond to the tetraquark states which have not been found yet. But a possibility of existence of these states is predicted in the framework of the combined approach. It has been shown that charge/neutral tetraquarks with hidden charm must have their neutral/charged partners with mass values which differ by few MeV. This assumption coincides with that proposed earlier by Maiani and Polosa [10] and can shed light on the nature of neutral $X(3872)$, $X(4350)$ and charged $Z_c(3885)^{\pm}$, $Z_c(3900)^{\pm}$, $Z_c(4020)^{\pm}$, $Z_c(4025)^{\pm}$, $Z_c(4200)^{\pm}$, $Z_c(4050)^{\pm}$, $Z_c(4250)^{\pm}$, $Z_c(4430)^{\pm}$ states. The quantum numbers J^{PC} of the $X(3872)$ meson have been recently determined by LHCb [11]. One can find that $X(3872)$ may be interpreted as tetraquark state with $J^{PC} = 1^{++}$, and $X(4350)$ as the tetraquark state with $J^{PC} = 2^{++}$. New state $Z_c(3900)^{\pm}$ observed by BES [12] together with $Z_c(4050)^{\pm}$, $Z_c(4250)^{\pm}$, $Z_c(4430)^{\pm}$ states may be interpreted as charge tetraquarks with $J^{PC} = 1^{+}$. New state $Z_c(4020)^{\pm}$ observed by BES [13] may be interpreted as charge tetraquark with $J^{PC} = 1^{+}$. The proposed approach doesn't distinguish the states $Z_c(3900)^{\pm}$ and $Z_c(3885)^{\pm}$ as well $Z_c(4025)^{\pm}$ and $Z_c(4020)^{\pm}$ states. The values of their masses and widths coincide in the framework of the combined approach. Two states (one charge and one neutral) with $J^{PC} = 1^{++}$ are expected to exist in the mass range of 4200 - 4300 MeV. The new charged state $Z_c(4250)^{\pm}$ observed by Belle may be a good candidate for the one of them.

To confirm that the predicted states actually exist and can be found experimentally, their widths and branching ratios were calculated [7, 9]. The feature of the considered states is their narrowness compared with light unflavored mesons, baryons and hybrids. The states we find in this model have small widths; their values are of the order of several tens of MeV. This fact facilitates experimental searches. The values of the calculated widths coincide (within the experimental error) with the experimentally determined values for the XYZ particles; the correspondence of the mass values has been discussed above. This fact strongly suggests that some of the XYZ particles may be interpreted as higher-lying charmonium states [6, 7] and tetraquarks as it can be verified by the experiments with antiproton beams with momentum up to 15 GeV/c and proton-proton collisions with momentum up to 26 GeV/c. The values of

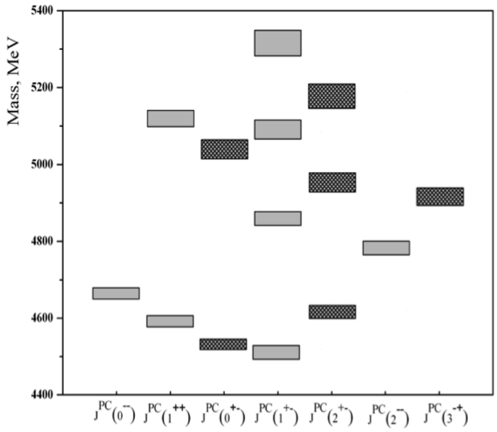

Figure 2: The spectrum of charmed hybrids with quantum numbers $J^{PC} = 3^{-+},\ 2^{--},\ 2^{+-},\ 1^{+-},\ 1^{++}, 0^{+-},\ 0^{--}$.

branching ratios in the considered decay channels of charmonium and exotics are of the order of $\beta \approx 10^{-1} - 10^{-2}$ dependent of their decay mode. From this one can conclude that the branching ratios are significant and searches for charmonium and exotics, and studies of the main characteristics of their spectrum seem to be promising.

3 Conclusion

The prospects for future exotics research are related with the results obtained below:

A combined approach has been employed to study charmonium and exotics on the basis of the quarkonium potential model and a confinement model that uses a three-dimensional sphere embedded into the four-dimensional Euclidian space of the decay products.

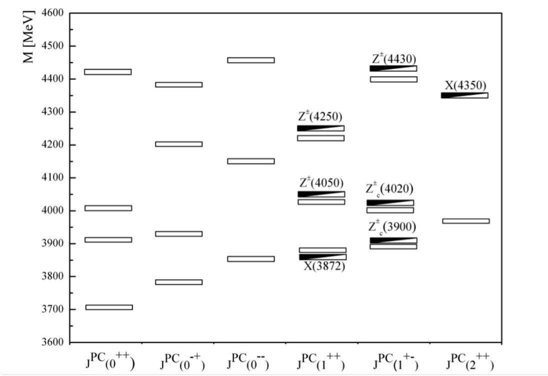

Figure 3: The spectrum of tetraquarks with hidden charm.

The most interesting and promising decay channels of charmed hybrids and tetraquarks with the hidden charm have been analyzed. Many new states above $D\bar{D}$ threshold are expected to exist in the framework of this model.

The recently discovered states with the hidden charm above the $D\bar{D}$ threshold (XYZ particles) have been analyzed. Ten of these states can be interpreted as higher-lying tetraquark states with hidden charm. The necessity of further studies of the XYZ particles and improved measurements of their main characteristics has been demonstrated.

References

[1] W. Erni *et al.*, arXiv:0903.3905v1 [hep-ex] (2009).

[2] N. Brambilla *et al.*, Eur. Phys. J. C 71: 1534, 1 (2011).

[3] J. Beringer *et al.*, Review of Particle Physics, Phys. Rev. 86 (2012).

[4] S. Godfrey and S. Olsen, Ann. Rev. Nucl. Part. Sci. 58, 51 (2008).

[5] S. Olsen, arXiv : 0909.2713v1 [hep-ex] (2009).

[6] M.Yu. Barabanov, A.S. Vodopyanov, Fizika Elementarnyh Chastits Atomnogo Yadra Pisma, 8, N.10, 63 (2011) / Phys. Part. Nucl. Lett. N.10, 1069 (2011).

[7] M.Yu. Barabanov, A.S. Vodopyanov, S. L. Olsen, Yadernaya Fizica, V.77, N.1, 1 (2014) / Phys. At. Nucl., V.77, N.1,1 26 (2014).

[8] M.Yu. Barabanov et al., Russ. Phys. J., 50, 1243 (2007).

[9] M.Yu. Barabanov et al., Hadronic J., 32, N.2, 159 (2009).

[10] N.V. Drenska, R. Fassini, A.D. Polosa, arXiv: 0902.2803 [hep-ph] (2009).

[11] R. Aaij et al., arXiv: 1302.6269v1 [hep-ex] (2013).

[12] M. Ablikim *et al.*, arXiv: 1303.5949v1 [hep-ex] (2013).

[13] M. Ablikim *et al.*, arXiv: 1308.2760v1 [hep-ex] (2013).

CP Violation in B Decays at LHCb

Shu-Faye Cheung on behalf of the LHCb collaboration

Department of Physics, University of Oxford, Oxford OX1 3RH, United Kingdom

DOI: http://dx.doi.org/10.3204/DESY-PROC-2014-04/243

A selection of recent results from studies of CP violation in the decays of B mesons are presented, which were performed using pp collision data at $\sqrt{s} = 7$ TeV and 8 TeV collected by the LHCb experiment during Run I, corresponding to an integrated luminosity of 3.0 fb^{-1}.

1 Model-independent measurement of γ with $B^{\pm} \to D(\to K^0_S\pi^+\pi^-, K^0_S K^+K^-)K^{\pm}$ decays

Indirect searches for New Physics (NP) can be performed at LHCb with precision measurements of the CKM Unitarity Triangle parameters. One of these, the angle $\gamma \equiv \arg[-(V_{ud}V^*_{ub})/(V_{cd}V^*_{cb})]$, can be measured in $B^{\pm} \to DK^{\pm}$ decays, where D is an admixture of D^0 and $\overline{D}^0$ mesons decaying to the same final state. The ratio of amplitudes $A(B^{\pm} \to \overline{D}^0K^{\pm})/A(B^{\pm} \to D^0K^{\pm})$ is $r_Be^{i(\delta_B \pm \gamma)}$, where r_B is the colour-suppression factor, δ_B is the strong-phase difference and γ is the weak-phase difference. LHCb has measured γ in $B^{\pm} \to DK^{\pm}$ decays with many D final states. These are summarised in [1] and have a combined measurement of $\gamma = (72.9^{+9.2}_{-9.9})^{\circ}$.

In the case $D \to K^0_S h^+h^-$, where $h = \pi$ or K, the strong-phase difference between the D^0 and $\overline{D}^0$ decay, δ_D, varies in the Dalitz plot. A model-independent method is used, in which averaged values of δ_D in bins of the Dalitz plot are provided externally. The relative signal yield in each Dalitz plot bin is given by the Cartesian parameters $x_{\pm} = r_B \cos(\delta_B \pm \gamma)$ and $y_{\pm} = r_B \sin(\delta_B \pm \gamma)$; the relative yield of flavour-tagged $D^0 \to K^0_S h^+h^-$ decays, which is measured using $\overset{(-)}{B}{}^0 \to (D^{*\pm} \to \overset{(-)}{D}{}^0\pi^{\pm})\mu^{\mp}X$ decays (X are any other particles produced in the $\overset{(-)}{B}{}^0$ decay that are not reconstructed); and the amplitude-weighted values of $\cos\delta_D$ and $\sin\delta_D$ integrated over the bin, which are obtained with quantum-correlated $\psi(3770) \to D\overline{D}$ decays by the CLEO experiment [2]. A model-dependent measurement of γ with $D \to K^0_S\pi^+\pi^-$ decays, in which the values of δ_D are obtained with an amplitude model of the D^0 decay, has also been performed at LHCb using 1.0 fb^{-1} of data [3].

Approximately 2260 (320) $B^{\pm} \to DK^{\pm}$, $D \to K^0_S\pi^+\pi^-$ ($K^0_S K^+K^-$) decays are selected. The Cartesian parameters $x_{\pm}$ and $y_{\pm}$ are directly measured and found to be $x_+ = (-7.7 \pm 2.4 \pm 1.0 \pm 0.4) \times 10^{-2}$, $x_- = (2.5 \pm 2.5 \pm 1.0 \pm 0.5) \times 10^{-2}$, $y_+ = (-2.2 \pm 2.5 \pm 0.4 \pm 1.0) \times 10^{-2}$ and $y_- = (7.5 \pm 2.9 \pm 0.5 \pm 1.4) \times 10^{-2}$ [4], where the uncertainties are statistical, experimental systematic, and the systematic due to the CLEO measurements, respectively. These are the most accurate measurements of $x_{\pm}, y_{\pm}$ to date. Figure 1 shows the measured values of $x_{\pm}$ and $y_{\pm}$ with likelihood contours corresponding to statistical uncertainties only. The CP observables are extracted and found to be $\gamma = (62^{+15}_{-14})^{\circ}$, $\delta_B = (134^{+14}_{-15})^{\circ}$ and $r_B = (8.0^{+1.9}_{-2.1}) \times 10^{-2}$ [4].

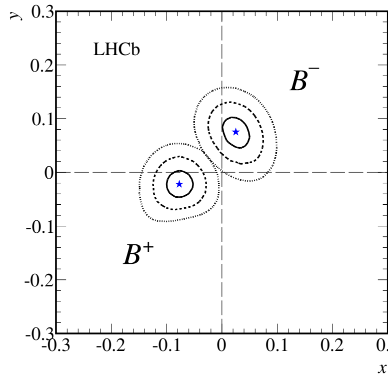

Figure 1: Central values (stars) of $x_\pm$ and $y_\pm$ and the 1-, 2- and 3-standard deviation regions for statistical uncertainties only [4].

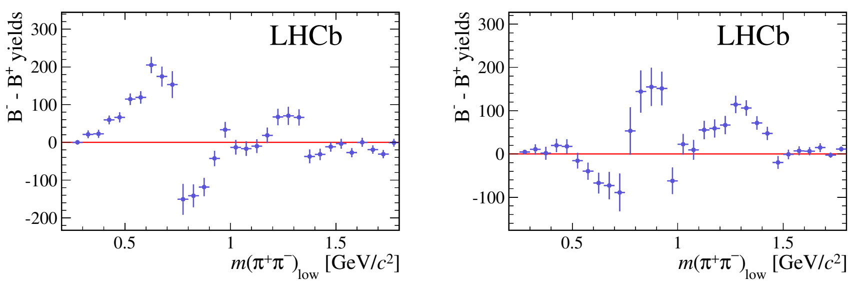

Figure 2: Difference between the number of $B^- \to \pi^-\pi^+\pi^-$ and $B^+ \to \pi^+\pi^+\pi^-$ events as a function of $m(\pi^+\pi^-$ low) in the region (left) $\cos\theta < 0$ and (right) $\cos\theta > 0$, where $\cos\theta$ is the helicity angle between like-sign pions in the $m(\pi^+\pi^-$ low) rest frame. [5]

2 Inclusive and local *CP* asymmetries in $B \to$ three-body charmless decays

Direct *CP* violation can occur through the presence of both weak- and strong-phase differences between tree- and loop-level diagrams of a given decay. In decays of charged B mesons to three charged charmless mesons, the CKM matrix elements involved give rise to the weak-phase difference while the strong-phase difference could be due to several sources, the relative strength of which may vary over the phase space. These sources can be classified into two categories, interference and rescattering, which can be studied by measuring local *CP* asymmetries.

Four channels are studied: $B^\pm \to \pi^\pm\pi^+\pi^-$, $K^\pm\pi^+\pi^-$, $\pi^\pm K^+K^-$ and $K^\pm K^+K^-$. The level of direct *CP* violation is quantified by A_{CP}, the asymmetry between the observed number of B^- and B^+ mesons, corrected for detection, production and kaon matter-interaction asymmetries. The inclusive A_{CP} measurements are $\mathcal{O}(1\%)$ and incompatible with zero, and are positive for $B^\pm \to \{\pi^\pm, K^\pm\}\pi^+\pi^-$ but negative for $B^\pm \to \{\pi^\pm, K^\pm\}K^+K^-$. Large asymmetries are observed in localised regions of the Dalitz plot: $A_{CP} = \mathcal{O}(10\text{–}30\%)$ in the region

$1.0 < m(\pi^+\pi^-), m(K^+K^-) < 1.5$ GeV/c^2. The oppositely-signed asymmetries for the different modes is a characteristic signature of *CPT* conservation in $\pi\pi \leftrightarrow KK$ rescattering. The dominance of long- over short-distance interference effects can be studied by measuring A_{CP} for $B^\pm \to \pi^\pm\pi^+\pi^-$ as a function of $m(\pi^+\pi^-$ low) for positive and negative $\cos\theta$, where $\cos\theta$ is the angle between the like-sign pions in the $m(\pi^+\pi^-$ low) rest frame. As can be seen in Figure 2, A_{CP} changes sign near the $\rho(770)$ resonance, and in different directions for the two $\cos\theta$ ranges. In this region of phase space, A_{CP} can be as large as 50–60% [5].

These findings reveal that direct *CP* violation is dominated by different physical processes inducing strong-phase differences across the phase space. The study of amplitude analyses is essential to understanding the contributions of these processes.

3 ϕ_s and T-odd triple product asymmetries in $B_s^0 \to \phi\phi$ decays

The $B_s^0 \to \phi\phi$ decay proceeds via loop diagrams only, allowing searches for new heavy particles participating in the quantum loops. This can be probed using the *CP*-violating phase ϕ_s, the phase difference between decays with and without mixing, which is small ($< 10^{-2}$) in the Standard Model (SM) and can be significantly enhanced in NP models [6].

The phase ϕ_s is measured by tagging the initial flavour of the B_s^0 meson at production, using flavour-tagging algorithms that have a combined tagging efficiency of 26% with a 33% mistag rate. The $\phi\phi$ final state is a linear combination of *CP*-even and *CP*-odd final states with different decay-time and angular distributions, hence an angular analysis in the helicity angle basis is performed to distinguish the various states, as seen in Figure 3. The data are corrected for their angular acceptance using simulated data and for their decay-time acceptance using $B_s \to D_s\pi$ decays. The B_s^0 mixing parameters are constrained to LHCb measurements. It is found that $\phi_s = -0.17 \pm 0.15\,(\text{stat.}) \pm 0.03\,(\text{syst.})$, which is in agreement with SM theory predictions. The level of direct *CP* violation $|\lambda|$, defined as the absolute ratio between the decay amplitudes of $B_s^0 \to \phi\phi$ and $\overline{B}_s^0 \to \phi\phi$, is found to be $|\lambda| = 1.04 \pm 0.07\,(\text{stat.}) \pm 0.03\,(\text{syst.})$. This is consistent with the hypothesis of no direct *CP* violation.

The $B_s^0 \to \phi\phi$ decay offers a second complementary probe of *CP* violation that is independent of decay time or initial B_s^0 flavour, and instead relies on a simple counting experiment. Two T-odd triple-product quantities can be constructed from the kinematics of the decay, $U \equiv \sin\Phi\cos\Phi$ and $V \equiv \pm\sin\Phi$, where Φ is the angle between the two $\phi \to K^+K^-$ decay planes. The sign of V depends on the value of $\cos\theta_1\cos\theta_2$, where $\theta_{1,2}$ is the angle between the K^+ track momentum in the $\phi_{1,2}$ meson rest frame and the $\phi_{1,2}$ momentum in the B_s^0 rest frame. The asymmetries in the signs of U and V, A_U and A_V, are *CP*-violating quantities with SM expectations close to zero. A non-zero asymmetry would indicate either the presence of *CP* violation or final state interactions. The results are consistent with the hypothesis of *CP* conservation, $A_U = -0.003 \pm 0.017 \pm 0.006$ and $A_V = -0.017 \pm 0.017 \pm 0.006$ [6], where the first uncertainty is statistical and the second uncertainty is systematic.

4 Conclusions

There is a broad and exciting programme of studies of *CP* violation in *B* decays at LHCb. Using data collected from Run I, many of these results have been comparable to those obtained

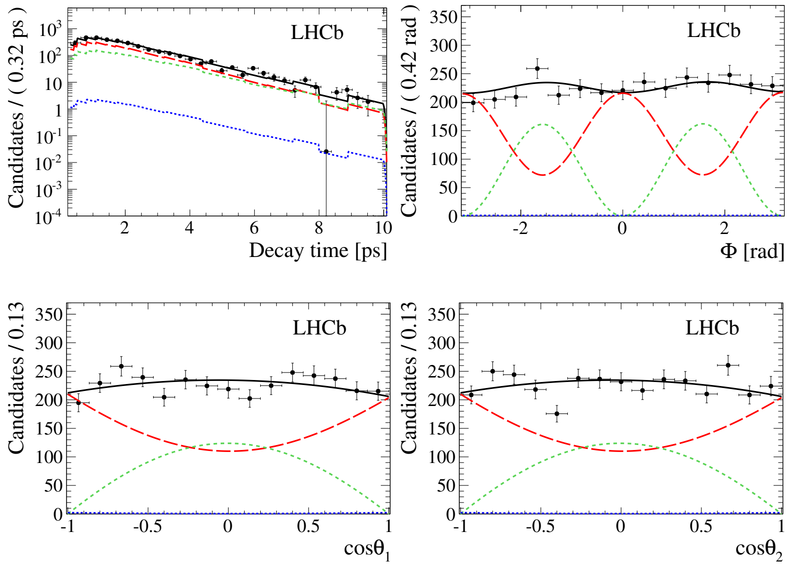

Figure 3: Decay time and helicity angle distributions of $B_s^0 \to \phi\phi$, where Φ is the angle between the two $\phi \to K^+K^-$ decay planes and $\theta_{1,2}$ is the angle between the K^+ track momentum in the $\phi_{1,2}$ meson rest frame and the $\phi_{1,2}$ momentum in the B_s^0 rest frame. The (black points) background-subtracted data are shown with the (solid black) result of the fit, and the (long-dashed red) CP-even P-wave, (short-dashed green) CP-odd P-wave and (dotted blue) S-wave contributions [6].

by the B-factories. Many of these results are statistically-limited and will be improved with the data collected during Run II in 2015–2018, which is expected to collect data corresponding to an integrated luminosity of 5 fb^{-1}.

Acknowledgments

Funding for this work, and attendance at this conference was provided by the Croucher Foundation (Hong Kong), St Cross College and the Department of Physics, University of Oxford.

References

[1] LHCb Collaboration, LHCb-CONF-2014-004 (2014).

[2] CLEO Collaboration, Phys. Rev. **D82** 112006 (2010).

[3] LHCb Collaboration, Nucl. Phys. **B888** 169-193 (2014).

[4] LHCb Collaboration, Submitted to JHEP, arXiv:1408.2748.

[5] LHCb Collaboration, Submitted to Phys. Rev. D, arXiv:1408.5373.

[6] LHCb Collaboration, Phys. Rev. **D90** 052011 (2014).

Recent results on the charmed hadron systems at Belle

Changwoo Joo[1] on behalf of the Belle Collaboration

[1]Seoul National Univ, 1 Gwanak-ro, Gwanak-gu, Seoul, 151-747, Korea

DOI: http://dx.doi.org/10.3204/DESY-PROC-2014-04/252

CP violation and mixing in the charm meson system are expected to be very small in the standard model (SM), hence it can be a good probe to search for new physics beyond the SM. The Belle experiment, with high statistics e^+e^- collision data taken at the KEKB energy-asymmetric collider using the Belle detector, is a very good place to study charmed hadron systems. In this presentation we report recent results from Belle on CP violation and mixing in the neutral D meson system. We also present recent results from Belle in the charmed baryon spectroscopy, including new measurements of mass, width, and absolute branching fractions of various charmed baryons.

The Belle experiment is excellent place to study charmed hadron systems since it has large relative cross-section for charmed hadron production and clean event environment combined with high luminosity. In this proceeding, we report recent results from Belle on CP violation and mixing in the neutral D meson system. We also present result from Belle in the charmed baryon spectroscopy.

1 Neutral D meson system

The mixing rate and the size of CP violation (CPV) in charm sector is expected to be very small in standard model (SM) [1, 2]. Thus, the measurement of $D^0-\bar{D}^0$ mixing and CPV could provide probe to search for beyeond SM [3, 4]. $D^0-\bar{D}^0$ mixing occures becauase the mass eigenstate ($|D_{H,L}>$) is different from flavor eigen sate ($|D^0>, |\bar{D}^0>$). The mass eigenstate can be represented by flavor eigenstate, namely $|D_{H,L}>= p|D^0> \pm q|\bar{D}^0>$. The phenomenology of meson mixing is decribled by two parameters, $x=\Delta M/\Gamma$ and $y=\Delta\Gamma/2\Gamma$, whrere ΔM and $\Delta\Gamma$ are mass and width differnce between two mass eigen state, Γ is average decay width of mass eigenstates. The direct CPV can be measured by decay rate comparison between paricle and anti-paricle system. The indirect CPV parameters are |q/p| and arg(q/p), the former is CPV in mixing and the later is CPV in interference of decay with and without mixing.

1.1 Mixing in $D^0 \to K^+\pi^-$ decay [5]

The mixing parameters of the K^0, B^0 and B^0_S mesons are well esteblished [6]. Rcently the D^0 mixing have been observed in hadron collider experiment [7, 8]. ; This is first observation of $D^0-\bar{D}^0$ minxing from e^+e^- collider by measuring time dependent ratio of the $D^0 \to K^+\pi^-$ and $D^0 \to K^-\pi^+$ decay. We named the $D^0 \to K^+\pi^-$ decay as wrong sign (WS) decay and $D^0 \to K^-\pi^+$ decay as right sign (RS) decay. The RS decay amplitude is sum of the amplitude from Cabibbo-favored (CF) decay $D^0 \to K^-\pi^+$ and $D^0 - \bar{D}^0$ mixing followed by the doubly Cabibbo-suppressed (DCS) decay $\bar{D}^0 \to K^-\pi^+$, where the later is much smaller than former one so it is neglected. The WS decay amplitude is sum of two comparable amplitudes from DCS decay $D^0 \to K^+\pi^-$ and $D^0 - \bar{D}^0$ mixing followed by the CF decay $\bar{D}^0 \to K^+\pi^-$. Then time-dependent WS to RS decay rates are $\Gamma_{RS}(\tilde{t}/\tau) \approx |A_{CF}|^2 e^{-\tilde{t}/\tau}$ and $\Gamma_{WS}(\tilde{t}/\tau) \approx |A_{CF}|^2 e^{-\tilde{t}/\tau}(R_D + \sqrt{R_D}y'\frac{\tilde{t}}{\tau} + \frac{x'^2+y'^2}{4}(\frac{\tilde{t}}{\tau})^2)$, respectively, the $\tilde{t}$ proper true decay time, τ is D^0 lifetime, $|A_{CF}|$ is the CF decay amplitude, R_D is the ratio of DCS to CF decay rates, $x' = xcos\delta + ysin\delta$ and $y' = ycos\delta - xsin\delta$ where δ is the strong phase difference between the DCS and CF decay. The time resolution in B factory is comparable with D^0 decay time, so we extract the time resolution function $R(t/\tau - \tilde{t}/\tau)$ from D^0 mean decay time. Then the WS, RS decay rate ratio becomes $\mathbf{R}(t/\tau) = \frac{\int_{-\infty}^{+\infty} \Gamma_{WS} R(t/\tau - \tilde{t}/\tau) d(\tilde{t}/\tau)}{\int_{-\infty}^{+\infty} \Gamma_{RS} R(t/\tau - \tilde{t}/\tau) d(\tilde{t}/\tau)}$.

The χ^2/ndf for mixing hypothesis is 4.2/7 and no mixing hypothesis is 33.5/9, the mixing hypothesis excludes non-mixing hypothesis with 5.1σ.

1.2 Mixing and indirect CPV in $D^0 \to K_s^0\pi^+\pi^-$ decay [9]

So far there is no evidence of indirect CP violation in D meson system. Experimental estimation of indirect CP violation is $1-|q/p| = 0.12\pm0.17$ [6]. This study is search for indirect CP violation using $D^0 \to K_s^0\pi^+\pi^-$ decay channel. The analysis is done with three dimensional decay amplitude analysis, two is dalizt plot variable $m(K_s^0\pi^+)$ and $m(K_s^0\pi^-)$, and the rest one is time. As a result, the indirect parameter is $|q/p| = 0.90^{+0.16+0.05+0.06}_{-0.15-0.04-0.05}$ and $arg(q/p)(^\circ) = -6\pm11\pm3^{+3}_{-4}$. It shows no evidence of indirect CP violation.

1.3 CPV in $D^0 \to \pi^0\pi^0$ decay [10]

CP violation in charm decay is very small to observe so experimantal observation could indicate new physics. So far only existing CP violation study of $D^0 \to \pi^0\pi^0$ decay is from CLEO [11], the direct CP asymmetry ΔA_{CP} is $(0.1 \pm 4.8)\%$. In this study, direct CPV is estimated using $D^0 \to \pi^0\pi^0$ decay. The asymmetry is $A_{rec} = \frac{N_{rec}^{D^{*+}\to D^0\pi_x^+} - N_{rec}^{D^{*-}\to D^0\pi_x^+}}{N_{rec}^{D^{*+}\to D^0\pi_x^+} + N_{rec}^{D^{*-}\to D^0\pi_x^+}} \approx A_{CP} + A_{FB}(cos\theta^*)$. The A_{CP} can be extracted removing A_{FB} using asymmetry on the $cos\theta^*$ where θ^* is polar angle of D^*. Using decay channel $D^0 \to \pi^0\pi^0$, the measured asymmetry is $A_{CP}(D^0 \to \pi^0\pi^0) = (-0.03 \pm 0.64(stat) \pm 0.10(sys))\%$ which is consistent with no CP violation.

2 New measurement of charmed baryon

2.1 Branching fraction of $\Lambda_c^+ \to pK^-\pi^+$ decay [12]

A number of charmed baryons decay into Λ_c^+. And $\Lambda_c^+ \to pK^-\pi^+$ is the reference mode for the measurement of branching fractions of the Λ_c^+ baryon, so it's important to measure the absolute branching fraction. The Particle Data Group combines several measurements from the ARGUS and CLEO Collaborations to determine $\mathcal{B}(\Lambda_c^+ \to pK^-\pi^+) = (5.0 \pm 1.3)\%$ [13, 14]. The dominant contribution to the uncertainty is from the model dependce of branching fraction extraction [15]. In the proceeding, we present the first model-independent absolute branching fraction measurement of the $\Lambda_c^+ \to pK^-\pi^+$ decay.

The absolute branching fraction is given by $\mathcal{B}(\Lambda_c^+ \to pK^-\pi^+) = \frac{N(\Lambda_c^+\to pK^-\pi^+)}{N_{inc}^{\Lambda_c^+} f_{bias}\varepsilon(\Lambda_c^+\to pK^-\pi^+)}$, where $N_{inc}^{\Lambda_c^+}$ is the number of inclusively reconstructed Λ_c^+, $N(\Lambda_c^+ \to pK^-\pi^+)$ is the number of reconstructed $\Lambda_c^+ \to pK^-\pi^+$ within inclusive Λ_c^+ sample, $\varepsilon(\Lambda_c^+ \to pK^-\pi^+)$ is reconstruction efficiency of $\Lambda_c^+ \to pK^-\pi^+$ decay within inclusive Λ_c^+ sample, f_{bias} is the factor that takes into account potential dependenace of the inclusiv Λ_c^+ reconstruction efficiency on the Λ_c^+ decay mode.

To get the inclusive Λ_c^+ baryons, we used missing mass method for $e^+e^- \to c\bar{c} \to D^{(*)-}\bar{p}\pi^+\Lambda_c^+$ decay. Then we search the decay product of $\Lambda_c^+ \to pK^-\pi^+$ decay in the sample of inclusive Λ_c^+ baryon. The efficiency of $\Lambda_c^+ \to pK^-\pi^+$ and f_{bias} are detemined by MC simluation. The MC simulation shows that Λ_c^+ inclusive reconstruction efficiency weakly depends on the Λ_c^+ decay mode, therefore we need correction for true inclusive Λ_c^+ sample. The factor $f_{bias} = \varepsilon^{inc}_{\Lambda_c^+\to pK^-\pi^+}/\bar{\varepsilon}^{inc}_{\Lambda_c^+}$ is necessay for this correction.

As a result, the branching fraction is $\mathcal{B}(\Lambda_c^+ \to pK^-\pi^+) = (6.84 \pm 0.24(stat) \pm^{+0.21}_{-0.27}(sys))\%$, that is consistant with previous result and this result improves the previous measurement by factor 5.

2.2 Measurement of mass and width of the $\Sigma_c(2455)^{0/++}$ and $\Sigma_c(2520)^{0/++}$ baryons [16]

The properties of the $\Sigma_c^{0/++}$ baryons have been measured many experiments, but uncertainty remains large [15]. For example, decay width of the $\Sigma_c^{0/++}$ is 10% of its central value, and the mass spilitting $m(\Sigma_c(2455)^{++}) - m(\Sigma_c(2455)^0)$ is about 40%. Because of mass hierarchy between u and d quarks, mass of $\Sigma_c^0(udc)$ should be havier than $\Sigma_c^{++}(uuc)$. However the experimetal results shows opposite mass hiearchy with large error [17]. In this situation, precise mass and width measurement is necessay.

The $\Sigma_c^{0/++}$ baryons are reconstructed via $\Sigma_c^{0/++} \to \Lambda_c^+(\to pK^-\pi^+)\pi_s^{-/+}$ decay channel, where π_s is low momentum pion. The feed down from $\Lambda_c(2595, 2620)^+$ is removed with mass cut on $m(\Lambda_c^+\pi^+\pi^-)$,

The fitting functions for signal is Breit-Wiegner function convolved with detector resolution function. The random back ground function is threshold function. There is feed down around $\Delta M = 185$ MeV/c^2, we confirmed that the origin of the peak is from $\Xi_c^0 \to \Lambda_c^+\pi^-$. This peak is described by Gaussian funcion. The χ^2/ndf for fit result is 350/347 for zero charge, 343/350 for double charge. The mass and width from fitting result is on table 1. This result shows better uncertainty than previous result.

	ΔM_0(MeV/c^2)	Γ(MeV/c^2)	M_0(MeV/c^2)
$\Sigma_c(2455)^0$	$167.29 \pm 0.01 \pm 0.02$	$1.76 \pm 0.04^{+0.09}_{-0.21}$	$2453.75 \pm 0.01 \pm 0.02 \pm 0.14$
$\Sigma_c(2455)^{++}$	$167.51 \pm 0.01 \pm 0.02$	$1.84 \pm 0.04^{+0.07}_{-0.20}$	$2453.97 \pm 0.01 \pm 0.02 \pm 0.14$
$\Sigma_c(2520)^0$	$231.98 \pm 0.11 \pm 0.04$	$15.41 \pm 0.41^{+0.20}_{-0.32}$	$2518.44 \pm 0.11 \pm 0.04 \pm 0.14$
$\Sigma_c(2520)^{++}$	$231.99 \pm 0.10 \pm 0.02$	$14.77 \pm 0.25^{+0.18}_{-0.30}$	$2518.45 \pm 0.10 \pm 0.02 \pm 0.14$

Table 1: The measurement of mass and with of the $\Sigma_c(2455)^{0/++}$ and $\Sigma_c(2520)^{0/++}$. The first error is stastical error and second error is systematical error. The third error on M_0 is from mass error of Λ_c^+

2.3 Search for doubly charmed baryon and charmed strange baryon at Belle [18]

In recent years, there has been significant progress in charmed baryon spectroscopy. So far, there are no experimentally established doubley charmed baryon. The SELEX collaboration reported evidence of Ξ_{cc}^{+} in the $\Lambda_c^+ K^- \pi^+$ and pD^+K^- final state [19]. However, the result is not supported by FOCUS, BABAR, Belle nor LHCb. In this study, we improve the search using more data and more channels.

The first decay channel is $\Xi_{cc}^{+(+)} \rightarrow \Lambda_c^+ K^- \pi^+(\pi^+)$ and $\Lambda_c^+ \rightarrow pK^-\pi^+$. We searched the mass region of 3.2∼4.0 GeV/c^2, no significance signal is seen in the data. The local significance is lower than 3σ. The upper limit of production cross section and Branching fraction with 95% C.L. is around 10fb^{-1}.

The sesond decay channel is $\Xi_{cc}^{+(+)} \rightarrow \Xi_x^0 \pi^+(\pi^+)$ and $\Xi_c^0 \rightarrow \Xi^0\pi-, \Lambda K^-\pi^+, pK^-K^-\pi^+$. We searched same mass range with first decay cheannel, still there is no significant signal over mass range. The highst signal is around 3.553 GeV/c^2, but it is not significant with look elsewhere effect.

And we also searched the strange charmed baryon $\Xi_c^+(3055)$ and $\Xi_c^+(3123)$, using the decay channel $\Xi_c^+(3055, 3123) \rightarrow \Lambda_c^+ K^- \pi^-$ over the mass range 2.9∼3.2 GeV/c^2. We observed the significant signal of $\Xi_c^+(3055)$ with 6.8σ, while no peak of $\Xi_c^+(3123)$. The upper limit of $\Xi_c^+(3123)$ cross section and branching ratio is $1.6 \pm 0.6 \pm 0.2\text{fb}^{-1}$.

In summary, searching $\Xi_{cc}^{+(+)}$ using more data and more decay channels doesn't show the signal over the mass range of 3.2∼4.0 GeV/c^2. For the strange charmed baryon search, we obersed $\Xi_c^+(3055)$ with 6.8σ, but couldn't see the peak of $\Xi_c^+(3123)$.

References

[1] A. A. Petrov, Int. J. Mod. Phys. A 21, 5686 (2006).

[2] A. F. Falk, Y. Grossman, Z. Ligeti, and A.A. Petrov, Phys. Rev. D 65, 054034 (2002).

[3] E. Golowich, J. Hewett, S. Pakvasa, and A.A. Petrov, Phys. Rev. D 79, 114030 (2009).

[4] Y. Grossman, A. L. Kagan, and Y. Nirm Phys. Rev. D 75, 036008 (2007).

[5] B. R. Ko *et al.*. (Belle Collaboration) Phys. Rev. Lett. **112**, 111801 (2014).

[6] Y. Aubert *et al.*. (Heavy Flavor Averaging Group), arXiv:1207.1158v2.

[7] R. Aaij *et al.*. (LHCb Collaboration), Phys. Rev. Lett. **110**, 101802 (2013).

[8] T. Aaltonen *et al.*. (CDF Collaboration), Phys. Rev. Lett. **111**, 231802 (2013).

[9] T. Peng *et al.*. (Belle Collaboration) Phys. Rev. D. **89**, 091103 (2014).

[10] N. K. Nisar *et al.*. (Belle Collaboration) Phys. Rev. Lett. **112**, 211601 (2014).

[11] G. Bonvicini *et al.*. (CLEO Collaboration) Phys. Rev. D. **63**, 071101 (2014).

[12] A. Zupanc *et al.*. (Belle Collaboration) Phys. Rev. Lett. **113**, 042002 (2014).

[13] H. Albrecht *et al.*. (ARGUS Collaboration) Phys. Lett. B. **207**, 109 (1988).

[14] G. D. Crawford *et al.*. (CLEO Collaboration) Phys. Rev. D. **45**, 752 (1992).

[15] J. Beringer *et al.*. (Particle Data Group) Phys. Rev. D. **86**, 01001 (2012).

[16] S. H. Lee *et al.*. (Belle Collaboration) Phys. Rev. D. **89**, 091102 (2014).

[17] E. M. Aitala *et al.*. (E791 Collaboration) Phys. Lett. B. **379**, 292 (1996).

[18] Y. Kato *et al.*. (Belle Collaboration) Phys. Rev. D. **89**, 052003 (2014).

[19] M. Mattson *et al.*. (SELEX Collaboration) Phys. Rev. Lett. **89**, 112001 (2002).

Exploring the long-distance structure of the $X(3872)$

Feng-Kun Guo[1], *Carlos Hidalgo-Duque*[2], *Juan Nieves*[2], *Altug Ozpineci*[3], *Manuel Pavón Valderrama*[4]

[1]Helmholtz-Institut für Strahlen- und Kernphysik and Bethe Center for Theoretical Physics, Universität Bonn, D-53115 Bonn, Germany
[2]Instituto de Física Corpuscular (IFIC), Centro Mixto CSIC-Universidad de Valencia, Institutos de Investigación de Paterna, Aptd. 22085, E-46071 Valencia, Spain
[3] Middle East Technical University - Department of Physics TR-06531 Ankara, Turkey
[4] Institut de Physique Nucléaire, Université Paris-Sud, IN2P3/CNRS, F-91406 Orsay Cedex, France

DOI: http://dx.doi.org/10.3204/DESY-PROC-2014-04/2

In this work we use an effective field theory (EFT) approach to study the $X(3872)$ resonance, assuming a heavy meson-heavy antimeson molecule as its inner structure. From this EFT we extract some direct consequences for the hidden charm and bottom hadronic spectrum.

Within this EFT we also study the decay $X(3872) \to D^0\bar{D}^0\pi^0$. This decay is unique since it is more sensitive to the long-distance part of the $X(3872)$ wave function than the $X(3872) \to J/\psi\pi\pi$ and $X(3872) \to J/\psi\pi\pi\pi$ modes. We also show that the possible $D\bar{D}$ Final State Interactions (FSI) effects can lead to experimental constrains on the Low Energy Constants (LECs) that appear in the EFT and the possible existence of a loosely $D\bar{D}$ bound state.

1 Introduction

The current understanding of the hadronic spectrum is a milestone in particle physics. The success of the conventional quark model (where mesons and baryons are the only possible quark composites) in the classification of known particles and the prediction of different states is outstanding. However, beyond the quark model there are other exotic possibilities that QCD allows. These exotics (glueballs, tetraquarks, hadronic molecules...), though theoretically predicted, have not been experimentally confirmed yet.

The existence of hadronic molecules, first predicted in the mid-70s by Voloshin and Okun [1] was based on the similarities these systems shared with the deuteron. The best candidate to fit this hadronic molecule description is the $X(3872)$, discovered by Belle in 2003 [2] in the $J/\psi\pi\pi$ channel. Based on the closeness to the $D\bar{D}^*$ threshold this resonance is thought to be a $D\bar{D}^*$ with quantum numbers $J^{PC} = 1^{++}$. These quantum numbers were later confirmed in 2011 by the LHCb collaboration [3]. Taking into account this experimental information, it seems likely that the hadronic molecule component of the $X(3872)$ wave function plays an important role in the description of the resonance.

In this work we use an EFT to describe these heavy meson-heavy antimeson molecules. In Sec. 2 the main features of this EFT are briefly explained since they have been extensively covered in previous works. In Sec. 3, the computation of the $X(3872) \to D^0\bar{D}^0\pi^0$ decay width is carried out. Finally some conclusions are established in Sec. 4.

2 The heavy meson-heavy antimeson EFT

In this section the EFT that is going to be used along this work is introduced. At leading order (LO), the description of heavy meson-heavy antimeson molecules can be done with a contact potential determined by Heavy Quark Spin Symmetry (HQSS) as proposed in [4]. This LO lagrangian, when considering the isospin degrees of freedom, depends exclusively on four undetermined LECs. Other subleading effects such as pion exchanges and coupled channel effects are less important than expected and can be taken into account by the errors of the order $\mathcal{O}\left(\frac{1}{m_Q}\right)$, that will be introduced to account for not considering the next order in the EFT expansion [5].

The lagrangian provides the kernel that is employed in a Lippmann-Schwinger Equation (LSE). Poles in the T-matrix give rise to the different molecular states. The LSE, however, has a ultraviolet divergent two-body loop function. This divergence can be treated employing several regularization methods. We are using a gaussian regulator Λ and we choose two different gaussian regulators $\Lambda = 0.5(1.0)$ GeV, see [6, 7] for details.

Now, assuming some experimental resonances are heavy meson-heavy antimeson molecules we can fix some linear combination of the four undetermined LECs in the lagrangian. For that purpose, we find that the $X(3872)$ and the $Z_b(10610)/Z_b'(10650)$ [10] are perfect candidates. As already said, the $X(3872)$ can be thought as a $D\bar{D}^*$ with quantum numbers $J^{PC} = 1^{++}$. In the Z_bs case, we are dealing with resonances whose quark content must be of, at least, four quarks since they have $I_{Z_b} = 1$. Even more, its closeness to the $B\bar{B}^*$ and $B^*\bar{B}^*$ threshold respectively, suggest that a molecular interpretation with quantum numbers $J^{PC} = 1^{+-}$ is very sensible.

Thanks to these two assumptions we can fix three different linear combinations on LECs. Two of them come from the $X(3872)$ assumption (where we have also taken into account the isospin violating decays in the fit, see [7] for further information) and the third one comes from the experimental masses of the Z_bs resonances. This means that there is still an undetermined LEC in our model, that we will call C_{0A} without loss of generality.

We have used this scheme in previous works, predictions for HQSS heavy meson-heavy antimeson molecules [6, 7, 8] and pentaquark-like states that will be partners of the $X(3872)$ and $Z_b(10610)/Z_b'(10650)$ resonances [9]. In these works we found that there was almost no dependence on the regulation method used and that the small differences that appear can be accounted in the expansion errors too.

3 $X(3872) \to D^0\bar{D}^0\pi^0$ decay

So far, the only experimental information about the $X(3872)$ we have used in the analysis is its mass and the ratio of its $X(3872) \to J/\psi\pi\pi$ and $X(3872) \to J/\psi\pi\pi\pi$ decay widths. In these decays, the $D(\bar{D})$ and $\bar{D}^*(D^*)$ components of the $X(3872)$ have to be close so its charm quark and antiquark can form a charmonium state. Therefore, we can extract little information about the long-distance structure of the $X(3872)$. This long-distance structure of the resonance could become a very important piece of information to differenciate between two exotic structures like tetraquarks and hadronic molecules.

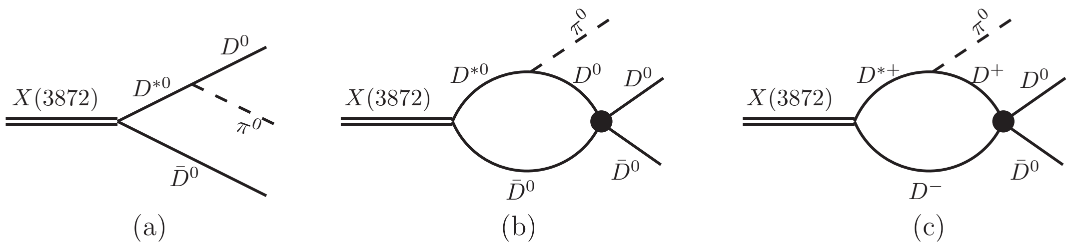

Figure 1: Feynman diagrams for the decay $X(3872) \to D^0\bar{D}^0\pi^0$. The charge conjugate channel is not shown but included in the calculations.

Hence, the detailed analysis of different decays where the $X(3872)$ inner components keep their individual properties is crucial for the full comprehension of the resonance. The $X(3872) \to D^0\bar{D}^0\pi^0$ (already observed in [11]) decay looks like a perfect probe of the long-distance structure of the $X(3872)$. As it can be seen in Fig.1, the $X(3872)$ can decay despite its $D^{*0}(\bar{D}^{*0})$ and $\bar{D}^0(D^0)$ inner components are substancially separated. It should already be noticed that this is the only $X(3872) \to D\bar{D}\pi$ decay channel since the charged decays are kinematically forbidden.

In this decay, there are two contributions. The tree level contribution is depicted in Fig.1a (and its corresponding charge conjugated diagram). From the $X(3872)$ pole residue we determine the $X(3872)D^0\bar{D}^0$ coupling and we obtain [12]:

$$\Gamma(X(3872) \to D^0\bar{D}^0\pi^0)_{\text{tree}} = 44.0^{+2.4}_{-7.2}\left(42.0^{+3.6}_{-7.3}\right)\ \text{keV}, \tag{1}$$

for $\Lambda = 0.5$ (1.0) GeV, respectively. Next, we include the possible FSI between the D-mesons and the $\bar{D}$-antimesons, as shown in the Feynman diagrams of Fig.1b and Fig.1c. In this case, we need for the computation of the decay width the four LECs of our model. Our results, therefore, will be a function of the undetermined LEC C_{0A}. The results obtained are displayed in Fig.2, being the grey band the results coming from the tree level calculation.

As can be observed, there is no appreciable dependence on the gaussian regulator in the results. However, the inclusion of FSI mechanism has created a *bump* in the decay width curve. This is caused by the interferences due to the possible existence of a $D\bar{D}$ bound state with quantum numbers $J^{PC} = 0^{++}$. For that reason, a precise experimental value of the $X(3872) \to D^0\bar{D}^0\pi^0$ decay width could be an important asset in the determination of the fourth, still undetermined, LEC and can also rule out or confirm the existence of this $D\bar{D}$ bound state, predicted in several theoretical models.

4 Conclusions

In this work, we have studied the decay of the $X(3872)$ resonance into $D^0\bar{D}^0\pi^0$ using an EFT based on a hadronic molecule assumption for the $X(3872)$ and HQSS. We show that $D\bar{D}$ FSI effects can be important specially if a near threshold pole exists. Besides, this decay may be used to measure the so far unknown parameter C_{0A} of the HQSS EFT employed in this work. Such information is valuable to better understand the interaction between heavy-light mesons and heavy-light antimesons.

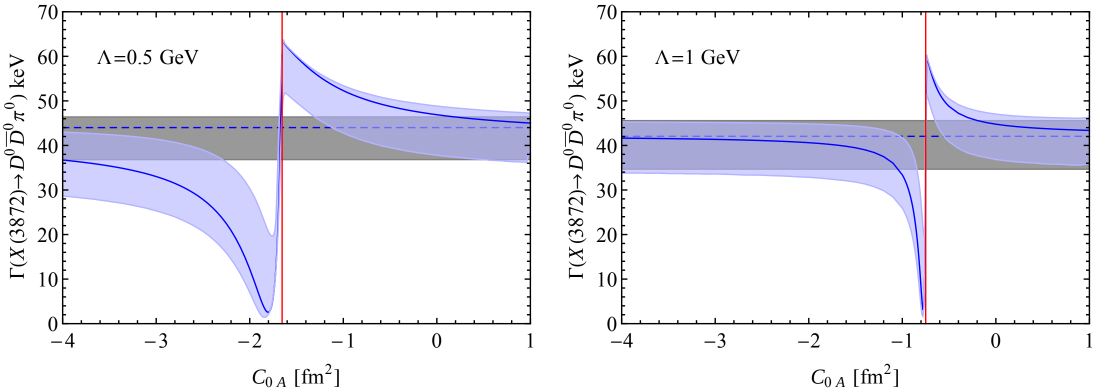

Figure 2: Dependence of the $X(3872) \to D^0\bar{D}^0\pi^0$ partial decay width on the C_{0A} LEC. The UV cutoff is set to $\Lambda = 0.5$ GeV (1 GeV) in the left (right) panel. The blue error bands contain $D\bar{D}$ FSI effects, while the grey bands stand for the tree level prediction. The vertical lines denote the values of C_{0A} for which a $D\bar{D}$ bound state is generated at the $D^0\bar{D}^0$ threshold.

Acknowledgments

C. H.-D. thanks the support of the JAE-CSIC Program. This work is supported in part by the DFG and the NSFC through funds provided to the Sino-German CRC 110 "Symmetries and the Emergence of Structure in QCD", by the NSFC (Grant No. 11165005), by the Spanish Ministerio de Economía y Competitividad and European FEDER funds under the contract FIS2011-28853-C02-02 and the Spanish Consolider-Ingenio 2010 Programme CPAN (CSD2007-00042), by Generalitat Valenciana under contract PROMETEO/2009/0090 and by the EU HadronPhysics3 project, grant agreement no. 283286.

References

[1] M. B. Voloshin and L. B. Okun, JETP Lett. **23** (1976) 333 [Pisma Zh. Eksp. Teor. Fiz. **23** (1976) 369].

[2] S. K. Choi *et al.* [Belle Collaboration], Phys. Rev. Lett. **91** (2003) 262001

[3] R. Aaij *et al.* [LHCb Collaboration], Phys. Rev. Lett. **110** (2013) 222001

[4] M. T. AlFiky, F. Gabbiani and A. A. Petrov, Phys. Lett. B **640** (2006) 238

[5] M. P. Valderrama, Phys. Rev. D **85** (2012) 114037

[6] J. Nieves and M. P. Valderrama, Phys. Rev. D **86** (2012) 056004

[7] C. Hidalgo-Duque, J. Nieves and M. P. Valderrama, Phys. Rev. D **87** (2013) 7, 076006

[8] F. K. Guo, C. Hidalgo-Duque, J. Nieves and M. P. Valderrama, Phys. Rev. D **88** (2013) 054007

[9] F. K. Guo, C. Hidalgo-Duque, J. Nieves and M. P. Valderrama, Phys. Rev. D **88** (2013) 5, 054014

[10] I. Adachi *et al.* [Belle Collaboration],

[11] G. Gokhroo *et al.* [Belle Collaboration], Phys. Rev. Lett. **97** (2006) 162002

[12] F. K. Guo, *et al.*, Eur. Phys. J. C **74** (2014) 2885

Chiral Perturbation Theory tests at NA48 and $NA62\text{-}R_K$ experiments at CERN

Flavio Costantini[1] for the NA48/2 Collaboration : Cambridge, CERN, Dubna, Chicago, Edinburgh, Ferrara, Firenze, Mainz, Northwestern, Perugia, Pisa, Saclay, Siegen, Torino, Wien and the NA62-R_K Collaboration: Birmingham, CERN. Dubna, Fairfax, Ferrara, Firenze, Frascati, Mainz, Merced, Moscow, Napoli, Perugia, Pisa, Protvino, Roma I, Roma II, Saclay, San Luis Potosi, Stanford, Sofia, Torino, TRIUMF.

[1]Dipartimento di Fisica, Università di Pisa and INFN Pisa
Largo B. Pontecorvo 3, 56127 Pisa (Italy)

DOI: http://dx.doi.org/10.3204/DESY-PROC-2014-04/16

Final results from an analysis of about 400 $K^\pm \to \pi^\pm\gamma\gamma$ rare decay candidates collected by the NA48/2 and NA62-R_K experiments at CERN during low intensity runs with minimum bias trigger configurations are presented. The results include a model-independent decay rate measurement and fits to Chiral Perturbation Theory (ChPT) description. The data support the ChPT prediction for a cusp in the di-photon invariant mass spectrum at the two pion threshold.

1 Introduction

The NA48/2 experiment at the CERN SPS has collected a large sample of charged kaon decays in 2003–04 (corresponding to about 2×10^{11} $K^\pm$ decays in the vacuum decay volume). The experiment featured simultaneous K^+ and K^- beams and was optimized for the search for direct CP violating charge asymmetries in the $K^\pm \to 3\pi$ decays [1]. Its successor, the NA62-R_K experiment, collected a 10 times smaller $K^\pm$ decay sample with low intensity beams and minimum bias trigger conditions in 2007–08. NA62-R_K used the same detector as NA48/2, while the data taking conditions were optimized for a measurement of the ratio of the rates of the $K^\pm \to \ell^\pm\nu$ decays ($\ell = e, \mu$) [2]. In particular, the main trigger chain required the presence of an electron ($e^\pm$).

The large data samples accumulated by both experiments have allowed precision studies of a range of rare $K^\pm$ decay modes. Recent measurements of the rare decay $K^\pm \to \pi^\pm\gamma\gamma$ (denoted $K_{\pi\gamma\gamma}$ below) from the above data samples [3, 4] are reported here.

2 Beam and detector

The beam line has been designed to deliver simultaneous narrow momentum band K^+ and K^- beams derived from the primary 400 GeV/c protons extracted from the CERN SPS. Secondary beams with central momenta of 60 GeV/c (for NA48/2) or 74 GeV/c (for NA62-R_K) were used.

The beam kaons decayed in a fiducial decay volume contained in a 114 m long cylindrical vacuum tank. The momenta of charged decay products were measured in a magnetic spectrometer, housed in a tank filled with helium placed after the decay volume. The spectrometer comprised four drift chambers (DCHs), two upstream and two downstream of a dipole magnet which provided a horizontal transverse momentum kick of 120 MeV/c (for NA48/2) or 265 MeV/c (for NA62-R_K) to charged particles. Each DCH was composed of eight planes of sense wires. A plastic scintillator hodoscope (HOD) producing fast trigger signals and providing precise time measurements of charged particles was placed after the spectrometer. Further downstream was a liquid krypton electromagnetic calorimeter (LKr), an almost homogeneous ionization chamber with an active volume of 7 m^3 of liquid krypton, $27X_0$ deep, segmented transversally into 13248 projective $\sim 2\times 2$ cm^2 cells and with no longitudinal segmentation. The LKr information is used for photon measurements and charged particle identification. An iron/scintillator hadronic calorimeter and muon detectors, not used in the present analysis, were located further downstream. A detailed description of the detector can be found in Ref. [5].

3 The $K^\pm \to \pi^\pm\gamma\gamma$ decay in the ChPT

Measurements of radiative non-leptonic kaon decays provide crucial tests of Chiral Perturbation Theory (ChPT) describing weak low energy processes. The $K_{\pi\gamma\gamma}$ decay has attracted the attention of theorists over the last 40 years [6, 7, 8, 9], but remains among the least experimentally studied kaon decays.

In the ChPT framework, the $K_{\pi\gamma\gamma}$ decay receives two non-interfering contributions at lowest non-trivial order $\mathcal{O}(p^4)$: the pion and kaon loop amplitudes which depend on an a priori unknown $\mathcal{O}(1)$ parameter $\hat{c}$, and the pole amplitude. Higher order unitarity corrections from $K \to 3\pi$ decays modify the decay spectrum significantly; in particular, they lead to non-zero differential decay rate at zero di-photon invariant mass [8]. The total decay rate is predicted to be $\mathcal{B}(K_{\pi\gamma\gamma}) \sim 10^{-6}$, with the pole amplitude contributing 5% or less [8, 9]. The ChPT predictions for the differential rate $d\Gamma/dz$ with $z = (m_{\gamma\gamma}/m_K)^2$, where $m_{\gamma\gamma}$ is the di-photon invariant mass, for several values of $\hat{c}$, are presented in Fig. 1. These spectra exhibit a characteristic cusp structure at twice the pion mass due to the dominant pion loop amplitude.

Experimentally, the only published $K_{\pi\gamma\gamma}$ observation is that of 31 K^+ decay candidates in the kinematic region 100 MeV/$c < p^*_\pi <$ 180 MeV/c (p^*_π is the π^+ momentum in the K^+ frame) by the BNL E787 experiment [10].

4 Measurements of the $K^\pm \to \pi^\pm\gamma\gamma$ decay

New measurements of the $K_{\pi\gamma\gamma}$ decay have been performed using two minimum bias data sets: 1) two special $K^\pm$ decay samples collected by the NA48/2 experiment at $\sim 10\%$ of the nominal beam intensity during 12 hours in 2003 and 54 hours in 2004; 2) a subset of the NA62-R_K data sample collected over the whole duration of the data taking with downscaled trigger conditions with an effective downscaling factor of about 20. The employed trigger conditions required a time coincidence of signals in both HOD horizontal and vertical strip planes within the same quadrant and an energy deposit of at least 10 GeV in the LKr calorimeter. The resulting effective kaon fluxes used for the NA48/2 and NA62-R_K $K_{\pi\gamma\gamma}$ analyses are similar, but the background conditions and resolution on kinematic variables differ significantly. The $K_{\pi\gamma\gamma}$ decay rate was measured with respect to the normalization decay chain with a large and well

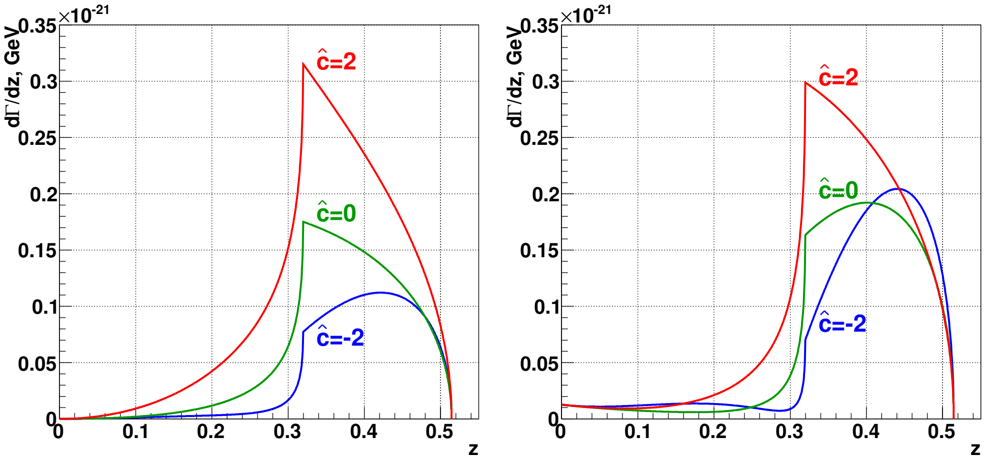

Figure 1: Differential rate ($d\Gamma/dz$) of the $K_{\pi\gamma\gamma}$ decays according to the $\mathcal{O}(p^4)$ (left) and $\mathcal{O}(p^6)$ (right) descriptions [7, 8] for several values of $\hat{c}$. The $\hat{c}$-independent pole contribution is also shown. For the $\mathcal{O}(p^6)$ parameterization, values of polynomial contributions [8] $\eta_i = 0$ and $K^\pm \to 3\pi^\pm$ amplitude parameters from a fit to experimental data [11] are used.

known branching fraction: the $K^\pm \to \pi^\pm\pi^0$ decay followed by the $\pi^0 \to \gamma\gamma$ decay. Signal and normalization samples have been collected with the same trigger logic.

Signal events are selected on the basis of spectrometer and LKr calorimeter information in the kinematic region $z = (m_{\gamma\gamma}/m_K)^2 > 0.2$ to reject the $K^\pm \to \pi^\pm\pi^0$ background, as well as other backgrounds from the π^0 decays, peaking at $z = (m_{\pi^0}/m_K)^2 = 0.075$. The residual background contamination is due to $K^\pm \to \pi^\pm\pi^0\gamma$ and $K^\pm \to \pi^\pm\pi^0\pi^0$ decays, with photons either missing the LKr acceptance of forming merged clusters in the LKr calorimeter. The event selection includes an upper limit for the transverse size of the LKr clusters, which reduces the background due to merged clusters. The $\pi^\pm\gamma\gamma$ invariant mass spectra of the selected $K_{\pi\gamma\gamma}$ candidates, with the expectations of the signal and background contributions from MC simulations, are displayed in Fig. 2: 149 (232) decay candidates with a background contamination of 10% (7%) are observed in the NA48/2 (NA62-R_K) data set.

A model-independent measurement of the z spectrum in the kinematic range $z > 0.2$ has been performed for the NA48/2 and NA62-R_K data sets. The partial branching fractions in bins of the z variable have been measured: they are model-independent because the considered z bin width is sufficiently small for the acceptances in z to have a negligible dependence on the assumed $K_{\pi\gamma\gamma}$ kinematical distribution. In addition, the y-dependence of the differential decay rate expected within the ChPT framework is weak [8, 9]. The final results of the measurements of the partial branching fractions in bins of the z variable are presented in Fig. 3 (left). The model-independent branching fraction in the kinematic region $z > 0.2$ is computed by summing over the z bins: $\mathcal{B}_{\rm MI}(z > 0.2) = (0.965 \pm 0.061_{\rm stat} \pm 0.014_{\rm syst}) \times 10^{-6}$.

Measurements of the ChPT parameter $\hat{c}$ have been made for both NA48/2 and NA62-R_K data samples by performing log-likelihood fits to the reconstructed z spectra. The data spectra of the z kinematic variable, together with signal and background expectations from simulations, are displayed in Fig. 3 (centre, right): they support the ChPT prediction of the cusp at $2m_\pi$ threshold. The values of the $\hat{c}$ parameter in the framework of the ChPT $\mathcal{O}(p^4)$

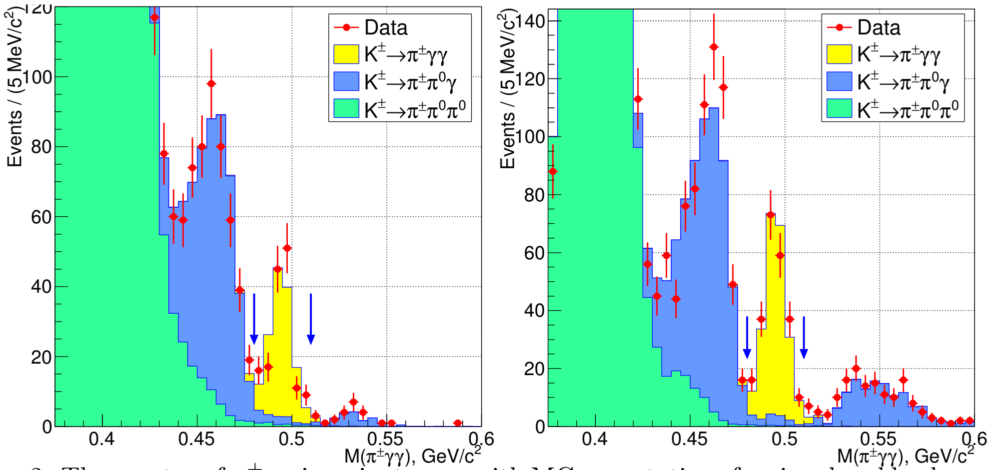

Figure 2: The spectra of $\pi^{\pm}\gamma\gamma$ invariant mass with MC expectations for signal and backgrounds: NA48/2 data (left) and NA62-R_K data (right). The signal region is between the 2 arrows.

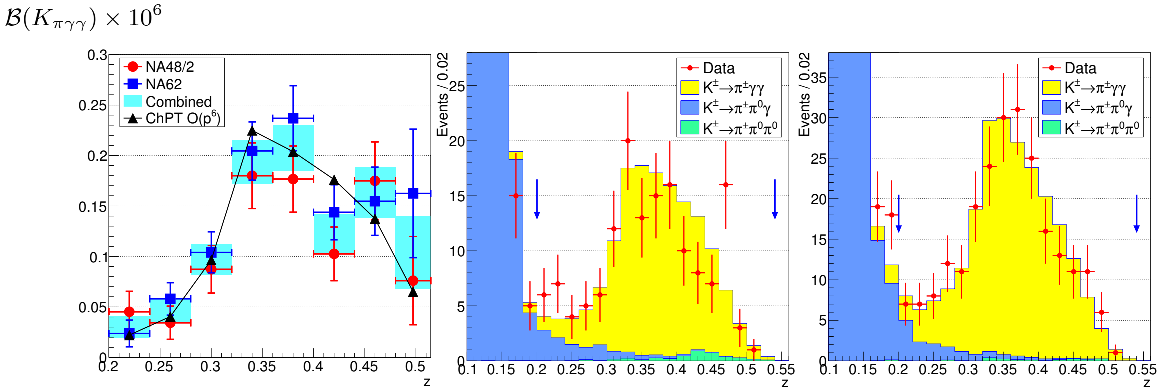

Figure 3: Left: measurements of partial model-independent branching fractions of the $K_{\pi\gamma\gamma}$ decay in bins of the z kinematic variable from the NA48/2 and NA62-R_K data samples. The spectra of $z = (m_{\gamma\gamma}/m_K)^2$ with MC expectations for signal (best fit) and backgrounds: NA48/2 data (centre) and NA62-R_K data (right). The signal region $(0.2 < z < 0.52)$ is between the 2 arrows.

and $\mathcal{O}(p^6)$ parametrizations according to the formulation of [8] have been obtained. The $\mathcal{O}(p^6)$ parametrization involves a number of external inputs. In this analysis, they have been fixed as follows: the polynomial contribution terms are $\eta_1 = 2.06$, $\eta_2 = 0.24$ and $\eta_3 = -0.26$ as suggested in [8], while the $K^{\pm} \to 3\pi^{\pm}$ amplitude parameters come from a fit to the experimental data [11].

The results of the fits are presented in Table 1: they are in agreement with the earlier BNL E787 ones. A combination of results from the two experiments has been performed, taking into account the large positive correlation of the systematic uncertainties of the two measurements. The combined results are also presented in Table 1. The uncertainties are dominated by the statistical ones; the systematic errors on the combined results are dominated by those due to background subtraction. The branching ratio in the full kinematic range corresponding to the combined value of the $\hat{c}$ parameter within the $\mathcal{O}(p^6)$ formulation is $\mathcal{B}(K_{\pi\gamma\gamma}) = (1.003 \pm 0.056) \times 10^{-6}$.

Table 1: Results of fits to the ChPT parameters [8] of the $K^\pm \to \pi^\pm\gamma\gamma$ di-photon mass spectra.

	NA48/2 measurement	NA62-R_K measurement	Combined
$\hat{c}$, $\mathcal{O}(p^4)$ fit	$1.37 \pm 0.33_{\rm stat} \pm 0.14_{\rm syst}$	$1.93 \pm 0.26_{\rm stat} \pm 0.08_{\rm syst}$	$1.72 \pm 0.20_{\rm stat} \pm 0.06_{\rm syst}$
$\hat{c}$, $\mathcal{O}(p^6)$ fit	$1.41 \pm 0.38_{\rm stat} \pm 0.11_{\rm syst}$	$2.10 \pm 0.28_{\rm stat} \pm 0.18_{\rm syst}$	$1.86 \pm 0.23_{\rm stat} \pm 0.11_{\rm syst}$

References

[1] J.R. Batley *et al.*, Eur. Phys. J **C52** (2007) 875.

[2] C. Lazzeroni *et al.*, Phys. Lett. **B719** (2013) 326.

[3] J.R. Batley *et al.*, Phys. Lett. **B730** (2014) 141.

[4] C. Lazzeroni *et al.*, Phys. Lett. **B732** (2014) 65.

[5] V. Fanti *et al.*, Nucl. Instrum. Methods **A574** (2007) 433.

[6] L.M. Sehgal, Phys. Rev. **D6** (1972) 367.

[7] G. Ecker, A. Pich and E. de Rafael, Nucl. Phys. **B303** (1988) 665.

[8] G. D'Ambrosio and J. Portolés, Phys. Lett. **B386** (1996) 403.

[9] J.-M. Gérard, C. Smith and S. Trine, Nucl. Phys. **B730** (2005) 1.

[10] P. Kitching *et al.*, Phys. Rev. Lett. **79** (1997) 4079.

[11] J. Bijnens, P. Dhonte and F. Persson, Nucl. Phys. **B648** (2003) 317.

Detailed study of the K_{e4} decay mode properties from the NA48/2 experiment at CERN

Patrizia Cenci[1] on behalf of the NA48/2 Collaboration: Cambridge, CERN, Dubna, Chicago, Edinburgh, Ferrara, Firenze, Mainz, Northwestern, Perugia, Pisa, Saclay, Siegen, Torino, Wien

[1]INFN Perugia, Via A. Pascoli, 06123 Perugia, Italy

DOI: http://dx.doi.org/10.3204/DESY-PROC-2014-04/17

The NA48/2 Collaboration at CERN has accumulated an unprecedented statistics of rare semileptonic four-body K_{e4} decay modes $K^{\pm} \to \pi^{+}\pi^{-}e\nu$ and $K^{\pm} \to \pi^{0}\pi^{0}e\nu$, with nearly 1% background contamination. Final results from the analyses of the full K_{e4} data samples are described. The most accurate measurements to date of form factors and branching ratios have been achieved by NA48/2, bringing new inputs to low energy QCD description and stringent tests of predictions from Chiral Perturbation Theory and Lattice QCD.

1 Introduction

The NA48/2 experiment at CERN has collected the largest world sample of charged kaon decays with the main goal of searching for direct CP violation [1]. The beam line was designed to deliver simultaneous K^{+} and K^{-} beams at 60 GeV/c central momentum, produced by 400 GeV/c primary protons from the CERN SPS impinging on a beryllium target. Charged particle momenta were measured by a magnetic spectrometer consisting of four drift chambers (DCH) and a dipole magnet. The spectrometer was located in a tank filled with helium at atmospheric pressure and followed by a scintillator trigger hodoscope. A liquid Krypton electromagnetic calorimeter was exploited to measure the energy of electrons and photons. A hadron calorimeter and a muon veto system, essential to distinguish muons from pions, were located further downstream. Details of the experimental apparatus are available in [2].

2 K_{e4} decay mode properties

The study of semileptonic four-body K_{e4} decays is extremely interesting due to the well-known Standard Model (SM) electroweak amplitude responsible for the leptonic part and the small number of hadrons in the final state. In the non-perturbative QCD regime, at energies below 1 GeV, the developments of Chiral Perturbation Theory (ChPT) [3] and Lattice QCD [4] have reached precision levels competitive with the most accurate experimental results.

The NA48/2 experiment has collected high statistics samples of $K^{\pm} \to \pi^{+}\pi^{-}e^{\pm}\nu$ [K_{e4}^{+-}] and $K^{\pm} \to \pi^{0}\pi^{0}e^{\pm}\nu$ [K_{e4}^{00}] candidates, several orders of magnitude larger than the world ones. The latest NA48/2 results from the study of K_{e4}^{+-} decays [5][6] and new results from K_{e4}^{00} data analysis [7] will be reviewed.

2.1 K_{e4} Form Factors and Branching Ratios

K_{e4} decay kinematics is conveniently described by five variables [8]: the squared dipion invariant mass $S_\pi = M^2_{\pi\pi}$, the squared dilepton invariant mass $S_e = M^2_{e\nu}$, the angle θ_π of the pion in the dipion rest frame with respect to the flight direction of the dipion in the kaon rest frame, the angle θ_e of the lepton in the dilepton rest frame with respect to the flight direction of the dilepton in the kaon rest frame, the angle ϕ between dipion and dilepton rest frames.

K_{e4} decay amplitude is given by the product of a leptonic weak current and a (V-A) hadronic current, expressed in terms of three axial-vector (F, G and R) and one vector (H) complex form factors. Due to the smallness of the electron mass, R does not contribute to K_{e4} decay rates. In the isospin symmetry limit, hadronic form factors can be developed in partial wave expansion and expressed in term of S- and P- wave components (the D-wave contribution can be neglected):

$$F = F_s e^{i\delta_s} + F_p e^{i\delta_p} cos\theta_\pi, \qquad G = G_p e^{i\delta_p}, \qquad H = H_p e^{i\delta_p}.$$

Considering a unique phase δ_p for all the P-wave form factors in absence of CP violating weak phases, the decay probability depends on the real form factor magnitudes F_s, F_p, G_p, H_p and a single phase shift $\delta = \delta_s - \delta_p$.

High precision measurements of K^{+-}_{e4} and K^{00}_{e4} hadronic form factors and branching ratios (BR) have been published by NA48/2 [5][6][7]. Decay rates are measured relative to the $K_{3\pi}$ normalization channels, $K^\pm \to \pi^+\pi^-\pi^\pm$ [$K^{+-}_{3\pi}$] for the K^{+-}_{e4} mode and $K^\pm \to \pi^0\pi^0\pi^\pm$ [$K^{00}_{3\pi}$] for the K^{00}_{e4} one. The main background sources are given, respectively, by $K^{+-}_{3\pi}$ and $K^{00}_{3\pi}$ events with a fake electron due to charged pion misidentification or with $\pi^\pm \to e^\pm\nu$ decays.

The measurements of BR(K^{+-}_{e4}) and BR(K^{00}_{e4}) are obtained from the number of reconstructed signal, background and normalization events, corrected for different acceptances and trigger efficiencies in the signal and normalization modes. The PDG [9] values are used for BR($K^{+-}_{3\pi}$) and BR($K^{00}_{3\pi}$). Since in both K_{e4} analyses the topologies of candidate and normalization events are similar in terms of the number of detected charged ($e^\pm$ or $\pi^\pm$) and neutral ($\pi^0\pi^0$ or $\pi^+\pi^-$) particles, signal and normalization samples are collected concurrently employing the same trigger logic and common selections as far as possible. This leads to the partial cancellation of systematic effects induced by imperfect beam description, local detector and trigger inefficiencies and makes the measurement independent on the absolute kaon flux measurements. A detailed Monte Carlo simulation has been developed to include full detector geometry, DCH alignment, local inefficiencies and beam properties.

K^{+-}_{e4} **decays.** Nearly 1.13×10^6 K^{+-}_{e4} candidates with about 0.6% background contamination have been reconstructed by NA48/2. The form factor analysis is performed in the five-dimensional space of the kinematic variables [8] to take into account the precise knowledge of experimental acceptance and resolution. The large data statistics allows to define grids of equal population five-dimensional boxes. Hadronic form factors and their dependence on energy are obtained by adjusting the expected number of simulated events to the observed data events. Positive and negative kaon charges are analysed separately to account for the different beam geometries. The results are consistent for both kaon charges and are combined according to their statistical error. Form factors are expressed as Taylor series expansion of $q^2 = S_\pi/(4m^2_{\pi^+}) - 1$ and $y^2 = S_e/(4m^2_{\pi^+})$ dimensionless invariants [10]. Only relative form factors can be measured, normalized to the overall scale factor f_s=$F_s(q^2 = 0, S_e = 0)$. The S- and P-wave form factors and their variation with energy have been measured [5][6]. F_s is described by one curvature and two slopes: $F_s = f_s[1 + (f'_s/f_s)q^2 + (f''_s/f_s)q^4 + (f'_e/f_s)y^2]$; G_p by one slope and an offset: $G_p = f_s[(g_p/f_s) + (g'_p/f_s)q^2]$; F_p and H_p by constants. The first evidence for a negative 5% contribution from F_p and for a S_e dependence of F_s have been established.

The BR value, evaluated from 16 statistically independent subsamples separately for K^+ and K^-, is $\mathrm{BR}(K_{e4}^{+-}) = (4.257 \pm 0.004_{stat} \pm 0.016_{syst} \pm 0.031_{ext}) \times 10^{-5}$, inclusive of $K_{e4\gamma}$ decays. The 0.8% total error is dominated by the external uncertainty from the PDG value of the normalization mode $\mathrm{BR}(K_{3\pi}^{+-})$.

The BR measurement allows assigning absolute values to the relative form factors. The overall form factor normalization is $f_s = 5.705 \pm 0.017_{exp} \pm 0.031_{ext}$, $(\sigma_{exp} = \sigma_{stat} \oplus \sigma_{syst})$. The main error is the external one, due to uncertainties on the PDG values of kaon lifetime, CKM matrix element $|V_{us}|$ and $\mathrm{BR}(K_{3\pi}^{00})$ [9]. The 0.6% total relative precision improves previous results of a factor of 2 to 4.

K_{e4}^{00} **decays.** An unprecedented statistics of 65210 K_{e4}^{00} candidates has been collected by NA48/2, with (1.00±0.02)% background [7]. The formalism for studying K_{e4}^{00} decays is simpler because of two identical particles, $\pi^0\pi^0$, in the final state. As G and H form factors are antisymmetric in the exchange of the two pions, they do not contribute to the decay probability. At leading order only the S-wave component of the partial wave expansion is present and the differential rate depends on a single complex hadronic form factor $F = F_s e^{i\delta_s}$ with magnitude F_s, whose variation with (S_π, S_e) has been studied. A data sample free of radiative effects is selected. F_s is estimated by fitting the data in the (S_π, S_e) plane (Dalitz plot) where the event density is proportional to F_s^2. A grid is defined with equal population bins. A sample of Monte Carlo simulated events, including acceptance and resolution effects, trigger efficiency, radiative corrections and a constant F_s value is distributed over the same grid as the data. A formalism based on the q^2 and y^2 variables has been used for a direct comparison with K_{e4}^{+-} results.

Fig. 1(a) shows the ratio of the q^2 distributions for data and simulated events in equal population bins. Above q^2=0 the distribution is similar to the K_{e4}^{+-} one, while it is depleted at negative values. The line corresponds to the empirical description using the best fit-parameters: a degree-2 polynomial for positive q^2 values and a cusp-like function below zero. Only statistical errors are represented. A possible interpretation of the observed deficit of events for negative q^2 values can be related to final state charge exchange scattering processes $(\pi^+\pi^- \to \pi^0\pi^0)$ in the K_{e4}^{+-} mode, as observed in the $K_{3\pi}^{00}$ mode analysis [11]. A more elaborate description of the K_{e4}^{00} amplitude is needed to extract more information on physical quantities from the result reported here. Fig. 1(b) shows the comparison of form factor results for K_{e4}^{+-} and K_{e4}^{00} data in the (q^2, y^2) formulation, displayed in the $(f_s'/f_s,\ f_s''/f_s)$ plane. All contours are 68% C.L., errors are statistical only. The smaller area in the charged mode is due to the larger statistics. The correlations between fitted parameters are very similar and the results for K_{e4}^{+-} and K_{e4}^{00} decays are consistent within statistical errors.

Exploiting a model independent form factor description, $\mathrm{BR}(K_{e4}^{00})$, inclusive of radiative decays, has been measured with respect to the $K_{3\pi}^{00}$ normalization mode. The global result is $\mathrm{BR}(K_{e4}^{00}) = (2.552 \pm 0.010_{stat} \pm 0.010_{syst} \pm 0.032_{ext}) \times 10^{-5}$, given by the combination of the values obtained for ten statistically independent sub-samples. The 1.4% relative precision is dominated by the external uncertainty from the normalization mode $\mathrm{BR}(K_{3\pi}^{00})$ [9]. This result improves the current world average BR by more than one order of magnitude.

Both total rate and form factor descriptions are used to obtain the absolute form factor value. A long distance electromagnetic correction δ_{EM} to the total rate, not yet available in the literature, should be taken into account. The absolute form factor value is $(1+\delta_{EM}) \times f_s = 6.079 \pm 0.012_{stat} \pm 0.027_{syst} \pm 0.046_{ext}$. The main external uncertainty is due to the errors on the PDG values of kaon lifetime, CKM matrix element $|V_{us}|$ and $\mathrm{BR}(K_{3\pi}^{00})$ [9]. A difference from the K_{e4}^{+-} result has been observed, statistically significant as experimental errors are mostly uncorrelated. A more precise theoretical description of the K_{e4}^{00} mode, including radiative,

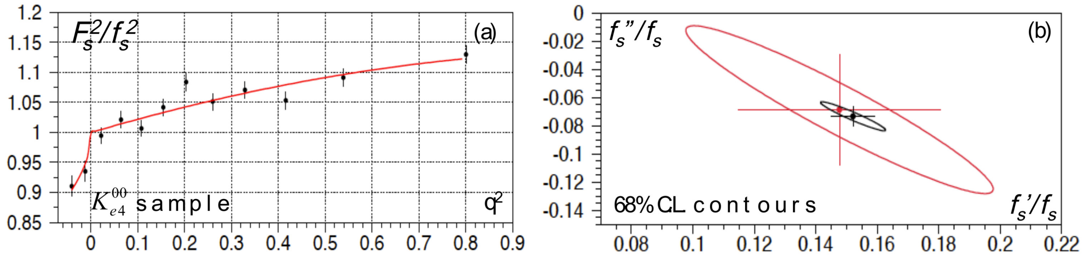

Figure 1: (a) Ratio of q^2 distributions for data and simulated K_{e4}^{00} events. The line corresponds to the empirical description using the best fit parameters. Errors are statistical only. (b) Form factor comparison in the (f_s'/f_s, f_s''/f_s) plane for K_{e4}^{+-} (black, smaller area) and K_{e4}^{00} (red) decays in the (q^2, y^2) series expansion formulation. Only statistical errors are plotted

isospin symmetry breaking and re-scattering effects, should be considered before drawing any solid conclusion.

Phase shift and scattering lenghts in the $\pi\pi$ system. The asymmetry of the dilepton with respect to the dipion system is strictly related to the phase difference between S- and P-waves in $\pi\pi$ scattering. Hadronic form factors in the S- and P-waves have been obtained from K_{e4}^{+-} data analysis, concurrently with the phase difference between the S- and P-wave states of the $\pi\pi$ system, leading to precise determinations of a_0^0 and a_0^2, the isospin I=0 and I=2 S-wave $\pi\pi$ scattering lengths, with accuracy competitive with the most elaborate theoretical predictions. Combining K_{e4}^{+-} results with the former NA48/2 measurements based on the study of $K_{3\pi}^{00}$ decays [12], an improved determination of a_0^0 and the first precise measurement of a_0^2 are obtained: $a_0^0 = 0.2210 \pm 0.0047_{stat} \pm 0.0040_{syst}$, $a_0^2 = -0.0429 \pm 0.0044_{stat} \pm 0.0028_{syst}$, $a_0^0 - a_0^2 = 0.2639 \pm 0.0020_{stat} \pm 0.0015_{syst}$ [5].

This result confirm the prediction of Lattice QCD and ChPT [13]. The latest world average experimental values are now dominated by the NA48/2 experimental precision.

References

[1] R. Batley *et al.*, Eur. Phys. J **C52** 875 (2007).

[2] V. Fanti *et al.*, Nucl. Instrum. Method **A574** 433 (2007).

[3] S. Weinberg, Physica A **96** 327 (1979).

[4] G. Colangelo *et al.*, Eur. Phys. J **C71** 1695 (2011).

[5] J. Batley *et al.*, Eur. Phys. J. **C70** 635 (2010).

[6] J. Batley *et al.*, Phys. Lett. **B715** 105 (2012).

[7] J. Batley *et al.*, J. High Energy Phys. **1408** 159 (2014).

[8] N. Cabibbo, A. Maksymowicz, Phys. Rev. **137** B433 (1965).

[9] J. Beringer *et al.*, Phys. Rev. **D86** 010001 (2012).

[10] G. Amoros, J. Bijnens, J. Phys. **G25** 1607 (1999).

[11] N. Cabibbo, Phys. Rev. Lett. **93** (2004) 121801.

[12] J. Batley *et al.*, Eur. Phys. J. **C64** 589 (2009).

[13] G. Colangelo, J. Gasser, H. Leutwyler, Phys. Lett. **B488** 261 (2000).

Recent flavor physics results at CMS

Paolo Ronchese[1]

[1]University and INFN Padova, via Marzolo 8, 35131 Padova, Italy

DOI: http://dx.doi.org/10.3204/DESY-PROC-2014-04/234

Thanks to the excellent tracking and muon identification performance, combined with a flexible trigger system, the CMS experiment at the Large Hadron Collider is conducting a rich and competitive program of measurements in the field of heavy flavor physics. In this talk we review our most recent results on heavy flavour physics, based on a data sample collected by the CMS detector.

1 Introduction

There are several motivations to study heavy flavour physics at LHC: advance beauty and charm spectroscopy, test QCD and effective theories, look for indirect evidence or constraints to new physics beyond the standard model, or simply try to have the best as possible description of the environment where direct new physics searches are conducted. In the following most recent results obtained by CMS will be shown.

All results are obtained with data collected at a center of mass energy $\sqrt{s} = 7$ TeV collected in 2011, with an integrated luminosity $\mathcal{L} \sim 5$ fb^{-1}, or $\sqrt{s} = 8$ TeV collected in 2012, with an integrated luminosity $\mathcal{L} \sim 20$ fb^{-1}. All measurements involve dimuons, most of the times originating from a resonance such as J/ψ or Υ. The presence of two muons in the final state allows maintaining a sustainable trigger rate at the high luminosities provided by LHC; the offline reconstruction of a vertex with the two muon candidates was also common for the involved analyses.

2 Mesons

The very rare exclusive decay $\mathcal{B}(B^0_{d,s} \to \mu^+\mu^-)$ was looked for since a very long time; the decay rate is highly suppressed and could be modified by new physics processes [1]. CMS measured its branching ratio by comparison with the decay $B^+ \to J/\psi K^+$, used for normalization:

$$\mathcal{B}(B^0_{d,s} \to \mu^+\mu^-) = \frac{N_{\rm sig}}{N_{\rm nrm}} \frac{\epsilon_{\rm nrm}}{\epsilon_{\rm sig}} \frac{f_u}{f_{d,s}} \mathcal{B}(B^\pm \to J/\psi K^\pm \to \mu^+\mu^- K^\pm) \tag{1}$$

The B^0_s to B^+ production cross section ratio f_s/f_u has been assumed to be equal to LHCb measurement [2] $f_s/f_d = 0.256{\pm}0.020$, the corresponding ratio for B^0_d has been assumed to be 1. Signal and background have been discriminated by categorizing events by mean of a BDT variable

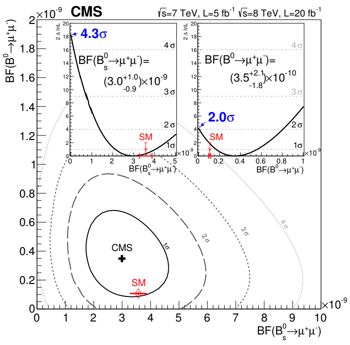

Figure 1: Comparison of CMS measurements with SM predictions in the $\mathcal{B}(B_s^0 \to \mu^+\mu^-), \mathcal{B}(B_d^0 \to \mu^+\mu^-)$ plane.

and fitting invariant mass distributions in each category to determine the signal yield and obtain the results [3]:

$$\mathcal{B}(B_s^0 \to \mu^+\mu^-) = (3.0^{+1.0}_{-0.9}) \times 10^{-9}, \qquad \mathcal{S} = 4.3\sigma,$$
$$\mathcal{B}(B_d^0 \to \mu^+\mu^-) = (3.5^{+2.1}_{-1.8}) \times 10^{-10}, \qquad \mathcal{S} = 2.0\sigma,$$
$$\mathcal{B}(B_d^0 \to \mu^+\mu^-) < 1.1 \times 10^{-9} \ (95\% \text{ C.L.})$$

A comparison with the SM predictions [4] is shown in Fig. 1.

A preliminary combination of these results with the corresponding from LHCb has been performed [5]; LHCb had updated its measurement of f_s/f_d in the meanwhile [6] so the result has been rescaled before the combination:

$$\mathcal{B}(B_s^0 \to \mu^+\mu^-) = (2.9 \pm 0.7) \times 10^{-9}, \ \ (f_s/f_u = 0.259 \pm 0.015),$$
$$\mathcal{B}(B_s^0 \to \mu^+\mu^-) = (3.6^{+1.6}_{-1.4}) \times 10^{-10}.$$

In the decay $B_s^0 \to J/\psi\phi$ the final state is unflavoured, so that it can be reached directly or after an oscillation $B_s^0 \to \bar{B}_s^0 \to J/\psi\phi$ leading to an interference between the two channels, and has no definite CP, so that an angular analysis is required to disentangle the odd and even components [7]. The differential decay rate

$$\frac{d^4\Gamma(B_s(t))}{d\Theta dt} = f(\Theta, t; \alpha) \propto \sum_{i=1}^{10} O_i(\alpha, ct) \cdot g_i(\Theta) \tag{2}$$

can be expressed as a function of decay time t and angles $\Theta = \vartheta, \varphi, \psi$, as shown in Fig. 2, with a set of parameters α, including the amplitude and phases of S-wave and P-wave processes, the B_s^0 lifetime τ_{B_s}, the width difference between the two CP states $\Delta\Gamma_s$ and the interference phase ϕ_s. When in the event we find a second b-hadron decaying semileptonically it can be used to determine the flavour, although with some dilution due to its own oscillation or cascade decays. The tagging information has been introduced in the differential decay rate and the events PDF has been fitted [8] by constraining the mass difference to the world average and assuming there's no direct CP violation:

$$\phi_s = (-0.03 \pm 0.11 \pm 0.03) \text{ rad},$$
$$\Delta\Gamma_s = (0.096 \pm 0.014 \pm 0.007) \text{ ps}^{-1}$$

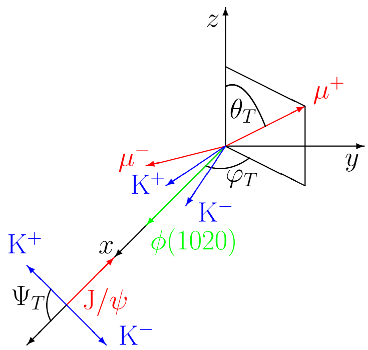

Figure 2: Angle definitions in $B_s^0 \to J/\psi\phi$ decays.

Another important heavy-flavoured hadron to study is the $B_c^\pm$, which carries two heavy flavours, beauty and charm, that can be produced only in higher order processes and decay in a competition between the c and b quarks. A measurement of its cross section production and decay branching ratio can help in understanding the involved processes and is of course propaedeutic for more refined investigations. CMS has studied $B_c^\pm$ mesons in the decay channels to J/ψ and one or three pion(s); a fit to the invariant mass peaks for the two channels allows a determination of the ratios of cross section times branching fraction [9]:

$$\frac{\sigma(B_c^\pm) \times \mathcal{B}(B_c^\pm \to J/\psi\pi^\pm)}{\sigma(B^\pm) \times \mathcal{B}(B^\pm \to J/\psi K^\pm)} = \left(0.48 \pm 0.05 \pm 0.04^{+0.05}_{-0.03}(\tau_{B_c})\right) \times 10^{-2},$$

$$\frac{\mathcal{B}(B_c^\pm \to J/\psi\pi^\pm\pi^+\pi^-)}{\mathcal{B}(B_c^\pm \to J/\psi\pi^\pm)} = 2.43 \pm 0.76^{+0.05}_{-0.03}.$$

The invariant mass of the $J/\psi\pi^\pm$ is shown in Fig. 3; the $B_c^\pm$ reconstruction efficiency has been determined assuming a lifetime $\tau_{B_c} = (0.452 \pm 0.032)$ ps and the effect of the corresponding uncertainty has been quoted explicitly in the systematic error.

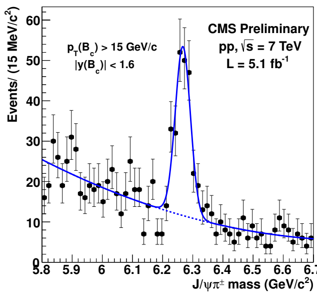

Figure 3: $J/\psi\pi^\pm$ invariant mass distribution.

3 Quarkonia

At CMS quarkonia are reconstructed by combining opposite charge muons and fitting a common vertex; this allowed the measurement of several properties of $\psi(n\mathrm{S})$ and $\Upsilon(n\mathrm{S})$, as production cross section and polarization. Recently the differential cross section for the production of prompt J/ψ and ψ' have been measured with 2011 data [10]; due to the integrated luminosity 100 times bigger than the one corresponding to 2010 data used for previous measurement the p_T acceptance was increased reaching 95 GeV in 4 rapidity bins. The event yield in the various p_T and rapidty bins was determined by mean of a simultaneous fit to invariant mass and flight distance to discriminate prompt and non prompt components while the acceptance was computed for several scenarios, corresponding to full longitudinal, transverse or null polarization. In Fig. 4 the differential cross section vs. p_T is shown, in the unpolarized production scenario.

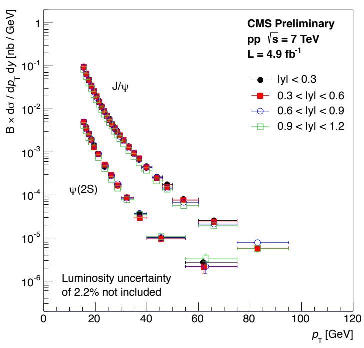

Figure 4: Differential cross section for prompt J/ψ and $\psi(2\mathrm{S})$ production.

The measurement of the simultaneous production of two J/ψ mesons in the proton-proton collisions provides general insight into how particles are produced in the collision; J/ψ pairs produced in single-parton scattering are strongly correlated, while large values of rapidity difference $|\Delta y|$ are possible for production due to double-parton scattering [11]. The differential cross section for the production of charmonium pairs has been measured [12] in bins of rapidity difference $|\Delta y|$; acceptance has been determined by assuming unpolarized J/ψ production. The results are shown in Fig. 5; the cross section increase at $|\Delta y| > 2.6$ can be a hint of double parton scattering.

In addition to S-wave quarkonia at LHC also P-wave states are produced; they contribute with their decay to J/ψ and Υ production while the relative production of themselves is sensitive to singlet or octet states in the production mechanism.

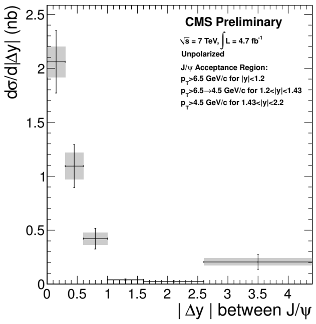

Figure 5: Double J/ψ production cross section vs. rapidity difference.

At CMS $\chi_b(1P)$ states can be reconstructed in the decay channel to $\Upsilon(1S)\gamma$, with the photon converting into an e^+e^- pair in the interaction with the detector material [13]; the conversion probability multiplied by the efficiency of reconstructing two low-p_T tracks is very small, but the mass resolution is high enough to distinguish the two states χ_{b1} and χ_{b2} having a very small mass difference $\Delta M = 19$ MeV. The ratio

$$R_b = \frac{\sigma(pp \to \chi_{b2}X)\mathcal{B}(\chi_{b2} \to \Upsilon(1S)\gamma)}{\sigma(pp \to \chi_{b1}X)\mathcal{B}(\chi_{b1} \to \Upsilon(1S)\gamma)} \tag{3}$$

has been measured in Υ transverse momentum bins and plotted in Fig. 6. No significant dependence on p_T was observed.

4 Conclusions

CMS has produced several results in heavy-flavour physics: B_s^0 decay to $\mu^+\mu^-$ has been observed, angular analysis in B_s^0 decays has been performed to measure width difference and mixing interference phase, single and double charmonium, as well as P-wave bottomonium cross sections have been measured to investigate production mechanisms.

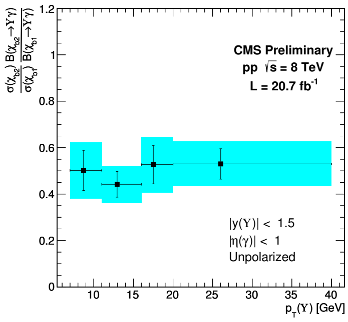

Figure 6: Cross section ratio $[\sigma(pp \to \chi_{b2}X)\mathcal{B}(\chi_{b2} \to \Upsilon(1S)\gamma)]/[\sigma(pp \to \chi_{b1}X)\mathcal{B}(\chi_{b1} \to \Upsilon(1S)\gamma)]$ vs. p_T^{Υ}, under the hypothesis of unpolarized production.

References

[1] K. De Bruyn *et al.*, Phys. Rev. Lett. **109** 041801 (2012).

[2] LHCb Collaboration, JHEP **04** 001 (2013).

[3] CMS Collaboration, Phys. Rev. Lett. **111** 101804 (2013).

[4] A. J. Buras *et al.*, Eur. Phys. J. **C72** 2172 (2012).

[5] CMS and LHCb Collaborations, CMS PAS BPH-13-007 (2014).

[6] LHCb Collaboration, LHCb-CONF-2013-011 (2013).

[7] I. Dunietz *et al.*, Phys. Rev. **D63** 114015 (2001).

[8] CMS Collaboration, CMS PAS BPH-13-012 (2014)

[9] CMS Collaboration, CMS PAS BPH-12-011 (2013).

[10] CMS Collaboration, CMS PAS BPH-14-011 (2014)

[11] C. Kom *et al.*, Phys. Rev. Lett. **107** 082002 (2011).

[12] CMS Collaboration, CMS PAS BPH-11-021 (2013).

[13] CMS Collaboration, CMS PAS BPH-13-005 (2013).

Search for exotics at *BABAR*

Elisabetta Prencipe[1] on behalf of the *BABAR* Collaboration

[1]Forschungszentrum Jülich, Leo Brandt Strasse, 52428 Jülich, Germany
(previously addressed at JGU, University of Mainz, Germany)

DOI: http://dx.doi.org/10.3204/DESY-PROC-2014-04/201

One of the most intriguing puzzles in hadron spectroscopy are the numerous charmonium-like states observed in the last decade, including charged states that are manifestly exotic. The *BABAR* experiment has extensively studied those in B meson decays, initial state radiation processes and two photon reactions. The study of the process $B \to J/\psi\phi K$, with a search for the resonant states X(4140) and X(4270) in their decays to $J/\psi\phi$, will be highlighted. The recent results of the Dalitz analysis of η_c to 3 pseudoscalar mesons, via 2-photon interactions, will be presented in this report [Contribution talk: ID 201].

1 Introduction

Several new Charmonium-like states have been observed at *BABAR*, revealing a spectrum too rich to be uniquely described by potential models[1]. Different hypotheses have been proposed from theorists to explain their nature, such as hybrid charmonium states, diquark-antidiquark states or $D^0\bar{D}^{0(*)}$ molecules[2]. The QCD spectrum is much richer than that of the naive quark model, as the gluons, which mediate the strong force between quarks, can also act as principal components of entirely new types of hadrons. These gluonic hadrons fall into two general categories: glueballs (excited states of pure glue) and hybrids (composed by a quark, an antiquark, and excited glue). The additional degrees of freedom carried by gluons allow glueballs and hybrids to have spin-exotic quantum numbers J^{PC} that are forbidden for normal mesons and other fermion-antifermion systems. Exotic quantum numbers (e.g. 0^{--}, 0^{+-}, 1^{-+}, 2^{+-}) are the easiest way to distinguish gluonic hadrons from $q\bar{q}$ states. Predictions for hybrids come mainly from calculations based on the bag model, flux tube model, and constituent gluon model and recently, with increasing precision, from Lattice QCD. New forms of matter, such as glueballs or molecular states, are predicted by QCD to populate the low mass region of the hadron mass spectrum[3]. This motivates the study of the J/ψ radiative and hadronic decays.

Two analyses will be shortly summarized in this report: the Dalitz analysis of $\eta_c \to K^+K^-\eta/\pi^0$ via 2-photon interactions and the study of the invariant mass systems of $J/\psi\phi$, $J/\psi K$ and KKK in B decays. The first is relevant to several issues in light meson spectroscopy, and it is recently published by *BABAR*[4]. No Dalitz plot analysis has been performed on η_C three-body decays until now. The second presents a new determination of the branching fraction (BF) of $B^{\pm,0} \to J/\psi K^+K^-K^{\pm,0}$ and $B^{\pm,0} \to J/\psi\phi K^{\pm,0}$, using eight times more data than that reported by the PDG[5], and search for exotic states.

2 Decay of $\eta_c \to K^+K^-\eta/\pi^0$ to via 2-photon interactions

Recently, a search for exotic resonances was performed by *BABAR* through Dalitz plot analyses of χ_{c1} states[6]. Scalar mesons are still a puzzle in light-meson spectroscopy, as there are too many states and they are not consistent with the quark model. In particular, the $f_0(1500)$ resonance, discovered in $\bar{p}p$ annihilations, has been interpreted as a scalar glueball[7]. However, no evidence for the $f_0(1500)$ state has been found in charmonium decays. Another glueball candidate is the $f_0(1710)$ discovered in radiative J/ψ decays. Recently, $f_0(1500)$ and $f_0(1710)$ signals have been incorporated in a Dalitz plot analysis of $B \to 3K$ decays[8]. Charmless $B \to XK$ could enanche gluonium production[9]. Another puzzling state is the $K_0^*(1430)$, never observed as clear peak in $K\pi$ invariant mass. Its parameters were measured from the LASS experiment in $K^-p \to K^-\pi^+n$[10].

We describe a study of the decays $\eta_c \to K^+K^-\eta$ and $\eta_c \to K^+K^-\pi^0$, with $\eta \to \pi^+\pi^-\pi^0$, $\eta \to \gamma\gamma$ and $\pi^0 \to \gamma\gamma$, produced in two-photon interactions. The data sample used is 519 fb^{-1} at *BABAR*. Two-photon events in which at least one of the interacting photons is not quasireal are strongly suppressed by a dedicated selection. A clear peak of η_c is seen, and well reconstructed in the invariant mass systems of $K^+K^-\eta$ and $K^+K^-\pi^0$. The Dalitz analysis is then performed for $\eta_c \to K^+K^-\eta$ and $\eta_c \to K^+K^-\pi^0$: the projection of the invariant mass distributions and their unbinned maximum likelihood fit are shown in Fig. 1, and 2. A clear peak at the mass of $K_0^*(1430)$ is observed in both cases, together with other expected structures. Amplitude parameterization is performed in a standard way for a pseudoscalar meson decaying to 3 pseudscalar mesons. Full interference is allowed among the amplitudes of all resonances in the Dalitz. No evidence for interferences between signal and background is found, so a sum of inchoerent resonances is used for fitting the sidebands. The non-resonant contribution is included in the fit. From our fit, we learn that the model provides an adeguate description of data for $\eta_c \to K^+K^-\eta$, while the isobar model does not describe properly the data for $\eta_c \to K^+K^-\pi^0$. Scanning the likelihood as function of the $K_0^*(1430)$ mass and width, we obtain: m($K_0^*(1430)$) = 1438 ± 8 ± 4 MeV/c^2 and $\Gamma(K_0^*(1430))$ = 210 ± 20 ± 12 MeV.

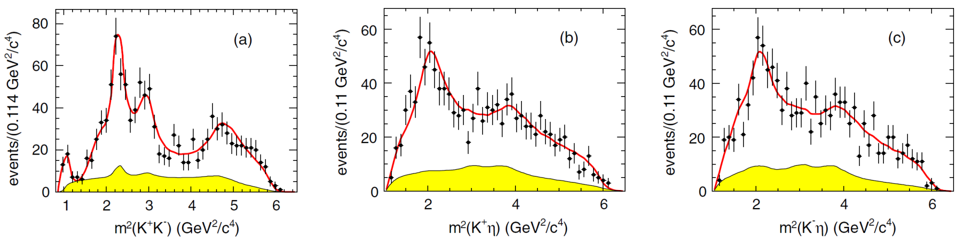

Figure 1: Projections from the Dalitz plot of $\eta_c \to K^+K^-\eta$. The shaded (yellow) histograms show the estimated background. The state $K_0^*(1430)$ is seen as clear peak in (b) and (c).

In this work also the pseudoscalar meson mixing angle is evaluated: $\theta_P = (3.1^{+3.1}_{-5.0})^\circ$, and it differs 2.9$\sigma$ deviation from expectations. This issue involves in theoretical discussions where the siglet and octet mixing angle should be considered separately.

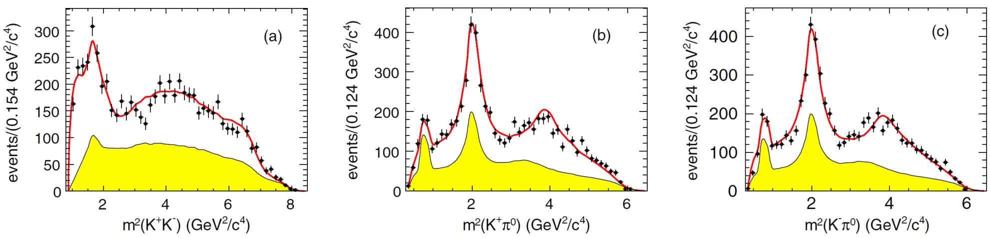

Figure 2: Projections from the Dalitz plot of $\eta_c \to K^+K^-\pi^0$. The shaded (yellow) histograms show the estimated background. The state $K_0^*(1430)$ is seen as clear peak in (b) and (c).

3 Analysis of the decay $B \to J/\psi KKK$

Several resonant structures, whose masses are above the $D\bar{D}^*$ threshold, are not predicted by potential models. For example, the X(3872) have been seen in $B \to XK, X \to J/\psi\ \pi^+\pi^-$, or Y(4260) was observed by investigating the process $e^+e^- \to \gamma_{ISR}X$, $X \to J/\psi\pi^+\pi^-$[11, 12, 13]; but no indication of new states has been observed in the $J/\psi\ K^+K^-$ invariant mass system, until the paper quoted in Ref. [14] highlighted the possibility of a couple of resonant states, decaying to $J/\psi\phi$, with $\phi \to K^+K^-$ and $J/\psi \to \mu^+\mu^-$. These observations are controversial. *Strangeness* in charmonium seems a sector still to be exploited. The rare decay $B \to J/\psi KKK$, in particular $B \to J/\psi\phi K$, is interesting because it is a promising place to search for new resonances, as it proceeds, at quark level, via the weak transition $b \to c\bar{c}s$. It could be a quasi 2-body decay, $B \to X_g K$, with $X_g \to J/\psi\phi$, where $X_g = |gc\bar{c}s\bar{s}>$, with gluonic contribution (g).

An unbinned maximum likelihood fit is performed to extract the yield and calculate the BFs. Detailed explanation on these calculations are presented in Ref. [15], together with the relevant discussion for the non-resonant K^+K^- contribution to the BF of $B \to J/\psi KKK$ and systematic uncertainty calculation. Here we report only the relevant information for the analysis of the three invariant mass distributions: $J/\psi\phi$, $J/\psi K$, KKK, for both B^+ and B^0 samples. In this analysis we calculate also: $R_\phi = \mathcal{B}(B^0 \to J/\psi\phi K_S^0)/\mathcal{B}(B^+ \to J/\psi\phi K^+) = 0.48 \pm 0.09 \pm 0.02$, and $R_{2K} = \mathcal{B}(B^0 \to J/\psi K^+K^-K_S^0)/\mathcal{B}(B^+ \to J/\psi K^+K^-K^+) = 0.52 \pm 0.09 \pm 0.03$; we find values in agreement with the expectation of the spectator quark model (e.g., ratio R$\sim$0.5). These are first measurements. For the first time the non-resonant K^+K^- contribution to the BF of $B \to J/\psi KKK$ is observed. No evidence of signal is found for $B^0 \to J/\psi\phi$, in agreement with theoretical predictions: we evaluate UL$<1.01 \cdot 10^{-6}$ at 90% confidence level (CL). We search for the resonant states reported by the CDF Collaboration in the $J/\psi\phi$ mass spectrum. The masses and the widths in our fit are fixed to values according to Ref. [14]. We observed significant efficiency decrease at low $J/\psi\phi$ mass, due to the inability to reconstruct slow kaons in the laboratory frame, as a result of energy loss in the beampipe and SVT material. We model the resonances with an inchoerent sum of two S-wave relativistic Breit-Wigner (BW) functions with parameters fixed to the CDF values [14]. A non-resonant contribution is described according to PHSP. The decay of a pseudoscalar meson to two vector states contains high spin contributions which could generate non-uniform angular distributions. However, due to the limited data sample (212 yield for B^+ and 50 for B^0, in the signal area, respectively) we do not include such angular terms, and assume that the resonances decay isotropically. The fit function is weighted by the inverse of the two-dimentional efficiency computed on the Dalitz plots (see the

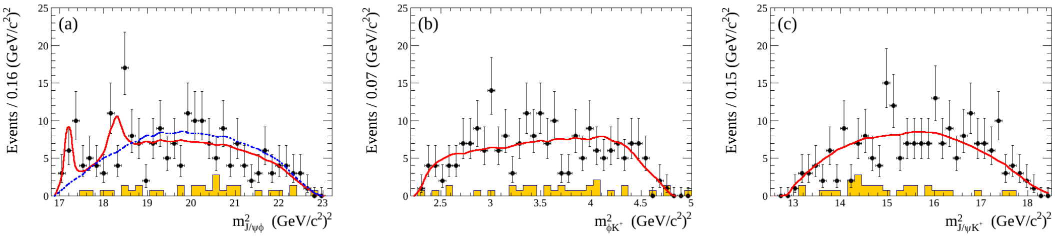

Figure 3: Dalitz plot projections for $B^+ \to J/\psi\phi K^+$ on (a) $m^2_{J/\psi\phi}$, (b) $m^2_{\phi K^+}$, and (c) $m^2_{J/\psi K^+}$. The continuous (red) curves are the results from fit model performed including the $X(4140)$ and $X(4270)$ resonances. The dashed (blue) curve in (a) indicates the projection for fit model with no resonances included in the fit. The shaded (yellow) histograms indicate the evaluated background. Within systematic effects, a significance $<2\sigma$ was found for both peaks in (a).

continuous red curve in Fig. 3. Using the Feldman-Cousins method[16], we obtain the ULs at 90% CL: $BF(B^+ \to X(4140)K^+) \times BF(X(4140) \to J/\psi\phi)/BF(B^+ \to J/\psi\phi K^+) < 0.135$, and $BF(B^+ \to X(4270)K^+) \times BF(X(4270) \to J/\psi\phi)/BF(B^+ \to J/\psi\phi K^+) < 0.184$. The $X(4140)$ limit may be compared with the CDF measurement of $0.149 \pm 0.039 \pm 0.024$ [14] and the LHCb limit of 0.07 [17]. The $X(4270)$ limit may be compared with the LHCb limit of 0.08. We find that the hypothesis that the events are distributed uniformly on the Dalitz plot gives a poorer description of the data.

References

[1] N. Brambilla *et all*, *CERN Yellow Report*, hep-ph/0412158 (2005); Eur. Phys. J. C **71**, 1534 (2011); arXiv:1404.3723 [hep-ph] (2014).

[2] Barnes and Godfrey, PRD **69**, 054008 (2004); Eichten, Lane and Quigg, PRD **69**, 094019 (2004); Swanson, PLB **588**, 189 (2004); Tornqvist, PLB **590**, 209 (2004); Suzuki, PRD **72**, 114013 (2005); Maiani, *et all*, PRD **71**, 014028 (2005).

[3] V. Mathieu, N. Kochelev and V. Vento, Int. J. Mod. E**18**, 1 (2009).

[4] J.P. Lees *et all* (*BABAR* Coll.), Phys. Rev. D **79**, 112004 (2014).

[5] B. Aubert *et all* (*BABAR* Coll.), Phys. Rev. Lett. **91**, 071801 (2003).

[6] G. S. Adams *et all* (CLEO Coll.) Phys. Rev. D **84**, 112009 (2011).

[7] C. Amsler and F. Close, Phys. Rev. D **53**, 295 (1996).

[8] J.P. Lees *et all* (BABAR Coll.) Phys. Rev. D **85**, 112010 (2012).

[9] X.-G. He and T.C. Yuan, hep-ph/0612108.

[10] D. Aston *et all* (LASS Coll.), Nucl Phys. **B296**, 493 (1988).

[11] B. Aubert *et all* (*BABAR* Coll.), Phys. Rev. D. **71**, 071103 (2005); Phys. Rev. D **77**, 111101 (2008); Phys. Rev. D. **73**, 011101 (2006).

[12] S.K. Choi *et all* (*Belle* Coll.), Phys. Rev. Lett. **91**, 262001 (2003);

[13] B. Aubert *et all* (*BABAR* Coll.), Phys. Rev. Lett. **95**, 142001 (2005);

[14] T. Aaltonen *et all* (CDF Coll.), Phys. Rev. Lett. **102**, 242002 (2009); hep-ex/1101.6058 (2011).

[15] J.P. Lees *et all* (BABAR Coll.), hep-ex/1407.7244 (2014).

[16] G. J. Feldman and R. D. Cousins, Phys. Rev. D. **57**, 3873 (1998).

[17] R. Aaij *et all* (LHCb Coll.), Phys. Rev. D **85**, 091103(R) (2012).

Chapter 12

String theory

Why does black hole describe the deconfinement phase?

Masanori Hanada

Stanford Institute for Theoretical Physics, Stanford University, Stanford CA 94305, USA
Yukawa Institute for Theoretical Physics, Kyoto University, Kitashirakawa Oiwakecho, Sakyo-ku, Kyoto 606-8502, Japan
The Hakubi Center for Advanced Research, Kyoto University, Yoshida-Ushinomiya-cho, Sakyo-ku, Kyoto 606-8501, Japan

DOI: http://dx.doi.org/10.3204/DESY-PROC-2014-04/160

In the gauge/gravity duality, the deconfinement transition in the gauge theory is identified with the formation of black hole in the dual gravity theory. By assuming this correspondence, many predictions on QGP have been made. In this talk, we justify this approach quantitatively, and also provide an intuitive understanding. Firstly we give quantitative evidence for this identification from the thermodynamic study of the supersymmetric theory. We show that string theory and gauge theory give the same answer, even at finite temperature, including the $1/N$ correction. Then we consider generic gauge theories and show that the deconfinement transition is the condensation of very long and self-intersecting QCD strings, which is analogous to the formation of a black hole in string theory.

1 Introduction

In the gauge/gravity duality conjecture [1], the deconfinement phase of the gauge theory is dual to a black hole geometry in the gravity side [2]. In the first part of this talk, we give quantitative evidence for this identification, by solving a concrete example in both gauge and gravity sides, at the level of the string theory (i.e. finite α' and finite g_s). In the second part, we give an intuitive way of understanding this correspondence, without referring to a sophisticated dictionary of the duality. Our argument does not assume the dual gravity description, and hence it is applicable to generic gauge theories including QCD.

2 Quantitative test of the gauge/gravity duality

Let us consider the $U(N)$ maximally supersymmetric Yang-Mills theory in flat $(p+1)$-dimensional spacetime ($p = 0, 1, 2$ and 3), whose action is given by

$$S = \frac{1}{g_{YM}^2}\int d^{p+1}x\ Tr\left\{\frac{1}{4}F_{\mu\nu}^2 + \frac{1}{2}\left(D_\mu X_i\right)^2 - \frac{1}{4}[X_i, X_j]^2\right\} + (fermions), \tag{1}$$

where μ, ν run from 1 to $p+1$ and X_i ($i = 1, 2, \cdots, 9-p$) are scalar fields. In [3], it has been conjectured that this theory is in the deconfining phase at any nonzero temperature, in the sense that the Polyakov loop has nonzero expectation value, and that it describes full string dynamics around the black p-brane. Near the horizon, the metric of the black p-brane geometry is given by

$$ds^2 = \alpha' \Bigg\{ \frac{U^{(7-p)/2}}{g_{YM}\sqrt{d_p N}} \left[-\left(1 - \frac{U_0^{7-p}}{U^{7-p}}\right) dt^2 + dy_{\parallel}^2 \right] + \frac{g_{YM}\sqrt{d_p N}}{U^{(7-p)/2}\left(1 - \frac{U_0^{7-p}}{U^{7-p}}\right)} dU^2 + g_{YM}\sqrt{d_p N} U^{(p-3)/2} d\Omega_{8-p}^2 \Bigg\}, \tag{2}$$

where the Yang-Mills coupling g_{YM} and the size of the gauge group N in the corresponding super Yang-Mills theory are used. A constant α' is the square of the string length, $(t, y_{\parallel})$ represent the $(p+1)$-dimensional extension of the brane, U and Ω are the radial and angular coordinate of the transverse directions, and U_0 is the place of the horizon. The Hawking temperature is

$$T_H = \frac{(7-p)U_0^{(5-p)/2}}{4\pi\sqrt{d_p g_{YM}^2 N}}, \tag{3}$$

where $d_p = 2^{7-2p}\pi^{(9-3p)/2}\Gamma((7-p)/2)$. The string coupling constant is given by

$$g_s = (2\pi)^{2-p} g_{YM}^2 \left(\frac{d_p g_{YM}^2 N}{U^{7-p}}\right)^{\frac{3-p}{4}}. \tag{4}$$

When $\lambda = g_{YM}^2 N$ is fixed, it behaves as $g_s \propto 1/N$, in the same way as in 't Hooft's identification. The Hawking temperature and the mass of the black brane are identified with the temperature and the energy $E \equiv -\partial \log Z/\partial\beta$ of the gauge theory, where Z is the partition function.

In this work we study the case of $p = 0$. The gauge theory is quantum mechanics of $N \times N$ matrices, which was originally proposed as the matrix model of M-theory [4]. It can be studied extensively by using the Monte Carlo method. In the gravity side, the black hole mass can be calculated by adding stringy corrections to the black 0-brane geometry shown above. The result is [5]

$$\frac{1}{N^2}E_{gravity} = (7.41\,T^{2.8} + a\,T^{4.6} + \cdots) + (-5.77\,T^{0.4} + b\,T^{2.2} + \cdots)\frac{1}{N^2} + O\left(\frac{1}{N^4}\right), \tag{5}$$

where $T = \lambda^{-1/3}T_H$ is dimensionless effective temperature and a, b are unknown constants. The energy $E_{gravity}$ is also made dimensionless, by multiplying $\lambda^{-1/3}$. In the following, we simply set $\lambda = 1$ without loss of generality. Higher order terms in each power of $1/N$ represent to the α' corrections, which appear because strings are not point-like. If the gauge/gravity duality conjecture is correct, this expression must be reproduced from the matrix quantum mechanics.

The $O(N^0)$ terms of the dual gravity prediction (5) have been tested previously. In particular, the α' correction $a\,T^{4.6}$ has been confirmed with $a = -5.58(1)$, by looking at $T \gtrsim 0.5$ [7].

In order to study the $1/N$ correction, we must study rather small values of N. Here we study $N = 3, 4$ and 5. (That we have to take N small caused a technical problem which required a proper treatment; see [8].) We also have to study low temperature where the α' correction becomes small, because there are too many fitting parameters otherwise. At $0.08 \le T \le 0.11$, we estimated the coefficient of $1/N^2$ by using a fitting ansatz $E_{gauge} = 7.41T^{2.8} + c_1(T)/N^2 + c_2(T)/N^4$ for each fixed value of T. We confirmed that $c_1(T)$ is consistent with $-5.77T^{0.4}$. This is very strong evidence that the gauge/gravity duality holds at quantum gravity level.

3 Why the deconfinement phase describes the black hole

In this section, motivated by the numerical confirmation in Sec. 2, we give an intuitive explanation for the duality based on [6]. As a concrete example, let us consider pure $U(N)$ Yang-Mills theory. The Hilbert space is spanned by Wilson loops acting on the vacuum $|0\rangle$, as $W_C W_{C'} \cdots |0\rangle$. Here W_C represent the Wilson loop along a closed contour C. In the standard identification of the Feynman diagrams and the string world-sheet [9], the Wilson loop is naturally interpreted as the creation operator of the string.

In the large-N limit and at sufficiently strong coupling, the energy of the string is approximately proportional to its length. In the confinement phase, the energy is of order N^0 per unit volume, and hence a typical state is a finite-density gas of loops with finite length. In this gas, two loops can intersect with each other and combined to form a longer string. Alternatively, when a loop intersects with itself, it can be split into two shorter loops. However such joining and splitting are suppressed at large-N.

In the deconfinement phase, the energy density is of order N^2. In this phase the loops necessarily intersect $O(N^2)$ times. Although the interaction at each intersection is $1/N$-suppressed, small interactions at many intersections accumulate to a non-negligible amount. A standard entropic argument shows that typical state consists of finitely many very long and self-intersecting strings, whose lengths are of $O(N^2)$. In the string theory, it is natural to interpret such very long and self-intersecting strings as a black hole [10, 11]. In this sense, *the deconfinement transition can be understood as the formation of a 'black hole' through condensation of QCD strings.*

When we identify the long string with a black hole, fluctuations of the string near the horizon are regarded as open strings attached to black hole (Fig. 1). In terms of the gauge theory, these open strings are open Wilson lines which have N color degrees of freedom at their endpoints. Therefore, we can interpret that the black hole is made from N D-branes.

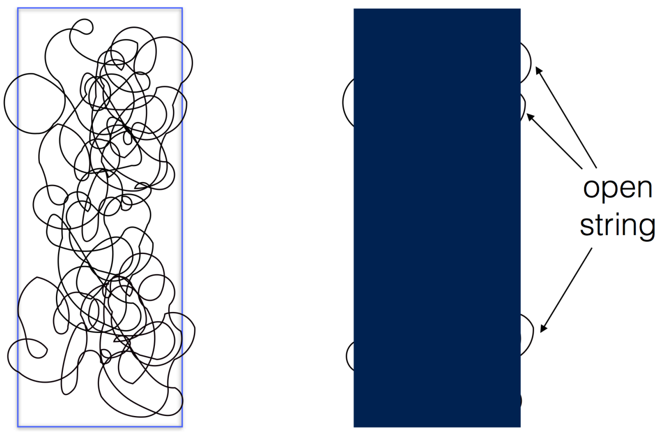

Figure 1: Closed string picture (left) and open string picture (right) [6].

In the Euclidean theory, the deconfinement is characterized by the condensation of the Polyakov loop, which can naturally be related to the black hole geometry in the gravity dual [2]. This can be explained from our picture as follows. First notice that the condensation of the

Polyakov loop is equivalent to the disappearance of the linear confinement potential between a pair of probe quark and anti-quark. In terms of strings, the linear potential in the confining phase appears because an open string connecting probes must be stretched as they are separated. In the deconfining phase, however, as soon as a short open string is introduced, it intersects with closed strings many times, and they immediately interact at one of the intersections to form a long open string (Fig. 2). Therefore, probes can be separated without stretching the open string, or equivalently, without costing energy. Note that the interaction is crucial for this argument; the deconfining phase cannot be described by free strings à la Hagedorn.

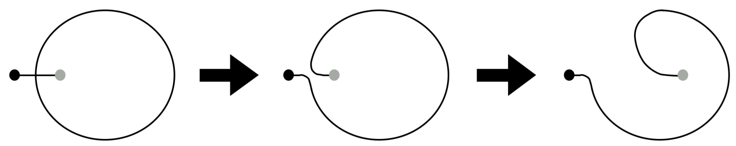

Figure 2: Deconfinement of a pair of probe quark and anti-quark [6].

In order to test this picture, we have estimated the deconfinment temperature of the lattice gauge theory with spatial lattice and continuum time [12]. We performed numerical simulation and confirmed the prediction.

Acknowledgments

I would like to thank Y. Hyakutake, G. Ishiki, J. Maltz, J. Nishimura and L. Susskind for collaborations. I was supported in part by the Grant-in-Aid of the Japanese Ministry of Education, Sciences and Technology, Sports and Culture (MEXT) for Scientific Research (No. 25287046), and the National Science Foundation under Grant No. PHYS-1066293 and the hospitality of the Aspen Center for Physics.

References

[1] J. M. Maldacena, Adv. Theor. Math. Phys. **2**, 231 (1998).
[2] E. Witten, Adv. Theor. Math. Phys. **2**, 505 (1998).
[3] N. Itzhaki, J. M. Maldacena, J. Sonnenschein and S. Yankielowicz, Phys. Rev. D **58**, 046004 (1998).
[4] T. Banks, W. Fischler, S. H. Shenker and L. Susskind, Phys. Rev. D **55**, 5112 (1997).
B. de Wit, J. Hoppe and H. Nicolai, Nucl. Phys. B **305**, 545 (1988).
[5] Y. Hyakutake, PTEP **2014**, no. 3, 033B04.
[6] M. Hanada, J. Maltz and L. Susskind, arXiv:1405.1732 [hep-th].
[7] M. Hanada, Y. Hyakutake, J. Nishimura and S. Takeuchi, Phys. Rev. Lett. **102**, 191602 (2009).
[8] M. Hanada, Y. Hyakutake, G. Ishiki and J. Nishimura, Science **344**, 882 (2014).
[9] G. 't Hooft, Nucl. Phys. B **72**, 461 (1974).
[10] L. Susskind, In *Teitelboim, C. (ed.): The black hole* 118-131.
[11] G. T. Horowitz and J. Polchinski, Phys. Rev. D **55**, 6189 (1997).
[12] J. B. Kogut and L. Susskind, Phys. Rev. D **11**, 395 (1975).

Chapter 13

New concepts and techniques for accelerators and particle detectors

Future Opportunities with Germanium Detectors at the China Jinping Underground Laboratories

Lucia Garbini[1], *Iris Abt*[1], *Sabine Irlbeck*[1], *Bela Majorovits*[1], *Matteo Palermo*[1], *Oliver Schulz*[1]
[1]Max-Planck-Institute for Physics, Föhringer Ring 6, 80805 München, Germany

DOI: http://dx.doi.org/10.3204/DESY-PROC-2014-04/8

The China Jinping underground Laboratory (CJPL) is the deepest underground laboratory in operation in the world. The extremely low muon flux makes CJPL a good candidate to host low background experiments looking for rare events like neutrino-less double-beta decays ($0\nu\beta\beta$ decay) or dark matter (DM) interactions. Feasibility and R&D studies are performed to combine these two searches in a common "One-Ton-Germanium facility" to be built in a low-background environment such as CJPL.

1 Rare event searches

The Standard Model (SM) is one of the most successful theories ever produced in physics. Nevertheless, there are experimental evidence, such as the presence of "Dark Matter" (DM) in the universe, neutrino oscillations and baryon asymmetry, which demands at least extensions of the SM framework. Neutrinos and DM are two sectors of particle physics which might give us hints about the expected new physics beyond the SM.

The isotope ^{76}Ge can decay via normal double beta ($\beta\beta$) decay. Thus, it is a candidate for neutrino less double beta ($0\nu\beta\beta$) decay and germanium detectors are used to search for it. The observation of ($0\nu\beta\beta$) decay would demonstrate Lepton Number Violation (LNV) and establish the neutrino as a Majorana particle. Germanium detectors are also used for direct DM searches. Weekly interacting massive particles (WIMPs) should interact in the germanium crystal depending on their mass and the cross section. So far neither DM nor ($0\nu\beta\beta$) decay has been observed and limits have been established on both these processes.

The requirements on the germanium detectors are quite different for the two searches. Nevertheless, detector development studies are being performed aiming to build a detector which fulfills the different technical requirements for both searches, and which can be used in a 1-ton germanium multipurpose facility. The huge exposure achievable with 1 ton of germanium will, however, not improve the sensitivity of the experiment unless the background is low enough. Therefore, such an experiment should be built as deep as possible underground.

2 The China Jinping Underground Laboratory

Several underground facilities are in operation all around the world. The deepest underground laboratory is the China JinPing Underground Laboratory (CJPL) [1] with a rock overburden of 2400 m and a measured muon flux [2] of around 60 muons per square meter per year. The

CJPL is located in the south western province of Sichuan in China. It was built in the central part of one of the support tunnels of the Jinping hydro-power project managed by the Yalong river company. It has a horizontal access suitable for heavy transports. Its total volume of 2000 m^3 is divided in three sections hosting three different experiments as shown in Fig. 1a.

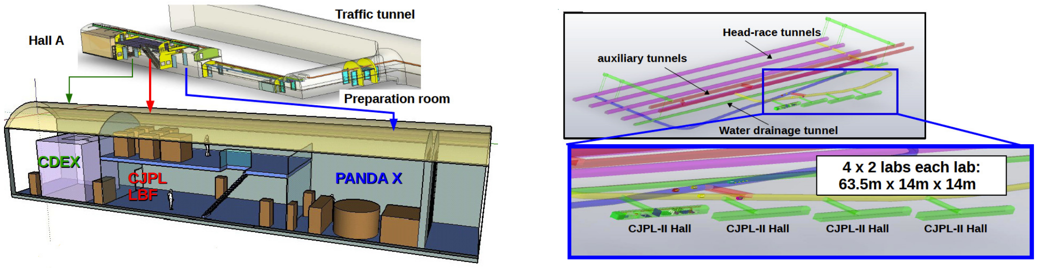

Figure 1: China Jinping Underground Laboratory: (a) shows the Experimental Hall A in CJPL-I; (b) shows the plan for CJPL-II with 4 new experimental double-halls.

The CJPL Low Background Facility [3] (CJPL-LBF) uses high purity germanium detectors as low background spectrometers to investigate environmental samples and select materials for low background experiments, especially for PANDA-X [4] and the China Dark Matter Experiment (CDEX) [5]. PANDA-X and CDEX are direct DM search experiments. The former uses liquid Xenon as target material, while the latter uses Germanium. PANDA-X has, in its first stage, a fiducial mass of 30 kg, easily scalable to 1 ton. Data taking is on going since March 2014, with first results already published in August 2014 [6]. CDEX, in its first stage CDEX-1, uses two high-purity germanium detectors. A 20 g low energy-threshold germanium detector is used to investigate how to lower the energy threshold and be sensitive to extremely low recoil energies corresponding to low-mass WIMP interactions. A 1 kg p-type point-contact germanium detector allows the CDEX collaboration to test software techniques to reject background events using pulse shape analysis. A first limit on WIMP interaction cross-sections was already published [7]. The CDEX collaboration plan to install further germanium detectors.

A plan to significantly enlarge CJPL to become CJPL-II [8] has already been accepted and tunneling will start in fall 2014. In Fig. 1b, the structure of CJPL-II is shown. Four new double halls, with a total volume of about 96000 m^3, will be built to host not only the physics experiments themselves, but also support technology.

CJPL is to become an international laboratory hosting experiments operated by international collaborations. In preparation of this, the Tsinghua university, operating the laboratory, has entered a Sino-German cooperation with the Max-Planck-Institute for physics (MPI) in Munich, the university of Tübingen and the Shanghai Jaotong university. Within this cooperation, germanium detector development and the realization of CJPL-II are discussed.

3 Detector development at the MPI in Munich

The feasibility of a 1-ton germanium multipurpose facility in a laboratory like CJPL is studied. Since the muon induced background would be extremely low in CJPL, other kinds of background will become more important. One of the most dangerous and often limiting sources of background, both for $0\nu\beta\beta$ decay and DM searches, is surface contamination, e.g. from lead, resulting in α-background. Therefore, it is really crucial to characterize the detector response to α particles in order to be able to identify such events. This is one of the physics goals of the detector development studies performed at the MPI with the GALATEA test stand [9].

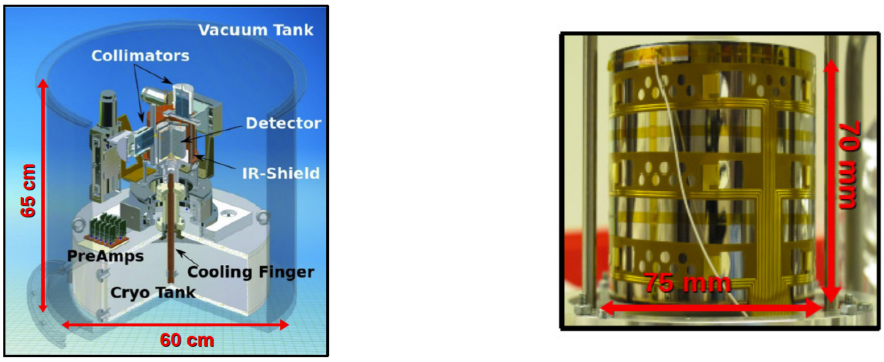

Figure 2: Detector development at the MPI: (a) a sketch of the GALATEA test stand [9]; (b) the detector prototype used to characterize alpha-induced events, Supersiegfried [10].

In Fig. 2a, a sketch of the GALATEA test stand is presented. The detector prototype SuperSiegfried (SuSie) [10] shown in Fig. 2b is an 18+1 fold segmented true-coaxial high-purity germanium detector. The 19th segment is a 5 mm thick disk at the top of the detector. Inside GALATEA, there is no material between source and detector and thus the detector can be probed also with minimally penetrating sources like alphas and betas. A system of three motors moves two collimators in order to facilitate 3d scans. A ^{241}Am source was placed inside the top collimator to irradiate the passivated top-surface of SuSie with alpha particles.

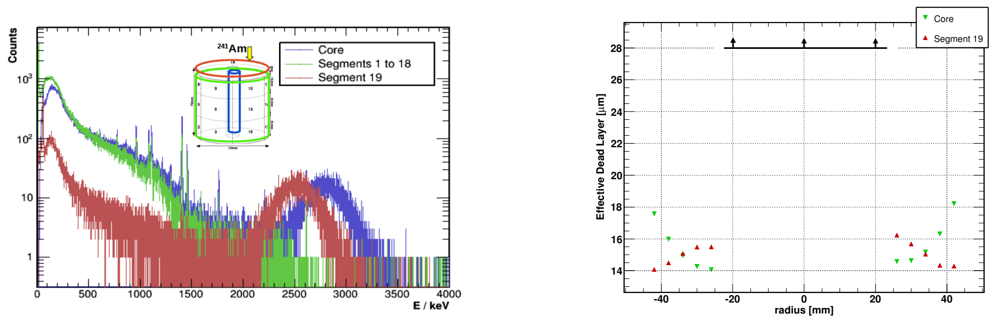

Figure 3: Top-surface scan with a ^{241}Am alpha source: (a) energy spectra as measured with (blue) the core, all 19 segments but the top segment (green) and the top segment (red); (b) the thickness of the effective dead layer at different radii for both electrons (green) and holes (red).

Figure 3a shows typical energy spectra obtained with SuSie when the top is irradiated with alphas at a given point. The blue histogram is the energy spectrum obtained from the core, the red histogram from the top segment and the green one from all the segments but the top segment. The bump around 2 MeV is due to the alpha radiation. It only occurs in the core and the top-segment spectra, because alphas of about 5 MeV only penetrate around 20 μm.

The detector has an effective dead layer on top which consists of the passivation layer and an area of low field underneath. Only energy deposited underneath that layer is recorded. The position of the bump in the spectrum, i.e. the average energy deposited in the detector, should indicate the loss in the effective dead layer. However, the position of the bump is different for core and top segment. This indicates that the picture of well defined layers is oversimplified. The energy recorded in the core (segment) is dominated by the drift of electrons (holes). The two different charge carriers are subject to different trapping effects. This is a typical feature of surface events [11]. If the source is placed at large radii, the electrons are trapped with a higher probability as the holes due to their long path and the effective dead layer is thicker for electrons than for holes. As the source is moved towards the core, i.e. the center of the detector, the situation reverses and holes are more likely trapped than electrons; the effective dead layer for electrons (holes) decreases (increases). Figure 3a shows the recorded spectra at a point where more holes than electrons are trapped and thus, the energy recorded in the core is higher than in the top segment. Figure 3b shows the thickness of the effective dead layers at different radii for electrons (green) and holes (red). At radii below 25 mm, the effective dead layers increase such that they cannot be probed with alphas; this is due to detector geometry.

4 Outlook and Acknowledgments

Germanium detectors are good candidates for future dark matter and $0\nu\beta\beta$ searches. The optimization of the detectors faces many challenges. The characterization of alpha events on the surface and their identification through spectra and pulse shape analysis is one of them. The groups involved plan to conduct further studies on the feasibility of a 1-ton detector at CJPL.

We would like to thank the Sino-German center in Beijing for funding the Sino-German cooperation on germanium detector development.

References

[1] H. S. Chen, Eur. Phys. J. Plus **127** (2012) 105.

[2] Y. C. Wu, X. Q. Hao, Q. Yue, Y. J. LI, J. P. Cheng, K. J. Kang, Y. H. Chen and J. Li *et al.*, Chin. Phys. C **37** (2013) 8, 086001 [arXiv:1305.0899 [physics.ins-det]].

[3] Y. Mi, H. Ma, Z. Zeng, J. Cheng, J. Su and Q. Yue, arXiv:1403.1724 [physics.ins-det].

[4] X. Cao, X. Chen, Y. Chen, X. Cui, D. Fang, C. Fu, K. L. Giboni and H. Gong *et al.*, Sci. China Phys. Mech. Astron. **57** (2014) 1476 [arXiv:1405.2882 [physics.ins-det]].

[5] K. J. Kang *et al.* [CDEX Collaboration], Front. Phys. China **8** (2013) 412 [arXiv:1303.0601 [physics.ins-det]].

[6] M. Xiao *et al.* [PandaX Collaboration], arXiv:1408.5114 [hep-ex].

[7] Q. Yue *et al.* [CDEX Collaboration], arXiv:1404.4946 [hep-ex].

[8] J. Li, X. Ji, W. Haxton and J. S. Y. Wang, arXiv:1404.2651 [physics.ins-det].

[9] I. Abt, A. Caldwell, B. Doenmez, L. Garbini, S. Irlbeck, B. Majorovits, M. Palermo and O. Schulz, arXiv:1409.0493 [physics.ins-det].

[10] D. Lenz PhD-thesis: Pulse Shapes and Surface Effects in Segmented Germanium Detectors

[11] S. Irlbeck PhD-thesis:The GALATEA Test Facility and a First Study of alpha-induced Surface Events in a Germanium Detector.

Upgrading the ATLAS Tile Calorimeter Electronics

Gabriel Popeneciu on behalf of the ATLAS Tile Calorimeter System collaboration
INCDTIM, Donat 67-103, 400293 Cluj-Napoca, Romania

DOI: http://dx.doi.org/10.3204/DESY-PROC-2014-04/63

The Tile Calorimeter is the central hadronic calorimeter of the ATLAS experiment at LHC. Around 2024, after the upgrade of the LHC the peak luminosity will increase by a factor of 5 compared to the design value, thus requiring an upgrade of the Tile Calorimeter readout electronics. Except the photomultipliers tubes (PMTs), most of the on- and off-detector electronics will be replaced, with the aim of digitizing all PMT pulses at the front-end level and sending them with 10 Gb/s optical links to the back-end electronics. One demonstrator prototype module is planned to be inserted in Tile Calorimeter in 2015 or 2016 that will include hybrid electronic components able to probe the new design.

1 Introduction

The first running of the Large Hadron Collider (LHC) with proton-proton collisions at centre of mass energies up to 8 TeV produced some significant results with the discovery of Higgs Boson and measurements of Standard model processes. For future running the LHC energy and luminosity will be increased in stages, ultimately resulting in the high luminosity HL-LHC. This stage is scheduled around 2024 and plans to increase the peak luminosity to a value of 5-7x10^{34}cm^{-2}s^{-1} with a pileup close to 200 collisions per beam crossing.

The HL-LHC presents some difficult challenges for the detectors because the new operational conditions imply a higher radiation level that can lead to single point failures of electronics or the integrated radiation dose can lead to a permanent component failure. Another challenge is in dealing with the events high rates which requires more efficient trigger algorithms.

The ATLAS Tile Calorimeter [1] (TileCal) is a cylindrical hadronic sampling detector with steel absorbers and scintillating plastic tiles, located in the most central region of the ATLAS experiment [2] at CERN. It consists of a central barrel (divided in half barrels) and two extended barrels along the beam axis. Each barrel is segmented azimuthally into 64 modules reading out up to 48 photomultiplier channels. The Photomultiplier Tubes (PMTs) and the front-end electronics are situated in the outermost part of the modules, in extractable so called super-drawers. TileCal contains a total of 256 super-drawers comprising 9852 PMT readout channels.

The light generated by charged particles crossing scintillating tiles are collected by wavelength shifting fibers and sent to the PMTs. The analog signals produced by PMTs are conditioned and digitized by the

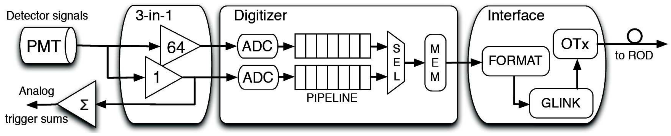

Figure 1: Current Tile Calorimeter readout architecture.

front-end electronics every 25 ns, while analog tower sums are transmitted to the Level-1 trigger system. When an accept trigger signal is received, data for the selected events are sent to the back-end electronics in the ATLAS counting room where the Read Out Driver (ROD) receives the data at 100 kHz maximum rate. Figure 1 shows the dataflow of the current readout architecture.

To meet the challenges of HL-LHC, a multi-phase upgrade program of the ATLAS experiment has been developed: Phase-0, Phase-I and Phase-II [3]. While TileCal mechanics and optics will stay together with their PMTs, TileCal electronics will undergo major upgrades, because by the time of Phase-II, the current electronics will have reached their end of life and the maximum total integrated radiation dose.

2 Tile Calorimeter electronics for HL-LHC

A full redesign and replacement of the readout electronics of Tile Calorimeter is mandatory to implement redundancy in the signal processing and power distribution, use of radiation-tolerant components and using reliable protocols with error correction for data transmission.

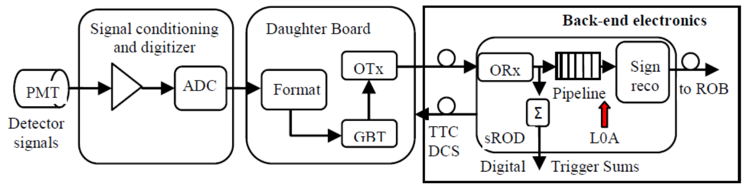

Figure 2: Tile Calorimeter readout architecture for the HL-LHC.

The readout architecture for Phase-II points to a full digital readout where the front-end electronics will transmit digital data from all the channels to the back-end electronics in the counting room for every bunch crossing using high-speed fibre optic links. The data will be pre-processed and transmitted to the first level of trigger with improved precision and granularity. The signal chain for the new readout architecture is shown in Figure 2.

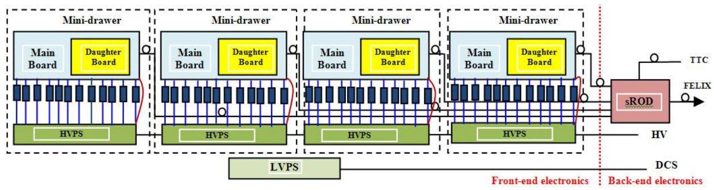

Figure 3: Block diagram of the upgraded super-drawer electronics.

Since redundancy is of utmost importance to achieve maximum reliability, the new front-end electronics will be split into four independent units operating in parallel [4], as is shown in Figure 3. The new design, moving from dependent drawers to independent mini-drawers, reduces the complexity and internal connections, provides a complete redundant readout from cell to back-end electronics and a redundant power supply system.

3 Tile Calorimeter Demonstrator Project

To evaluate and qualify the new concept, a prototype called TileCal Demonstrator was developed. In order to gain field experience with the new design, the Demonstrator will replace one super-drawer of the current system for next LHC Run 2 and it must be compatible with present system insofar as it also provides analog trigger signals. Due to this functionality, the prototype is called hybrid Demonstrator. The existing system was redesigned with the respect to mechanics, electronics, and power distribution.

Mechanics - The current front-end electronics are installed in super-drawers, each composed of two drawers. The modularity implemented by the new concept allows half size drawers called mini-drawers, so that one super-drawer is composed of four mini-drawers. Each mini-drawer is equipped with up to 12 PMTs with corresponding Front-end boards, one Main board, one Daughter board, one High Voltage regulation board and one Adder base board as is shown in Figure 4 (left). The mini-drawers offer a good alignment precision, required in insertion and extraction procedures, due to the improved mechanical links between mini-drawers and a more efficient internal water cooling system. Electrical services organized in two flexible carriers provide easy connection and disconnection of all electrical and optical cables.

The advantages of the Demonstrator super-drawer, shown in Figure 4 (right), consist in an easier access and reduced demand for wide detector opening for TileCal electronics servicing. Also, failing mini-drawers can be more easily replaced than in the present situation, with a minimal radiation exposure of the servicing personnel.

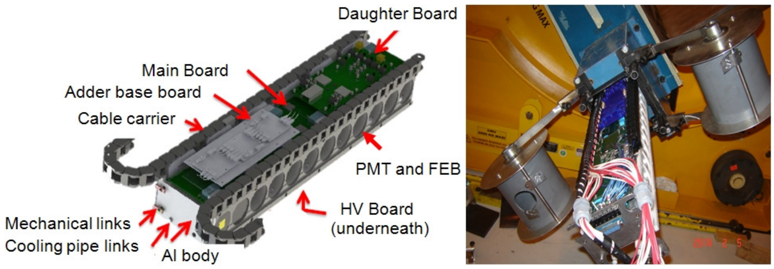

Figure 4: Mini-drawer design (left), Demonstrator and manipulation tooling (right).

Electronics - To improve the reliability and redundancy the new electronics are made as independent as possible and taking in consideration the predicted radiation levels, reliable radiation tolerant components are used.

Front-End Boards (FEB) - three different alternatives are being evaluated: modified 3-in-1 card (redesign of existing FEB), FE-ASIC alternative (including ADCs in an ASIC) and QIE alternative (a charge integrating ASIC). The Demonstrator prototype is equipped with the first version, still based on discrete components but with better linearity, lower noise than current version and acceptable radiation tolerance.

Main Board (MB) - provides the control, monitoring and readout of the FEBs and delivers digitized data to the Daughter Board [5]. MB prototype is divided into halves each hosting six FEBs. Each half has a separated low voltage power supply and is diode-ORed with the other half, ensuring the complete functionality if the power supply for one half stops working.

Daughter Board (DB) - provides high speed communication between the front-end and back-end electronics using redundant high speed links at data rates 10 Gb/s [6]. DB implements slow control functionalities as the distribution of Detector Control System (DCS) commands needed for the control and monitoring of the Main Board and the high voltage power supplies. DB prototype is divided into two separate halves, each equipped with one Kintex 7 field-programmable gate array (FPGA) and one Quad Small Form-factor Pluggable (QSFP) optical module and it can be remotely configured from back-end electronics via safe path using tolerant GBTx and will in turn be able to configure Main Board FPGAs.

Power - Instead of the current daisy-chain power distribution that has proved to be prone to voltage drops, each super-drawer will be outfitted with redundant power supplies.

Low Voltage power distribution - use a three stage power scheme with 200 V from the control room to local power supplies in the TileCal module. Boards receive down-regulated power at +10 V and Point Of Load (POL) regulators locally produce the required voltages. Diode coupling two independent 10 V supplies will provide increased redundancy.

High Voltage power distribution - two solutions are under evaluation to provide HV to the front-end electronics: voltage regulation in ATLAS counting room versus front-end (HV Opto board). For Demonstrator is implemented the second solution, introducing the possibility of switching on/off individual PMTs, based on the current design and for a better linearity the passive dividers have been replaced by active ones.

Back-End Electronics - The upgraded Read Out Driver (sROD) [7] performs the following functions: receiving and processing readout data, interfacing the DCS and the front-end electronics, as well as the reception and distribution of Timing Trigger and Control (TTC) information towards the detector. It was developed a prototype, able to readout a complete hybrid Demonstrator super-drawer. The connectivity between the two Xilinx FPGAs and the optical modules and peripherals is shown in Figure 5. The Virtex 7 FPGA is connected to 4 QSFP providing high speed communication with front-end electronics at a maximum data rate of 160 Gb/s. The Kintex 7 FPGA interfaces the hybrid Demonstrator with current system sending data to the present ROD and receiving TTC information and interfaces with trigger system.

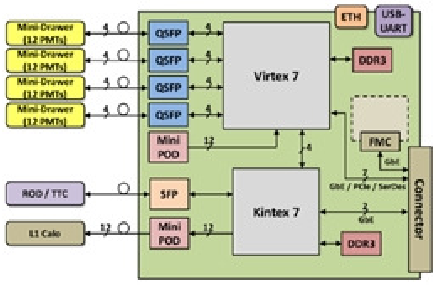

Figure 5: Block diagram of sROD Demonstrator.

4 Summary

The new operational conditions for HL-LHC, with higher radiation levels and data rates, require the implementation of a complete redesign of the Tile Calorimeter readout electronics.

The upgrade plan is to develop a system with full digitization of signals and data transmission at bunch-crossing rate, with a reduced number of possible single points of failure, higher radiation tolerance and higher redundancy on the readout and in power distribution.

To gain an experience and to evaluate the Tile Calorimeter new electronics before the full replacement around 2024, it was developed a hybrid Demonstrator which combines current features, like analog path with the requirements for Phase-II upgrade. It is planned to outfit one full Tile Calorimeter module with the hybrid Demonstrator electronics during first ATLAS opening in LHC Run 2.

References

[1] ATLAS Collaboration, Eur. Phys. J. 1193 (2010).
[2] ATLAS Collaboration, JINST **3** S08003 (2008).
[3] ATLAS Collaboration, CERN-LHCC 2012-022, https://cds.cern.ch/record/1502664/ (2013).
[4] F. Tang *et al.*, IEEE Trans. Nucl. Sci. **60** 1255-1259 (2013).
[5] F. Tang *et al.* on behalf of ATLAS Tile Clorimeter Group, IEEE NSS-MIC Conf. Proc. 6829443 (2013).
[6] S. Muschter *et al.* on behalf of ATLAS Tile Clorimeter Group, JINST **8** C03025 (2013).
[7] F. Carrio *et al.* on behalf of ATLAS Tile Clorimeter Group, JINST **9** C02019 (2014).

Perspectives for the Phase II Upgrade of CMS

David Petyt[1] for the CMS collaboration

[1]STFC Rutherford Appleton Laboratory, Didcot OX11 0QX, United Kingdom

DOI: http://dx.doi.org/10.3204/DESY-PROC-2014-04/194

The LHC Phase II upgrade (HL-LHC) will provide considerable increases in instantaneous and integrated luminosities, leading to a total of 3000 fb^{-1} by around 2035. This data will allow precision measurements of Higgs properties and vector boson scattering processes, and will provide substantially higher sensitivity to searches for new physics. Various subdetectors of CMS will need to be upgraded in order to operate efficiently in such a high rate and high radiation environment. CMS will receive new tracking detectors and new forward instrumentation for calorimetry and muon tagging along with an increase in the capability of the online trigger and data acquisition system. The CMS Phase II upgrade program and the expected performance of the replacement detectors will be reviewed.

1 Introduction

The CMS detector [1] has been designed to provide high performance in the harsh radiation environment of the LHC. During LHC Run I, the detector has recorded data with instantaneous luminosities close to the design goal of 1×10^{34} $\text{cm}^{-2}\text{s}^{-1}$, with an average number of simultaneous interactions per bunch crossing (pileup) of about 25. The excellent performance of the CMS detector and reconstruction algorithms in this environment has led to the discovery of a Higgs-like boson in 2012 [2].

The HL-LHC upgrade, planned for 2025, will significantly increase the instantaneous luminosity that can be provided to CMS, with a total integrated luminosity of 3000 fb^{-1} expected to be delivered by 2035. It has been shown [3] that the significantly larger dataset provided by HL-LHC can considerably expand the sensitivity and reach of CMS to various key physics signatures, including the precise measurement of Higgs boson couplings (including VBF processes), searches for supersymmetry and heavy vector gauge bosons, and precise measurements of electroweak processes.

The large instantaneous and integrated luminosities provided by the HL-LHC upgrade place stringent constraints on the performance, radiation tolerance and longevity of the CMS subdetectors and readout systems. Figure 1 shows the predicted fluence of neutrons in CMS after an accumulated dose of 3000 fb^{-1}. The fluence reaches 1×10^{16} n/cm^2 in the pixel detector and forward calorimeters. In addition, the level of pileup will increase significantly, with an average of about 140 interactions per bunch crossing expected at an instantaneous luminosity of 5×10^{34} $\text{cm}^{-2}\text{s}^{-1}$. The modifications to CMS that will be required to maintain the current level of performance in this challenging enviromnent are summarised below.

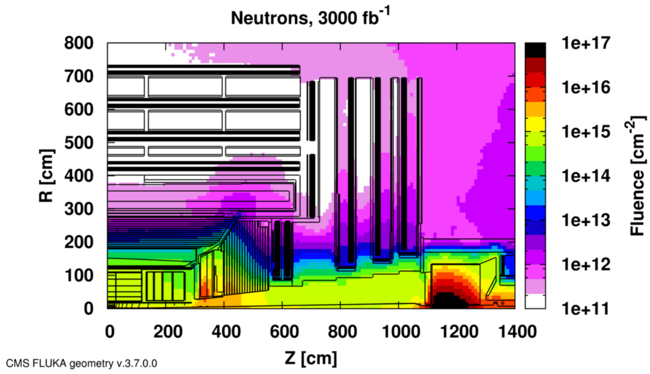

Figure 1: Neutron fluence in the CMS cavern after an integrated luminosity of 3000 fb^{-1}.

2 Upgrade Plans

2.1 Tracker and Pixel detectors

The CMS Tracker will suffer significant radiation aging and must be completely replaced for Phase II. The granualarity of both the outer tracker and pixel detectors will be increased by about a factor of 4 in order to maintain adequate track reconstruction performance at the much higher pileup levels expected at HL-LHC luminosities. For the outer tracker, this will be achieved by shortening the lengths of silicon sensor strips relative to those in the current detector. The upgraded pixel detector will implement smaller pixels and thinner sensors to achieve improved impact parameter resolution and better two-track separation. The pixel coverage will also be extended close to $|\eta| = 4$ to provide increased tracking acceptance and improved suppression of pileup contributions in forward jets. Significant R&D activity is ongoing to identify suitable radiation tolerant silicon sensor technologies and to develop protoype readout modules and support structures.

The predicted performance of the Phase II detector at 140 PU is shown in Figure 2, and is compared to the performance of the Phase I tracker at 50 PU. A number of design improvements will lead to a much lighter outer Tracker providing significantly improved p_T resolution and a lower rate of photon conversions, compared to the present detector. In addition, the module design will be capable of providing fitted tracks with p_T >2 GeV to the Level-1 trigger at 40 MHz. This will ensure powerful background rejection at the earliest stage of the online event selection.

2.2 Calorimeters

The electromagnetic and hadronic endcap calorimeters will also suffer significant radiation damage, and must be replaced for Phase II. Two concepts are currently under consideration, with the potential for higher radiation tolerance and finer granularity to mitigate pileup effects. These include an Electromagnetic Endcap calorimeter, with a Shashlik design (LYSO or CeF_3 crystals interleaved with tungsten plates) followed by a Hadronic Endcap (HE) which would be a rebuild of the present brass/scintillator detector with more radiation tolerant components. The second concept is a High Granularity Calorimeter (HGC) with planes of silicon sensors and

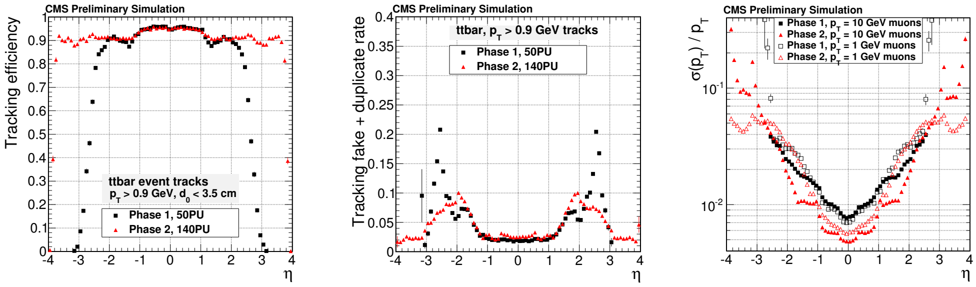

Figure 2: Projected performance of the Phase II tracker for events with an average pileup of 140. The performance of the Phase I tracker for 50 PU is shown for comparison. Left: tracking efficiency; Centre: rate of fake/duplicate tracks; Right: track momentum resolution. The plots assume no detector ageing.

tungsten or brass absorber, organised in electromagnetic and hadronic sections, followed by a rebuilt brass-scintillator HE to provide a total depth of $10\lambda_I$. A more detailed description of these designs can be found in [4].

The front-end electronics of the barrel electromagnetic calorimeter will also be replaced. The data will be transferred off-detector at 40 MHz, simultaneously overcoming present limitations in trigger latency (6.4 μs) and acceptance rate. A new front-end chip will be designed with a shorter shaping time to mitigate the anticipated aging-induced noise increase in the avalanche photodiodes (APD), and for better out-of-time pileup rejection.

2.3 Muon detectors

To maintain good Level-1 muon trigger acceptance in the endcap regions ($1.5 < |\eta| < 2.4$) it is proposed to enhance the existing muon stations with additional chambers that make use of new detector technologies with higher rate capability. The front two stations are in a region where the magnetic field is still reasonably high and will use Gas Electron Multiplier (GEM) chambers for good position resolution. The two rear stations will use low-resistivity Resistive Plate Chambers (RPC) with lower granularity but good timing resolution to mitigate backgrounds. In addition, the implementation of a GEM station behind the new endcap calorimeters is being proposed in order to increase the coverage for muon detection to $|\eta| \simeq 3$.

2.4 Trigger

The Level-1 (L1) trigger accept rate will be increased to provide maximum acceptance for interesting physics events during Phase II running. The trigger latency will also be increased to 12.5 μs to provide sufficient time for the hardware track reconstruction and the matching of tracks to muons and calorimeter energy deposits. This change will require upgrades of the readout electronics in several of the existing subdetectors that will be retained for Phase II. With these modifications, CMS is expected to be able to operate up to 200 PU without significant data loss.

Based on the expected performance of the trigger with track information, we propose to operate with a L1-trigger acceptance rate of 500 kHz for beam conditions corresponding to 140

PU. This will allow us to maintain similar thresholds to those anticipated for use in Phase I.

2.5 Online and offline computing

The Data Acquisition (DAQ) system will be upgraded to provide the increase of bandwidth and computing power needed to accommodate the larger event size and L1 trigger rate. The bandwidth and computing power requirements will increase relative to Phase I by factors of about 10 and 15 respectively for operation at 140 PU. This is within the projected network and computing technology capabilities that are expected to exist at the time of Phase II. The rate of recorded data will increase at 140 PU to about 5 kHz from the corresponding LHC Run 1 levels of between 0.5 and 1.0 kHz. To minimize the computing needs, both for online and offline reconstruction, a significant R&D effort has started to improve the algorithms used for data reconstruction and to adapt the CMS software and computing model to new technologies and resources.

2.6 Infrastructure

Planning for the installation of the new subdetectors for Phase II is still at an early stage, but an initial evaluation of the work sequence and time estimates indicates that the full scope of work can be accomplished in a shutdown of approximately 30 months duration. This is anticipated to take place during LHC Long Shutdown 3 (2023-2025).

3 Summary

The HL-LHC upgrade will provide a large additional dataset that will allow the full exploitation of the physics potential of the LHC. CMS has conducted a detailed study to determine the necessary requirements to operate efficiently in such a high rate and high radiation environment. New tracking devices and forward calorimeters with enhanced radiation tolerance and granularity will be required. Significant upgrades to the capability of the online trigger and data acquisition systems are also needed to maintain and enhance the acceptance to interesting physics signals. Dedicated R&D programmes and prototyping steps are ongoing to identify suitable technologies and to finalise detector designs. These will be documented in a Technical Proposal, to be released in 2015, and in Technical Design Reports, to be completed in 2016-17.

References

[1] CMS Collaboration, *The CMS Experiment at the CERN LHC*, JINST **3** (2008) S08004.

[2] CMS Collaboration, *Observation of a new boson at a mass of 125 GeV with the CMS experiment at the LHC*, Phys. Lett. **B716** 1 (2012).

[3] CMS Collaboration, *Projected Performance of an Upgraded CMS Detector at the LHC and HL-LHC: Contribution to the Snowmass Process*, `arXiv:1307.7135`

[4] M. Peruzzi, *Evolution studies of the CMS ECAL endcap response and upgrade design options for High-Luminosity LHC*, these proceedings.

Evolution Studies of the CMS ECAL Endcap Response and Upgrade Design Options for High-Luminosity LHC

Marco Peruzzi on behalf of the CMS Collaboration

Institute for Particle Physics, ETH Zurich
Otto-Stern-Weg 5, CH-8093 Zurich, Switzerland

DOI: http://dx.doi.org/10.3204/DESY-PROC-2014-04/196

The operation of the CMS electromagnetic calorimeter (ECAL) during the High-Luminosity running of the LHC will be characterized by radiation levels and hadron fluences significantly beyond the design values. Moreover, a large increase in the number of proton-proton interactions per bunch crossing is expected with respect to the current conditions. Studies of the ECAL performance evolution based on LHC collision data, as well as irradiation and beam tests, indicate that its endcaps will need to be upgraded. An overview of the different replacement options under consideration is presented.

Introduction

The CMS electromagnetic calorimeter (ECAL) is a homogeneous crystal calorimeter. It consists of 75,848 lead tungstate ($PbWO_4$) scintillating crystals. ECAL is separated into a barrel region, covering the pseudorapidity range up to $|\eta| = 1.479$, and two endcap regions that extend the coverage up to $|\eta| = 3$. The crystals are arranged in a hermetic and quasi-projective geometry. $PbWO_4$ features a small radiation length (0.89 cm), a small Molière radius (2.19 cm), and a fast scintillation response. These properties have made it possible to build a compact and granular homogeneous calorimeter providing excellent energy resolution, response linearity and particle identification capability at the LHC [1].

Very different operating conditions are expected for the High-Luminosity (HL) running of the LHC, that is scheduled to take place between about 2025 and 2035, up to a final delivered integrated luminosity of about 3000 fb^{-1}. The instantaneous luminosity is expected to reach a value of $5 \cdot 10^{34}$ cm^{-2} s^{-1}, with about 140 proton-proton interactions taking place on average in the same bunch crossing (pileup). The radiation levels in the endcap region are strongly position-dependent. At high values of the pseudorapidity ($|\eta| \sim 2.6$), the photon dose rate will be about 30 Gy/h and the fluence of energetic hadrons will be of the order of $1.8 \cdot 10^{14}$ cm^{-2}. These values exceed by a factor of at least four those the ECAL was designed to withstand.

The ECAL has played a crucial role in many analyses performed with LHC collision data, including the discovery of the Higgs boson in CMS [2]. This will still be the case for a large class of physics analyses that will be performed with HL-LHC data. Therefore, the long-term physics reach of the CMS experiment will strongly depend on an enduring ECAL performance. It is crucial to understand in detail how the properties of $PbWO_4$ crystals evolve under irradiation

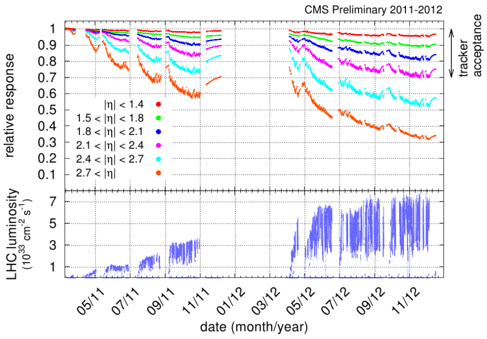

Figure 1: Relative response to laser light measured by the ECAL laser monitoring system, averaged over all crystals in bins of pseudorapidity, for the 2011 and 2012 data taking periods. [3]

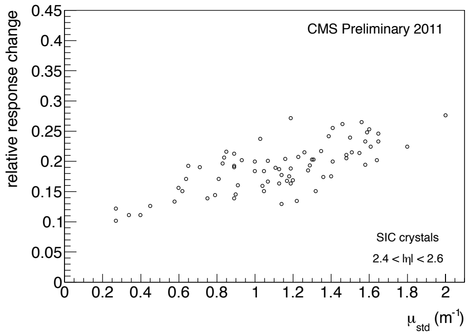

Figure 2: Correlation between relative change of response from ECAL monitoring data and the absorption coefficient, μ_{std}, induced by a standard γ irradiation in crystals produced by the Shanghai Institute of Ceramics. [4]

and to study the performance of the calorimeter in high pileup conditions.

Performance evolution

A loss of transparency of the $PbWO_4$ crystals under irradiation has been established with the LHC collision data collected so far [3]. A laser light injection system has been used to continuously monitor this effect during the data-taking. The loss of transparency has been observed to be strongly correlated with the LHC instantaneous luminosity and with the crystal position in the detector, being the largest at high values of $|\eta|$ (Fig. 1). These monitoring data have been used to correct the crystal response as a function of time and stabilize the energy scale of objects whose energy measurement is based on ECAL.

The main mechanism leading to the transparency loss observed in the detector so far is the formation of colour centres due to ionizing radiation. This type of damage is not cumulative and recovers with time when the irradiation stops (as can be seen in Fig. 1). The loss of transparency measured in the detector with collision data correlates with the results obtained from photon irradiation during the crystal quality control tests before installation (Fig. 2). However, another component of transparency loss is observed to arise after hadron irradiation [4]. It consists of an induced absorption length due to interactions of energetic hadrons with the crystal lattice. It does not recover at room temperature when irradiation stops and therefore builds up during the data-taking. At the large values of integrated luminosity expected at the HL-LHC, this ageing component will become the dominant one. The transparency loss extends throughout the $PbWO_4$ transmission band and causes the lower band edge to shift towards higher wavelengths. The residual light output is expected to be about 10% of the nominal one at $|\eta| \sim 2$ after 3000 fb^{-1}, leading to a contribution to the Higgs diphoton invariant mass peak resolution of the order of several percent (Fig. 3) [5]. On the other hand, the transparency loss will remain acceptable in the barrel region, because of the much lower radiation levels there.

Another effect due to crystal transparency loss is the amplification of the effective noise in the ECAL readout electronics. The electric signal pulse from the ECAL photosensors is sampled by an ADC at 40 MHz. A conversion factor from ADC counts to energy is then applied. While the electronic noise stays constant in units of ADC counts, the loss of transparency will lead to larger conversion factors, effectively amplifying the energy equivalent of the noise. This effect will strongly degrade the trigger performance in the endcap region, increasing the energy thresholds required on electron and photon triggers. The ECAL resolution will also be worsened by non-uniformity of light collection and non-linearity. In conclusion, all terms (stochastic, noise, constant) of the endcap ECAL resolution are worsened by the crystal hadron radiation damage [6]. Moreover, the large number of pileup interactions expected at the HL-LHC will significantly increase the detector occupancy. In these conditions, energy deposits from adjacent bunch crossings will bias the crystal energy readout. The main handle available to fight this effect is increasing the detector granularity.

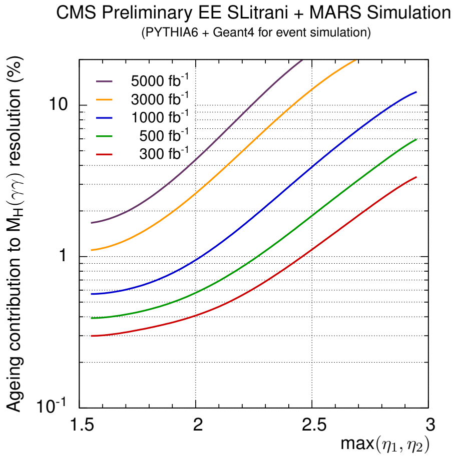

Figure 3: Contribution to the Higgs mass resolution due to the ECAL ageing, for the two photon decay of the Higgs boson in the endcap regions. [5]

Upgrade options

The loss of performance justifies an upgrade of the ECAL endcaps for operation in HL-LHC conditions. Several options have been studied for replacing the CMS electromagnetic and hadronic (HCAL) calorimeters in that region with sampling calorimeters based on new technologies, with finer granularity than the existing devices. The two main design schemes under consideration are described in the following sections.

Sampling design using inorganic scintillating crystals

A sampling calorimeter based on radiation-hard inorganic scintillating crystals interleaved with heavy absorber material plates has been proposed to replace the ECAL endcaps. The light produced in the crystals is wavelength-shifted and extracted towards the photosensors by capillaries or fibres running in the longitudinal direction of the channel (Fig. 4). Two scintillating materials under consideration are LYSO and CeF_3. Both have been studied in irradiation tests and have been shown to be able to withstand larger hadron fluences than $PbWO_4$ (Fig. 5) [7]. CeF_3 even shows a spontaneous recovery of the hadron damage when irradiation stops. The proposed absorber material is tungsten. This design aims at a stochastic term in the calorimeter resolution of about 10%. The low radiation length and Molière radius of this configuration lead to a very compact and granular design. Two prototypes have been realized and successfully tested in beams. One uses LYSO crystals with fibres running through the channel; the other uses CeF_3 crystals with fibres running along chamfers located at the channel corners [8].

High-granularity design

A replacement of both ECAL and HCAL endcaps with a highly segmented (longitudinally and transversally) system, based principally on silicon sensors, has also been proposed. The aim of this design is to obtain an excellent three-dimensional shower profile reconstruction and particle identification. The current proposal consists of a total of about 600 m^2 of silicon sensors of different thickness, segmented into about 9 million channels and interleaved with varying amounts of heavy absorber material. Current R&D studies aim at a highly integrated design of sensors, absorber material and cooling infrastructure.

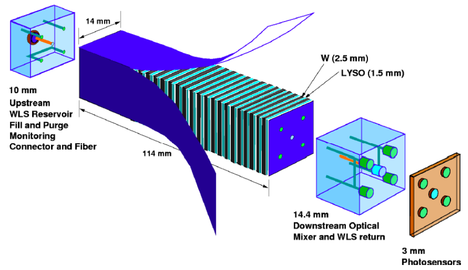

Figure 4: Sketch of a Shashlik configuration based upon interleaved W and LYSO scintillating crystal layers.

Conclusions

The High-Luminosity running of the LHC poses a significant challenge in terms of radiation levels and number of pileup interactions. The mechanisms of radiation damage to the ECAL $PbWO_4$ crystals have been studied with LHC data and irradiation tests and have been found to lead to a strong loss of physics performance in the endcap regions in HL-LHC conditions, while the barrel region will continue to perform well. It is therefore necessary to replace the ECAL endcaps with a more radiation-hard and granular detector. Two options are currently being considered: one is based on a sampling design using heavy inorganic scintillators, while the other consists of a high-granularity silicon-based detector.

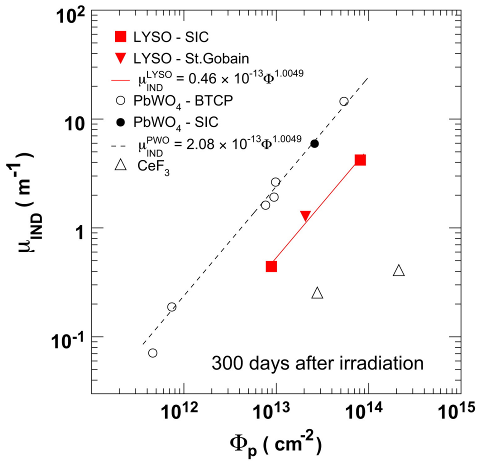

Figure 5: Induced absorption at the peak-of-emission wavelength for $PbWO_4$, LYSO and CeF_3, measured longitudinally through the crystals, as a function of integrated proton fluence, for various producers - SIC, BTCP, St. Gobain. [7]

References

[1] CMS Collaboration, JINST **8** (2013) P09009 [arXiv:1306.2016 [hep-ex]].

[2] CMS Collaboration, Phys. Lett. B **716**, 30 (2012) [arXiv:1207.7235 [hep-ex]].

[3] CMS Collaboration, CMS-DP-2013-007.

[4] CMS Collaboration, CMS-DP-2012-027.

[5] CMS Collaboration, CMS-DP-2013-026.

[6] CMS Collaboration, CMS-DP-2013-022.

[7] G. Dissertori *et al.*, Nucl. Instrum. Meth. A **745** (2014) 1 [arXiv:1309.3872 [physics.ins-det]].

[8] R. Becker *et al.*, [arXiv:1405.6202 [physics.ins-det]].

The STAR Heavy Flavor Tracker (HFT)

Joachim Schambach[1], Eric Anderssen[2], Giacomo Contin[2], Leo Greiner[2], Joe Silber[2], Thorsten Stezelberger[2], Xiangming Sun[3], Michal Szelezniak[4], Flemming Videbæk[5], Chinh Vu[2], Howard Wieman[2], Sam Woodmansee[2]

[1]University of Texas, 1 University Station, Austin, TX 78712, USA
[2]Lawrence Berkeley National Laboratory, Berkeley, CA 94720
[3]Central China Normal University (CCNU), Wuhan, China
[4]Institut Pluridisciplinaire Hubert Curien (IPHC), Strasbourg, France
[5]Brookhaven National Laboratory, Upton, NY 11973, USA

DOI: http://dx.doi.org/10.3204/DESY-PROC-2014-04/83

The heavy quark hadrons are suggested as a clean probe for studying the early dynamic evolution of the dense and hot medium created in high-energy nuclear collisions. The Heavy Flavor Tracker (HFT) of the STAR experiment, designed to improve the vertex resolution and extend the measurement capabilities in the heavy flavor domain, was installed for the 2014 heavy ion run of RHIC. It is composed of three different silicon detectors arranged in four concentric cylinders close to the STAR interaction point. The two innermost layers are based on CMOS monolithic active pixels (MAPS), featured for the first time in a collider experiment, and the two outer layers are based on pads and strips. The two innermost HFT layers are placed at a radius of 2.8 and 8 cm from the beam line and accommodate 400 ultra-thin (50 μm) high resolution MAPS sensors arranged in 10-sensor ladders to cover a total silicon area of 0.16 m^2. Each sensor includes a pixel array of 928 rows and 960 columns with a 20.7 μm pixel pitch, providing a sensitive area of $\sim 3.8\ cm^2$. The sensor features 185.6 μs readout time and 170 mW/cm^2 power dissipation, allowing it to be air cooled, which results in a global material budget of only 0.5% radiation length per layer in the run 14 detector. A novel mechanical approach to detector insertion enables effective installation and integration of the pixel layers within a 12 hour shift during the on-going STAR Run. After a detailed description of the design specifications and the technology implementation, the detector status and operations during the 200 GeV Au+Au RHIC run of 2014 will be presented in this paper. A preliminary estimation of the detector performance meeting the design requirements will be reported.

1 Introduction

Results from experiments over the last decade at the Relativistic Heavy Ion Collider (RHIC) suggest that a hot and dense matter with strong collectivity has been formed in central Au+Au collisions with energies up to $\sqrt{s} = 200\ GeV$ [1]. The high temperatures and densities of nuclear matter generated in these collisions create conditions in which a phase of deconfined quarks and gluons, the so-called Quark-Gluon Plasma (QGP), should exist. Due to their mass, heavy quarks such as charm and bottom quarks, are only produced by hard processes early in the collision and not by thermal processes after the equilibration of the plasma, which makes mesons containing

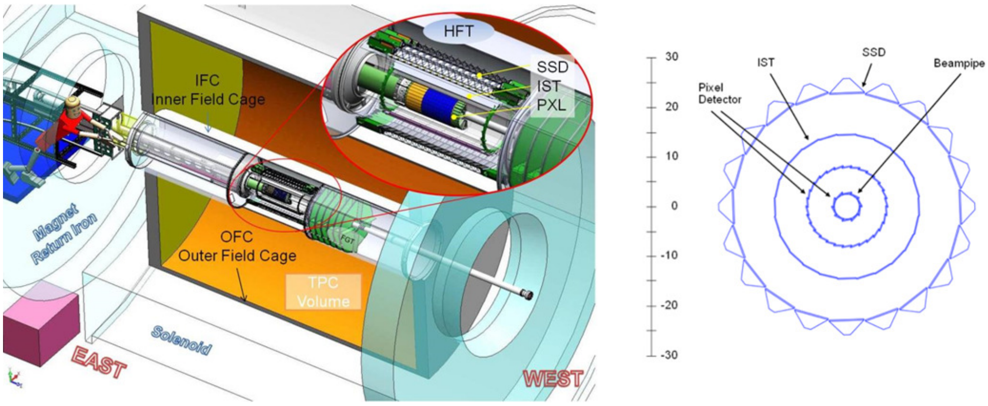

Figure 1: Schematic view of the HFT inside the TPC inner field cage.

heavy quarks an ideal probe for studying the initial conditions of the produced QGP. Most of these heavy quarks produced in the collision end up in open heavy flavor particles that in the past were hard to detect in the STAR experiment due to their low abundance and the large combinatorial background. For that reason STAR installed a new micro-vertex detector for the 2014 heavy ion run at RHIC, called the "Heavy Flavor Tracker" [2], which allows the direct topological reconstruction of the decay vertices from open heavy flavor meson decays which happen close the primary collision vertex due to the small decay length of open heavy flavor particles.

2 HFT and PXL Design

The STAR experiment uses a Time Projection Chamber (TPC) inside a 0.5 T magnetic field as its main tracking detector. Using tracks found in the TPC, the primary interaction vertex can be resolved with a Distance of Closest Approach (DCA) pointing resolution of about 1 mm. Open flavor mesons that are produced at the collsion vertex have a decay length that is very small; for example the $c\tau$ of the D^0 meson is 120 μm. Thus, to be able to reconstruct these decay vertices, the primary physics requirements on the new "HFT" detector system is to provide vertex pointing resolution to resolve vertices displaced from the primary vertex by less than about 150 μm. The basic idea in the design of the HFT is to use tracks found in the TPC and add additional space points on these tracks towards the primary vertex with increasing resolution. The HFT therefore consists of 3 different silicon detector subsystems arranged in 4 concentric layers around the primary vertex as seen in Figure 1: the "Silicon Strip Detector" (SSD), the "Intermediate Silicon Tracker" (IST), and the "PIXEL" (PXL) detector.

The outermost Si detector system, the SSD is an existing detector consisting of double sided silicon strip modules with a 95 μm pitch at a distance of of 22 cm from the beam. The electronics for this detector was upgraded to achieve faster trigger rates compatible with other STAR detectors. The IST at 14 cm radius consists of single-sided double-metal silicon pad sensors with a 600 μm x 6 mm pitch. The SSD and IST detector layers redundantly guide tracks from the TPC to the two innermost layers of the HFT, the PXL detector.

The PXL detector, shown in Figure 2, consists of two layers at radii 2.8 cm and 8 cm using

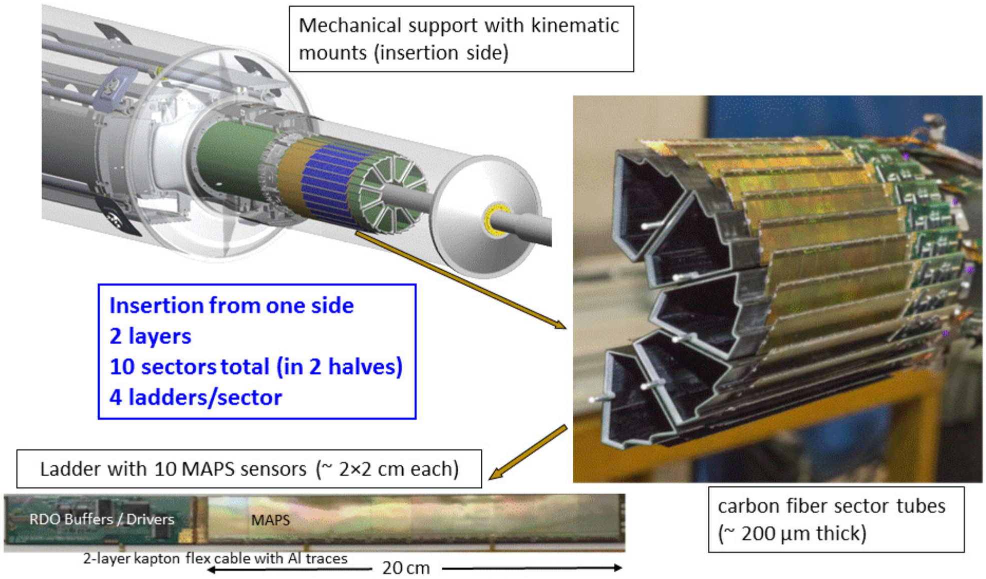

Figure 2: Schematic view of the PXL sub-detector system of the HFT.

state-of-the-art ultra thin CMOS Monolithic Active Pixel Sensors (MAPS) [3, 4, 5, 6]. Mechanically, the PXL detector is subdivided into 10 sectors, each consisting of a thin trapezoidal carbon fiber sector tube with four 10-sensor ladders mounted on each tube, one at the inner diameter, and 3 at the outer diameter. The sensors are thinned to 50 μm thickness, and are mounted on an aluminum conductor flex cable that provides the signal path to the electronics at the end of the flex cable containing the buffers and drivers for the sensor signals. This construction results in a total radiation length X/X_0 of as little as 0.4% per layer in the low-mass region.

The sectors are assembled into two halves on unique mechanical supports that allow for the insertion and retraction of the whole PXL detector from one side side of STAR in only about 12 hours, by pushing the detector halves along rails inside a support cylinder and locking them into a reproducible position with kinematic mounts. The sensor chip used for the PXL detector is the "Ultimate" sensor developed by IPHC in Strasbourg, France. These sensors use pixels with a pitch of 20.7 μm pitch arranged in a 928 (rows) by 960 (columns) array (a total of $\sim 890k$ pixels per sensor) on a 20.22 mm x 22.71 mm chip with a high-resistivity epitaxial layer for increased radiation hardness and increased signal-to-noise performance. Each pixel includes readout and correlated double sampling (CDS) circuitry for signal extraction and noise subtraction. The readout is done by reading each pixel row in parallel through programmable threshold discriminators at the end of each column. The resulting digital data are then passed through a zero-suppresion logic block located below the pixel array on the same chip, which delivers run-length encoded hit addresses for up to 9 hit clusters per row to on-chip memory for intermediate buffering. The memory is arranged in two banks of up to 1500 words each which allows simultaneous read and write operations. The data are read out bit-serially from one of these memory banks over two "Low-Voltage Differential Signaling" (LVDS) outputs per sensor, each running at 160MHz. The signal integration time of the whole sensor is

185.6 μs. Configuration by the JTAG protocol allows the control of many internal parameters and programming of internal test features. A power dissipation of only $\sim 170\ mW/cm^2$ allows these sensors to be operated at room temperature with just air cooling. The readout electronics for the PXL detector follows the mechanical segmentation of the detector and is divided into 10 parallel identical systems. After leaving the ladders, the sensor signals are transmited over $\sim 2m$ of thin twisted pair cables to "Mass Termination Boards" (MTB) at the end of the mechanical structure of the PXL system, which contain buffers and drivers for the signals, as well as latchup protected power supplies for the sensors. Each MTB services the 4 ladders of one sector, i.e. there are 10 MTBs in the PXL detector. Each MTB is connected to an FPGA-based Readout (RDO) board in the low radiation area of the STAR experimental hall with $\sim 11\ m$ of twisted-pair cable. The 10 RDO boards are mounted in a 9U-size crate; each RDO provides trigger based hit selection, buffers and formats the resulting data into event structures, and then sends it over 100 m optical fiber to one of two PCs in the STAR DAQ room, where the data are combined with the rest of the STAR data for event building and final storage. Control, configuration and monitoring of the PXL sensors is done from a control PC, which is connected via USB to the RDO boards. The control PC interfaces to the STAR Slow Controls system to provide monitoring and control of the PXL system to the STAR shift crew.

3 PXL Status and Performance

Two complete PXL detectors and 40 spare ladders have been fabricated by the fall of 2014, and the first PXL detector was installed before the 2014 heavy ion run of RHIC. Because of production issues only 2 of the inner ladders were produced with Aluminum-conductor flex cables, while the rest of the ladders were constructed using alternative Copper-conductor flex cables. This resulted in an increase of the radiation length from the design value of 0.4% to 0.5%. The SSD and IST detectors were installed into STAR during the fall of 2013, while the PXL detector was installed in January of 2014, shortly before the beginning of the 2014 heavy ion run of RHIC. The PXL detector was inserted and cabled into the STAR TPC inner flied cage and operational within a 2 day installation. At the time of the first PXL detector installation all 400 sensors of the PXL system were tested to be working properly with less than 2000 bad pixels out of more than 365 million total. The discriminator thresholds were adjusted to give a fake hit rate of $\sim 1.5 * 10^{-6}$ for all sensors based on an automatic scan of noise rates versus discriminator threshold.

Before the beginning of the heavy ion run the PXL and IST detectors were included in a STAR cosmics run. This run was used for commisioning and integration of the PXL readout electronics with the existing STAR DAQ, Trigger, and Slow Controls systems. Data from this cosmics run were used for alignment and efficiency studies of the PXL detector. The efficiency of the PXL detector was obtained from these data by finding (straight) cosmics ray tracks in the TPC with hits on 3 PXL sensors, and looking for hits on a fourth sensor at the position of a straight-line fit through these three hits extrapolated to the fourth sensor. The analysis of these data were done before normal beam operation and before detector operation optimization was complete. Nevertheless, the average efficiency over all sensors was determined to be 97.2%.

During construction all pixel positions on the sectors as well as the position of the sectors within a detector half were measured in a coordinate measurement machine (CMM). The different parts of the PXL system were then aligned using these same cosmic ray data by looking at the residuals resulting from comparing hit positions to the track projections and adjusting

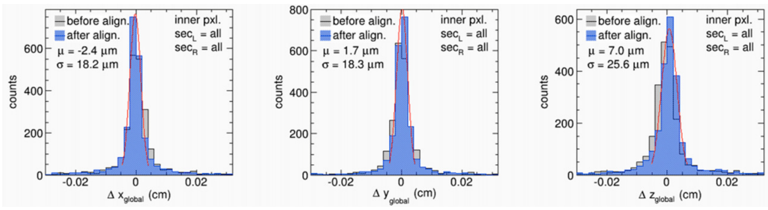

Figure 3: PXL hit residual to cosmic track before and after PXL sector-to-sector alignment.

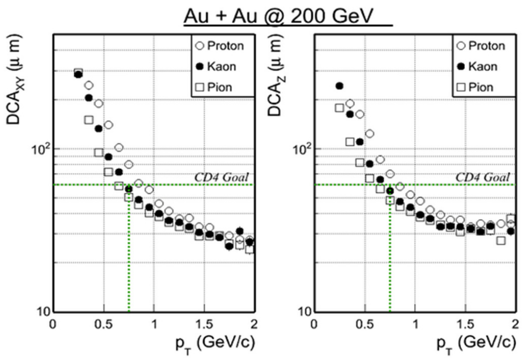

Figure 4: DCA resolution in x-y (left panel) and z (right panel) for TPC tracks with 1 IST hit and hits in both layers of PXL vs. transverse momentum.

the positions of the sensors in order to minimize these residuals. Gaussian fits to these residuals after the alignment was done result in a $\sigma \leq 25\ \mu m$ (see Figure 3), which exceeds the PXL design goals.

The cosmic ray run was followed by a run period of Au+Au collisions at 14.5 GeV from mid February until mid March 2014, which was used to optimize the sensor performance and minimal data taking during stable beam operation. The next 14 weeks were devoted to 200 GeV Au+Au collisions during which a total of $1.2B$ mimimum bias events with PXL included were recorded. Daily PXL noise runs with beam collisions were taken to reassess the sensor status, find hot or not-working pixels, and to verify the noise levels. Periodic threshold-vs-noise scans were performed to readjust the discriminator thresholds. During the final ^{3}He+Au run of RHIC, PXL was only occasionally turned on for further performance and sensor damage studies.

After the survey and preliminary alignment corrections described above were completed, the 200 GeV data were used to estimate the pointing resolution of the PXL detector to the interaction vertex. The DCA resolution for tracks found in the TPC which include 1 IST hit and 1 hit in both layers of PXL as a function of transverse momentum p_T for protons, pions and kaons are shown in Figure 4. For kaons with $p_T = 750 MeV/c$ this DCA resolution exceeds the design goal of 60 μm, in fact, for p_T larger than 1.5 GeV/c, the DCA resolution is better than 30 μm. A more detailed deterimination of the alignment corrections is still ongoing which will further improve these results.

During the 14.5 GeV Au+Au run and into the first two weeks of the 200 GeV Au+Au run first indications of sensor damage manifested itself that seemed to be related to the STAR radiation environment. The sensor damage took on many different forms: increased digital current, damaged or total loss of pixel columns, damaged configuration registers, loss of full or partial sub arrays, etc. Most of the damage occured in the sensors of the innermost layer of PXL, but even some sensors in the outer layer displayed these kind of damages. After several changes to the operational parameters of the running detector when this damage was detected, further damage to the installed detector for the rest of the run was greatly reduced or stopped. These methods included: turning on the PXL sensors when the collision rate started to fall below a certain threshold, power-cycling the sensors and reloading the sensor configutration periodically, and, most importantly, reducing the threshold at which the power supplies would over-current closer to the normal operational current of the sensors. A total of 15 of the 400 sensors in the PXL detector were damaged, which still allowed us to complete the physics run successfully. We plan on implementing these operational methods from the beginning of the 2015 RHIC run, thus hopefully limiting damage to the PXL sensors in the future. Further investigations of the cause of the observed damage is ongoing.

4 Conclusions

The new HFT micro-vertex detector at STAR enables or enhances open heavy flavor measurements at STAR, thus allowing us to study the early dynamic evolution of the dense and hot medium created in high-energy heavy ion collisions at RHIC. As part of this detector, state-of-the-art MAPS technology was used successfully for the first time in a collider experiment in the PXL subdetector. All three sub-detector systems of the HFT were installed and commisioned during the 2014 RHIC heavy ion run, and more than 1.2 billion Au+Au 200 GeV minimum bias events were recorded with the IST and PXL detectors included. Preliminary studies of the DCA pointing resolution performance show that the detector meets or exceeds the design goals. A second PXL detector was constructed during the summer of 2014 and will be installed in STAR before the 2015 RHIC run. The PXL ladders with damaged sensors were replaced after the 2014 run, and this detector was shipped to STAR to serve as a hot spare. Sensor damage related to the radiation environment in STAR was observed, but seems to be very limited by implementing operational methods.

Acknowledgments

We gratefully acknowledge the PICSEL group of IPHC Strasbourg (M. Winter *et al.*) for the development of the PXL detector sensors.

References

[1] J. Adams *et al.*, Nucl. Phys. A, vol. 757, 102 (2005).

[2] D. Beavis *et al.*, *The STAR Heavy Flavor Tracker Technical Design Report*, available at: https://drupal.star.bnl.gov/STAR/starnotes/public/sn0600 (2011).

[3] C. Hu-Guo, *et al.*, Nucl. Instr. And Meth. **A623** 480 (2010).

[4] A. Dorokhov *et al.*, Nucl. Instr. And Meth. **A624** 432 (2010).

[5] A. Dorokhov *et al.*, Nucl. Instr. And Meth. **A650** 174 (2011).

[6] L. Greiner *et al.*, Nucl. Instr. And Meth. **A650** 68 (2011).

Evaluation of the MPD/NICA detector capabilities for studies of hyperon production in HIC

Veronika Vasendina, Alexander Zinchenko for the MPD Collaboration

JINR, 141980 Dubna, Moscow region, Russia

DOI: http://dx.doi.org/10.3204/DESY-PROC-2014-04/178

One of the main tasks of NICA/MPD physics program is a study of the strangeness production in nuclear collisions. In this paper the MPD detector performance for measurements of Λ, $\bar{\Lambda}$, Ξ^-, $\bar{\Xi}^+$, Ω^- and $\bar{\Omega}^+$ hyperons in central Au+Au collisions at NICA energies is presented.

1 Introduction

The main goal of studying heavy-ion collisions is to explore the properties of nuclear matter under extreme density and temperature conditions. Production of strange particles is of particular interest because enhanced production of rare strange hadrons (Ξ^-, $\bar{\Xi}^+$, Ω^-, $\bar{\Omega}^+$), in A+A collisions (relative to the yields from elementary pp reactions) was predicted as a signal for the QGP formation [1].

At present, a complete theoretical description of the (multi)strangeness production mechanism at collision energies ($\sqrt{s}$) of several GeV has not yet been achieved. In order to better understand the dynamics of hot and dense hadronic matter the MPD experiment at NICA [2] will provide new precise experimental data on the total yields, rapidity, transverse momentum, and azimuthal angle distributions of hyperons. The production of baryons and antibaryons with different strangeness content in central heavy ion collisions will be compared with that in proton induced reactions where no QGP formation is expected.

The goal of this study is to evaluate the performance of the MPD detector for reconstruction of hyperons in Au+Au collisions.

2 MPD detector: geometry, event reconstruction and particle identification

The detailed description of the MPD geometry can be found in Refs. [2, 3, 4]. The present analysis is based on the detectors covering the mid-rapidity region ($|\eta| <1.3$): the main tracker Time Projection Chamber (TPC) and barrel Time-Of-Flight system (TOF), comprising a so-called start version. The overall detector material budget is dominated by the contribution from the TPC inner and outer cages which are multilayer structures made of composite materials like kevlar and tedlar with high strength and long radiation length. As a result, the total amount of the material does not exceed 10% of the radiation length in the region of interest.

The track reconstruction method is based on the Kalman filtering technique (see, e.g. [5]) and the number of TPC points per track was required to be greater than 10 to ensure a good precision of momentum and dE/dx measurements. In addition, we have restricted our study to the mid-rapidity region with $|\eta| <1.3$. The track finding efficiency in TPC for primary and secondary tracks is shown in Fig. 1 as a function of the track transverse momentum. The transverse momentum resolution as a function of p_T can be seen on the right panel of Fig. 1. The result has been obtained with the assumption on the TPC coordinate resolution of 0.5 and 1.0 mm in transverse and longitudinal directions, respectively.

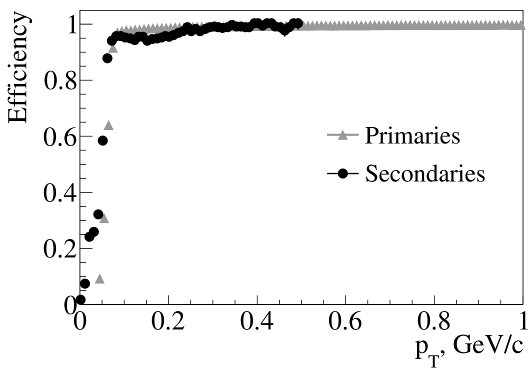

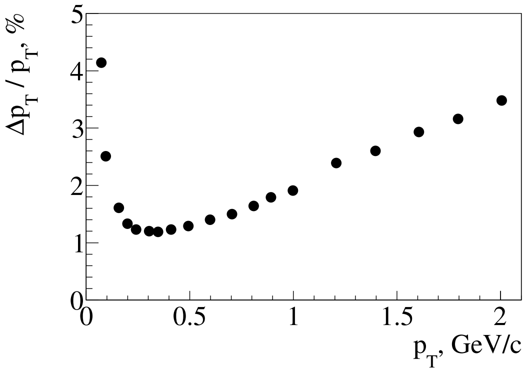

Figure 1: Track reconstruction efficiency as a function of track p_T for primary and secondary particles (left); relative transverse momentum resolution for primary tracks with $|\eta| <1.3$ reconstructed in TPC (right).

The reconstructed tracks served as an input to the primary and secondary vertex reconstruction procedures based on the Kalman filtering formalism [6].

For all the reconstructed in the TPC tracks the specific energy loss dE/dx is calculated as a truncated mean of the charges of TPC hits assigned to the tracks. The truncation level of 70% was chosen, i.e. 30% of hits with the highest charges were excluded from the mean value.

Next, the TPC reconstructed tracks are extrapolated to the TOF detector and matched to the TOF hits. For the matched candidates the mass square (M^2) is derived through the relation:

$$M^2 = (p/q)^2 \left(\frac{c^2 t^2}{l^2} - 1 \right)$$

where p is the track momentum, q is its charge, t is the time-of-flight from TOF, l is the path length from the collision vertex to the TOF hit, and c is the speed of light.

Particle identification (PID) in the MPD experiment will be achieved by combining specific energy loss (dE/dx) and time-of-flight measurements. The basic detector parameters, namely, dE/dx and TOF resolutions of $\sigma_{dE/dx} \approx 6\%$ and $\sigma_{TOF} \approx 100$ ps will provide a high degree of selectivity for hadrons at momenta below 2 GeV/c.

An identified hadron candidate is assumed to lie within the boundaries of the PID ellipse (3σ around the nominal position for a given particle specie) in the $dE/dx - M^2$ space . In addition, the probability for a given particle to belong to each of the species can be calculated knowing the widths of the corresponding distributions (along the dE/dx and M^2 axes) and the difference from the predicted position for the specie. It was found that by requiring this probability to be greater than 0.75 one can obtain high PID efficiency and low contamination.

3 Simulations: event generator, data sets and results

The software framework for the MPD experiment (MpdRoot [7]) is based on FairRoot and provides a powerful tool for detector performance studies, development of algorithms for reconstruction and physics analysis of the data [2]. The event samples used for the present study were produced with the UrQMD [8] generator at $\sqrt{s} = 9$A GeV.

Produced by the event generators particles have been transported through the detector using the GEANT3 transport package (describing particle decays, secondary interactions, etc.).

Multistrange hyperons were reconstructed using their decay modes into a charged particle and a Λ hyperon followed by Λ decay into a proton and a pion. The event topology (decay of a relatively long-lived particle into two particles) defines the selection criteria: relatively large distance of the closest approach (DCA) to the primary vertex of decay products, small track-to-track separation in the decay vertex, relatively large decay length of the mother particle. Moreover, both the DCA and two-track separation cuts should be more efficient if applied in χ^2 - space, i.e if normalized to their respective errors.

For $\Xi^{\pm}$ ($\Omega^{\pm}$) Λ-candidates in the invariant mass interval $\pm 3\sigma$ around the peak position were combined with negative pions (kaons) to form $\Xi^{\pm}$ ($\Omega^{\pm}$)-candidates. In the selection procedure, additional acceptance cuts were introduced to find the significance maximum for this cascade decay topology.

The results for hyperon simulations (Figs. 2-4) have been obtained for 10^4 to $5 \cdot 10^5$ central events, corresponding to about 30 seconds - 28 minutes of running time at the NICA collision rate of 6 kHz [9].

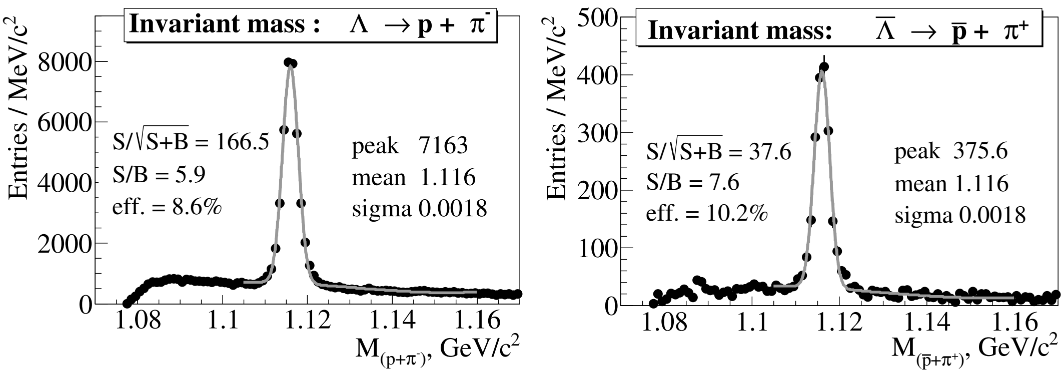

Figure 2: Reconstructed invariant mass of proton (antiproton) and π^- (π^+).

During the selection procedure we observed a large drop in the overall reconstruction efficiency when the low-p_T cut-off of decay products was increased from 0.1 to 0.2 GeV/c. Therefore, keeping the MPD detector ability of reconstructing very low momentum particles (at least, down to $p_T = 0.1$ GeV/c - see left panel of Fig. 1) is of crucial importance for measurements of multistrange hyperons.

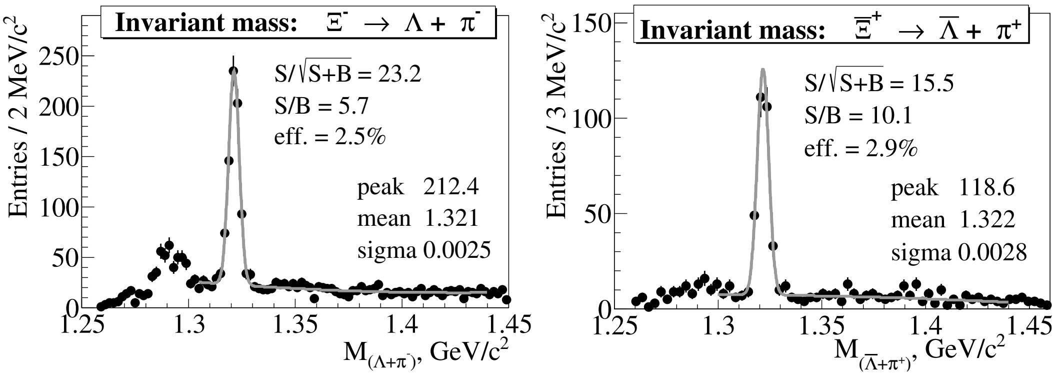

Figure 3: Reconstructed invariant mass of Λ ($\bar{\Lambda}$) candidate and π^- (π^+).

In conclusion we can mention that the current design of the MPD/NICA detector will make it possible to reconstruct (multi)strange hyperons in central Au+Au collisions with the invariant mass resolution of $\lesssim$3.5 MeV/c^2, efficiency above 1% and signal-to-background ratio $S/B \gtrsim 6$.

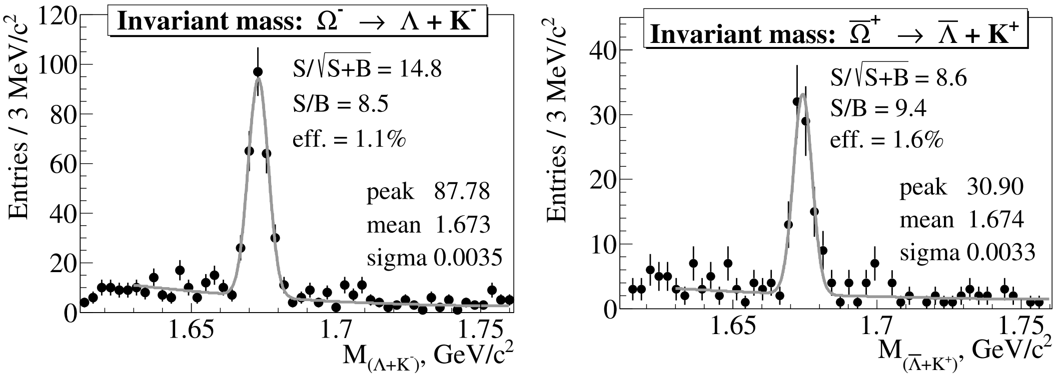

Figure 4: Reconstructed invariant mass of Λ ($\bar{\Lambda}$) candidate and K^- (K^+).

References

[1] J. Rafelski and B. Mulle, Phys. Rev. Lett. **48** 1066 (1982).

[2] K. U. Abraamyan et al., Nucl. Instrum. Meth. **A628** 99 (2011).

[3] http://nica.jinr.ru/files/CDR_MPD/MPD_CDR_en.pdf.

[4] A. Zinchenko, these Proceedings.

[5] R. Fruehwirth, Nucl. Instr. and Meth. **A262** 444 (1987).

[6] R. Luchsinger and Ch. Grab, Comp. Phys. Comm., **76** 263 (1993).

[7] http://mpd.jinr.ru/.

[8] http://urqmd.org/.

[9] http://nica.jinr.ru.

Study of Tin-Silver Solder Ball Bump Bonded Hybrid Silicon Pixel Detector

S. Arab[1], *S. Choudhury*[1], *G. Dolinska*[1], *E. Garutti*[2], *K. Hansen*[1], *M. Hoffmann*[2], *I. Korol*[1], *H. Perrey*[1], *D. Pitzl*[1], *J. Pöhlsen*[2], *V. Sola*[2], *S. Spannagel*[1], *G. Steinbrück*[2]

[1]Deutsches Elektronen-Synchrotron DESY - Hamburg, Germany
[2]University of Hamburg, Germany

DOI: http://dx.doi.org/10.3204/DESY-PROC-2014-04/45

For the connection of front-end readout chips to a silicon sensor of a hybrid pixel detector an in-house flip-chip bump bonding process using precision tin-silver solder balls has been implemented at DESY. The electrical testing of the bump connections follows immediately using an automated probe station by sensing a capacitively induced charge. The bump bonding quality and results from thermal stress testing has been reported. The pixel detector modules have been evaluated in the DESY electron test beam in terms of tracking efficiency and position resolution which has been summarized.

1 Introduction

The process of bump bonding of the silicon sensor to the front-end readout electronics is defining step in the fabrication of a hybrid pixel detector and the procedure of pixel detector module production at DESY with bump bonding of the front-end readout chip to the silicon sensor and quality tests of the bump bond by electrical method and radioactive source have been outlined. The module has also been tested in the electron beam at DESY in terms of charge collection, noise, tracking efficiency and position resolution. The PSI designed and IBM fabricated front-end readout chip [1] measuring 150 x 100 μm^2 has been used to establish the process of high precision tin-silver solder ball bump bonding at DESY to the silicon sensor [2] fabricated from 285 μm thick silicon. The pixels are arranged in an array of 52 columns and 80 rows in a single read-out chip with a double column readout structure for data and time stamp buffers. The new readout chip is an evolution of the one used for the present detector with lower charge thresholds and increased readout link speeds with higher time stamp and data buffer sizes and Fast Input Fast Output (FIFO) buffer. The sensor technology remains the same with n$^+$ in n substrate as the collection of electrons is advantageous because of their higher mobility compared to holes, which causes a larger Lorentz drift of the signal charges. This drift leads to charge sharing between neighbouring pixels and thus improves the spatial resolution. Furthermore, the higher mobility of electrons makes them less prone to trapping, which leads to a higher signal charge after high fluences of charged particles. After irradiation induced space charge sign inversion, the highest electric field in the sensor is located close to the n$^+$ electrodes used to collect the charge, which is also an advantage. The choice of n-substrate requires a double sided sensor process, meaning that both sides of the sensor need photo-lithographic processing. The double sided sensors have a guard ring scheme where all sensor edges are at a ground potential, which greatly simplifies the design of detector modules which ensures a high signal charge at moderate bias voltages ($\leq$ 600 V) after high hadron fluences. The n-side isolation is implemented through a moderated p-spray technique with a punch through biasing grid. The sensor wafer sample in this study has been obtained from PSI which were processed on approximately 285 μm thick n-doped diffusion oxygenated float zone silicon.

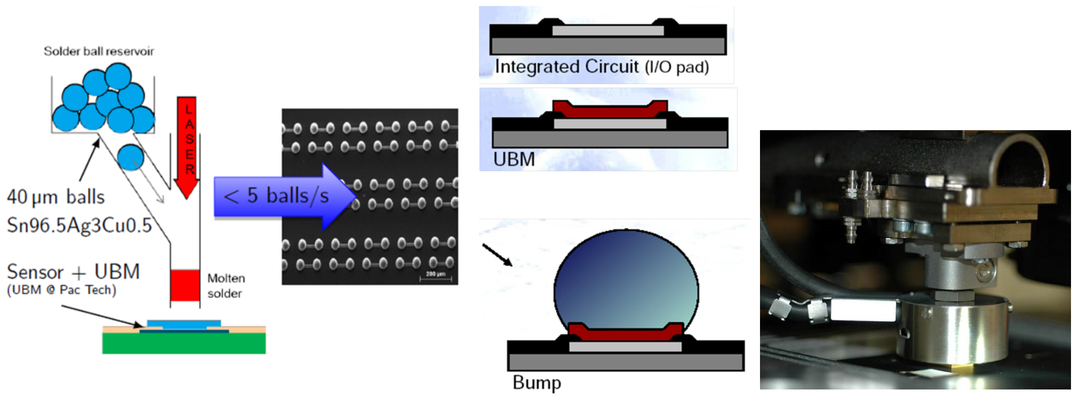

Figure 1: The bump bonding process with the solder ball deposition from SB^2 laser jetting system and the Femto flip-chip bonder for the connection of the sensor and readout chip.

2 Sn-Ag Solder Ball Bump Bonding at DESY

The bump bonding process remains a crucial and the most expensive step towards production of a silicon pixel detecor module and this process has been assembled at DESY with a SB^2 laser jetting system [3] and flip chip bonder [4] to make high precision tin-silver solder ball connections of the readout chip to the silicon sensor.

2.1 Bump Bonding Technique

The bump bonding process can be divided into 3 steps: under-bump metal (UBM) composed of Ni-Pd-Au deposition, solder sphere deposition, and flip chip bonding with re-flow soldering followed by the bare module electrical tests. This is done using an SB^2 step motor controlled bump deposition machine from PacTech. Solder balls of 40 μm diameter with a composition of 96.5% Sn, 3% Ag and 0.5% Cu are dropped though a capillary, molten by a laser and then placed onto the bump pad of the sensors where they solidify. The step-motor places the solder balls with a rate just below 5 Hz, which results in approximately 5 h bump deposition time per sensor with a 16-chip assembly. The next step is the bonding of the sensor onto the read-out chip using a Finetech Femto flip-chip bonder, to form the mechanical and electrical connection. The electronics wafers are thinned by back grinding and the sensor and electronics wafer are cut to get the sensor tiles and the front-end chips. The readout chip is aligned on the sensor tile in such a way that the front-end bumps face the relative sensor bump pads. The tuning of the process parameters has been performed using glass substrates in order to better investigate the effects on bumps by simple inspection under microscope. The chosen mating pressure is 160 N/chip, applied on the wafers heated around the melting point of tin at 240°C in a formic acid atmosphere. The resulting bump height after the flip-chip bonding process is 26 μm (reduced from 40 μm diameter solder ball).

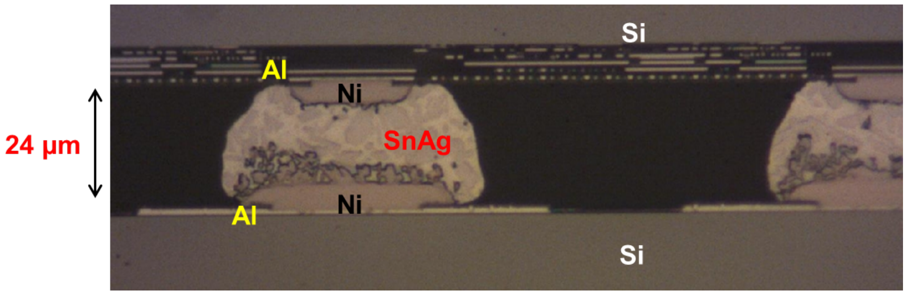

Figure 2: The side view of the bump bonds with the nodule cut across vertically and polished to examine under microscope.

2.2 Test of Bump Bonding Quality

To test that the front-end readout chip is performing as expected, scans of the analog response is carried out. The sensor is kept at a bias voltage of -100 V. A charge is injected into each pixel 10 times and the response recorded. The result should equal 10 and should have a uniform output for a perfect chip, and the result is as expected for 4160 pixels in the single chip module. This is termed as the “pixel alive test” which is to demonstrate the fully functional pixels in the module. The next step is electrical testing of the quality of the bumps and this is done by charge pulses and inducing the charge capacitively directly through the air capacitance between the readout chip and the sensor and then reading out the analog pulse height through the sensor and subsequently bump bonds. In case of missing bumps, the pulse height distribution would be at zero and if the pulse is read through good bumps, then this would be seen at positive values. The pulse height map is shown in Figure 3 with 2 missing bumps at the top left corner (row 0 col 78, row 0 col 79) and 4158 perfect bonds well separated and at positive values. This test is reconfirmed with a radioactive β-ray source. A ^{90}Sr source has been used for inducing signals in the sensor. The β-spectrum of the daughter decay of ^{90}Y has an endpoint energy of about 2.3 MeV and therefore contains particles which approximate a minimum ionising particle. From the hit map, 2 missing bonds can be seen at the top left edge of the module thereby confirming the validity of the electrical testing.
The module is then subjected to several thermal stress cycles from temperature -17°C to +25°C back and forth over a span of one week. The bump bonding test is performed before the start of the the thermal stress cycle and then at the end of each high and low temperature cycle and finally at the end of the cycle, and all tests show the same result as had been obtained previously in Figure 3 showing that the connections are intact and no dislocation of the bumps have taken place due to the thermal stress. The thermal stress cycle establishes the strenghth of the solder ball bump connections and its ability to withstand temperature fluctuations.

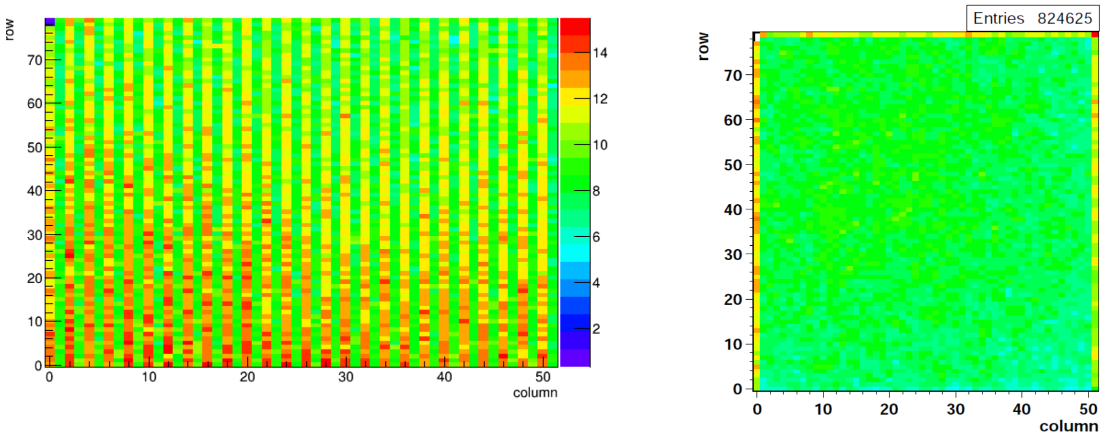

Figure 3: The pulse height map for bump bonding test from capacitively induced charge across the sensor through the air gap capacitor between readout chip and sensor (on left) and the hit map from a β-ray ^{90}Sr source for confirmation of the bump bonding electrical test (on right).

3 Beam Test Studies in DESY Electron Beam

New detectors are required to be tested in an environment similar to that in which they will be exposed in order to determine the performance. A beam test, where the device is read out within a beam of particles, is preferable to using a radioactive source in a laboratory since the statistics will be much higher. The particle type and energy is usually well known within a beam test, however the exact position of a particle at any given time is difficult to determine. Therefore, a set of well understood detectors known as a telescope is used in beam test experiments to track the charged particles. These tracks can be reconstructed offline to evaluate the efficiency and charge sharing performance of the devices under test for various parameters such as the tilt angle, threshold or bias voltage.

3.1 Test Beam Experimental Setup at DESY

The data studied in this analysis was taken at the DESY electron beam with the EUDET pixel telescope having 6 planes of Mimosa 26 sensor developed for ILC [5] with the pixel device under test midway and a reference pixel for timing reference mounted at the end of the beam line. The DESY synchrotron accelerates electrons and then a carbon fibre placed in the beam line produces photons through bremsstrahlung radiation. These photons impact a metal plate which converts them to pairs of electron and positron. A dipole magnet spreads the beam out as a function of the sign and energy. The desired beam energy within the range of 1-6 GeV is chosen with a collimator. The beam line has been configured to provide 5.2 to 5.6 GeV electrons. The beam size is approximately 3 cm (FWHM) and the beam intensity has been tuned to 1 kHz/cm^2. The EUDET telescope [6, 7] consists of two arms each equipped with three sensors. The positions of the sensors along the beam axis can be adapted to the respective requirements. Between the two arms optional mechanical x-y support stage that allows to position the Pixel Device Under Test (DUT) and Reference Pixel (REF) with a few micron precision is installed. Since the telescope is read out at a rate of 112 μs in a rolling shutter mode and the DUTs are read out every 400 ns, the reference sensor is primarily there to

determine if a hit on the DUT is registered thus serving as a timing reference. The sensors are read out by dedicated data-reduction boards that transfer their data to a computer where the data acquisition software is running. A trigger system including four scintillators connected to photomultiplier tubes allows to trigger on particles passing the telescope. For this, two pairs of scintillators (1x2 cm^2), each pair perpendicular to each other, are located in coincidence either side of the telescope to trigger on the incident particles.
The Mimosa sensors typically provide a signal-to-noise ratio for minimum ionising particles (MIPs) of 20-40 and a detection efficiency for MIPs of $> 99\%$ depending on the thresholds. The Mimosa 26 sensor is a combination of the Mimosa 22 sensor [8] and the SuZe01 chip [9] that performs online data sparsification. The sensor is subdivided into 1152 columns of 576 pixels with a pitch of 18.4 μm providing a high granularity. The sensitive area of the sensors is approximately 21 x 10.6 mm^2. On each pixel an amplification and CDS circuit is implemented. The sensor is read out in a column-parallel mode with a pixel-readout frequency of 80 MHz which results in a integration time of about 112 μs. Each column is equipped with a discriminator that performs an offset compensation and a second column double sampling.

3.2 Readout Chip Characterization and Data Acquisition

A threshold setting is required for the front-end card to limit the noise recorded from the module. The output from a threshold scan for the pixel device is tuned to 3100 electrons which is important for charge sharing and influences position resolution and efficiency after irradiation. The measured noise is 160 electrons obtained from the width of the threshold curve. There is a higher level of noise for a lower threshold tuning. The noise for the SnAg bump bonded pixel modules at DESY is similar to Indium bump bonded pixel modules at PSI with the same readout chip.
The data acquisition system is the one for EUDET pixel telescope with a flexible data acquisition software (EUDAQ) [10, 11, 12] for testing the pixel module with the MIMOSA sensors of the telescope system for track interpolation and extrapolation to the DUT. The hardware of the telescope and of the connected DUTs is read out by separate producer tasks that are connected to the "run control" and the "data collector". The latter receives the data streams, builds the events and stores the data on the storage device. The "log collector" provides an interface for the producers for the collection of logging messages. One part of the EUDAQ software is the online-monitoring system (RootMonitor) that makes use of the object-oriented data analysis framework ROOT [13] implemented in C++. The RootMonitor can be used together with the EUDAQ system during data taking as well as a stand-alone application reading and analysing raw data files. The RootMonitor is able to handle different sensor types for the various telescope planes. It provides a simple fixed-frame cluster reconstruction algorithm. Seed pixel candidates are identified and starting from the pixel with the highest signal-to-noise ratio clusters are constructed by joining neighbouring pixel to the cluster if certain thresholds are fulfilled. Thus it starts from one hit candidate and then assigns all 8 neighbouring hit pixels to the cluster. This procedure is repeated until all hit pixel are joined into clusters. The cluster position is reconstructed in the RootMonitor by determining the centre-of-gravity for each cluster which is a signal-weighted average of the pixel positions belonging to the cluster.

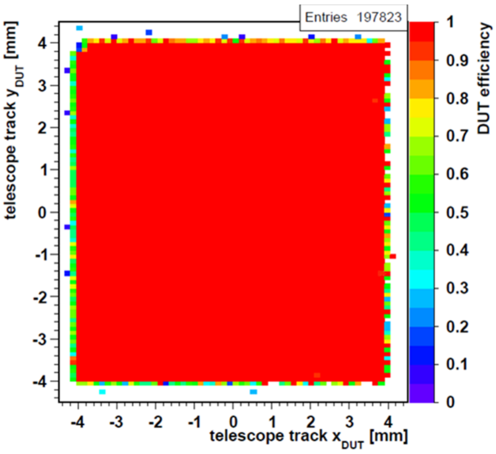

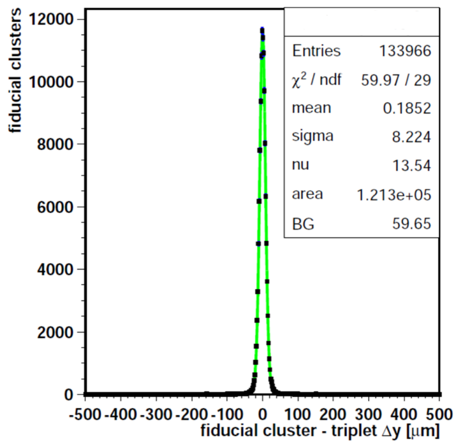

Figure 4: The map of tracking efficiency in a single-chip module (on left) and the position resolution with a fit to Gaussian (on right).

3.3 Test Beam Measurements and Data Analysis

The offline analysis software (EUTelescope) [14, 15] for the telescope data is based on Marlin [16, 17, 18] and Linear Collider In / Out (LCIO) [19, 20]. The EUTelescope software makes use of the Marlin analysis framework which divides the analysis in several individual small tasks. The behaviour of these processors can be controlled with steering files. The data is stored in the LCIO format which was developed to provide a persistent data model and interface. The pedestal and noise information are determined and hit pixels are grouped into clusters by applying a loose selection and quality criteria. The cluster coordinates are transformed from the local reference frame to the global telescope reference frame using the geometry description provided by the GEAR [21] package. After determining the alignment constants of the individual planes, the fitter reconstructs tracks using this collection of corrected hits. These tracks can be used for an extrapolation to the DUT surface in order to determine the predicted positions of hits in the DUT plane. For all hit pixels the number of neighbouring hit pixels is determined, whereas diagonal neighbours are ignored. The list of hit pixels obtained in the previous step is sorted with decreasing neighbours in order to determine the seed candidates. For pairs of pixel with equal number of neighbours, the pixel with the larger number of diagonal neighbours is preferred. The resulting list is processed starting from the seed candidate with the highest number of neighbours. All hit pixels in a fixed x-y frame around the seed pixel are merged into the cluster and removed from the pixel collection and from the list of seed candidates.
In order to be able to reconstruct tracks with the telescope and to extrapolate these tracks to the DUT plane, the geometrical positions of the sensor planes have to be known with high precision. Beam particles passing the telescope planes create clusters in the sensors which are spatially correlated between the individual planes. The EUTelescope software packages provides a processor (EuTelMille) that uses MILLEPEDE [22, 23] for the determination of the alignment constants in order to reduce the bias and the uncertainty of the fitted track parameters and to minimize the χ^2 of the tracks. Each parametrisation of a track depends on local parameters that vary between the tracks and on global parameters - the alignment constants. The processor

EuTelMille takes as an input a collection of hits and then for all combination of hits straight lines are fitted to these groups of hits independently in x and y direction. In order to suppress fake tracks resulting from combinatoric background, cuts on the residual distributions for all sensor planes can be specified in the corresponding steering file. The derivatives of the tracks with respect to all local and global parameters are stored in a binary file that can be read by Millepede. The Millepede software determines in a simultaneous linear least-squares fit of all local and global track parameters the alignment constants for the sensor planes.
Charge sharing improves track position resolution, but charge that is shared between two (or more) neighbouring pixels reduces the charge each pixels receives. This increases the likelihood that the charge per pixel is below threshold, but this is done away with a low charge threshold. Charge sharing will increase when the sensor is tilted, since particle tracks will pass through multiple pixels. The coordinate measured by a pixel detector is obtained by the position of the centre of the cluster of hit pixels associated with a track, plus a correction (conventionally called the η function) which is a function of the charge sharing, the cluster width and the track angle. The position resolution is calculated by comparing the track position interpolated by the telescope planes and the pixel hit position calculated using charge sharing between rows. The difference of this distribution which is termed as the residual is fitted to a Gaussian. The residuals are calculated separately for x and y and are the difference between the position of the reconstructed track and the position of the cluster centre. The Gaussian shape is due to charge sharing at the edge of the pixels and is wider with increase in multiple scattering. The best position resolution of 7.0 μm for the lower threshold of 1.8 ke is reached at the angle where optimal charge sharing between neighboring pixels occurs, that is where the particles most likely traverse two pixel cells. This optimal angle is determined by the pixel geometry from inverse tangent of the ratio of pixel width in row direction to sensor thickness and is 19.3° along the row direction in which the pixels have a width of 100 μm and the sensor thickness being 285 μm. The position resolution of 7.0 μm is obtained from the residual width 8.2 μm in Figure 4, correcting for the telescope resolution of 4.3 μm.
The tracking efficiency for a pixel sensor is defined as the ratio of the number of measured hits close to a track, against the total hits predicted. These expected hits are determined using reconstructed tracks from the beam test. The tracks are extrapolated from the telescope hits to the DUT plane. To reduce fake tracks, a matching hit in the reference sensor is required. The tracking efficiency is thus defined as the ratio of the DUT hit linked to isolated telescope track with link to REF hit to all the isolated telescope tracks with link to REF hit. The isolation in the telescope track is required due to pileup in the telescope (3-5 tracks/event) which leads to confusion and random overlays at the REF plane. With the module tilted at 19.3°, the efficiency is 99.96% in the fiducial region as observed in Figure 4 and is also observed to remain constant with time. Finally, the test beam profile at vertical tracking incidence in Figure 5 reaffirms the electrical bump bonding test in the laboratory with the observed 2 missing bump connections.

4 Conclusion

The procedure for Femto flip-chip bump bonding with a SB^2-Jet (Laser Solder Jetting System) using high pecision Sn-Ag solder balls to connect the read-out chip to the silicon sensor has been successfully implemented at DESY for production of a hybrid silicon pixel detector. The SB^2 solder ball jetter places the Sn-Ag bumps at a rate of 4.5 Hz and then a flip chip bonder makes

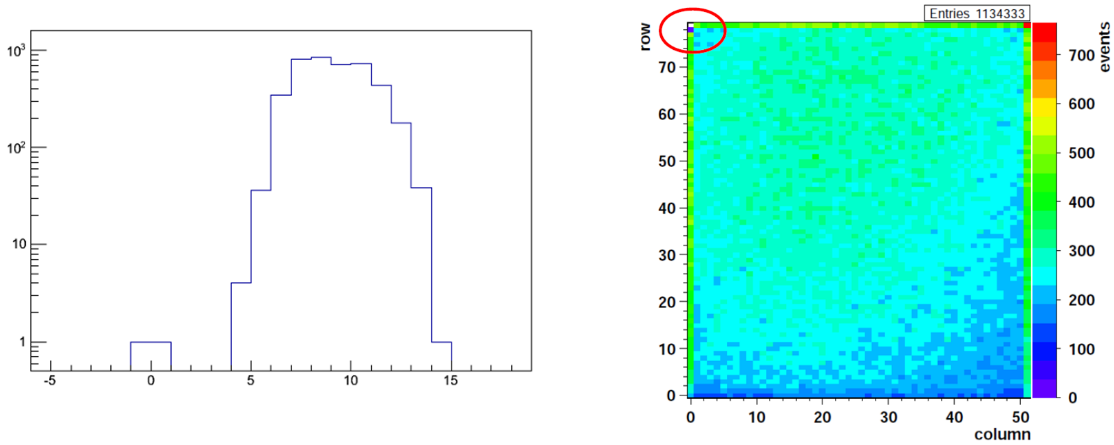

Figure 5: The pulse height distribution from capacitively induced charge across the sensor through the air gap capacitor between readout chip and sensor showing bump bonding test (on left) and the test beam profile shown at vertical incidence to reaffirm the bump bonding electrical test (on right).

the connection at 240°C with 160 N tacking force with re-flow in a formic acid atmosphere. The quality for the bump bonding has been tested electrically and with radioactive source in the laboratory and using the electron test beam at DESY and subsequently through several thermal stress cycles and the module quality is found to be excellent. The position resolution of the module is 7.0 μm with a tracking efficiency of up to 99.96% in the fiducial region for the optimum charge sharing tilt angle between pixels. In a similar way other high quality modules have been produced and tested at DESY successfully preparing the laboratory for the production of a silicon pixel detector.

Acknowledgments

The authors would like to thank the pixel detector group of Roland Horisberger at PSI for the front-end readout chip and sensor used for this study and the DESY accelerator personnel for the smooth and steady delivery of the test beam during the data taking periods.

References

[1] H. Chr. Kaestli et. al., "Design and performance of the CMS pixel detector readout chip", Nucl. Instr. Meth. A 565, 188 (2006).

[2] T. Rohe et. al., "Planar sensors for the upgrade of the CMS pixel detector", Nucl. Instr. Meth. A 650, 136 (2011).

[3] PacTech - Solder Jetting & Solder Deballing and Reballing, URL *http://www.pactech.com/index.php?option=com_content&view=article&id=16&Itemid=6.*

[4] FineTech - Femto Flip-Chip Bonder, URL *http://eu.finetech.de/products/micro-assembly/fineplacerr-femto.html.*

[5] J. Brau, Y. Okada and N. Walker (Ed.) et. al., "ILC Reference Design Report Volume 1 - Executive Summary", arXiv:0712.1950 [physics.acc-ph].

[6] D. Haas, "The EUDET High Resolution Pixel Telescope - Towards the Final Telescope", EUDET-Report-2008-02, 2008.

[7] L. Reuen and J. Furletova, "JRA1 - The DEPFET sensor as the first fully integrated DUT in the EUDET pixel telescope: The SPS test beam 2008", EUDET-Memo-2008-34, 2008.

[8] G. Claus et. al., "JRA1 Milestone IDC Prototype ready", EUDET-Memo-2008-03, 2008.

[9] A. Himmi et. al., "A Zero Suppression Micro-Circuit for Binary Readout CMOS Monolithic Sensors", Proceedings of TWEPP-09: Topical Workshop on Electronics for Particle Physics, Paris (France), pg. 426-430, 2009.

[10] M. Pohl, D. Haas and E. Corrin, "JRA1 - Data acquisition system", EUDET-Memo-2006-07, 2006.

[11] D. Haas, "The DAQ for the EUDET pixel telescope", Proceedings of 2007 International Linear Collider Workshop (LCWS07 and ILC07), Hamburg (Germany).

[12] E. Corrin, "EUDAQ Software User Manual", EUDET-Memo-2010-01, 2010.

[13] R. Brun and F. Rademakers, "ROOT: An object oriented data analysis framework", Nucl. Instr. Meth. A 389, 81 (1997).

[14] A. Bulgheroni et. al., "Eutelescope: tracking software", EUDET-Memo-2007-20, 2007.

[15] A. Bulgheroni et. al., "EuTelescope - the JRA1 tracking and reconstruction software: a status report (Milestone)", EUDET-Memo-2008-48, 2008.

[16] F. Gaede, "Marlin and LCCD: Software tools for the ILC", Nucl. Instrum. Meth. A 559, 177 (2006).

[17] "Marlin". URL *http://ilcsoft.desy.de/portal/software_packages/*.

[18] J. Engels and F. Gaende, "Marlin - A Software Framework for ILC detector R&D", EUDET-Report-2007-11, 2007.

[19] F. Gaede et. al., "LCIO: A persistency framework for linear collider simulation studies", arXiv: physics/0306114.

[20] "LCIO", URL *http://lcio.desy.de/*.

[21] "GEAR - A geometry description toolkit for ILC reconstruction software". URL *http://ilcsoft.desy.de/portal/software_packages/gear*.

[22] V. Blobel and C. Kleinwort, "A New Method for the High-Precision Alignment of Track Detectors", DESY-02-077 pg. 10, 2002.

[23] V. Blobel, "Millepede", URL *http://www.desy.de/ blobel*.

Chapter 14

Poster contributions

Measurement of Drell-Yan and associated jet cross section at low and high invariant masses

Samantha Dooling[1]

[1]DESY, Notketraße 85, 22607 Hamburg, Germany
on behalf of the CMS Collaboration

DOI: http://dx.doi.org/10.3204/DESY-PROC-2014-04/281

The first measurement of the Drell-Yan and associated jet cross section as a function of the Drell-Yan mass is presented using an integrated luminosity of 4.9 fb^{-1} in the di-muon channel of proton-proton collisions recorded with the CMS detector. Cross Sections as a function of the Drell-Yan transverse momentum are measured differentially in the Drell-Yan mass. The p_{T} spectrum of the Drell-Yan allows to study multiple-gluon emissions and resummation effects.

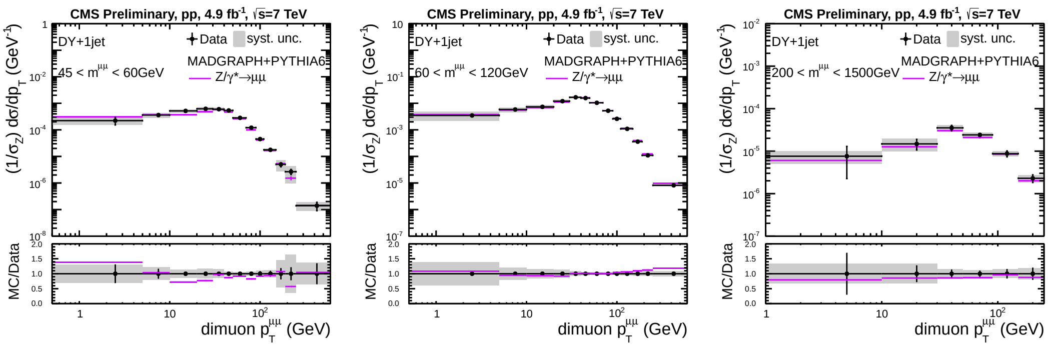

Figure 1: Di-muon p_{T} distribution at low and high invariant masses for DY+1 jet production. Corrected data is compared to MC predictions.

The production of Drell-Yan (DY) lepton pairs in hadron-hadron collisions is a suitable process to study the effect of the soft-gluon resummation in perturbative quantum chromodynamics (pQCD). While DY lepton pair production at large transverse momenta can be described by fixed order calculations in pQCD, at small p_{T} resummation of soft gluons to all orders in perturbation theory is required [1].

The detailed measurements of inclusive DY lepton pair production as well as DY lepton pair production in association with jets, especially in the mass range above the Z mass (and in the range of $m^{\mu\mu} \sim 125$ GeV), is important for a later comparison with Higgs production, which can be used to determine the differences of soft gluon and multi-jet resummation in a quark or gluon induced process [2].

The p_{T} spectrum of the DY lepton pair is of special interest to test contributions from perturbative multi-gluon resummation. In the case of the inclusive DY production the maximum of the DY p_{T} distribution is around 5 GeV. When requiring DY in association with additional jets the maximum shifts to higher p_{T} and the phase space for multi-gluon emissions is enlarged. In Fig. 1 the comparison of DY production and at least one jet above a p_{T} of 30 GeV is shown. The first measurement of the differential DY and associated jets cross section as a function of the DY di-muon mass is presented in [3]. The di-muon p_{T} distribution for DY+1 jet production in the invariant mass regions of 45-60, 60-120, and 200-1500 GeV is presented. The corrected data points are compared to matrix element plus parton shower predictions. The MC generator MADGRAPH+PYTHIA6 is used. MADGRAPH produces the DY boson with maximum four hard partons in the matrix element calculation at leading-order. The underlying event and parton shower is generated by PYTHIA6 using the tune Z2*. The comparison to data presents a good agreement over the whole phase space.

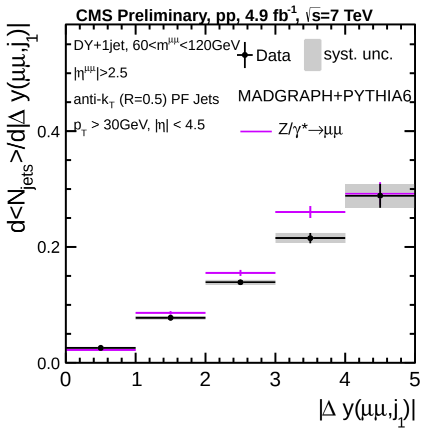

Figure 2: Average jet multiplicity as a function of the rapidity separation between the leading jet and the forward DY production.

Multi-jet emissions in a rapidity interval between the DY pair and the leading jet is a sensitive probe for multi-gluon emissions. The average jet multiplicity of jets with $p_{\mathrm{T}} > 30$ GeV between the leading jet and the forward DY production ($|\eta^{\mu\mu}| > 2.5$) as a function of the rapidity separation $|\Delta y(\mu\mu, \mathrm{j})|$ is presented in Fig. 2. The average jet multiplicity increases with increasing separation between the DY lepton pair and the leading jet from 0 to 0.3 at large rapidity separation. The general behaviour is reproduced by MADGRAPH simulation.

Acknowledgements

I am grateful to the PANIC organizers and staff for the invitation to an exciting conference. I want to thank all PANIC participants for a nice atmosphere and interesting discussions.

References

[1] Dokshitzer, Y. L. and Diakonov, D. and Troian, S. I., Phys. Lett. B**79** (1978) 269, Collins, J. C. and Soper, D. E. and Sterman, G. F., Nucl. Phys. B**250** (1985) 199.

[2] Cipriano, P. and Dooling, S. and Grebenyuk, A. and Gunnellini, P. and Hautmann, F. and Jung, H. and Katsas, P., Phys. Rev. D**88** (2013) 097501.

[3] CMS Collaboration, CMS-PAS-FSQ-13-003, "Measurement of the double differential Drell-Yan and associated jet cross sections at low and high invariant masses in proton-proton collisions at $\sqrt{s} = 7$ TeV", http://cds.cern.ch/record/1670353 (2014).

Hadroproduction of electroweak gauge boson plus jets and TMD parton density functions

Samantha Dooling[1]

[1]DESY, Notketraße 85, 22607 Hamburg, Germany

DOI: http://dx.doi.org/10.3204/DESY-PROC-2014-04/282

If the production of electroweak gauge bosons final states is sensitive to effects of the initial state's transverse momentum distribution, appropriate generalizations of QCD shower evolution are required. We propose a method to treat these effects based on QCD transverse momentum dependent (TMD) factorization at high energy. We illustrate the approach presenting results for production of W-boson + n jets at the LHC.

The approach of collinear factorization, which separates the long-distance terms and the short-distance contributions in the cross section calculation in the collinear approximation, is very successful for sufficiently inclusive observables. However, for more exclusive observables, like e.g. the boson transverse momentum $p_\perp$, the cross section also depends on the scale $p_\perp$. It is necessary to include consistently $p_\perp$ effects already at the beginning of the calculation, which were neglected in the traditional approaches.

We propose an approach to electroweak boson plus jets production, which takes into account dynamical and kinematical issues via transverse momentum dependent (TMD) QCD evolution equations, with corresponding parton density functions and perturbative matrix elements. Traditional approaches have focused on the boson spectrum in the low-$p_\perp$ Sudakov region, and on the treatment of large logarithms for transverse momenta small compared to the boson invariant mass. Our work treats physical effects which persist at high $p_\perp$ and can affect final states with high jet multiplicities.

We use the transverse momentum dependent QCD factorization [1], which is valid up to arbitrarily large $p_\perp$. We couple this with CCFM [2] evolution equations for TMD gluon and valence quark densities using the results recently obtained in [3]. Using the parton branching Monte Carlo implementation of TMD evolution developed in [3] we make predictions, including uncertainties, for final-state observables associated with W-boson production. We study jet transverse momentum spectra and azimuthal correlations. We use the TMD distribution set JH-2013-set2 [3]. We compare the results to the measurements of ATLAS ($|\eta^{\text{jet}}| < 4.4$) and CMS ($|\eta^{\text{jet}}| < 2.4$). The uncertainties on the predictions are determined according to the method [3].

Figure 1 (top) shows the total transverse energy distribution H_{T} for production of W-boson + ≥ 1 jets, with $p_{\text{T}}^{\text{jet}} > 30$ GeV. In Fig. 1 (middle) we present the $p_\perp$ spectrum of the third jet associated with W production. It is observed that the detailed shapes of the subleading jets can be described by the TMD formalism. In Fig. 1 (bottom) the angular correlation in azimuthal separation between the third jet and the W-boson. Predictions of the structure of angular correlations are a distinctive feature of the TMD exclusive formulation. The shape of the experimental measurements is well described, within the theoretical uncertainties, both at large $\Delta\phi$ and down to the decorrelated, small-$\Delta\phi$ region.

In conclusion, this work shows how TMD evolution equations at high energies can be used to take into account QCD contributions to the production of electroweak bosons plus multi-jets due to finite-angle soft gluon radiation, and estimate the associated theoretical uncertainties. This will be relevant both to precision studies of Standard Model physics and to new physics searches for which vector boson plus jets are an important background.

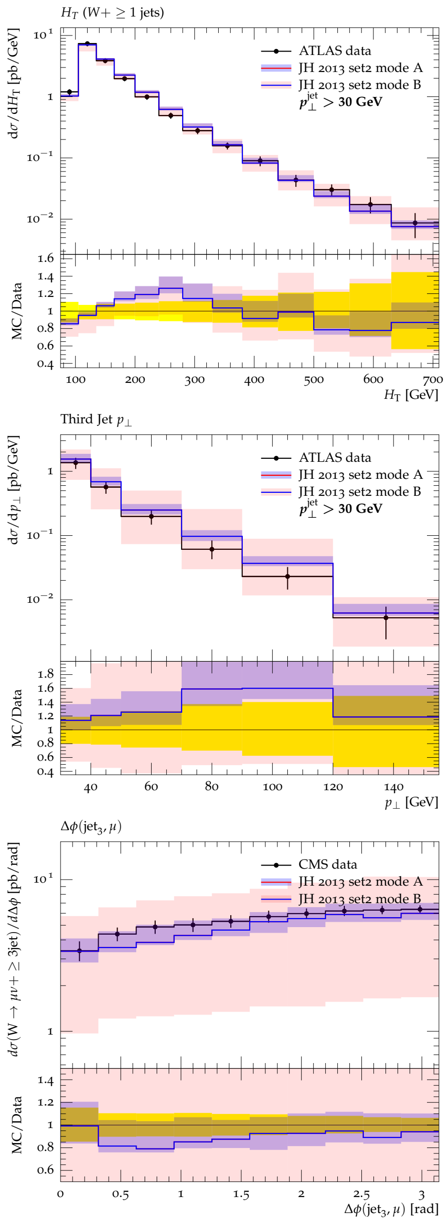

Figure 1: Total transverse energy H_T, third jet $p_\perp$, and angular correlation in final states with W-boson + jets at the LHC.

Acknowledgements

We are grateful to the PANIC organizers and staff for the invitation to an exciting conference. We want to thank all PANIC participants for a nice atmosphere and interesting discussions.

References

[1] S. Catani, M. Ciafaloni and F. Hautmann, Phys. Lett. B242 (1990) 97; Nucl. Phys. B366 (1991) 135; Phys. Lett. B307 (1993) 147; S. Catani and F. Hautmann, Phys. Lett. B315 (1993) 157; Nucl. Phys. B427 (1994) 475

[2] M. Ciafaloni, Nucl. Phys. B296 (1988) 49, S. Catani, F. Fiorani and G. Marchesini, Nucl. Phys. B336 (1990) 18, G. Marchesini, Nucl. Phys. B445 (1995) 49.

[3] F. Hautmann and H. Jung, Nucl. Phys. B883 (2014) 1

[4] S. Dooling, F. Hautmann and H. Jung, Physics Letters B736 (2014) 293

The Z' Boson of the Minimal $B - L$ Model as a Higgs Boson Factory

A. Gutiérrez-Rodríguez

Facultad de Física, Universidad Autónoma de Zacatecas
Apartado Postal C-580, 98060 Zacatecas, México.

DOI: http://dx.doi.org/10.3204/DESY-PROC-2014-04/20

We study the Higgs boson production in the minimal $B - L$ model at the future linear colliders ILC and CLIC, with the reactions $e^+e^- \to (Z, Z') \to Zh$. We evaluate the total cross section of Zh considering the complete set of Feynman diagrams at tree level.

1 Introduction

The existence of a heavy neutral (Z') vector boson is a feature of many extensions of the Standard Model (SM). In particular, one (or more) additional $U(1)'$ gauge group provides one of the simplest extensions of the SM. Additional Z' gauge bosons appear in Grand Unified Theories (GUTs) [1], Superstring Theories [2], Left-Right Symmetric Models (LRSM) [3] and in other models such as models of composite gauge bosons [4]. In particular, it is possible to study some phenomenological features associated with this extra neutral gauge boson by considering a minimal $B - L$ (baryon number minus lepton number) model.

The $B - L$ symmetry plays an important role in various physics scenarios beyond the SM: Firstly, the gauge $U(1)_{(B-L)}$ symmetry group is contained in a GUT described by a $SO(10)$ group [5]. Secondly, the scale of the $B-L$ symmetry breaking is related to the mass scale of the heavy right-handed Majorana neutrino mass terms providing the well-known see-saw mechanism [6] to explain light left-handed neutrino masses. Thirdly, the $B - L$ symmetry and the scale of its breaking are tightly conneted to the baryogenesis mechanism through leptogenesis [7] via sphaleron interactions preserving $B - L$.

The minimal $B - L$ model [8] is attractive due to its relatively simple theory structure, and the crucial test of the model is the detection of the new heavy neutral (Z') gauge boson. Analyses of precision electroweak measurements indicate that the new Z' gauge boson should be heavier than about 1.2 TeV [9]. On the other hand, recent bounds from the LHC indicate that the Z' gauge boson should be heavier than about 2 TeV [10], while future LHC runs at 13 TeV could increase the Z' mass bounds to higher values, or we may be lucky and find evidence for its presence. Further studies of the Z' properties will require a new linear collider [11], which will also allow us to perform precision studies of the Higgs sector. Detailed discussions on the minimal $B - L$ model can be found in the literature [8, 12].

It is possible to search for the Higgs boson from this model using the process of Higgstralung, a mechanism similar to the one used to search for the SM Higgs boson. However, the existence of a new heavy gauge bosons could also provide new Higgs production mechanisms, which could probe its non-standard origin. In this work, we are analyzing how the Z' gauge boson of the minimal $U_{(B-L)}$ model could be used as a factory of Higgs bosons.

Our aim in the present work is to analyze the Higgs production cross section from processes like $e^+e^- \to (Z, Z') \to Zh$ in the framework of the minimal $B - L$ model.

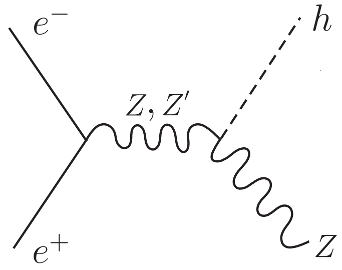

Figure 1: Feynman diagram for the process $e^+e^- \to Zh$ in the minimal $U(1)_{(B-L)}$ model.

2 The Total Cross section of the Process $e^+ + e^- \to Zh$

In this section, we calculated the Higgs production cross section via the process $e^+e^- \to Zh$ in the context of the minimal $U_{(B-L)}$ model at a future high-energy and high-luminosity linear electron-positron colliders, such as the ILC or CLIC.

The contributing Feynman diagram is shown in figure 1. The expression for the respective cross section in the context of the minimal $U(1)_{(B-L)}$ model is given by

$$\begin{aligned}
\sigma(e^+e^- \to Zh) &= \frac{\pi\alpha^2[(g^e_V)^2 + (g^e_A)^2]}{48 s x^2_W (1-x_W)(1-m^2_Z/s)^2}\sqrt{\lambda}[\lambda + 12 m^2_Z/s] \\
&+ \frac{[f(\theta')\cos\beta - g(\theta')\sin\beta]^2[(g'^{e}_V)^2 + (g'^{e}_A)^2]}{384\pi s(1-x_W)(1-m^2_{Z'}/s)^2}\sqrt{\lambda'}[\lambda' + 12 m^2_{Z'}/s] \\
&+ \frac{\alpha[f(\theta')\cos\beta - g(\theta')\sin\beta][g^e_V g'^{e}_V + g^e_A g'^{e}_A]}{24 s x_W(1-x_W)(1-m^2_Z/s)(1-m^2_{Z'}/s)}\sqrt{\lambda}[\lambda + 12 m^2_Z/s],
\end{aligned} \tag{1}$$

where

$$\begin{aligned}
\lambda &= (1 - x_Z - x_h)^2 - 4x_Z x_h, & \lambda' &= (1 - x_{Z'} - x_h)^2 - 4x_{Z'} x_h, \\
f(\theta') &= \sin 2\theta'\left(\frac{4m^2_Z}{v^2} - g^2_1\right) + \frac{4 g_1 m_Z}{v}\cos 2\theta', & g(\theta') &= \frac{4v'}{v} g^2_1 \sin 2\theta', \\
g^e_V &= \frac{1}{2}\cos\theta' + 2x_W\cos\theta' + \frac{2g'_1}{g}\cos\theta_W\sin\theta', & g^e_A &= \frac{1}{2}\cos\theta', \\
g'^{e}_V &= -\frac{1}{2}\sin\theta' + 2x_W\sin\theta' + \frac{2g'_1}{g}\cos\theta_W\cos\theta', & g'^{e}_A &= -\frac{1}{2}\sin\theta',
\end{aligned}$$

with $x_Z = m^2_Z/s$, $x_{Z'} = m^2_{Z'}/s$, $x_h = m^2_h/s$, $x_W = \sin^2\theta_W$, $\beta = \frac{\pi}{9}$, $v = 246$ GeV, $v' = 2000$ GeV.

The first term of equation 1 corresponds to the cross section from the process with the exchange of a Z boson, while the second and third term comes from the contribution of the minimal $U(1)_{(B-L)}$ model and of the interference respectively. The SM expression for the cross section of the reaction $e^+e^- \to Zh$ can be obtained when the mixing angle and the coupling constant are decoupled in the limited $\theta' = 0$ and $g_1' = 0$. In this case the terms that depend on θ' and g_1' in equation 1 are zero and the total expression is reduced to the one given in ref. [13] for the SM.

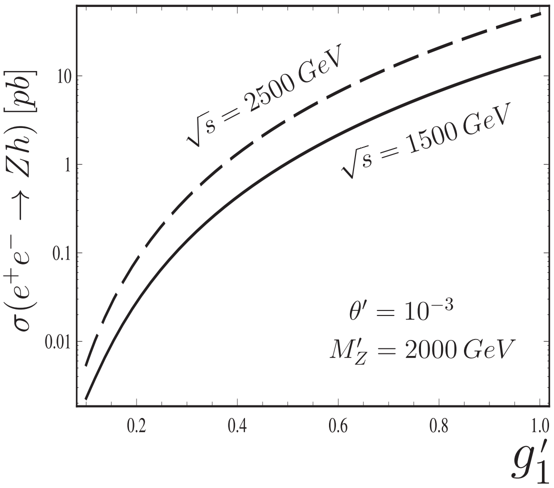

Figure 2: The total cross section for the process $e^+e^- \to Zh$ as a function of the coupling constant g_1'.

3 Results and Conclusions

Using the numerical values $\alpha = 1/128$, $x_W = \sin^2\theta_W = 0.2314$, $m_Z = 91.18$ GeV, $M_h = 125$ GeV, and $\Gamma_Z = 2.49$ GeV, we obtain the cross section $\sigma = \sigma(\sqrt{s}, m_{Z'}, \theta', g_1')$.

We plot the total cross section of the reaction $e^+e^- \to Zh$ in figure 2 as a function of the coupling constant g_1' for $m_{Z'} = 2000$ GeV and $\sqrt{s} = 1500, 2500$ GeV. We observed that the total cross section increases as g_1' increases.

In conclusion, we have analyzed the total cross section of the reaction $e^+e^- \to Zh$ in the context of the minimal $U(1)_{(B-L)}$ model with an additional heavy gauge boson at the high energies expected at the ILC and CLIC colliders. We observed an increase in the total cross section when g_1', the free parameter of the $U(1)_{(B-L)}$, increases.

Acknowledgments

We acknowledge the support received from the organizing committee of the 20th Particles & Nuclei International Conference (PANIC 14) Hamburg, Germany 2014. We also appreciate the support of PIFI (México).

References

[1] R. W. Robinett, *Phys. Rev.* **D26**, 2388 (1982).

[2] M. Green and J. Schwarz, *Phys. Lett.* **B149**, 117 (1984).

[3] R. N. Mohapatra and G. Senjanovic, *Phys. Rev. Lett.* **44**, 912 (1980).

[4] U. Baur, *et al.*, *Phys. Rev.* **D35**, 297 (1987).

[5] W. Buchmuller, C. Greub and P. Minkowski, *Phys. Lett.* **B267**, 395 (1991).

[6] R. N. Mohapatra and G. Senjanovic, *Phys. Rev. Lett.* **44**, 912 (1980).

[7] M. Fukugita and T. Yanagida, *Physics of Neutrinos and Applications to Astrophysics*, (Springer, Berlin, 2003).

[8] L. Basso, A. Belyaev, S. Moretti and C. H. Shepherd-Themistocleous, *Phys. Rev.* **D80**, 055030 (2009).

[9] P. Langacker, *Rev. Mod. Phys.* **81**, 1199178 (2009).

[10] S. Chatrchyan, *et al.*, *Phys. Rev.* **D87**, 114015 (2013).

[11] B. C. Allanach, *et al.,* arXiv: hep-ph/0403133.

[12] J. L. Díaz-Cruz, *et al.*, *J. Phys. G: Nucl. Part. Phys.* **40**, 125002 (2013).

[13] V.D. Barger, K.m. Cheung, A. Djouadi, B.A. Kniehl and P.M. Zerwas, *Phys. Rev.* **D49**, 79 (1994).

$1/N_c$ corrections to the baryon axial vector current in large-N_c chiral perturbation theory

María A. Hernández-Ruiz

Unidad de Ciencias Químicas, Universidad Autónoma de Zacatecas,
Apartado Postal 585, 98160, Zacatecas, México.

DOI: http://dx.doi.org/10.3204/DESY-PROC-2014-04/23

We study the effects of the decuplet-octet mass difference for the baryon axial vector current at one-loop order in large-N_c baryon chiral perturbation theory, where N_c is the number of color. The baryon axial vector current is considered within the combined framework of large-N_c baryon chiral perturbation theory and the baryon axial vector couplings are extracted. We extend the g_A analysis by including all effects that are suppressed by $1/N_c^2$ relative to the tree level value, which includes taking into account the nonvanshing decuplet-octet mass difference.

1 Introduction

The generalization of quantum chromodynamics (QCD) from $N_c = 3$ to $N_c \gg 3$ color charges, called large-N_c QCD, has opened a path to substantial progress in understanding strong interactions at both the formal and phenomenological levels. Formal successes spring from the fact that large-N_c QCD exhibits a well-defined limit, meaning that the renormalization group equations remain finite and nontrivial as $N_c \to \infty$. Phenomenological successes build on these formal $1/N_c$ power-counting results, but add one extra ingredient: Observables calculated to appear at relative orders $\mathcal{O}(1/N_c)$, $\mathcal{O}(1/N_c^2)$, and so on, which is precisely the origin of the $1/N_c$ expansion [1].

In the large-N_c limit a spin-flavor symmetry emerges for baryons and this symmetry can be used to classify large-N_c baryon states and matrix elements [1, 2], which has led to remarkable insights into the understanding of the nonperturbative QCD dynamics of hadrons. Applications of this formalism to the computation of static properties of baryons range from masses, couplings to magnetic moments [3, 4], to name but a few. In particular, in this work we will describe the baryon axial-vector couplings, and as a result we obtain corrections at relative orders $\mathcal{O}(1/N_c)$ and $\mathcal{O}(1/N_c^2)$. This work is organized as follows. In Section 2, the renormalization of the baryon axial vector current is presented, and contains a detailed numerical analysis, our conclusions are presented in Section 3.

2 Renormalization of the baryon axial vector current

The baryon axial vector current A^{kc} is renormalized by the one-loop diagrams displayed in Fig. 1. These loop graphs have a calculable dependence on the ratio m_Π/Δ, where m_Π is the meson mass and $\Delta \equiv M_T - M_B$ is the decuplet-octet mass difference. The contribution from Fig. 1(a,b,c) contains the full dependence on the ratio Δ/m_Π and can be written as [5]

$$\begin{aligned} \delta A^{kc} &= \frac{1}{2}\left[A^{ja},\left[A^{jb},A^{kc}\right]\right]\Pi^{ab}_{(1)} - \frac{1}{2}\left\{A^{ja},\left[A^{kc},\left[\mathcal{M},A^{jb}\right]\right]\right\}\Pi^{ab}_{(2)} \\ &+ \frac{1}{6}\left(\left[A^{ja},\left[\left[\mathcal{M},\left[\mathcal{M},A^{jb}\right]\right],A^{kc}\right]\right] - \frac{1}{2}\left[\left[\mathcal{M},A^{ja}\right],\left[\left[\mathcal{M},A^{jb}\right],A^{kc}\right]\right]\right)\Pi^{ab}_{(3)} + \ldots . \end{aligned} \quad (1)$$

The baryon axial vector current A^{kc} is a spin-1 object, an octet under $SU(3)$, and odd under time reversal. Its $1/N_c$ expansion reads

$$A^{kc} = a_1 G^{kc} + \sum_{n=2,3}^{N_c} b_n \frac{1}{N_c^{n-1}}\mathcal{D}_n^{kc} + \sum_{n=3,5}^{N_c} c_n \frac{1}{N_c^{n-1}}\mathcal{O}_n^{kc}, \quad (2)$$

where the unknown coefficients a_1, b_n, and c_n have expansions in powers of $1/N_c$ and are order unity at leading order in the $1/N_c$ expansion. At $N_c = 3$ the series (2) can be truncated as

$$A^{kc} = a_1 G^{kc} + b_2 \frac{1}{N_c}\mathcal{D}_2^{kc} + b_3 \frac{1}{N_c^2}\mathcal{D}_3^{kc} + c_3 \frac{1}{N_c^2}\mathcal{O}_3^{kc}. \quad (3)$$

The matrix elements of the space components of A^{kc} between SU(6) symmetric states yield the values of the axial vector couplings. For the octet baryons, the axial vector couplings are g_A, as defined in experiments in baryon semileptonic decays, normalized in such a way that $g_A \approx 1.27$ for neutron β decay. The other terms are spin-dependent and represent $\mathcal{M}_{hyperfine}$ introduced in the $1/N_c$ baryon chiral Lagrangian [5]

$$\mathcal{M}_{hyperfine} = \frac{m_2}{N_c} J^2. \quad (4)$$

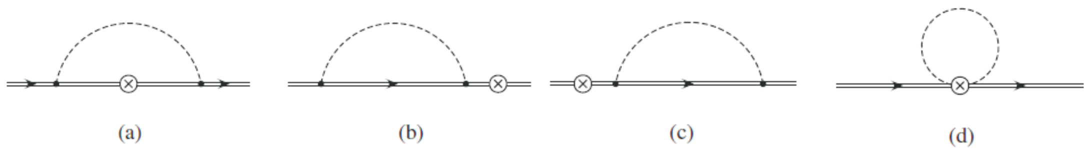

Figure 1: One loop corrections to the baryon axial vector current.

In Eq. (5), $\Pi^{ab}_{(n)}$ represents a symmetric tensor which contains meson loop integrals with the exchange of a single meson: A meson of flavor a is emitted and a meson of flavor b is reabsorbed. This tensor decomposes into flavor singlet **1**, flavor octet **8**, and flavor **27** representations as [5]

$$\Pi^{ab}_{(n)} = F^{(n)}_{\mathbf{1}}\delta^{ab} + F^{(n)}_{\mathbf{8}} d^{ab8} + F^{(n)}_{\mathbf{27}}\left[\delta^{a8}\delta^{b8} - \frac{1}{8}\delta^{ab} - \frac{3}{5}d^{ab8}d^{888}\right], \quad (5)$$

The función $F^{(n)}(m_\Pi, \Delta, \mu)$ along with its derivatives are given explicitly in [3]

$$F^{(n)}(m_\Pi, \Delta, \mu) \equiv \frac{\partial^n F(m_\Pi, \Delta, \mu)}{\partial \Delta^n}. \quad (6)$$

Operator products axial vector current and hyperfine mass	Orders $(1/N_c)$	Operator products SU(6) spin-flavor
AAA	$\mathcal{O}(1/N_c)$	$GGG, GG\mathcal{D}_2, G\mathcal{D}_2\mathcal{D}_2, GG\mathcal{D}_3$ and $GG\mathcal{O}_3$
	$\mathcal{O}(1/N_c^2)$	$\mathcal{D}_2\mathcal{D}_2\mathcal{D}_2, G\mathcal{D}_2\mathcal{D}_3$ and $G\mathcal{D}_2\mathcal{O}_3$
$AAA\mathcal{M}$	$\mathcal{O}(1/N_c)$	$GGGJ^2$ and $GG\mathcal{D}_2J^2$
	$\mathcal{O}(1/N_c^2)$	$GD_2D_2J^2$, $GG\mathcal{D}_3J^2$ and $GG\mathcal{O}_3J^2$
$AAA\mathcal{M}\mathcal{M}$	$\mathcal{O}(1/N_c)$	$GGGJ^2J^2$
	$\mathcal{O}(1/N_c^2)$	$GG\mathcal{D}_2J^2J^2$

Table 1: Relative orders $(1/N_c)$ to the operator products.

3 Results and Conclusions

In summary, we conclude that in the large-N_c limit, decuplet and octet baryon states become degenarate, the difference Δ between the SU(3) invariant masses of the decuplet and octet baryons given by $\Delta \equiv M_T - M_B \propto 1/N_c$.

The analysis was performed at one-loop order, where the corrections to the baryon axial vector coupling arise at relative orders $1/N_c$, $1/N_c^2$, and so on, which is precisely the origin of the $1/N_c$ expansion. The predicted values for g_A are listed in Table 1. Our final results referring to the degeneracy limit $\mathcal{O}(\Delta^0)$, and in the case of a nonvanishing decuplet-octet mass difference for both $\mathcal{O}(\Delta^1)$ and $\mathcal{O}(\Delta^2)$ have been analyzed in Ref. [3, 6]. In Table 1 shows the numerical values of the g_A axial vector couplings for various semileptonic processes in the $1/N_c$ expansion, individually for the flavor singlet **1**, octet **8**, and **27** contributions, the degeneracy limit (AAA), the leading ($AAA\mathcal{M}$), and the next-to-leading ($AAA\mathcal{M}\mathcal{M}$). The singlet corrections are $1/N_c$ suppressed with respect to the tree-level value. Subsequent suppressions of the octet and **27** contributions are also noticeable. The results are perfectly consistent both with the expectations from the $1/N_c$ expansion and the experimental data.

Acknowledgments

The author would like to express their gratitude to Local Organizing Committee of PANIC2014 also acknowledge support.

References

[1] E. E. Jenkins, Ann. Rev. Nucl. Part. Sci. **48**, 81 (1998) [hep-ph/9803349].

[2] R. F. Dashen, E. E. Jenkins and A. V. Manohar, Phys. Rev. D **51**, 3697 (1995) [hep-ph/9411234].

[3] R. Flores-Mendieta, M. A. Hernandez-Ruiz and C. P. Hofmann, Phys. Rev. D **86**, 094041 (2012). [arXiv:1210.8445 [hep-ph]].

[4] G. Ahuatzin, R. Flores-Mendieta and M. A. Hernandez-Ruiz, Phys. Rev. D **89** (2014) 3, 034012 [arXiv:1011.5268 [hep-ph]].

[5] R. Flores-Mendieta, C. P. Hofmann, E. Jenkins and A. V. Manohar, Phys. Rev. D **62**, 034001 (2000). [arXiv:hep-ph/0001218].

[6] R. Flores-Mendieta and C. P. Hofmann, Phys. Rev. D **74**, 094001 (2006). [arXiv:hep-ph/0609120].

Process	Total	Tree	**1**		**8**		**27**	
			Figures 1(a)-1(c), $\mathcal{O}(\Delta^0)$					
			$\mathcal{O}(\frac{1}{N_c})$	$\mathcal{O}(\frac{1}{N_c^2})$	$\mathcal{O}(\frac{1}{N_c})$	$\mathcal{O}(\frac{1}{N_c^2})$	$\mathcal{O}(\frac{1}{N_c})$	$\mathcal{O}(\frac{1}{N_c^2})$
$n \to pe^-\bar{\nu}_e$	1.275	1.121	−0.212	−0.338	0.079	0.292	0.004	−0.001
$\Sigma^\pm \to \Lambda e^\pm \nu_e$	0.629	0.745	−0.042	−0.321	−0.005	0.147	−0.002	0.000
$\Lambda \to pe^-\bar{\nu}_e$	−0.879	−0.628	0.175	0.133	−0.058	−0.063	0.000	0.003
$\Sigma^- \to ne^-\bar{\nu}_e$	0.340	0.704	0.442	−0.783	−0.037	0.022	−0.001	0.008
$\Xi^- \to \Lambda e^-\bar{\nu}_e$	0.361	−0.117	0.077	−0.023	−0.047	0.206	0.005	−0.019
$\Xi^- \to \Sigma^0 e^-\bar{\nu}_e$	0.820	0.793	−0.150	−0.239	−0.028	−0.104	0.004	0.008
$\Xi^0 \to \Sigma^+ e^-\bar{\nu}_e$	1.160	1.121	−0.212	−0.338	−0.041	−0.145	0.005	0.012

TABLE 2: Relative orders $1/N_c$ and $\mathcal{O}(\Delta^0)$ to the coupling constants g_A.

1		**8**		**27**	
Figures 1(a)-1(c), $\mathcal{O}(\Delta^1)$					
$\mathcal{O}(\frac{1}{N_c})$	$\mathcal{O}(\frac{1}{N_c^2})$	$\mathcal{O}(\frac{1}{N_c})$	$\mathcal{O}(\frac{1}{N_c^2})$	$\mathcal{O}(\frac{1}{N_c})$	$\mathcal{O}(\frac{1}{N_c^2})$
−0.103	0.464	0.048	−0.218	0.000	−0.002
−0.026	0.065	0.012	−0.052	0.000	0.001
0.084	−0.490	−0.018	0.138	0.000	0.002
−0.029	−0.239	−0.003	0.047	0.000	−0.001
−0.032	0.398	0.009	−0.050	0.000	0.003
−0.073	0.328	−0.017	0.077	0.000	−0.002
−0.105	0.466	−0.024	0.109	0.000	−0.003

Continuing, TABLE 2: Relative orders $1/N_c$ and $\mathcal{O}(\Delta^1)$ to the coupling constants g_A.

1		**8**		**27**		**1**	**8**	**27**
Figures 1(a)-1(c), $\mathcal{O}(\Delta^2)$						Figure 1(d)		
$\mathcal{O}(\frac{1}{N_c})$	$\mathcal{O}(\frac{1}{N_c^2})$	$\mathcal{O}(\frac{1}{N_c})$	$\mathcal{O}(\frac{1}{N_c^2})$	$\mathcal{O}(\frac{1}{N_c})$	$\mathcal{O}(\frac{1}{N_c^2})$	$\mathcal{O}(\frac{1}{N_c})$	$\mathcal{O}(\frac{1}{N_c})$	$\mathcal{O}(\frac{1}{N_c})$
0.002	−0.043	0.001	−0.023	0.000	0.000	0.303	−0.101	0.002
0.002	−0.023	−0.001	0.006	0.000	0.000	0.201	−0.067	0.001
0.000	0.030	0.000	0.008	0.000	0.000	−0.170	−0.028	0.004
−0.004	−0.006	0.000	0.002	0.000	0.000	0.190	0.032	−0.004
−0.001	−0.008	0.000	−0.005	0.000	0.001	−0.032	−0.005	0.001
0.001	−0.030	0.000	−0.008	0.000	−0.001	0.214	0.036	−0.005
0.002	−0.043	0.000	0.011	0.000	−0.001	0.303	0.050	−0.007

Continuing, TABLE 2: Relative orders $1/N_c$ and $\mathcal{O}(\Delta^2)$ to the coupling constants g_A.

Forward-backward multiplicity correlations in pp collisions at high energy in Monte Carlo model with string fusion

Vladimir Kovalenko, Vladimir Vechernin

Saint Petersburg State University, Russia

DOI: http://dx.doi.org/10.3204/DESY-PROC-2014-04/82

The correlations between multiplicities in two separated rapidity windows, is studied in the framework of the Monte Carlo model based on the picture of string formation in elementary collisions of colour dipoles. The hardness of the elementary collisions is defined by a transverse size of the interacting dipoles. The dependencies of the forward-backward correlation strength on the width and position of the pseudorapidity windows, as well as on transverse momentum range of observed particles were studied. It is demonstrated that taking into account of the string fusion effects improves the agreement with the available experimental data.

1 Introduction

Long-range correlation studies between observables in two separated rapidity windows are considered [1] as a tool for investigation of the initial stages of the hadronic and nuclear collisions, preceding the creation of a hot and dense medium. Because of the non-perturbative nature of multiparticle production in a soft region, one has to apply the various semiphenomenological approaches, such as the model of quark-gluon string formation. At high energies, due to multiparton interactions, the formation of several pairs of strings becomes possible. The interaction between the strings could be observed as a collective phenomena in pp collisions.

Experimentally, the multiplicity correlation coefficient, defined as $b_{\rm corr} = \frac{\langle n_B n_F\rangle - \langle n_B\rangle\langle n_F\rangle}{\langle n_F^2\rangle - \langle n_F\rangle_2}$, has been measured in a wide energy range [2–4] as a function of pseudorapidity windows width, their position and transverse momentum region. In the present paper, we study $b_{\rm corr}$ using the Monte Carlo model, that incorporates string collectivity effects in the form of string fusion [5], and compare the results with the data at $\sqrt{s}$ from 200 to 7000 GeV.

2 Monte Carlo model

The Monte Carlo model [6] is based on the partonic picture of nucleon interaction. It preserves the energy and angular momentum conservation in the nucleon initial state and uses the dipole approach [7] for description of elementary partonic collisions. Multiplicity and transverse momentum are obtained in the approach of colour strings, stretched between projectile and target partons. The interaction of strings is realized in accordance with the string fusion model prescriptions [5]. Namely the mean multiplicity μ and the mean transverse momentum p_T of the particles produced from a cluster of k overlapping strings are related to those (μ_1, p_{T1}) from a single string: $\mu = \sqrt{k}\mu_1, p_T = \sqrt[4]{k}p_{T1}$. For realization of the string fusion prescription, we have used the discrete approach, in which a lattice with the cell area equal to the string transverse area πr_{str}^2 is introduced. The strings are thought to be fused if their transverse position centres belong to the same cell. For the multiplicity from one string (or a cluster of fused strings) we used Poisson distribution, with Gaussian transverse momentum spectra of produced particles.

However, in order to provide to provide the possibility of a direct comparison with experimental data, the correct description of the transverse momentum spectra is required. For this purpose the MC model [6] has been extended by taking into account the hardness of elementary collision. For this the mechanism similar to the one in DIPSY event generator [7], has been incorporated in our model with the string fusion. It was assumed that the hardness an elementary collision is inversely proportional to the transverse size of the interacting dipoles: $d_i = |\vec{r}_1 - \vec{r}_2|, d_i' = |\vec{r}_1{}' - \vec{r}_2{}'|$. The mean transverse momentum of particles produced by a single string has the contributions from both edges of the string plus the additional constant term p_0, corresponding to the intrinsic string transverse momentum: ${p_T}_1{}^2 = \frac{1}{d_i^2} + \frac{1}{d_i'^2} + p_0^2$. Accordingly, in the version with string fusion, the transverse momentum of a cluster of strings: $p_T^4 = \sum_{i=1}^{k} {p_T}_{1_i}{}^4$, where ${p_T}_{1_i}{}^2 = \frac{1}{d_i^2} + \frac{1}{d_i'^2} + p_0^2$.

Parameters of the model are constrained from the data on total inelastic cross-section and multiplicity [6]. In the present study, for the case with string fusion we have used r_{str}= 0.2fm (in the case with string fusion). For the intrinsic string transverse momentum we have used $p_0 = 0.2\text{GeV}/c$, which provides a reasonable description of the transverse momentum distribution in pp collisions at the LHC energies.

3 Results

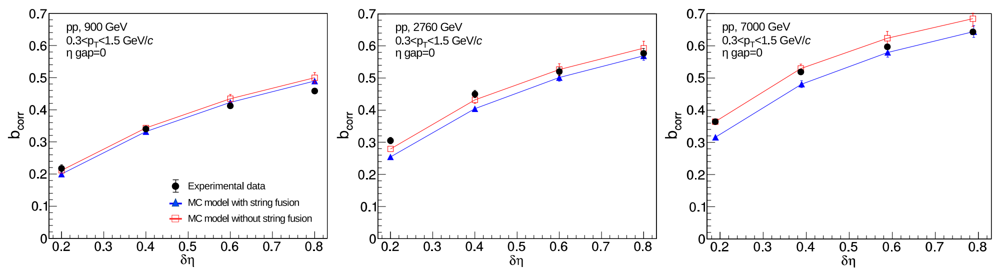

Figure 1: Correlation coefficient as a function of the pseudorapidity windows width ($\delta\eta$) at midrapidities (η gap = 0). Lines – the results of calculation in the model with and without string fusion, points – the experimental data [2].

Figure 1 shows the dependence of the correlation coefficient on the width of the pseudorapidity windows at three energies. The cuts on the transverse momentum ($0.3 < p_T < 1.5\text{GeV}/c$) applied in MC model calculations, enable direct comparison with the ALICE experimental data [2]. It was found that the general trends, like the growth of b_{corr} with collision energy and width of pseudorapidity windows) are well described by the model. The role of string fusion raises with $\sqrt{s}$, but using only midrapidity experimental data on multiplicity correlation coefficient at present energies it is hard to distinguish between cases with and without string fusion. Also, it should be noted that at the small gap between rapidity windows there is a contribution of short-range correlation effects in the data (such as the decays of resonances), which are currently not accounted by the model.

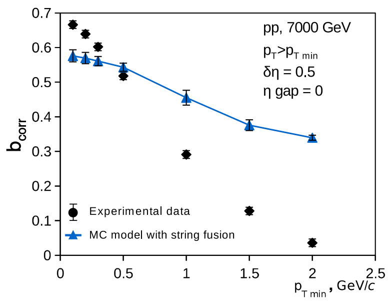

Figure 2: Correlation coefficient as a function of the lower transverse momentum bound. Line – the result of calculation in Monte Carlo model with string fusion, points – the experimental data [3].

In Fig. 2 the dependence of b_{corr} on the transverse momentum region of accounted particles is shown. The correlation coefficient is studied as the function of the lower bound of the p_T interval, and compared to the ATLAS experimental data [3]. The qualitative agreement of b_{corr} with experimental data is found. The increase of $p_{T\,\text{min}}$ is accompanied by the decrease of the multiplicity in the given transverse momentum region, which restricts the phase space for particle production and the number of “active” strings, which leads to the decrease of correlation coefficient. Numerically, the model calculations overestimate the value of the correlation coefficient in the hard transverse momentum area. It could be an indication that the direct approach with the soft strings is applicable at the p_T region below $\sim 1\text{GeV}/c$, and different processes (such as jet fragmentation) begin playing a role at higher p_T. On the other hand, this dependence is very sensitive to the shape of the transverse momentum spectra. Whereas, the description of the p_T spectra in our approach has an effective character and does not account the jet production and other hard phenomena accurately.

Figure 3 shows the dependence of b_{corr} on the η gap at four energies, calculated in the Monte Carlo model, with a comparison to the experimental data [3, 4]. The model calculations do not discriminate pp and p$\bar{\text{p}}$ scattering. The model reproduces the growth of the correlation coefficient with collision energy and qualitatively describes the decrease of the correlation coefficient with with increase of the gap between pseudorapidity windows. Note that the short-range effects, such as the resonances decays and jets, which could contribute to the correlation coefficient at small η gap are not accounted by the model. The results indicate that taking into account of the string fusion effects improves the agreement with the data.

4 Summary and conclusions

The forward-backward multiplicity correlation strength in pp collisions at high energy is studied in the Monte Carlo model with string formation and fusion. The Monte Carlo model reasonably describes the main features of the behaviour of the correlation coefficient in a wide energy range, such as general growth of the correlation coefficient with collision energy and with increase of pseudorapidity window size. The decrease of b_{corr} with the increase of the gap between windows and with increase of the lower p_T bound is also qualitatively described. It is found that the version of the model with inclusion of string fusion effects is better supported by the data compared to the case without string fusion.

Acknowledgments

The authors acknowledge Saint-Petersburg State University for the research grant 11.38.197.2014. V. Kovalenko acknowledges Saint-Petersburg State University for the Special Rector's Scholarship. He is also grateful to the Dynasty Foundation.

References

[1] B. Alessandro *et al.* (ALICE Collaboration), J. Phys. G **32**, 1295 (Section 6.5.15, p. 1749) (2006).

[2] G.A. Feofilov *et al.* (for ALICE collaboration), PoS (Baldin ISHEPP XXI) 075 (2012).

[3] G. Aad *et al.* (ATLAS Collaboration), JHEP 07, 019 (2012).

[4] R.E. Ansorge *et al.* (UA5 Collaboration), Z. Phys C **37** 191 (1988).

[5] N.S. Amelin, N. Armesto, M.A. Braun, E.G. Ferreiro, C. Pajares, Phys. Rev. Lett. **73** 2813 (1994);
M.A. Braun, R.S. Kolevatov, C. Pajares, V.V. Vechernin, Eur. Phys. J. C **32** 535 (2004);
M.A. Braun, C. Pajares, and V.V. Vechernin, Phys. Let. B **493** 54 (2000).

[6] V.N. Kovalenko, Phys. Atom. Nucl. **76** 1189 (2013), arXiv:1211.6209 [hep-ph];
V. Kovalenko, V. Vechernin, PoS (Baldin ISHEPP XXI) 077 (2012), arXiv:1212.2590 [nucl-th];
V. Kovalenko, PoS (QFTHEP 2013) 052 (2013).

[7] C. Flensburg, G. Gustafson, L. Lönnblad, Eur. Phys. J. C **60** 233 (2009);
G. Gustafson, Acta Phys. Polon. B **40** 1981 (2009);
C. Flensburg, G. Gustafson, L. Lönnblad, JHEP 8, 103 (2011).

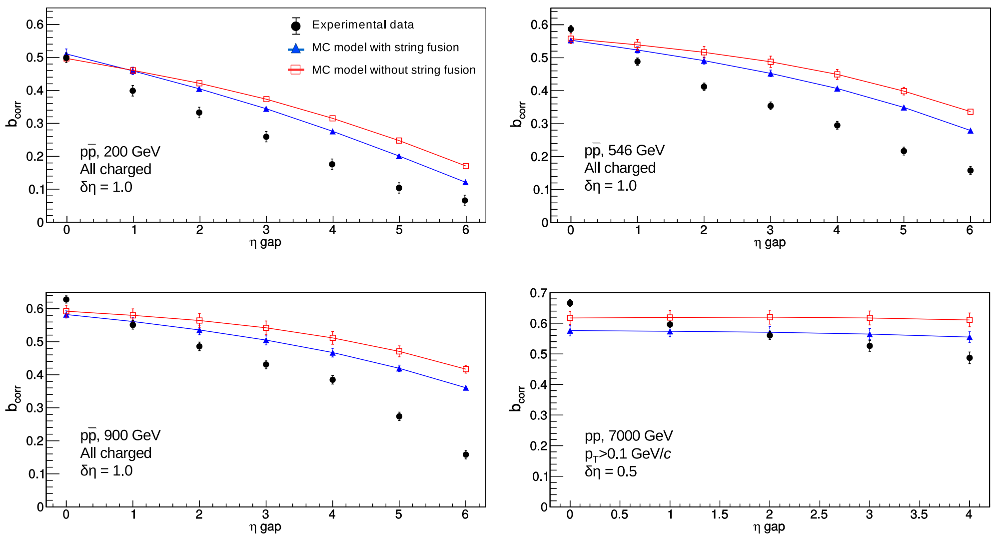

Figure 3: Correlation coefficient as a function of the pseudorapidity gap. Lines – calculation in Monte Carlo model with and without string fusion, points – experimental data [3, 4].

On the Binding Energies of Λ-Hyperons in Hyperhydrogen

Patrick Achenbach, Josef Pochodzalla, Florian Schulz

Institut für Kernphysik, Johannes Gutenberg-Universität, 55099 Mainz, Germany

DOI: http://dx.doi.org/10.3204/DESY-PROC-2014-04/12

The study of the binding energies of the Λ-hyperon in the lightest hypernuclei can reveal details of the strong nucleon-hyperon interaction. The binding energy of the Λ-hyperon, B_Λ, is defined as the Λ-hyperon separation energy from the non-strange core: $B_\Lambda = (M_{core} + M_\Lambda - M_Y)c^2$ where M_Y, M_{core} and M_Λ are the masses of the hypernucleus, its core and the Λ-hyperon respectively.

For many decades visual detectors like nuclear emulsions, with spatial resolutions better than one micrometer to track production and decay, and helium bubble chambers were employed. The masses of hypernuclei $A < 14$ were determined by analyzing the kinetic energies of decay products from the weak pionic decays. No bound states of Λp or Λn were found. The lightest systems are the s-shell ($A \leq 5$) hyperhydrogen and hyperhelium isotopes. The statistical error for the binding energies in light hypernuclei with the emulsion method ranges from 0.02 MeV for ${}^{5}_{\Lambda}$He to more than 0.7 MeV for ${}^{8}_{\Lambda}$He [1–3]. In one of these compilations a possible systematic error of 0.15 MeV [3] is quoted. In a later work by D.H. Davis systematic errors of the order of 0.04 MeV are given [4].

This era was followed by spectroscopic measurements at secondary, mesonic beams achieving energy resolutions of the order of $\Delta B_\Lambda \sim 1.5$ MeV (FWHM) [5]. Only recently energy resolutions of ~ 0.5 MeV (FWHM) have been achieved in the $(e, e'K^+)$ reaction using a dedicated kaon spectrometer at Jefferson Lab. The best reaction spectroscopy data in terms of resolution was reported for ${}^{12}_{\Lambda}$B [6] and ${}^{7}_{\Lambda}$He [7]. During the last three years the new method of decay-pion spectroscopy was pioneered at the Mainz Microtron MAMI, that has the potential to achieve mass measurements of several light hypernuclei with a precision comparable or better than with the emulsion technique.

${}^{3}_{\Lambda}$H decay mode	N	B_Λ (MeV)	Ref.
${}^{3}_{\Lambda}\text{H} \to \pi^- + {}^{1}\text{H} + {}^{2}\text{H}$	24	$+0.23 \pm 0.11$	[1]
${}^{3}_{\Lambda}\text{H} \to \pi^- + {}^{3}\text{He}$	58	$+0.06 \pm 0.11$	[1]
both modes	82	$+0.15 \pm 0.08$	[1]
${}^{3}_{\Lambda}\text{H} \to \pi^- + {}^{1}\text{H} + {}^{2}\text{H}$	16	-0.11 ± 0.13	[2]
${}^{3}_{\Lambda}\text{H} \to \pi^- + {}^{3}\text{He}$	86	$+0.05 \pm 0.08$	[2]
both modes	102	$+0.01 \pm 0.07$	[2]
${}^{3}_{\Lambda}\text{H} \to \pi^- + {}^{1}\text{H} + {}^{2}\text{H}$	6	$+0.33 \pm 0.21$	[3]
${}^{3}_{\Lambda}\text{H} \to \pi^- + {}^{3}\text{He}$	26	$+0.13 \pm 0.15$	[3]
both modes	32	$+0.20 \pm 0.12$	[3]
mean (both modes)	204	$+0.13 \pm 0.05$	[1]

Table 1: Binding energies of ${}^{3}_{\Lambda}$H from emulsion experiments as compiled by Refs. [1–3]. The number of uniquely identified events, N, for determining B_Λ is given for two decay modes. The mean value was evaluated in Ref. [1] using both modes.

The lightest strange nuclear system is the hypertriton ${}^{3}_{\Lambda}$H, found to be just bound. Available data on ${}^{3}_{\Lambda}$H is summarized in Table 1. From the Table it is seen that the number of uniquely identified events for determining B_Λ was in total of the order ~ 200 from different decay modes, analyzed and compiled in three different works. The mean value was evaluated in Ref. [1] using both decay modes to be (0.13 ± 0.05) MeV. The distribution of binding energies of ${}^{3}_{\Lambda}$H determined from pionic two-body and three-body decays is shown in Fig. 1. The FWHM of the distribution of binding energies is 2.1 MeV corresponding to a width $\sigma = 0.89$ MeV if the distribution were Gaussian, which would allow for a determination of its mean value with a statistical uncertainty of $\Delta B_\Lambda = 0.89\,\mathrm{MeV}/\sqrt{204} = 0.06$ MeV. The published B_Λ values are shown in Fig. 2. From the data one can deduce that the mean B_Λ value of the 176 events of the two-body mode is 0.07 MeV and of the 46 events of the three-body mode is 0.13 MeV. The B_Λ values evaluated by Ref. [2] and by Ref. [1] differ by (0.14 ± 0.11) MeV.

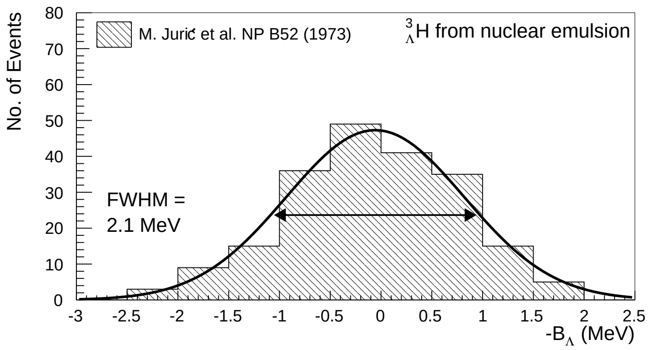

Figure 1: Distribution of binding energies of ${}^{3}_{\Lambda}$H determined from pionic two-body and three-body decays observed in emulsion experiments as compiled in Ref. [1]. A Gaussian function was fitted to the distribution for the illustration of the dispersion of the values with a FWHM of 2.1 MeV. The total number of events was 204 and the mean value was evaluated in Ref. [1] to be $B_\Lambda = 0.13 \pm 0.05$ MeV.

When going from a mass $A = 3$ to a $A = 4$ system the binding energy of the Λ-hyperon increases by about 1 MeV. Table 2 summarizes the B_Λ values for ${}^{4}_{\Lambda}$H. The mean value was evaluated in Ref. [1] using only three-body decay modes to be (2.04 ± 0.04) MeV. In the same publication the B_Λ values for the $\pi^- + {}^1\mathrm{H} + {}^3\mathrm{H}$ decay mode, 2.14 ± 0.07 MeV, and for $\pi^- + {}^2\mathrm{H} + {}^2\mathrm{H}$ mode, 1.92 ± 0.12 MeV, are reported separately. They differ by (0.22 ± 0.14) MeV. The mean B_Λ value of the 760 events of the two-body mode reported by Refs. [2, 3] is 2.28 MeV which would indicate a ~ 0.2 MeV stronger binding. This decay mode is not included because of the larger systematic error in the pion range-energy relation for pion ranges greater than 3 cm [1].

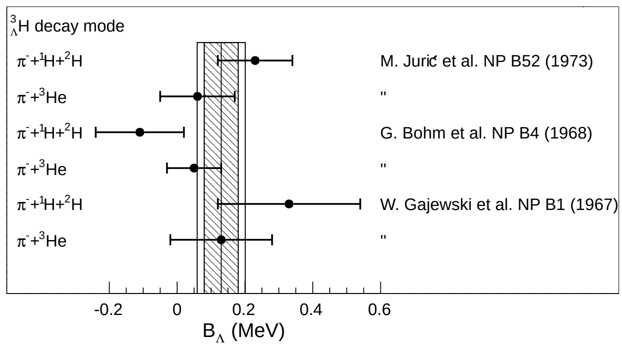

Figure 2: Measurements of the binding energy of ${}^{3}_{\Lambda}$H determined from two-body and three-body pionic decays observed in emulsion experiments [1–3] (with statistical errors only). The mean value was evaluated in Ref. [1] (shaded bands with statistical and total uncertainties).

The mirror pair of hypernuclei $^4_\Lambda$H and $^4_\Lambda$He is especially important because it is used as the main source of information about the charge symmetry breaking (CSB) in the ΛN interaction. Charge symmetric interactions do not distinguish between the nucleon isospin channels Λp and Λn. CSB effects in the strong interaction occurs because of the difference between the masses of the quarks in hadronic and nuclear systems. In mirror hypernuclei the binding energies of the Λ-hyperon could reveal CSB contributions in the strong interaction. The distribution of binding energies of $A = 4$ hypernuclei is shown in Fig. 3. The binding energies for the (0^+) ground states, $B_\Lambda(^4_\Lambda\mathrm{H}) = 2.04 \pm 0.04$ MeV and $B_\Lambda(^4_\Lambda\mathrm{He}) = 2.39 \pm 0.03$ MeV systematically differ, the difference being $\Delta B_\Lambda = 0.35 \pm 0.06$ MeV. However, the FWHM of the distributions of binding energies is larger than 1 MeV. The Coulomb correction due to core compression induced by the presence of the Λ-hyperon in the nucleus was calculated to be less than 0.05 MeV [8]. If the mirror pair difference is as large as 0.35 MeV the CSB effect in the ΛN interaction would be much larger than in the NN interaction.

$^4_\Lambda$H decay mode	N	B_Λ (MeV)	Ref.
$^4_\Lambda\mathrm{H} \to \pi^- + {}^1\mathrm{H} + {}^3\mathrm{H}$	56	$+2.14 \pm 0.07$	[1]
$^4_\Lambda\mathrm{H} \to \pi^- + {}^2\mathrm{H} + {}^2\mathrm{H}$	11	$+1.92 \pm 0.12$	[1]
both three-body modes	67	$+2.08 \pm 0.06$	[1]
$^4_\Lambda\mathrm{H} \to \pi^- + {}^1\mathrm{H} + {}^3\mathrm{H}$	63		[2]
$^4_\Lambda\mathrm{H} \to \pi^- + {}^2\mathrm{H} + {}^2\mathrm{H}$	7		[2]
both three-body modes	70	$+2.08 \pm 0.06$	[2]
$^4_\Lambda\mathrm{H} \to \pi^- + {}^4\mathrm{He}$	552	$+2.29 \pm 0.04$	[2]
$^4_\Lambda\mathrm{H} \to \pi^- + {}^1\mathrm{H} + {}^3\mathrm{H}$	21		[3]
$^4_\Lambda\mathrm{H} \to \pi^- + {}^2\mathrm{H} + {}^2\mathrm{H}$	2		[3]
both three-body modes	23	$+1.86 \pm 0.10$	[3]
$^4_\Lambda\mathrm{H} \to \pi^- + {}^4\mathrm{He}$	208	$+2.26 \pm 0.07$	[3]
mean (three-body)	155	$+2.04 \pm 0.04$	[1]

Table 2: Binding energies of $^4_\Lambda$H from emulsion experiments as compiled by Refs. [1–3]. The number of uniquely identified events for determining B_Λ is given for three decay modes. The mean value was evaluated in Ref. [1] using only the three-body modes.

At the Mainz Microtron MAMI the first high-resolution spectroscopy of pions from decays of hypernuclei was performed. The associated strangeness production with the incident electron beam on a thin ^{9}Be target was tagged by the detection of kaons with the spectrometer KAOS. Pions were detected in coincidence with two high-resolution spectrometers. Details on the setup, the experimental conditions, and the identification of pionic weak decays can be found in Refs. [9, 10]. The binding energy of stopped $^4_\Lambda$H was deduced from the two-body decay mode $^4_\Lambda\mathrm{H} \to \pi^- + {}^4\mathrm{He}$ with a 10^{-3} relative momentum resolution [11]. Details on the statistical and systematic error are found in the reference.

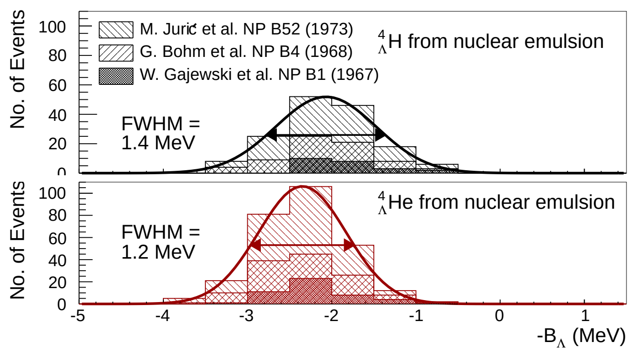

Figure 3: Distribution of binding energies of $^4_\Lambda$H and $^4_\Lambda$He determined from pionic three-body decays observed in emulsion experiments as compiled in Refs. [1–3]. A Gaussian function was fitted to the distribution for the illustration of the dispersion of the values with a FWHM of 1.2–1.4 MeV. The total number of events was 155 resp. 279 and the mean value was evaluated in Ref. [1] to be $B_\Lambda = 2.04 \pm 0.04$ MeV resp. 2.39 ± 0.03 MeV.

In Fig. 4 the preliminary MAMI result on the binding energy of ${}^{4}_{\Lambda}$H is compared to the emulsion experiments [1–3]. Full circles present evaluations from three-body decays, open circles from two-body decays, error bars on the emulsion values are statistical only. The mean values were evaluated in Ref. [1] excluding data from the two-body decay mode, where the shaded bands show statistical and total uncertainties. The error bars on the MAMI value are statistical (inner) and total (outer). The figure also shows the data from the pioneering decay-pion spectroscopy with a stopped K^{-}-beam at KEK [12].

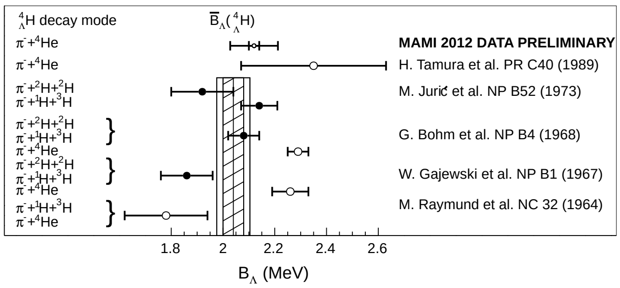

Figure 4: Measurements of the binding energy of ${}^{4}_{\Lambda}$H determined from different pionic decays. Details are discussed in the text.

A major effort in hypernuclear physics is to understand the interaction between hyperons and nucleons. Parameters of many employed phenomenological models are fitted to reproduce the binding energies of light hypernuclei. Many theoretical descriptions include ΛNN three-body forces and charge symmetry breaking terms to yield an agreement with available experimental data over a wide range of hypernuclear masses. In the literature the binding energies of the light hyperhydrogen isotopes are often quoted with errors of $0.04 - 0.05$ MeV. One should be aware of systematic errors. A cross-check of the experimental values with an independent method with high resolution seems timely and necessary.

This work was supported in part by Deutsche Forschungsgemeinschaft (SFB 1044), by Carl Zeiss Foundation, by European Community Research Infrastructure Integrating Activity HadronPhysics2 (SPHERE).

References

[1] Jurić, M. et al., Nucl. Phys. **B52** 1 (1973).

[2] Bohm, G. et al., Nucl. Phys. **B4** 511 (1968).

[3] Gajewski, W. et al., Nucl. Phys. **B1** 105 (1967).

[4] Davis, D. H., Nucl. Phys. **A547** 369 (1992).

[5] Hashimoto, O. and Tamura, H., Prog. Part. Nucl. Phys. **57** 564 (2006).

[6] Tang, L. et al. (HKS Collaboration), Phys. Rev. **C90** 034320 (2014).

[7] Nakamura, S. N. et al. (HKS Collaboration), Phys. Rev. Lett. **110** 012502 (2013).

[8] Bodmer, A. and Usmani, Q., Phys. Rev. **C31** 1400 (1985).

[9] Achenbach, P. et al. (A1 Collaboration), Few-Body Syst. **55** 887 (2014).

[10] Esser, A. et al. (A1 Collaboration), Nucl. Phys. **A914** 519 (2013).

[11] Esser, A., Nagao S., Schulz, F., Achenbach, P. et al. (A1 Collaboration), *Observation of ${}^{4}_{\Lambda}$H hyperhydrogen by decay-pion spectroscopy in electron scattering*, arXiv:1501.06823 (2015).

[12] Tamura, H. et al., Phys. Rev. **C40** 479 (1989).

Two Component Model with collective Flow for Hadroproduction in heavy-ion Collisions.

Nadezda Chernyavskaya[1,2], *Alexander Bylinkin*[1,2], *Andrey Rostovtsev*[3]

[1]ITEP, Bolshaya Cheremushkinskaya 25, 117218, Moscow, Russia
[2]MIPT, Institutskiy per. 9, 141700 Dolgoprudny, Moscow Region, Russia
[3]IITP RAS, Bolshoy Karetny per. 19, 127994 Moscow, Russia

DOI: http://dx.doi.org/10.3204/DESY-PROC-2014-04/47

Hadroproduction in high-energy collisions can be described by two distinct mechanisms [1, 2]. In this approach [1] the charged particle spectra are aproximated as a function of the particles' transverse momentum p_T by a sum of an exponential (Boltzmann-like) and a power-law distributions:

$$\frac{d\sigma}{p_T dp_T} = A_e \exp\left(-E_{Tkin}/T_e\right) + \frac{A}{(1+\frac{p_T^2}{T^2 \cdot N})^N}, \tag{1}$$

where $E_{Tkin} = \sqrt{p_T^2 + M^2} - M$ with M equal to the produced hadron mass. A_e, A, T_e, T, N are the free parameters obtained from the fit to the experimental data. The exponential term stands for the release of 'thermalized' particles by the preexisting valence quarks and a quark-gluon cloud coupled to them inside the colliding baryon. The power-law term accounts for the fragmentation of mini-jets formed by the secondary partons produced at the first stage of the collision.

The goal of this work is to compare the shapes of charged hadron spectra produced in $\gamma\gamma$ and pp interactions (already studied in [2, 3]) with a more complex case of heavy-ion collisions.

ALICE Collaboration [4] provides data on lead-lead collisions in the range of transverse momentum p_T up to 50 GeV. Figure 1 shows experimental data on $\gamma\gamma$ [5], pp [6] and lead-lead [4] collisions fitted with the parameterization introduced (1). From the shape of the lead-lead collision's spectrum one can notice that an additional power-law term is needed to describe the data in terms of the introduced approach :

$$\frac{d\sigma}{p_T dp_T} = A_e \exp\left(-E_{Tkin}/T_e\right) + \frac{A}{(1+\frac{p_T^2}{T^2 \cdot N})^N} + \frac{A_1}{(1+\frac{p_T^2}{T_1^2 \cdot N_1})^{N_1}} \tag{2}$$

For heavy-ion collisions nuclear modification factor R_{AA} is an important variable. Figure 2(a) shows R_{AA} for lead-lead collisions measured at ALICE [4] together with contributions from the three terms of eq. (2) independently, each of them divided over the spectrum in pp-collisions measured at the same c.m.s. energy [6]. Studying of the R_{AA} for lead-lead collisions at ALICE [4] can help us to understand the following picture of hadroproduction [7]:

1. The bulk of low-p_T particles originates from the 'quark-gluon soup' formed in the heavy-ion collision and has an exponential p_T distribution, as shown by the red dashed line in Figs. 1 and 2.

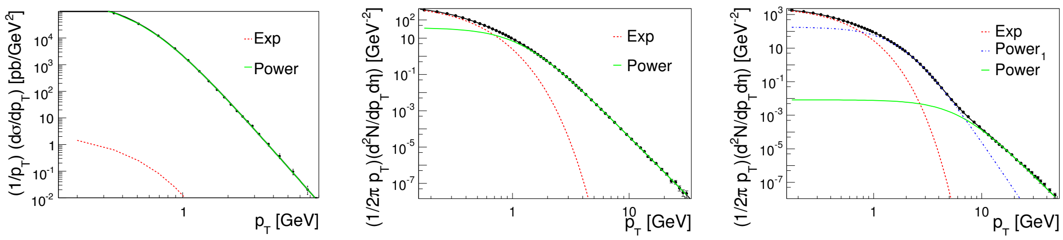

(a) (b) (c)

Figure 1: Charged particle spectra in $\gamma\gamma$ [5] a), pp [6] b) and in central lead-lead collisions [4] c) fitted to the function (2): the red (dashed) line shows the exponential term and the green (solid) and blue (dash-dot) lines - two power-law terms.

2. The high-p_T tail (green solid line in Figs. 1 and 2) accounts for the mini-jets that pass through the nuclei. When these jets hadronize into final state particles *outside* the nuclei, we get the same power-law term parameter N as in pp-collisions (Figs. 1 b) and c)), resulting in a constant suppression (R_{AA}) of high-p_T (> 20 GeV) particles (Fig. 2). While passing through the nuclei these jets should loose about $\frac{dE}{dz} \cdot R_A \sim 7$ GeV [8], where R_A is the radius of the nuclei. Therefore, hadrons with $p_T < 7$ GeV produced from these jets will be largely suppressed, as it seen in the Fig. 2.

3. However if the mini-jet fragmentation occurs before the produced particles leave the nuclei volume, they are affected by multiple rescatterings from the media, loose energy and their distribution (blue dash-dot line in Fig. 1 and 2) becomes closer to the exponent.

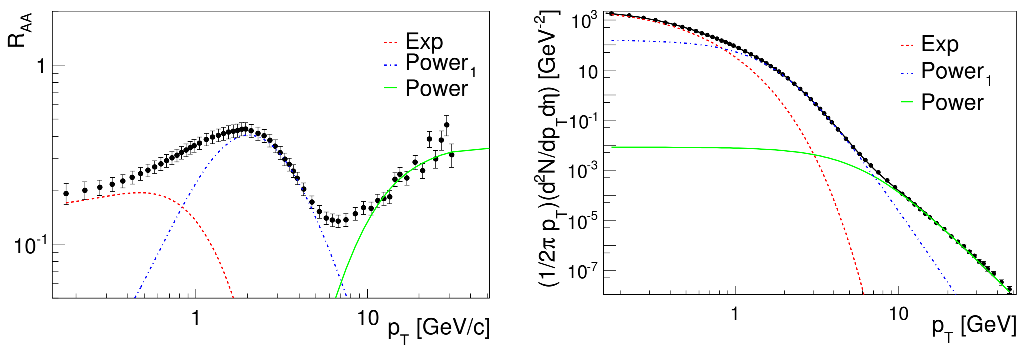

(a) (b)

Figure 2: (a): R_{AA} measured for central Pb-Pb collisions [4] shown with the terms of (2) independently divided over the fit (1) of the pp-data at the same c.m.s energy: the red (dashed) line shows the exponential term and the green (solid) and blue (dash-dot) lines - two power-law terms. (b): Central lead-lead collisions [4] fitted with (4): the red (dashed) line shows the hydrodynamic term and the green (solid) and blue (dash-dot) lines - two power-law terms.

One can see, hadroproduction dynamics can be characterized by complexity (number of involved partons) of the colliding system: $\gamma\gamma$ collisions, pp-collisions, heavy-ion collisions.

In heavy-ion collisions when a large colliding system is formed, one should also take effects of the ‘collective motion’ into account [9] and the multiparticle production is usually considered in terms of relativistic hydrodynamics. Therefore, it is suggested to modify the introduced approach (1) using recent theoretical calculations [9]. The idea of hydrodynamic approach is that the thermalized system expands collectively in longitudinal direction generating the transverse flow by the high pressure in the colliding system. The distidution function is still the Boltzmann distribution, but it is boosted to the expanding system. According to this approach the radiation of thermalized particles can be parameterized by the following formula:

$$\frac{\mathrm{dn}}{p_T \mathrm{d}p_T} \propto \int_0^R r \ \mathrm{d}r \ m_T \ I_0 \left(\frac{p_T \sinh \rho}{T_e} \right) K_1 \left(\frac{m_T \cosh \rho}{T_e} \right), \tag{3}$$

where $\rho = tanh^{-1}\beta_r$ and $\beta_r(r) = \beta_s(\frac{r}{R})$, with β_s standing for the surface velocity. In this analysis we take $\beta_s = 0.5c$ which is consistent with previous observations [9]. We substitute the exponential term in (1) by (3) and use this hydrodynamic approach to fit the recent experimental data on lead-lead collisions measured by the Alice Collaboration [4] at $\sqrt{s} = 2.76$ TeV. These data are shown in Fig. 2(b) together with the fit:

$$\frac{\mathrm{d}n}{p_T \mathrm{d}p_T} = A_e \cdot \int_0^R r \ \mathrm{d}r \ m_T \ I_0 \left(\frac{p_T \sinh \rho}{T_e} \right) K_1 \left(\frac{m_T \cosh \rho}{T_e} \right) + \frac{A}{(1 + \frac{p_T^2}{T^2 \cdot N})^N} + \frac{A_1}{(1 + \frac{p_T^2}{T_1^2 \cdot N_1})^{N_1}}. \tag{4}$$

Hydrodynamic extension slightly modifies the description of data and an additional power-law term is still needed. But the temperatures T_e obtained from the fits with and without transverse flow taken into account differ significantly [12] (Fig. 3)

The thermalized production of charged hadrons (described by function (3)) can be extracted from the whole statistical ensemble and in this paper it is proposed to study the variations of the temperature-like parameter T_e in (3) with the centrality and the c.m.s. energy in heavy-ion collisions. It is interesting to consider the experimental data measured at RHIC and LHC together and combine it in terms of energy density. In this paper we consider the experimental data measured in AuAu collisions at $\sqrt{s} = 200$ GeV/N and $\sqrt{s} = 130$ GeV/N by PHENIX [13, 14] and PbPb collisions at $\sqrt{s} = 2.76$ TeV/N by ALICE [4].

Having calculated the energy density ε based on theoretical caculations [15], one can plot the temperature T_e extracted from (4) as a function of it, as shown in Fig. 3. A smooth transition in the T_e values between ALICE and RHIC measurements is observed.

One can notice interesting behavior of the temperature T_e as a function of energy density ($\varepsilon \propto T_e^4 + B$), which is in a good agreement with the Bag model [16], with $B = 0.25$ GeV/fm^3, as determined from the fit in Fig. 3. Next, one can see that the temperature T_e of the final state particles reaches a certain limit for high energy densities. This might be explained from QGP theory that considers the phase transition temperature T_c from QGP to final state hadrons. For high values of ε one can notice, that the observed freeze-out temperature is $T_{fo} \approx 145$ MeV, and (as one can expect) is slightly below the critical temperature $T_c \sim 155 - 160$ MeV for QGP obtained in different calculations [17, 18]. That gives us another confirmation of applicability of such an approach (4) to decribe hadroproduction in heavy-ion collisions.

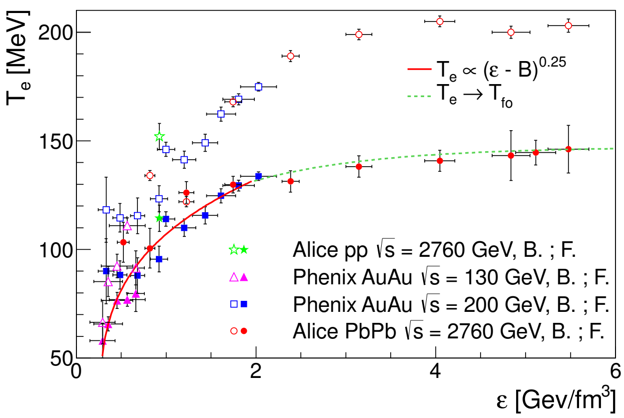

Figure 3: Temperature of the final state hadrons coming from the 'thermalized' part of the spectra in heavy-ion collisions as a function of energy density. Full points show the results extracted from the fit by taking into account the collective flow 4 (F. in the legend); open points show the results when using a fit with the Boltzmann exponent 2 (B. in the legend). Solid line stands for the $T_e \propto (\varepsilon - B)^{0.25}$ fit and dashed line shows $T_e \to const$ behavior.

References

[1] A. A. Bylinkin and A. A. Rostovtsev, Phys. Atom. Nucl. **75** (2012) 999 Yad. Fiz. **75** (2012) 1060; A. A. Bylinkin and A. A. Rostovtsev, arXiv:1008.0332 [hep-ph].

[2] A. A. Bylinkin and A. A. Rostovtsev, arXiv:1404.7302 [hep-ph].

[3] A. A. Bylinkin and A. A. Rostovtsev, Eur. Phys. J. C **72**, 1961 (2012) arXiv:1112.5734 [hep-ph].

[4] B. Abelev *et al.* [ALICE Collaboration], Phys. Lett. B **720** (2013) 52 [arXiv:1208.2711 [hep-ex]].

[5] G. Abbiendi *et al.* [OPAL collaboration], Phys.Lett.B**651**:92-101,2007

[6] B. B. Abelev *et al.* [ALICE Collaboration], Eur. Phys. J. C **73** (2013) 2662 [arXiv:1307.1093 [nucl-ex]].

[7] A. A. Bylinkin, N. S. Chernyavskaya and A. A. Rostovtsev, Phys. Rev. C **90** (2014) 018201 [arXiv:1405.3055 [hep-ph]].

[8] X. -N. Wang, Phys. Rept. **280** (1997) 287 [hep-ph/9605214].

[9] E. Schnedermann, J. Sollfrank and U. W. Heinz, Phys. Rev. C **48** (1993) 2462 [nucl-th/9307020].

[10] C.Tsallis, J.Stat.Phys., **52**, 479, 1988.

[11] R. Hagedorn, Riv. Nuovo Cim. **6N10** (1984) 1.

[12] A. A. Bylinkin, A. A. Rostovtsev and N. S. Chernyavskaya, arXiv:1305.0387 [hep-ph].

[13] S. S. Adler *et al.* [PHENIX Collaboration], Phys. Rev. C **69** (2004) 034909 [nucl-ex/0307022].

[14] K. Adcox *et al.* [PHENIX Collaboration], Phys. Rev. C **69** (2004) 024904 [nucl-ex/0307010].

[15] I. N. Mishustin and J. I. Kapusta, Phys. Rev. Lett. **88** (2002) 112501 [hep-ph/0110321].

[16] A. Chodos, R. L. Jaffe, K. Johnson, C. B. Thorn and V. F. Weisskopf, Phys. Rev. D **9** (1974) 3471.

[17] F. Karsch, K. Redlich and A. Tawfik, Eur. Phys. J. C **29** (2003) 549 [hep-ph/0303108].

[18] A. Majumder and B. Muller, Phys. Rev. Lett. **105** (2010) 252002 [arXiv:1008.1747 [hep-ph]].

Identification of hadronic tau decays in CMS.

Raman Khurana[1] on behalf of the CMS collaboration

[1] Saha Institute of Nuclear Physics, Kolkata-700 064, India

DOI: http://dx.doi.org/10.3204/DESY-PROC-2014-04/181

The algorithm used for reconstruction and identification of hadronic tau decays by the CMS experiment at the LHC is presented. The tau reconstruction in CMS takes advantage of the particle-flow algorithm which allows to reconstruct individual hadronic decay modes. The performance of the algorithm in terms of tau identification efficiency and rates for jets to be misidentified as hadronic tau decays is measured in *pp* collision data recorded in 2012 at a center-of-mass energy ($\sqrt{s}$) of 8 TeV, corresponding to an integrated luminosity of 19.7 fb^{-1}.

1 Tau leptons and their decay

Tau is the heaviest known lepton ($m_\tau = 1.78$ GeV/c^2) which decays into lighter leptons (BR $\sim 35\%$) or hadrons τ_h (BR $\sim 65\%$) in the presence of upto two neutrinos. CMS has developed Hadron Plus Strips (HPS) [1, 2] algorithm for reconstruction of hadronic tau decay modes. It uses decay mode identification techniques which allows to reconstruct hadronic tau decays, denoted by τ_h, with high efficiency and suppress the potentially large backgrounds from quarks and gluons that occasionally hadronize into low particle multiplicity jets.

2 Particle Flow and Hadron Plus Strips algorithm

CMS utilises the fine granularity of the calorimeters, precision tracking and muon system to identify and reconstruct final state particles in an event. This is achieved by the use of particle flow (PF) [3] algorithm to make the best use of information available from all the sub-detectors and reconstruct all the stable partiles (namely, charged hadrons, photons, neutral hadrons, muons and electrons) in the detector. The resulting list of particles is used to reconstruct hadronic decays of taus by the HPS algorithm.

The HPS algorithm is designed to reconstruct individual decay modes of the tau. This requires reconstruction of the neutral pions that are produced in the majority of hadronic tau decays. The high probability for photons originating from $\pi^0 \to \gamma\gamma$ decays to convert within the volume of the tracking detector is accounted for by clustering the photon constituents of the jet that seeds the tau reconstruction into $\eta - \phi$ *strips*. The size of the strips, 0.20×0.05, is enlarged in η direction, taking into consideration the bending of e^+e^- pairs produced by photon conversions in the 3.8 Tesla magnetic field. Strips containing one or more photons and passing a cut $p_T > 2.5$ GeV on the sum of photon transverse momenta are kept as π^0 candidates for further processing. The τ_h candidates are built by combining the the neutral objects with charged hadrons reconstructed by the PF algorithm. Figure 1 (left) shows the

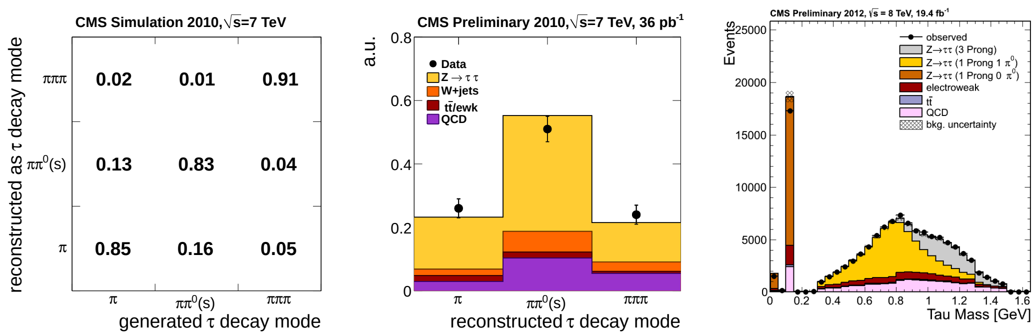

Figure 1: Performance of the decay mode reconstruction.

fraction of generated taus of a given type reconstructed in a certain decay mode for a sample of simulated $Z \to \tau\tau$ events. A data-to-Monte Carlo (MC) comparison in $Z \to \tau\tau \to \mu\tau_h$ events of the number of taus reconstructed in different tau decay modes and of the τ_h candidate mass is shown in Figure 1.

Requiring reconstructed hadronic tau candidates to pass strict isolation requirements constitutes the main handle to reduce the large jet background. Being colorless and produced in decays of colorless bosons, tau leptons are typically isolated with respect to other particles in the event, and so are their decay products, in contrast to quark and gluon jets. The isolation sum is computed using two different approaches :

- Cut based isolation : The isolation of the τ_h candidates is computed by summing the transverse momenta of charged particles of $p_T > 1$ GeV plus photons of $E_T > 1.5$ GeV within a cone of size of $\triangle R = 0.5$ centered on the τ_h direction. The contribution of pile-up to the τ_h isolation is subtracted by means of $\triangle\beta$ corrections.

$$I_\tau = \Sigma p_T^{charged}\,(d_Z < 0.2 \text{ cm}) + \max\,(p_T^\gamma - \triangle\beta, 0) \tag{1}$$

  The $\triangle\beta$ corrections are computed by summing the p_T of charged particles that have a longitudinal impact parameter $d_Z > 0.2$ cm with respect to the τ_h production vertex and are within a cone of size $\triangle R = 0.8$ around the τ_h direction. The sum is scaled by a factor 0.4576, chosen to make the τ_h identification efficiency insensitive to pile-up.

$$\triangle\beta = 0.4576 \cdot \Sigma p_T^{charged}\,(d_Z > 0.2 \text{ cm}) \tag{2}$$

- Multivariate (MVA) approach : The MVA-based tau identification discriminator utilizes the transverse impact parameter of *leading* (highest p_T) track of the τ_h candidate. In case of τ_h candidates reconstructed in the three charged hadron decay mode the distance between the tau production and decay vertex, reconstructed by fitting the three tracks to a common vertex, is used as additional handle to remove the jet $\to \tau_h$ background. A boosted decision tree discriminator (BDT) has been trained to discriminate hadronic tau decays (*signal*) from quark and gluon jets (*background*).

Several working points are provided, corresponding to looser or tighter cuts on the isolation p_T-sum I_τ and on the MVA output respectively, and yielding different tau identification efficiency and jet $\to \tau_h$ misidentification rates.

3 Efficiency and misidentification rate

The efficiency to identify hadronic tau decays is measured in Z$\rightarrow \tau\tau \rightarrow \tau_\mu\tau_h$ events selected in the 2012 data using the *tag*-and-*probe* method. The hadronic tau identification efficiency ϵ_τ is defined as the ratio of the number of genuine hadronic taus passing the tau identification discriminator under study over the total number of genuine hadronic taus:

$$\epsilon_{tau} = \frac{N^{\tau}_{pass}}{N^{\tau}_{pass} + N^{\tau}_{fail}} \tag{3}$$

The number of hadronic taus passing and failing the tau identification discriminator under study, N^{τ}_{pass} and N^{τ}_{fail}, is obtained via a simultaneous template fit. The multiplicity of tracks within a cone size $\triangle R = 0.5$ around the τ_h candidate, N_{tracks}, is used as observable to perform the fit. The efficiency measured in data and simulation is shown in Fig. 2 along with the data-to-simulation scale factors for both cut based and MVA-based tau identification discriminators. The probability for quark and gluon jets to be misidentified as hadronic tau decays is measured in QCD multijet events. The results are shown in Fig 3.

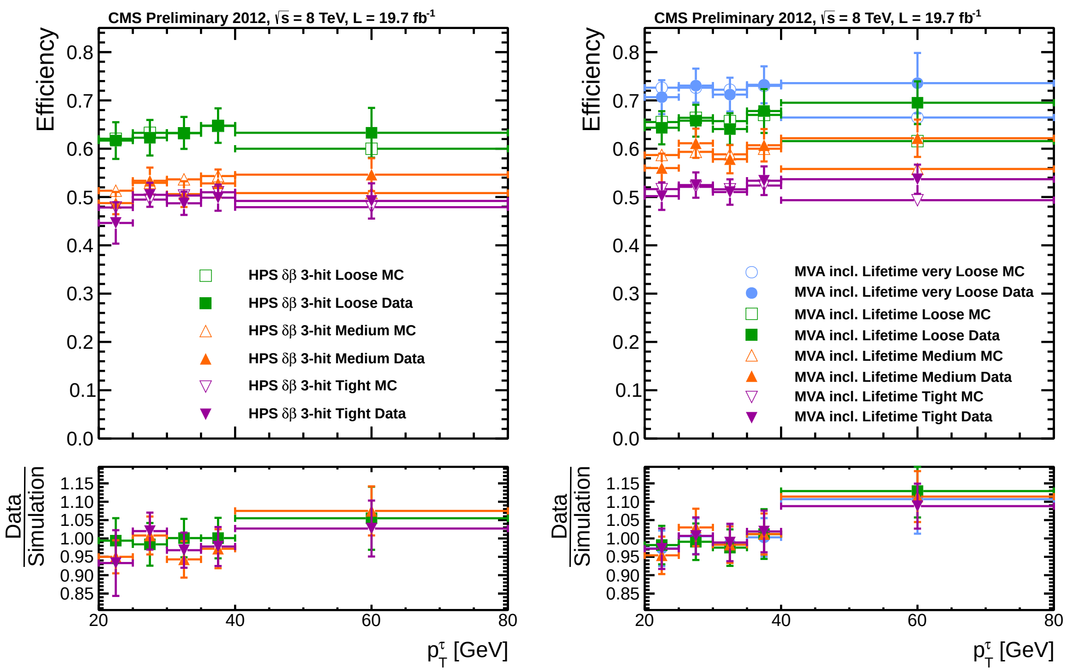

Figure 2: Tau identification efficiency measured as function of p_T in $Z \rightarrow \tau\tau \rightarrow \tau_\mu\tau_h$ events compared to Monte Carlo predictions, for the cut based HPS combined isolation (left) and for the MVA-based tau identification discriminator that includes tau lifetime information (right).

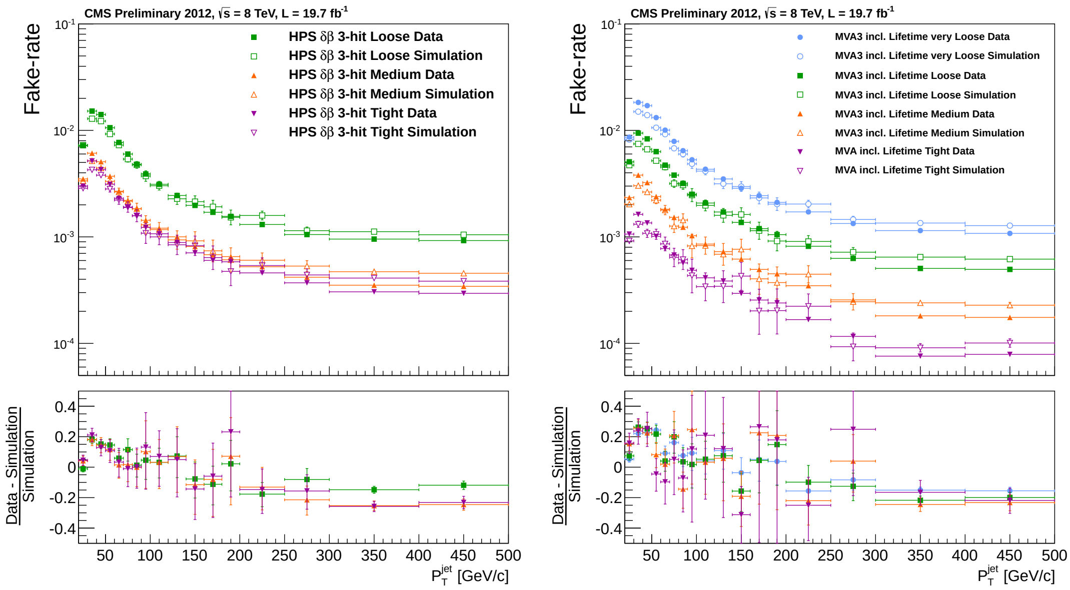

Figure 3: Jet $\to \tau_h$ misidentification rate in QCD multijet events, for cut based (left) and MVA-based (right) tau identification discriminators.

4 Conclusions

CMS has developed an advanced and robust τ_h reconstruction algorithm, which has been successfully commissioned with the data collected in LHC run 1. The decay mode of the tau is reconstructed correctly with a probability higher than 80%. The tau identification efficiency amounts to 50–60% and is almost independent as function of p_T, while the jet $\to \tau_h$ misidentification rate varies strongly with p_T, ranging from about 1% for low p_T jets and loose tau identification criteria to $\mathcal{O}(10^{-4})$ for high p_T jets and tight tau identification criteria.

References

[1] CMS Collaboration, *Performance of tau-lepton reconstruction and identification in CMS*, *JINST* **7** (2012) P01001, [`ins-det/1109.6034`].

[2] CMS Collaboration, Tau ID Performance, CMS-DP-2014-015, https://cds.cern.ch/record/1704439

[3] CMS Collaboration, Particle-Flow Event Reconstruction in CMS and Performance for Jets, Taus, and E_T^{miss}, CMS-PAS PFT-09-001 (2009).

Search for Supersymmetry in Events with one Photon, Jets and missing transverse Energy at $\sqrt{s} = 8$ TeV

Maximilian Knut Kiesel on behalf of the CMS collaboration

1. Physikalisches Institut B, RWTH Aachen University, Aachen, Germany

DOI: http://dx.doi.org/10.3204/DESY-PROC-2014-04/278

Gauge mediated supersymmetry breaking (GMSB) [1] is a scenario for physics beyond the standard model (SM) which can stabilize the mass of the SM Higgs boson, allow the grand unification of forces, and avoid the flavor problems endemic in other SUSY breaking scenarios.

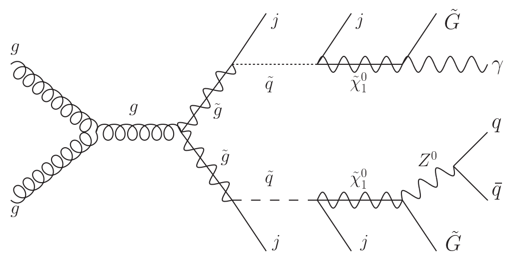

Figure 1: Event diagram for a typical photon final state expected within the GGM framework for a wino-like neutralino. A gluino pair is produced, which decays via squarks to neutralinos. The neutralinos decay to a photon or Z boson and a gravitino.

This search [2] is interpreted in the context of General Gauge Mediation (GGM) [3], in which the lightest SUSY particle is the gravitino ($\tilde{G}$) and the next-to-lightest SUSY particle the lightest neutralino ($\tilde{\chi}_1^0$), which can decay to a photon and a $\tilde{G}$ if the $\tilde{\chi}_1^0$ is bino- or wino-like. A typical process is shown in Fig. 1. R-parity is assumed to be conserved.

The data was recorded with the CMS detector [4] at the LHC during the 2012 run period with a center-of-mass energy of $\sqrt{s} = 8\,\mathrm{TeV}$. It corresponds to an integrated luminosity of $19.7\,\mathrm{fb}^{-1}$. On trigger level, one photon candidate with large transverse momentum and hadronic activity is required.

For the signal region, events with at least one photon reconstructed in the central part of the detector and with a transvere momentum $p_{\mathrm{T}^*} \geq 110\,\mathrm{GeV}$, hadronic activity $H_\mathrm{T} \geq 500\,\mathrm{GeV}$, two jets, missing transverse energy $\not{E}_\mathrm{T} \geq 100\,\mathrm{GeV}$, but no electrons nor muons are selected. The $\not{E}_\mathrm{T}$ and the particles which are clustered to jets are reconstructed using the particle-flow (PF) algorithm. The H_T is the scalar sum of the transverse momentum of all jets and all photon-like objects. The transverse momentum of the photon (p_{T^*}) is not estimaded by the energy deposit in the electromagnetic calorimeter only, but is estimated by the $p_\mathrm{T}$of the matched jet to the photon. This measurement of the transverse momentum is compatible for real photons and jets with a large neutral electromagnetic component. This is important for the major background estimation method, which relies on a similar kinematic for both types of objects. In addition, the photon identification requires that the energy deposits in the calorimeters must be photon-like. To discriminate between electrons and photons, the activity in in the

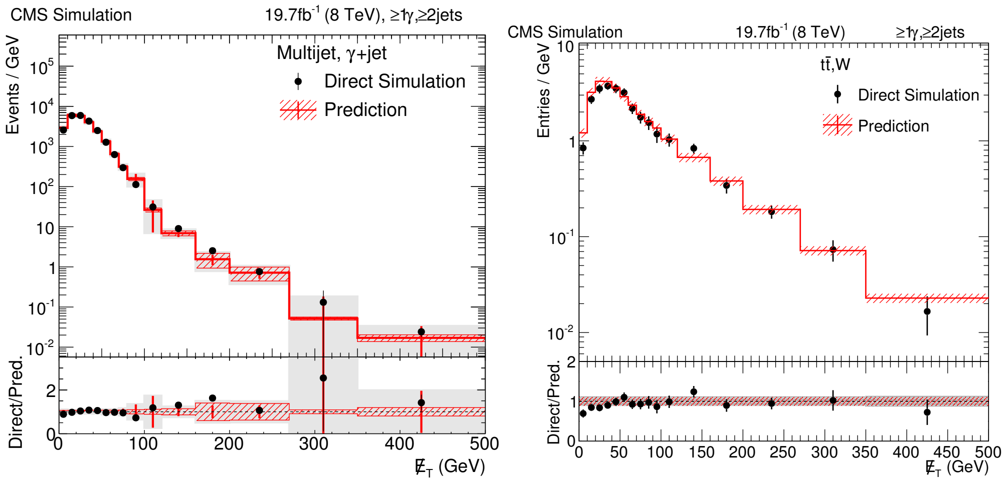

Figure 2: $\not\!\!E_{\mathrm{T}}$ distribution for simulated multijet and photon plus jet events (left) and simulated $\mathrm{t\bar{t}}$ and W boson events (right). The hatched area shows the systematical uncertainty of the data-driven background estimation method, and the gray area the total uncertainty.

tracker between vertex and the energy deposit in the calorimeter is restricted. Photons are also required to be isolated from other particles. Therefore, the sums of p_T of all charged hadrons, neutral hadrons and photons (except for the photon candidate itself), reconstructed with the PF algorithm within $\Delta R < 0.3$ to the photon candidate are calculated. These isolation deposits from charged hadrons ($\mathrm{I}_\pm$), neutral hadrons (I_0), and photons (I_γ) are required to be smaller than a threshold depending on the photon's transverse momentum.

The dominant background from SM processes origins from photon plus jet, or multijet events where one jet is misidentified as a photon. Mismeasurement of jets can lead to large $\not\!\!E_{\mathrm{T}}$ in these events. The contribution of these events to the signal region is estimated simultaneously from events with photon-like jets and low missing transverse energy using data. The photon-like jets are similar to the photon with respect to the shower shape, the tracker activity and the hadronic component, but have larger isolation deposits $\mathrm{I}_\pm$, I_0, and I_γ. The ratio of the number of events in the signal region to the number of events in this control region is calculated for $\not\!\!E_{\mathrm{T}} < 100\,\mathrm{GeV}$ in bins of p_{T^*} and the hadronic recoil. Hadronic recoil is the vectorial sum of the p_T of all jets, excluding the photon(-like) object. Events of the control sample with $\not\!\!E_{\mathrm{T}} \geq 100\,\mathrm{GeV}$ are scaled by this weight to estimate the contribution of multijet and photon plus jet production in the signal region. This method is tested on simulation: Figure 2 (left) shows the $\not\!\!E_{\mathrm{T}}$ distribution for simulated multijet and photon plus jet events compared to the prediction by the method described above. The direct simulation is in agreement with the prediction from simulation.

The contribution from electrons being misidentified as photons is estimated also from data. The probability of an electron faking a photon ($f_{e\to\gamma}$) is measured using the tag-and-probe method with $Z \to ee$ events. The rate is evaluated in bins of p_{T}, number of tracks emerging from the Z-boson vertex, and the number of vertices. A multidimensional fit is used to parametrize the misidentification probability. To estimate the background, a control region with electrons is defined by selecting photon candidates with hits in the tracker, which can be extrapolated to the energy deposit in the calorimeter. This sample is scaled event-by-event by $f_{e\to\gamma}$. Figure 2 (right)

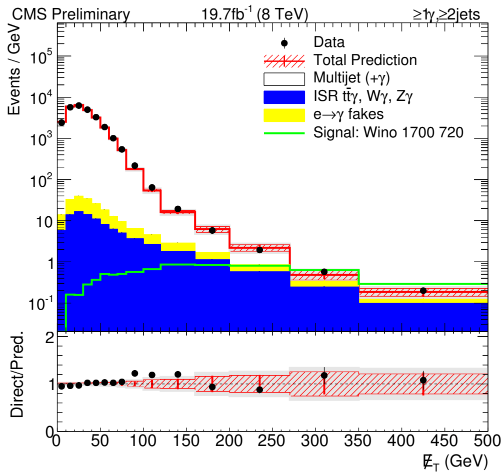

Figure 3: Total standard model background prediction as a function of $\not{E}_T$ compared to data. In addition GGM signal benchmark point with a wino-like neutralino with a neutralino mass of 375 GeV, a squark mass of 1700 GeV, and a gluino mass of 720 GeV is shown. The bottom ratio plot shows the event yields relative to the total background prediction. The hatched area represents the systematic uncertainty, the error bars the statistic uncertainty and the gray band the total uncertainty.

shows the $\not{E}_T$ distribution for simulated $t\bar{t}$ and W boson events compared to the prediction by the method described above. The direct simulation is in agreement with the prediction from simulation. Especially for high $\not{E}_T$, initial and final state radiation (ISR/FSR) contribute to the signal region. MADGRAPH [5] is used to simulate $t\bar{t}\gamma$, $W\gamma$, and $Z\gamma \rightarrow \nu\nu\gamma$ processes, which are scaled by a common scale factor. This scale factor is estimated by comparing MCFN [6] calculations, cross-section measurements and verification in a control region with $Z\gamma \rightarrow \mu\mu\gamma$ events. Events with electrons or muons are rejected in order to reduce the contribution from events with initial and final state radiation.

Figure 3 shows the total SM background prediction and the signal selection as function of $\not{E}_T$. A signal benchmark point with a $\tilde{\chi}_1^0$ mass of 375 GeV, a squark mass of 1700 GeV, and a gluino mass of 720 GeV is drawn in addition. The data is in agreement with the SM background prediction. The event yields, the background composition and the yields for the same signal benchmark point is shown in Table 1 for the bins used in the statistical interpretation. The result is interpreted in the GGM framework for bino- or wino-like neutralino scenarios as function of squark and gluino masses. The $\tilde{\chi}_1^0$ mass (and in the wino-like neutralino scenario the lightest chargino mass) is set to 375 GeV. Multi-channel counting experiments in the six distinct $\not{E}_T$-bins shown in Table 1 are combined into a single limit. The CL_s method is used to determine exclusions at 95% confidence level. Possible contamination of signal in the control sample used for background estimation is found to be of the order of 5–40%, and is considered in the limit calculation. Figure 4 shows the observed cross section limit (left) and the corresponding exclusion contours (right) for a wino-like neutralino scenario. For the bino-like neutralino scenario, gluino (squark) masses of 1100 (1350) GeV are excluded.

$\not{E}_T$ Range [GeV]	[100, 120)	[120, 160)	[160, 200)	[200, 270)	[270, 350)	[350, ∞)
Multijet(+photon)	991±164	529±114	180±69	95.6±45	11.7±12	9.1±9
Electron	37.3±4	42.5±5	23.0±3	19.2±2	7.7±1.0	4.1±0.6
ISR/FSR	53.6±27	72.5±36	44.9±23	40.1±20	19.7±10	14.7±7
Background	1082±166	644±119	248±73	155±50	39.0±16	27.8±12
Data	1286	774	232	136	46	30
Signal	18.8±3	53.1±5	50.5±5	82.3±7	77.7±7	67.3±6
Backg. from signal	2.1	5.0	5.6	9.9	26.7	13.5
Acceptance [%]	0.3	0.9	0.8	1.3	1.2	1.1
Exp. limit [pb]	5.23	1.21	0.57	0.24	0.14	0.11
Obs. limit [pb]	6.03	1.89	0.55	0.21	0.18	0.11

Table 1: Resulting event yields, estimated background, and yields for a GGM signal scenario for a wino-like neutralino scenario with a neutralino mass of 375 GeV, a squark mass of 1700 GeV, a gluino mass of 720 GeV, and a cross section of 316 fb. The combined observed (expected) CLs cross-section limit for this point is 99 fb (91 fb) at 95% CL.

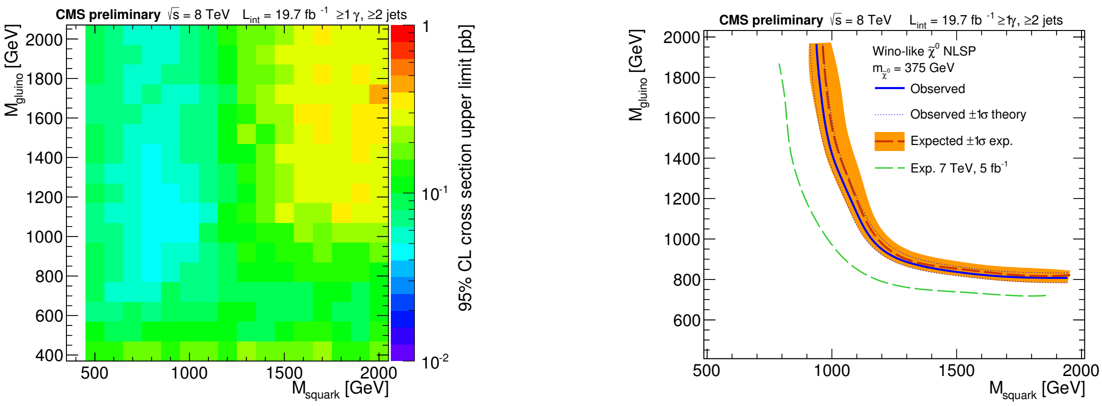

Figure 4: Observed upper limits (left) and exclusion contours (right) at 95% C.L. on the signal cross section in the gluino-squark mass space for the wino-like neutralino scenario. The exclusion contour of the previous analysis [7] is drawn in addition.

References

[1] Pierre Fayet. Mixing Between Gravitational and Weak Interactions Through the Massive Gravitino. *Phys.Lett.*, B70:461, 1977.

[2] CMS Collaboration. Search for supersymmetry in events with one photon, jets and missing transverse energy at $\sqrt{s} = 8$ TeV. CMS-PAS-SUS-14-004. 2014.

[3] Patrick Meade, Nathan Seiberg, and David Shih. General Gauge Mediation. *Prog.Theor.Phys.Suppl.*, 177:143–158, 2009.

[4] S. Chatrchyan et al. The CMS experiment at the CERN LHC. *JINST*, 3:S08004, 2008.

[5] Johan Alwall, Michel Herquet, Fabio Maltoni, Olivier Mattelaer, and Tim Stelzer. MadGraph 5 : Going Beyond. *JHEP*, 1106:128, 2011.

[6] John M. Campbell, Heribertus B. Hartanto, and Ciaran Williams. Next-to-leading order predictions for $Z\gamma$+jet and Z $\gamma\gamma$ final states at the LHC. *JHEP*, 1211:162, 2012.

[7] Serguei Chatrchyan et al. Search for new physics in events with photons, jets, and missing transverse energy in pp collisions at $\sqrt{s} = 7$ TeV. *JHEP*, 1303:111, 2013.

Statistical criteria for possible indications of new physics in tritium β-decay spectrum

Aleksei Lokhov[1], *Fyodor Tkachov*[2]

[1]Dept. of Experimental Physics, Institute for Nuclear Research RAS, 142190 Troitsk, Russia
[2]Dept. of Theoretical Physics, Institute for Nuclear Research RAS, 117312 Moscow, Russia

DOI: http://dx.doi.org/10.3204/DESY-PROC-2014-04/167

The method of quasi-optimal weights is applied to constructing (quasi-)optimal criteria for various anomalous contributions in experimental spectra. Anomalies in the spectra could indicate physics beyond the Standard Model (additional interactions and neutrino flavours, Lorenz violation etc.). In particular the cumulative tritium β-decay spectrum (for instance, in Troitsk-ν-mass, Mainz Neutrino Mass and KATRIN experiments) is analysed using the derived special criteria. Using the power functions we show that the derived quasi-optimal criteria are efficient statistical instruments for detecting the anomalous contributions in the spectra.

1 Introduction

Studying anomalies in experimental spectra extends our understanding of experimental setups. Besides anomalous contributions could also indicate new physics beyond the Standard Model. For instance, in tritium β-decay spectra possible additional interactions can lead to a step-like anomaly near the end-point while the excistance of the forth neutrino (with the mass of a few keV) induces a kink structure in the region of several keV from the end-point. Here we consider these two possible anomalous contributions.

The search for an anomaly should be based on a statistically reliable inference about presence or absence of the anomaly. Such inference is provided by special statistical criteria. One can construct the criteria according to each particular situation and accounting for some additional information about the theoretical model or experimental setup. The various approaches here are as follows:

1. Direct fit with additional parameters (the mass of neutrino and the mixing parameter, the amplitude and the position of the step) [1], [2], [3].
2. Searching for the kink with various filters [3].
3. Wavelet analysis [4].
4. Seaching for special functional dependencies.
5. Constructing special statistical criteria for the heavy neutrino or the step accounting for the uncertainties of other parameters (based on the method of quasi-optimal weights [5]). In the paper we present two examples of construction of the special statistical tests.

2 Step-like anomaly in Troitsk-ν-mass spectrum

Any deviations at the very end of the spectrum have crucial influence on the estimations of the neutrino mass squared. The spectrum of the Troitsk-ν-mass experiment is cumulative. The numbers of electrons are measured for a set of energies (these numbers have Poisson distributions). After that the measured data points are fitted with the theoretical curve. There are four fitted parameters in the Troitsk-ν-mass spectrum. One of them is the neutrino mass squared.

The first data analysis [1], performed with the standard Minuit routines, yielded rather controversial result: the estimate of the neutrino mass squared lies far beyond physically relevant range, it appears to be large and negative. This was interpreted as due to an excess of electrons near the end-point energy of the tritium β-decay spectrum; in cumulative spectra, such an excess takes the form of a step. Such a step is described by two parameters, the height and the position. Including these into the fit, a satisfactory value for the neutrino mass squared was obtained.

The recently finished new analysis [2] (exploiting the method of the quasi-optimal weights [5] and improved theoretical model of the experimental setup as well), yielded physically relevant values (within errors) of the neutrino mass squared while the step-structure has not been accounted for. The goodness-of-fit test included into the fitting procedure is not tuned to feel the anomalous contributions of this step-like form. It will be nice to have convenient, robust statistical criteria, particularly targeted to the described anomaly. We also should take into account that the position of the step is unknown and even may vary in time. We have constructed three special criteria and with them one can perform the standard procedure of the test of hypotheses [6], [7]. The null-hypothesis is that the height of the step is zero, the alternative - the height is positive. We use the fit from the new analysis [2].

The first criterion is constructed via routines of the method of quasi- optimal moments. And it is by construction the Locally Most Powerful (LMP) one. Locally here means near the null-hypothesis. The distributions for the experimental counts are $f_i(N) = \frac{\mu_i'^N e^{-\mu_i'}}{N!}$, where $\mu_i' \to \begin{cases} \mu_i + \Delta_-, i > m \\ \mu_i + \Delta_+, i \leq m \end{cases}$, i stands for the number of an experimental point. Here m is defined by the inequality $E_m \leq E_{st} \leq E_{m+1}$. Constructing the weights

$$\omega_i^+(N) = \frac{\partial \ln f_i}{\partial \Delta_+} = \begin{cases} 0, & i > m \\ \frac{N}{(\mu_i+\Delta_+)} - 1, & i \leq m \end{cases}, \omega_i^-(N) = \frac{\partial \ln f_i}{\partial \Delta_-} = \begin{cases} 0, & i \leq m \\ \frac{N}{(\mu_i+\Delta_-)} - 1, & i > m \end{cases}$$

and solving the corresponding equations $h^{exp} = \sum_i \omega_i = 0$ one obtains the statistics of the LMP criterion $\overline{\Delta} = \Delta_+ - \Delta_-$ – the estimate for the height of the step. $\overline{\Delta}$ can be also presented as a weighted sum of experimental counts $\overline{\Delta} = \sum_{i=1}^{M} w_i \cdot N_i$

Recalling the uncertainty of the step position it is useful to decrease the sensitivity of our criteria to the position of the step, even loosing some sensitivity to the step itself. For this we slightly change the weights in the sum of the LMP test (see Fig. 1), to suppress the values near the position of the step, saving the properties of the LMP test in the rest areas. The corresponding statistics is $S_{q-opt} = \sum_i^k w_i \cdot \xi_i$, where $\xi_i = \frac{N_i - \mu_i}{\sqrt{\mu_i}}$ and $w_i = \begin{cases} \frac{(m-i)}{m}, & i \leq m, \\ \frac{(m-i)}{M-m}, & i > m. \end{cases}$

One more criterion, $S_{pair} = \sum_i \xi_i \cdot \xi_{i+1}$, constructed somehow speculatively, exploits the following idea: if the anomaly is a deviation of several neighbour points to one side of the fitting curve (Fig. 3) than it will increase the value of the statistics S. Thus the pairwise neighbours' correlations test can be used as a criterion for rather general class of anomalies.

We can compare all these criteria using the standard tool of Power Functions. The power function is simply the probability of a criterion to reject the null hypothesis while it is in fact false. As on can see on Fig. 4 the LMP (1) is the best here, the quasi-optimal (2) is slightly less powerful, the pairwise neighbours correlations test (3) comes third and the conventional tests (4,5) are the least sensitive. The situation changes if the assumed position of the step is not correct. The left graph in Fig. 5 shows that the LMP test (1) is loosing its sensitivity rather rapidly while two other special tests remain rather powerful.

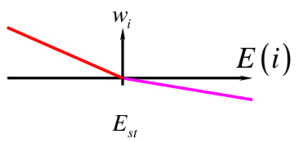

Figure 1: The quasioptimal weights for the step-like anomaly searches

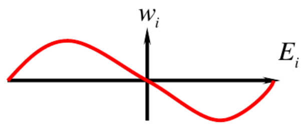

Figure 2: The quasioptimal weights for the heavy neutrino searches

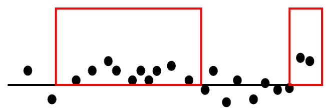

Figure 3: The idea of the pairwise neighbours correlations criterion

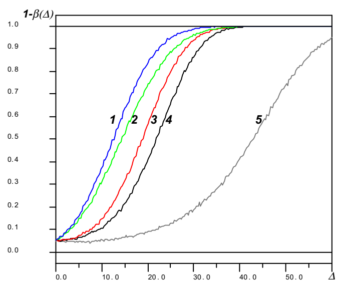

Figure 4: The power functions for the special and conventional criteria

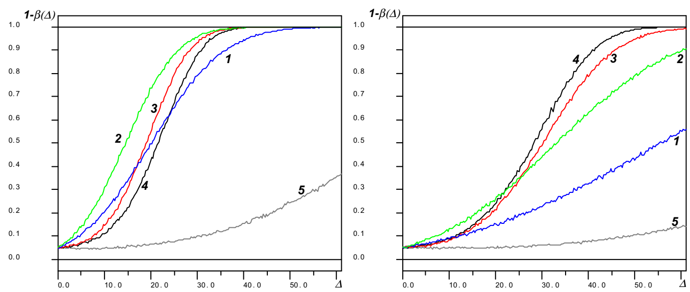

Figure 5: The power functions of the five criteria for the cases when the actual step position is shifted from the assumed position E_m by 12 eV (left) and 25 eV (right)

3 Heavy neutrino searches

Similarly to the case of step-like anomaly one can derive special criteria for the search of a heavy neutrino in β-decay spectrum

$$\frac{d\Gamma}{dE} = \sin^2\theta \left(\frac{d\Gamma}{dE}\right)_{m_{keV}} + \cos^2\theta \left(\frac{d\Gamma}{dE}\right)_{m_{light}}.$$

The spectrum $\frac{d\Gamma}{dE}(E_i, m) = S_{i,m}$ is again measured in a number of points with various retarding potentials. The spectrum is defined by the mixing parameter $U^2 = \sin^2\theta$ and the mass of the heavy neutrino m_{keV}. The mass of the light neutrino is considered to be $m_{light} = 0$. Thus the theoretical means are $\mu_i' = U^2 S_{i,m_H} + (1 - U^2) S_{i.m=0}$. The first test (the LMP) is obtained via the method of quasi-optimal weights and it is by construction the most sensitive one in case when the mass of the heavy neutrino is well-known. The corresponding weights are as follows:

$$\omega_i = \frac{\partial \ln f_i}{\partial U^2} = \left(\frac{N}{U^2 S_{i,m_H} + (1 - U^2) S_{i,m=0}} - 1 \right) \cdot (S_{i,m_H} + S_{i,0}).$$

Using these weights one constructs an equation $\frac{1}{M} \sum_{i=1}^{M} \omega_i = 0$ for the mixing parameter estimate $\widehat{U^2}$ – the statistics of the LMP criterion.

To reduce the sensitivity of our test to the mass we modify the weights (for instance, as shown in Fig. 2) to obtain the quasi-optimal criterion $S_{q-opt} = \sum_i^k w_i \cdot \xi_i$. It is more robust and require no information about the exact mass of the additional neutrino. The universal pairwise neighbours correlatiosn test can be exploited in the case of kink searches as well.

4 Conclusions

We illustrated the new approach to the search for anomalies in experimental spectra with account for the parameters with uncertainties (the position of the step-like anomaly and the mass of the additional neutrino in our examples). We showed that the Locally Most Powerful criterion for each anomalous contribution can be constructed via the method of quasi-optimal moments. Than the LMP test can be tuned to reduce the influence of the unknown parameters of the spectra. With the help of the power functions the constructed criteria are proved to be more efficient in searches for the specific anomalous contributions. The next step is to compare the sensitivity of the constructed tests with the wavelet analysis [4], direct fitting and search for the kink with filters [3]. The approach appears to be useful for the future searches of the heavy neutrino in Troitsk [8], [9] and Karlsruhe [3].

One of the authors (A.L.) would like to thank Christian Sander and Alexander Schmidt for the invitation to participate in PANIC14, Matthias Kasemann, Kristina Price and all the organising committee for their fantastic job in organising this conference.

The work has been supported by RFBR grant 14-02-31055.

References

[1] V.M. Lobashev, Nucl. Phys. A. **719** 153 (2003).

[2] V.N. Aseev *et al.*, Phys. Rev. D. **84** 112003 (2011).

[3] S. Mertens *et al.*, arXiv:1409.0920 (2014).

[4] S. Mertens *et al.*, arXiv:1410.7684 (2014).

[5] F.V. Tkachov, arXiv:physics/0704127 (2006).

[6] A.V. Lokhov, F.V. Tkachov, P.S. Trukhanov, Nucl. Instrum. Meth. A**686** 162 (2012).

[7] A.V. Lokhov, F.V. Tkachov, P.S. Trukhanov, Nucl. Phys. A **897** 218 (2013).

[8] D. Abdurashitov *et al.*, arXiv:1403.2935 (2014).

[9] A.I. Belesev *et al.*, J. Phys. G: Nucl. Part. Phys **41** 015001 (2014).

Monitoring of Cabling Activities during the LHC LS1

Stefano Meroli, Simao Costa Machado, Fabio Formenti, Marten Frans, Jean-Claude Guillaume, Serge Oliger, Daniel Ricci

CERN, European Organization for Nuclear Research, 1211 Geneve 23, Switzerland

DOI: http://dx.doi.org/10.3204/DESY-PROC-2014-04/176

The development of a reliable monitoring system was a key element in the successful consolidation and upgrade of the cabling infrastructure of the CERN accelerator complex during the LHC first shutdown period. This paper presents the implementation and use of this monitoring system during the two year-long shutdown, focusing on improvements delivered in project management and providing practical examples of applications.

1 Introduction

The Large Hadron Collider (LHC) at CERN entered into its first long shutdown period (LS1) in February 2013 [1]. In this framework, the consolidation and upgrade of the cabling infrastructure of the CERN accelerator complex represented one of the most challenging projects in terms of complexity and workload [2]. The undertaking has required substantial project management effort and a significant deployment of resources, consisting of CERN staff and industrial support contractors [3]. A monitoring system has been then developed to support the project management dealing with project preparation and execution.

2 The goals

The consolidation and upgrade of the cabling infrastructure consisted of a large number of activities distributed over 350 worksites. They were carried out to a tight schedule and often in radioactive environments or as part of a coordinated activity with other CERN groups. Table 1 provides a numerical summary of the project.

	Project cost	Cable length installed	Connectors installed
Copper Cabling	14.3 MCHF	1000 km	21000
Optical Fibre Cabling	7.3 MCHF	260 km	95000
Total	21.6 MCHF	1260 km	116000

Table 1: Consolidation and upgrade of the cabling infrastructure, the main numbers.

Performing the cabling activities in these conditions turned out to be very demanding in terms of work organization and execution, requiring anticipation of strategic actions and a fast turn-around control of project status.

For this reason CERN has developed a ***comprehensive*** monitoring system, supporting the project management, to deal with all critical aspects of the project such as duration, cost, resource availability, safety (namely: radiation dose absorbed by the personeel) and installation quality. During the LS1 the monitoring system has served the dual purposes of recording project performance as well as of predicting its future evolution, warning on possible coming issues and easing the identifications of delays and the implementation of changes to the project.

3 The monitoring system structure

The monitoring system consisted of a set of software, tools and procedures working together with the aim of summarizing the large number of data sources in simple graphs and tables.

Weekly meeting with industrial support contractors, inspections on the worksites as well as reports from activity supervisors have assured ***quick*** feedback on the six most challenging aspects of the project. Based on this input, a dedicated software system processed the information allowing comparisons of actual outcomes with the original baseline and forecasts. The scheme in Figure 1 shows the structure implemented with the six aspects monitored.

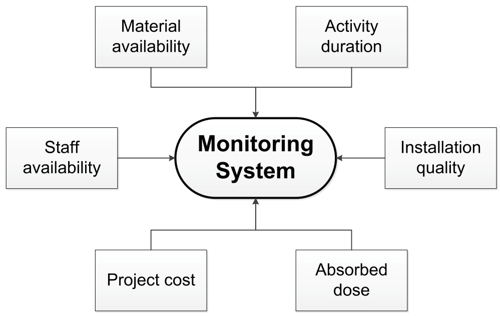

Figure 1: Monitoring system structure.

The ***activity duration*** was followed through an in-house software system called GESMAR, in which industrial support staff introduced on a daily basis the information for each pulled cable, connector assembly and test. They also updated the progress of the mechanical installation, the cable removal, the reworking and activity verification. Stock availability and timely delivery of the ***material*** on the worksite were verified in parallel. The number of CERN and industrial support contractor ***staff*** deployed on the worksite (roughly 150 people in total) was constantly monitored by using the accelerator access control systems installed on the site or through feedback from the activity supervisors. Monitoring of the ***project cost*** was required to make sure that the project remained within the budget margin. Reports on payments to industrial contractors were provided together with forecasts of budget engagements. The CERN safety rules demand a precise estimation and follow up of the ***radiation dose*** absorbed by workers. Daily reports alerted project manager in case the absorbed dose exceeded the estimated limit. Finally the ***quality*** of the installation delivered to the users was verified by continuous field inspections. Warning notes were issued in case of the quality requirements were at risk of not being satisfied.

4 Data analysis and reporting

Automatic reports on overall project performance were extracted daily and used as indicators. Offline analysis and the cross checking of the collected data allowed detection of potential activity issues like planning delays, resources constraints or failures to comply with the approved working procedures.

The example of the PS Booster cabling activity has showed the effectiveness of the tool (see Figure 2). During the cabling installation, the tool predicted that the radiation dose absorbed by the workers would exceed the safety limit, alerting management and allowing a pre-emptive adjustment to the method used.

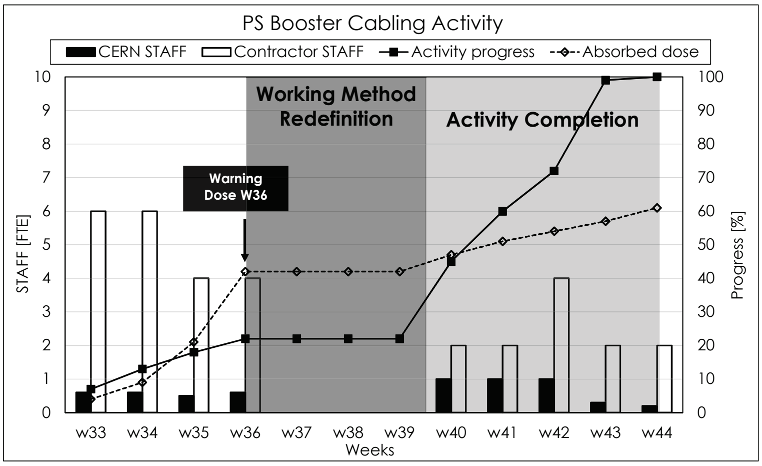

Figure 2: PS Booster activity report.

Figure 3 shows a set of graphs used to review the overall project performance.

The number of activities completed was monitored weekly in order to define the overall project completion percentage. More or less resources were assigned to the worksites in case of delay or required acceleration of the schedule, guaranteeing the respect of the deadlines and preventing a domino effect on the whole project planning. As it can be seen in Figure 3(a) the actual progress followed the original baseline all along the LS1. Only a minor delay occurred due to the addition of unforeseen activities to the planning, slowing down the overall project execution.

Figure 3(b) shows the non-conformities detected on the worksites grouped by four categories: organization (i.e. problem related to the industrial support contract internal organisational), planning (i.e. non respect of the mutually deadlines agreed), quality (i.e. problems associated to the quality of the works performed) and security (i.e. non respect of safety rules and regulations). The analysis allowed the identification, classification and definition of corrective actions for the installations, delivering improvement to the working method and bringing about significant improvements to the global quality of the installations.

Figures 3(c) and (d) show respectively the industrial support contract and CERN staff load curve over the entire LS1 period. Forecast load curves, based on estimates of future workload, have allowed resource requirements to be set up in advance. During 2014, additional resources had been put in place to cope with unforeseen cabling activities, leading management to engage an additional industrial support contract. The load curves also addressed changes to the planning to mitigate manpower constraints. Activities were anticipated or postponed to smooth as much as possible the load curve and prevent wherever possible the presence of troublesome peaks and holes (planning "agility").

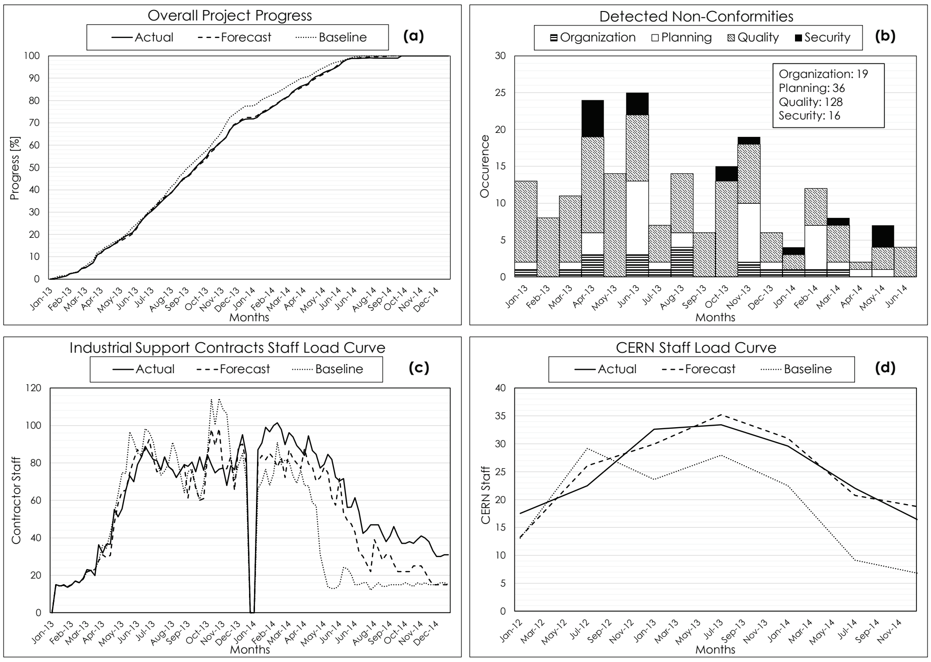

Figure 3: (a) overall project progress; (b) distribution of non-conformities detected during the work execution; (c) industrial support contract staff load curve; (d) CERN staff load curve

5 Conclusion

The implementation of a monitoring system played a fundamental role in the successful execution of the cabling activities during the LS1. About 1300 kilometers of cables, distributed in different machine areas and representing an investment of about 21.6 MCHF, have been installed respecting the schedule. The system proved its effectiveness throughout the LS1 by assisting the project management in the definition of anticipated strategic actions and to implement changes to the project. Furthermore the tool supported the improvement of the general working method allowing the Long Shutdown 2 to be planned on a much more informed basis.

Acknowledgments

Authors wish to thank James Dilwyn Devine for supporting in the review of this document.

References

[1] K. Foraz *et al.*, *LHC Long Shutdown: a parenthesis for a challenge*, 4th International Particle Accelerator Conference IPAC13, Shanghai, Cina (2013).

[2] F. Duval, *LS1: electrical engineering upgrades and consolidation*, Chamonix Workshop on LHC Performance, Chamonix, France (2012).

[3] S. Meroli *et al.*, *The management of large cabling campaigns during the Long Shutdown 1 of LHC*, JINST **C03042** 9 (2014).

Search for supersymmetry in opposite-sign same-flavour lepton pairs with the CMS detector

Jan-Frederik Schulte[1] on behalf of the CMS Collaboration

[1]I. Physikalisches Institut B, RWTH Aachen University, Germany

DOI: http://dx.doi.org/10.3204/DESY-PROC-2014-04/283

A search for Supersymmetry in events with opposite-sign same-flavour lepton pairs is presented. This final state, in addition to requirements on the number of jets and missing transverse energy, allows for a large reduction as well as a precise estimation of standard model backgrounds. In the cascade decays of new heavy particles, correlated production of leptons can lead to distinctive 'edges' in the dilepton invariant mass spectrum, caused by the mass differences between the new particles. Presented is the search for such a mass edge in a dataset of pp collisions at $\sqrt{s} = 8\,\text{TeV}$, corresponding to $19.4\,\text{fb}^{-1}$, collected with the CMS detector [1] at the CERN LHC.

This analysis [2] focuses on the correlated production of same-flavor (SF) opposite-sign (OS) leptons in cascade decays of new heavy particles. Examples for this are decays of the second neutralino into the first neutralino and a SF OS lepton pair, either via an intermediate slepton or on- or off-shell Z bosons, as illustrated in Fig. 1. The mass difference between the two neutralinos sets an upper limit on the invariant mass of the lepton pair, leading to a characteristic edge. The experimental signatures of these decays are the SF OS lepton pair, missing transverse energy (E_T^{miss}) from the undetected LSPs, and several jets from other parts of the cascade and the decay of the second initially produced sparticle.

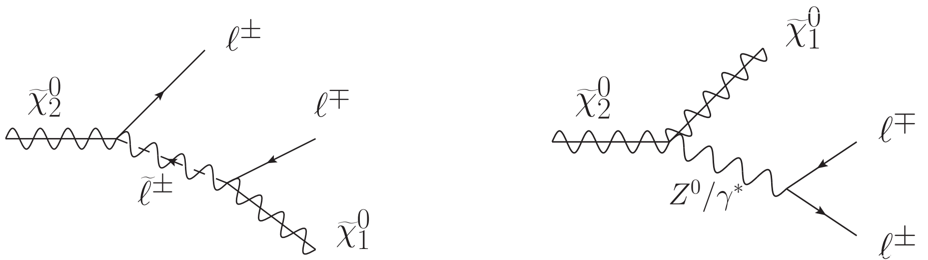

Figure 1: Diagrams of the possible decay modes of the second neutralino resulting in an edge in the dilepton invariant mass sepctrum.

The considered event samples are collected with dilepton triggers, requiring two light leptons (e,μ) with $p_T > 17\,\text{GeV}$ for the first and $p_T > 8\,\text{GeV}$ for the second lepton. Events are then required to contain two SF OS light leptons with $p_T > 20\,\text{GeV}$ and a pseudorapidity of $|\eta| < 2.4$. The dilepton invariant mass $m_{\ell\ell}$ is required to be greater than 20 GeV. The event sample is split into the 'central' (both leptons $|\eta| < 1.4$) and 'forward' (at least on lepton $|\eta| > 1.6$) regions. Three regions are defined in E_T^{miss} and the number of jets $\mathrm{N_{jets}}$. A control region enriched in events produced by the Drell-Yan process requires $\mathrm{N_{jets}} \geq 2$ and $E_T^{miss} < 50\,\mathrm{GeV}$. Events with exactly two jets and E_T^{miss} between 100 GeV and 150 GeV fall into a control region dominated by top-pair production. Finally, the signal region is defined by requiring either $E_T^{miss} > 150\,\mathrm{GeV}$ and $\mathrm{N_{jets}} \geq 2$, or $E_T^{miss} > 100\,\mathrm{GeV}$ and $\mathrm{N_{jets}} \geq 3$. A kinematic fit considers the mass range from 20 GeV to 300 GeV, while for a counting experiment the range is restricted to 20 GeV to 70 GeV.

Two types of standard model (SM) backgrounds contribute to the signal selection. The main source of backgrounds are flavor-symmetric processes, which produce SF lepton pairs as often as opposite flavor (OF) pairs. They are in turn dominated by dileptonic decays of top pairs, but also the Drell-Yan process where the boson decays to two tau leptons, W boson pair production or misidentified leptons contribute. The second type of backgrounds are processes producing a Z boson decaying into two light leptons.

Flavor-symmetric backgrounds are predicted from the OF sample, which in principle has the same event yield and kinematic properties as the SF sample. As this symmetry might be broken by the different efficiencies for trigger, reconstruction and identification of the different lepton flavors, a correction factor is derived from two independent methods, utilizing orthogonal event samples. The first method is the direct measurement of the ratio $R_{SF/OF}$ in the top-pair dominated control region. This method is limited by the statistical uncertainties of this measurement. The second method measures the efficiencies of the dilepton triggers (ϵ_{ee}^{trig},$\epsilon_{\mu\mu}^{trig}$,ϵ_{OF}^{trig}) as well as the ratio of the selection efficiencies for muons and electrons $r_{\mu e}$. The correction factor is then calculated as $R_{SF/OF} = \frac{1}{2}(r_{\mu e} + \frac{1}{r_{\mu e}})\frac{\sqrt{\epsilon_{ee}^{trig}\epsilon_{\mu\mu}^{trig}}}{\epsilon_{OF}^{trig}}$. The precision of this method is limited by the systematic uncertainties introduced by the extrapolation of the efficiency measurements into the signal region. The results from both methods are consistent and are combined according to their respective uncertainties. The resulting values are $R_{SF/OF} = 1.00 \pm 0.04$ for central leptons and $R_{SF/OF} = 1.11 \pm 0.07$ for forward leptons.

For the counting experiment at low $m_{\ell\ell}$, the background from SM processes containing a Z boson is estimated by first deriving an estimate for the contribution of these processes on the Z peak for $m_{\ell\ell}$ between 81 GeV and 101 GeV with two independent methods. The first one uses the balance of the Z against the jets in the event to predict the contribution of these backgrounds in regions with high E_T^{miss}. The second predicts the contribution from Z bosons using events with single photons. The results of both methods are consistent and are averaged according to their uncertainties. The prediction for the Z peak region is extrapolated to low masses using a scale factor, determined in the Drell-Yan enriched control region.

The results of the counting experiment at low invariant masses are shown in Tab. 1. For the dominant flavor-symmetric backgrounds a precision of the estimate of 5% for the central region and 10% for the forward region has been achieved. In the forward region there is good agreement between background expectation and observation, while in the central region there is a small excess with a local significance of 2.6σ. This can also be seen in Fig. 2, which shows the invariant mass distribution in the signal region separately for central and forward leptons.

The search for a kinematic edge in the dilepton mass spectrum is performed using an unbinned maximum likelihood fit, simultaneous to the ee, $\mu\mu$ and OF event samples in both the central and forward lepton selection. The only parameter shared between the models for the forward and central selection is the position of the edge $m_{\ell\ell}^{edge}$. The fit model consists of four components. The signal model is a triangular shape, smeared with the expected detector

	Central	Forward
Observed [SF]	860	163
Flav. Sym. [OF]	$722 \pm 27 \pm 29$	$155 \pm 13 \pm 10$
Drell–Yan	8.2 ± 2.6	1.7 ± 1.4
Total estimates	730 ± 40	157 ± 16
Observed – Estimated	130^{+48}_{-49}	6^{+20}_{-21}
Significance [σ]	2.6	0.3

Table 1: Results of the counting experiment for event yields in the signal regions. Statistical and systematic uncertainties are added in quadrature, except for the flavor symmetric backgrounds.

resolution:

$$\mathcal{P}_S(m_{\ell\ell}) = \frac{1}{\sqrt{2\pi}\sigma} \int_0^{m_{\ell\ell}^{edge}} dy \cdot y \cdot e^{\frac{-(m_{\ell\ell}-y)^2}{2\sigma^2}}. \tag{1}$$

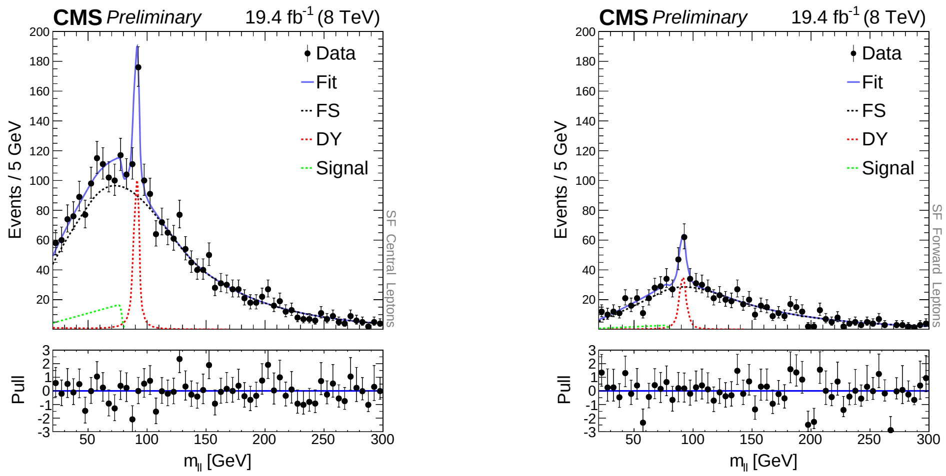

Figure 2: Invariant mass distriubtions in the signal region. The data is shown as black points, while the background prediction is shown as a red line. The total uncertanty on the background is indicated in blue. The Drell-Yan background component is shown in green (colored version can be found online).

Backgrounds containing a Z boson are described by a Breit-Wigner distribution convolved with a double-sided Crystal Ball function for the peak component and a falling exponential for the continuum component. The model is in a first step fitted in the Drell-Yan enriched control region. Afterwards, all parameters are fixed and only the normalization is a free parameter in the fit in the signal region. Flavor-symmetric backgrounds are described by a model consisting of three parts; a kinematic turnon at low $m_{\ell\ell}$, an exponential fall at high $m_{\ell\ell}$, and a polynomial to describe the transition between the two:

$$\mathcal{P}_{FSE}(m_{\ell\ell}) = \begin{cases} \mathcal{P}_{FSE,1}(m_{\ell\ell}) = c_1 \cdot m_{\ell\ell}^{\alpha} & \text{if } 20GeV < m_{\ell\ell} < m_{\ell\ell}^{(1)} \\ \mathcal{P}_{FSE,2}(m_{\ell\ell}) = \sum_{i=0}^{3} c_{2,i} \cdot m_{\ell\ell}^{i} & \text{if } m_{\ell\ell}^{(1)} < m_{\ell\ell} < m_{\ell\ell}^{(2)} \\ \mathcal{P}_{FSE,3}(m_{\ell\ell}) = c_3 \cdot e^{-\beta m_{\ell\ell}} & \text{if } m_{\ell\ell}^{(2)} < m_{\ell\ell} < 300GeV \end{cases}$$

The background yields for the flavor-symmetric backgrounds in the SF and OF categories are connected via the correction factor $R_{SF/OF}$, which is a nuisance parameter in the fit. The fit results are shown in Tab. 2. The best fitted value for the edge position is 78.7±1.4 GeV and the fitted signal yield is 126±41 events in the central and 22±20 events in the forward region. The local significance of the result is 2.4σ. The invariant mass distributions together with the fit result are shown in Fig. 3.

	Central	Forward
Drell–Yan	158 ± 23	71 ± 15
Flav. Sym. [OF]	2270 ± 44	745 ± 25
$R_{SF/OF}$	1.03	1.02
Signal events	126 ± 41	22 ± 20
$m_{\ell\ell}^{\text{edge}}$ [GeV]	78.7 ± 1.4	
Local Significance [σ]	2.4	

Table 2: Results of the unbinned maximum likelihood fit for event yields in the signal regions.

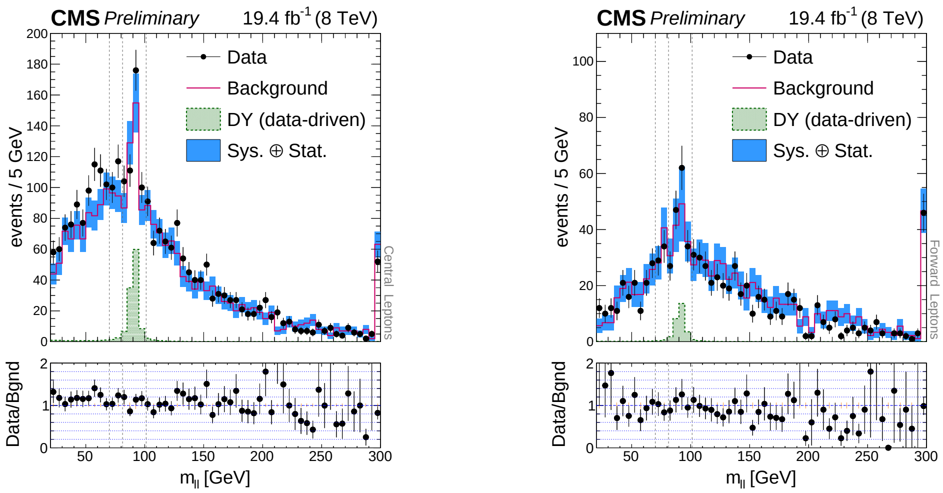

Figure 3: Invariant mass distriubtions in the signal region. The data is shown as black points, while the fit result is shown in blue. The different fit components are shown in green for the signal model, black for the model for flavor-symmetric backgrounds and in red for the Drell-Yan background (colored version can be found online).

A search for Supersymmetry in same-flavor opposite-sign dilepton events with jets and E_T^{miss} has been presented. SM backgrounds are predicted from data with high precision. A fit is performed in search for a edge in the dilepton invariant mass spectrum. Although a small excess has been observed at low invariant masses, no evidence for a statistically significant signal has been observed. This result highlights the opportunities of high precision searches at the LHC and preparations are ongoing to repeat this analysis in 2015.

References

[1] S. Chatrchyan et al. The CMS experiment at the CERN LHC. *JINST*, 3:S08004, 2008.

[2] Search for physics beyond the standard model in events with two opposite-sign same-flavor leptons, jets, and missing transverse energy in pp collisions at sqrt[s] = 8 TeV. Technical Report CMS-PAS-SUS-12-019, CERN, Geneva, 2014.

Chiral two- and three-nucleon interactions used in ring diagram method for binding energy of ^{4}He

Yiharn Tzeng[1], *Shwu-Yun Tsay Tzeng*[2], *T. T. S. Kuo*[3]

[1]Institute of Physics, Academia Sinica, Taipei 11529, Taiwan, ROC
[2]Dept. of Electro-Optical Engineering, National Taipei University of Technology, Taipei 10608, Taiwan, ROC
[3]Department of Physics, State University New York at Stony Brook, New York 11794, USA

DOI: http://dx.doi.org/10.3204/DESY-PROC-2014-04/50

In this work, we carry out ring-diagram calculationsfor ^{4}He using the chiral N^{3}LO two-nucleon potential V_{2N} with and without the inclusion of an in-medium three-nucleon (NNN) force $\bar{V}_{3N}$, derived from the leading-order chiral NNN force V_{3N}.

The ring-diagram method [1] is based on the the linked-diagram expansion [2] where the ground-state energy shift ΔE_0 is given by $\Delta E_0 = E_0 - E_0^{\text{free}} = \lim_{t' \to -\infty} [\frac{\langle \Phi_0 | V U(0,t') | \Phi_0 \rangle}{\langle \Phi_0 | U(0,t') | \Phi_0 \rangle}]_{\text{linked}}$ with $U(0,t')$ the time-evolution operator, and E_0 and E_0^{free} respectively the true and non-interacting ground-state energies of the nuclear system with the nuclear hamiltonian $H = T + V$, Φ_0 the system's unperturbed shell-model ground-state wave function. Here we take $V = V_{2N} + \bar{V}_{3N}$.

In calculating ΔE_0, we include only all-order sum of the *pphh* ring diagrams as illustrated in Fig. 1. As shown, diagrams (b), (c) and (d) are respectively the 1st-, 4th- and 8th-order *pphh* diagrams. It may be noted that our ring-diagram calculation reduces to the usual Hartree-Fock (HF) one if only the first order ring diagram (b) is included. A main purpose of our present work is to study the effect of the particle-hole excitations, which are not included in the HF case, to the binding energies of finite nuclei. Indicated by (a) of the Figure is the mean field single particle (s.p.) propagators where the HF one-bubble insertions are included to all orders.

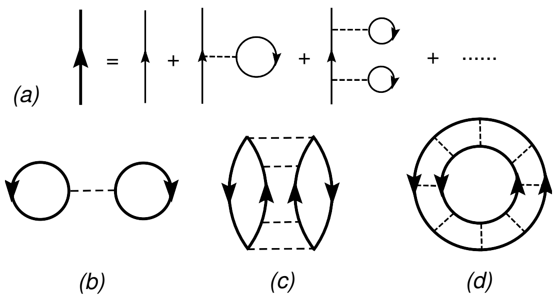

Figure 1: The *pphh* ring-diagrams for the ground state energy shift of closed-shell nuclei; (a) self-energy insertions on the single-particle propagator, and (b) to (d) all-order ring diagrams.

Summing up these ring diagrams to all orders, one has the ground-state energy shift from V as [1]

$$\Delta E_0 = \int_0^1 d\lambda \sum_m \sum_{ijkl \in P} Y_m(ij,\lambda) Y_m^*(kl,\lambda) \times \langle ij|V|kl\rangle, \tag{1}$$

where (i,j,k,l) are each a shell-model s. p. wave function, and P denotes a chosen shell-model space composed of a set of hole (h) and particle (p) orbits.

The amplitudes Y above are calculated from an RPA-type equation, namely

$$\sum_{ef} [(\epsilon_i + \epsilon_j)\delta_{ij,ef} + \lambda(1 - n_i - n_j)\langle ij|V|ef\rangle] \times Y_m(ef,\lambda) = \omega_m(\lambda) Y_m(ij,\lambda); \quad (i,j,e,f) \in P, \tag{2}$$

where λ is a strength parameter, to be integrated from 0 to 1 as in Eq. 2. The occupation factors are $n_a = 1$ for $a = h$, and $= 0$ otherwise. Thus the amplitudes $Y_m(ij)$ has only either hh ($i = h$, $j = h'$) or pp ($i = p$, $j = p'$) components. The transition amplitudes Y can be classified into two types, one dominated by hh and the other by pp components. We include only the former, denoted by Y_m, for the calculation of the all-order sum of the $pphh$ ring diagrams.

We use HF s.p. spectrum ϵ_j in the above RPA equation, as indicated earlier in Fig. 1, namely $\epsilon_j = \langle j|K_{sp}|j\rangle + \sum_h \langle jh|V|jh\rangle$ where K_{sp} denotes the s. p. kinetic energy operator. Note that j and h are each oscillator s. p. wave function.

To carry on, we need first describe the V_{3N} to be employed. The leading contribution to V_{3N} occurs at N^{2}LO in the chiral power counting and is composed of a long-range two-pion exchange $V_{3N}^{2\pi}$, a medium-range one-pion exchange $V_{3N}^{1\pi}$, and a pure contact interaction V_{3N}^{ct}:

$$V_{3N}^{(2\pi)} = \sum_{i \neq j \neq k} \frac{g_A^2}{8 f_\pi^4} \frac{\vec{\sigma}_i \cdot \vec{q}_i \, \vec{\sigma}_j \cdot \vec{q}_j}{(\vec{q_i}^2 + m_\pi^2)(\vec{q_j}^2 + m_\pi^2)} F_{ijk}^{\alpha\beta} \tau_i^\alpha \tau_j^\beta, \tag{3}$$

$$V_{3N}^{(1\pi)} = -\sum_{i \neq j \neq k} \frac{g_A c_D}{8 f_\pi^4 \Lambda_\chi} \frac{\vec{\sigma}_j \cdot \vec{q}_j}{\vec{q_j}^2 + m_\pi^2} \vec{\sigma}_i \cdot \vec{q}_j \, \vec{\tau}_i \cdot \vec{\tau}_j, \qquad V_{3N}^{(\mathrm{ct})} = \sum_{i \neq j \neq k} \frac{c_E}{2 f_\pi^4 \Lambda_\chi} \vec{\tau}_i \cdot \vec{\tau}_j, \tag{4}$$

with $g_A = 1.29$, $f_\pi = 92.4$ MeV, $\Lambda_\chi = 700$ MeV, and $m_\pi = 138.04$ MeV/c^2 the average pion mass, $\vec{q}_i = \vec{p_i}' - \vec{p}_i$ is the difference between the final and initial momentum of nucleon i and $F_{ijk}^{\alpha\beta} = \delta^{\alpha\beta}\left(-4c_1 m_\pi^2 + 2c_3 \vec{q}_i \cdot \vec{q}_j\right) + c_4 \epsilon^{\alpha\beta\gamma} \tau_k^\gamma \vec{\sigma}_k \cdot (\vec{q}_i \times \vec{q}_j)$. The low-energy constants $c_1 = -0.76\,\mathrm{GeV}^{-1}$, $c_3 = -4.78\,\mathrm{GeV}^{-1}$, and $c_4 = 3.96\,\mathrm{GeV}^{-1}$ appear already in the N^{2}LO two-nucleon potential and are thus constrained by low-energy NN phase shifts [3]. The constants c_D and c_E are typically fit to reproduce the properties of light nuclei [4, 5].

As mentioned earlier, the interaction $V = (V_{2N} + \bar{V}_{3N})$ will be employed in our calculations. V_{2N} is the NN interaction obtained from a N^{3}LO chiral two-body potential [6] and $\bar{V}_{3N}$ is a density-dependent two-body interaction obtained from the chiral three nucleon force by closing one pair of external lines and summing over the filled Fermi sea (k_F) of nucleons [7]. $\bar{V}_{3N}$ and V_{3N} are related by $\langle ab|\bar{V}_{3N}|cd\rangle = \sum_{h \leq k_F} \langle abh|V_{3N}|cdh\rangle$, where the matrix elements are anti-symmetrized. Possible over-counts are carefully treated. $\bar{V}_{3N}$ is dependent of k_F or its corresponding density n.

We then calculate effective low momentum V_{low-k} matrix elements [8] from V_{2N} and V_{3N} for the use in the ring diagram calculations. Starting from the half-on-shell T-matrix in the

Lippmann-Schwinger equation, one defines the effective low-momentum T-matrix as

$$T_{\text{low}-k}(p',p,p^2) = V_{\text{low}-k}(p',p) + \int_0^{\Lambda} q^2 dq V_{low-k}(p',q) \frac{T_{low-k}(q,p,p^2)}{p^2 - q^2 + i0^+} \tag{5}$$

where Λ denotes a momentum space cut-off and $(p',p) \leq \Lambda$. The T-matrix in Eq.(5) is required to satisfy the condition $T(p',p,p^2) = T_{low-k}(p',p,p^2)$; $(p',p) \leq \Lambda$. Earlier studies shew nuclear properties obtained from V_{low-k} being rather insensitive on Λ in the vicinity of 2.1 fm^{-1} [8]. Hence we set the cut-off in Eq. (5) $\Lambda \approx 2.1\ \text{fm}^{-1}$.

To calculate the V_{low-k} matrix with V_{3N} included, we have used the Bertsch formula $\hbar\omega = 45.0A^{-1/3} - 25.0A^{-2/3}$. we adopt the magnitudes of parameters c_D, c_E in Eqs. (4) from the c_E vs. c_D curve in [5] where the authors determined values of these two parameters from fitting binding energies of $A = 3$ nuclei. The nucleon density arising from the contact term [7] of Eq. (4) for the nucleus is chosen from the experimental charge density profile $\rho(r)$ vs. r from [9] as that approximately at the nucleus' RMS radius. The RMS radius for ^{4}He is 1.6757 fm [10] In this way, we set the density around the RMS radius to be $0.3\rho_0$ for ^{4}He, with $\rho_0 = 0.17/\text{fm}^3$.

The empirical Coulomb energy $E_{coul}/A = 0.717 \times Z^2/A^{4/3}$ is added to the nuclear system's ground state energy. Note that the non-interaction ground state energy E_0^{free} already takes care of the center of mass motion part. Hence our ring diagram expansion of ΔE_0 involves no CM excitation problems.

Shown in Fig. 2 is the dependence of ground state energy per nucleon (or -BE/A) for ^{4}He on the 3N force constant c_D appearing in Eq. (4). In the figure, results from the first order ring diagram ("HF"), up to the second order one("Up to 2nd"), and all order ring diagrams ("Ring(all)") are all calculated with V_{3N} included. Experimental data [11] are displayed for comparison. Although the contribution from diagrams up to the second order one improves quite significantly comparing to that from the first order one alone, contribution from higher order diagrams is needed to fill the discrepancy so that the experimental binding energy can be obtained.

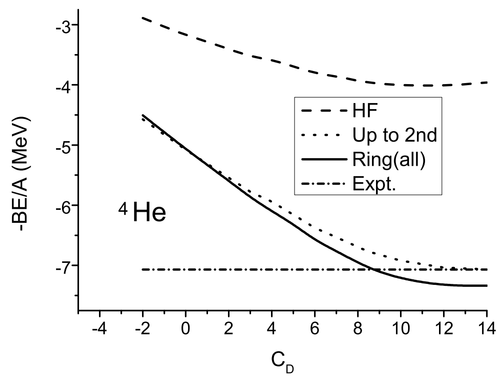

Figure 2: Dependence of $-BE/A$ of ^{4}He on the parameter c_D of V_{3N}.

As shown in Table I, our results from $V_{2N} + \bar{V}_{3N}$ with parameter c_D= 8.5 and its corresponding c_E from [5] at density ρ/ρ_0= 0.3 for ^{4}He fits the experimental data [11] quite well. In the Table we also examine the importance of V_{3N} to the nuclear binding energy. As expected, the binding energy obtained from V_{2N} alone is too weak. The deviation between results with and without V_{3N} gets wider when all ring diagrams are included.

Table 1: Ground-state energy E_0/A (or -BE/A)(in MeV) of ^{4}He calculated with 1st-, (1st+2nd)- and all-order ring diagrams. The parameter $c_D = 8.5$ of $\bar{V}_{3N}$ is employed.

		ρ/ρ_0	1st	1st+2nd	all rings	Expt
^{4}He	V_{2N}	–	-3.46	-5.36	-5.39	
	$V_{2N}+\bar{V}_{3N}$	0.3	-3.96	-6.77	-7.05	-7.073

In conclusion, our calculated ground state energy per nucleon fits the experimental data quite well when V_{3N} is added in and all orders of ring diagrams are included. Contributions from ring diagrams with orders higher than 2 can not be ignored. As expected, binding energy obtained with V_{2N} alone is too weak. This study shows that the three-nucleon force is important in nuclear systems. We have found that the above results are also true for several other closed-shell nuclei. This will appear in other separate publications.

References

[1] H. Q. Song, S. D. Yang and T.T.S. Kuo, Nucl. Phys. **A462**, 491 (1987); Yiharn Tzeng, T. T. S. Kuo,Nucl. Phys. A485, 85 (1988).

[2] T. T. S. Kuo and E. Osnes, *Lecture Notes in Physics* (Springer-Verlag, New York), Vol. 364 (1990) p.1.

[3] M. C. M. Rentmeester, R. G. E. Timmermans, and J. J. de Swart, Phys. Rev. C **67** (2003) 044001.

[4] A. Nogga, H. Kamada and W. Glockle, Phys. Rev. Lett. **94**, 944 (2000); S.C. Peiper, K. Varga and R. B. Waringa, Phys. Rev. **C66**, 044310 (2002).

[5] P. Navratil, V.G. Gueorguiev, J.P. Vary, W.E. Ormand and A. Nogga, Phys. Rev. Lett. **99**, 042501 (2007).

[6] D. R. Entem, R. Machleidt, and H. Witala, Phys. Rev. C **65**, 064005 (2002).

[7] J. W. Holt, N. Kaiser and W. Weise, Phys. Rev. **C79**, 054331 (2009); J. W. Holt, N. Kaiser and W. Weise, Phys. Rev. **C81**, 024002 (2010).

[8] S. K. Bogner, T. T. S. Kuo and L. Coraggio, Nucl. Phys. **A684**, (2001) 432; S. K. Bogner, T. T. S. Kuo, L. Coraggio, A. Covello, and N. Itaco, Phys. Rev. C **65**, 051301(R) (2002); S. K. Bogner, T. T. S. Kuo, and A. Schwenk, Phys. Rep. **386**, 1 (2003).

[9] J.S.Mccarthy, I. Sick, and R.R. Whitney, Phys. Rev. C **15**, 1396 (1977); H. de Vries, C.W. de Jager, and C. de Vries, At. Data Nucl. data Tables, **36**, 495 (1987)

[10] I. Angeli, K.P. Marinova, Atomic and Nucl. Data Tables **99** 69 (2013).

[11] B.Pfeiffer,K.Venkataramaniaih,U.Czok,C.Scheidenberger, Atomic and Nucl. Data Tables **100** 403-535 (2014); Nuclear data from Brookhaven National Laboratory, http://www.nndc.bnl.gov/chart/

Higgs boson as a gluon trigger: the study of QCD in high pile-up environments

H. Van Haevermaet[1,2], *P. Cipriano*[1], *S. Dooling*[1], *A. Grebenyuk*[3], *P. Gunnellini*[1,2], *F. Hautmann*[4,5,6], *H. Jung*[1,2], *P. Katsas*[1]

[1]Deutsches Elektronen Synchrotron, D 22603 Hamburg
[2]Universiteit Antwerpen, Elementaire Deeltjes Fysica, B 2020 Antwerpen
[3]Université Libre De Bruxelles, I.I.H.E., B 1050 Bruxelles
[4]University of Sussex, Physics & Astronomy, Brighton BN1 9QH
[5]University of Oxford, Physics Department, Oxford OX1 3NP
[6]Rutherford Appleton Laboratory, Chilton OX11 0QX

DOI: http://dx.doi.org/10.3204/DESY-PROC-2014-04/280

1 Introduction

To study QCD one typically measures processes in single proton-proton collisions. A particular interesting one is the Drell-Yan $q\bar{q} \xrightarrow{\gamma^*/Z^0} l^+l^-$ process, which is produced through an electroweak current that couples to quarks. A big advantage is its clean final state, which only involves the decay leptons. This allows us to use the process to precisely measure quark structure functions, quark induced parton showers, and underlying event properties. The properties and structure functions of gluons however, have to be determined indirectly. But with the recent discovery [1] of the Higgs boson, this picture changes. In the heavy top limit, the Higgs boson directly couples to gluons and can be produced with the gluon fusion $gg \to H$ process through a colour singlet current [2]. The access to this new production process opens up a whole new interesting area of possible QCD measurements, where we can directly study gluon induced effects. In addition, if we only look at decay channels of the Higgs boson like $H \to ZZ \to 4l$, we have access to the same clean final state as in the Drell-Yan process. In order to produce enough statistics for detailed measurements, current accelerators like the LHC at CERN have to operate at very high beam intensities. This high luminosity allows one to measure differential distributions, e.g. the transverse momentum [3] of the Higgs, but it also creates a condition in which on average much more than one proton-proton collision happens per bunch crossing. This so called pile-up (PU) can easily reach, given the LHC run conditions, scenarios where PU = 40 (i.e. 40 additional proton-proton collisions occur on top of the one signal event). This implies that the phase space will be completely filled with extra hadronic activity coming from the pile-up events, which makes a study of QCD in the Higgs or Drell-Yan channels extremely difficult. To assess whether one can still perform QCD measurements in such harsh environments we initiated a new program using the Higgs boson as a gluon trigger [4]. The main idea is to compare Higgs and Drell-Yan production in the same invariant mass range, and then look at different observables, such as the transverse momentum of the bosons, to measure the difference in soft multi-gluon emissions. Here we present pile-up studies to show whether the Higgs to Drell-Yan comparison stays valid in high pile-up environments.

The Monte Carlo event generator samples used in this study are all produced with Pythia 8.185 [5]. All samples contain proton-proton collisions at $\sqrt{s}$ = 7 TeV, with the 4C tune [6] to describe the underlying event properties. The Higgs sample is generated by activating the gluon fusion process $gg \to H$, while the Drell-Yan sample is generated using the single Z^* production process $f\bar{f} \to Z^{0*}$. The bosons are produced within the same invariant mass range of 115 < M < 135 GeV and in addition, to avoid complications with the leptonic final states, they are set stable. The Higgs mass is set to 125 GeV. To study the effect of additional pile-up events, samples with a fixed amount of PU = 5 and PU = 20 are produced. This is done by adding a specified number of small-p_{T} QCD process events to the signal event. All jets are constructed with the anti-k_{T} algorithm [7] with a distance parameter R = 0.5.

2 Transverse momentum spectra

Initial studies presented in [4] show the implicit difference in the inclusive p_{T} spectra of Higgs and Drell-Yan production, due to different soft gluon emissions. Here we analyse what happens when one includes additional PU events. By definition, as we put the bosons stable, the p_{T} spectra should be independent. This is confirmed in figure 1a, where both the PU = 0 and PU = 20 scenarios are compared for Higgs and Drell-Yan production. Thus, if the experimental reconstruction of the leptonic decay products is stable in high PU environments, the p_{T} spectrum should be stable. One can then take the ratio (Higgs/DY) of both spectra and use this observable to directly quantify the gluon versus quark radiation effects.

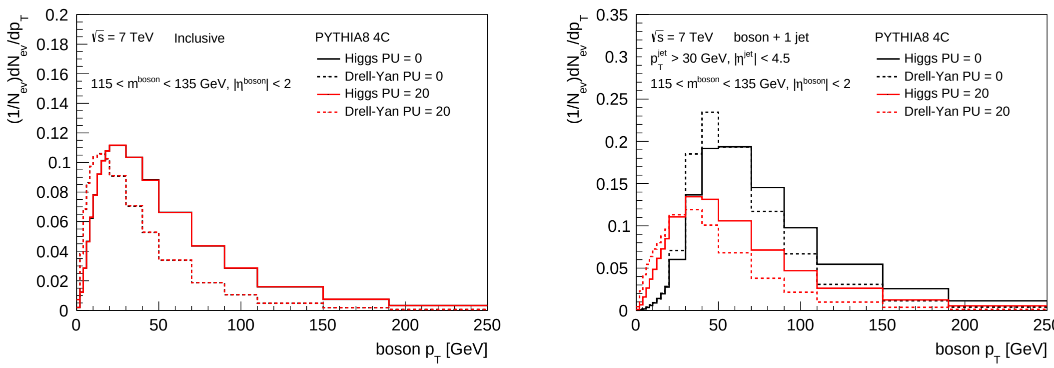

(a) (b)

Figure 1: The inclusive (a) and boson + 1 jet (b) Higgs and Drell-Yan transverse momentum p_{T} spectra for PU = 0 and PU = 20 scenarios.

In addition, one can look at the boson + 1 jet production process. This topology is expected to be more sensitive to gluon versus quark emission effects, as hard radiation accompanies the boson production. However, requiring an additional hard jet ($p_{\mathrm{T}} > 30$ GeV/c, $|\eta| < 4.5$) shifts the spectrum towards higher transverse momenta as a result of the induced p_{T} balance between the boson and the hard jet. As such, the contribution of gluon versus quark induced effects will actually become less pronounced in the p_{T} spectrum. These effects are illustrated in figure

1b. Furthermore, figure 1b also shows the results of adding additional PU events. In this case, both spectra shift to lower values. This is the consequence of jet mismatching that occurs due to the extra PU activity. That is, in the presence of PU, there is a higher probability that a high p_{T} jet comes from an independent PU interaction and is identified as the jet coming from the signal event, which can result in a matching of a high p_{T} jet with a low p_{T} boson.

3 Underlying event observables

A very interesting observable to study QCD in proton-proton collisions is the underlying event activity [8]. Common measurements [8, 9] look at the charged particle multiplicity and scalar p_{T} sum in the so called *transverse* region, which is defined as $60^{\mathrm{o}} < |\Delta\phi| < 120^{\mathrm{o}}$, with $\Delta\phi$ the difference in azimuthal angle between the charged particle and the leading (high p_{T}) object, in our case the Higgs or Z boson, that defines the hard scale of the event. With the produced boson in the *towards* region ($|\Delta\phi| < 60^{\mathrm{o}}$), and the recoil jet in the *away* region ($|\Delta\phi| > 120^{\mathrm{o}}$), the transverse region is only sensitive to the underlying event. Furthermore, when only the leptonic decay channel of the bosons is considered, one has access to a clean final state, with no contributions from final state radiation (FSR), resulting in a sensitivity to only initial state radiation (ISR) and multiple parton interactions (MPI). Obviously, when including additional proton-proton collisions to the event, the number of charged particles (and the scalar p_{T} sum) will increase drastically and directly scale to the number of PU events. However, we can show that when we subtract the underlying event activity in the Drell-Yan process, from the underlying event in the Higgs process, i.e.:

$$\frac{dn}{dp_{\mathrm{T}}}\,(\mathrm{H}-\mathrm{DY}) = \frac{dn}{dp_{\mathrm{T}}^{\mathrm{H}}} + \frac{dn}{dp_{\mathrm{T}}^{\mathrm{PU}}} - \left(\frac{dn}{dp_{\mathrm{T}}^{\mathrm{DY}}} + \frac{dn}{dp_{\mathrm{T}}^{\mathrm{PU}}}\right), \tag{1}$$

the PU contribution completely cancels out. This is confirmed in figures 2a and 2b that show the result of the subtraction. For both additional PU activity of 5 and 20 the subtracted underlying event stays stable. This implies that even in high PU environments one is able to measure small-p_{T} QCD physics. It is possible to subtract the PU contribution and study the difference in underlying event activity between Higgs and Drell-Yan production, which is directly sensitive to gluon versus quark induced ISR.

4 Summary

The Higgs $gg \to H$ production process provides new perspectives for interesting QCD measurements that allow us to directly probe gluon physics. This is possible due to the electroweak current, which, in the heavy top limit, directly couples to gluons. In addition, the colour singlet state and leptonic decay channels allow us to study events in which no complications from final state effects occur. We presented a novel method that compares Higgs and Drell-Yan production in the same invariant mass and rapidity range to perform a direct measurement of gluon versus quark induced processes. First we investigated the inclusive and boson + 1 jet p_{T} spectra. The inclusive spectrum is found to be sensitive to soft multi-gluon emissions, and is stable in high PU environments. The boson + jet event topologies however suffer from PU effects, that originate from the jet mismatching between signal and PU events. In addition we also studied the underlying event activity by looking at the charged particle multiplicity and scalar Σp_{T} in

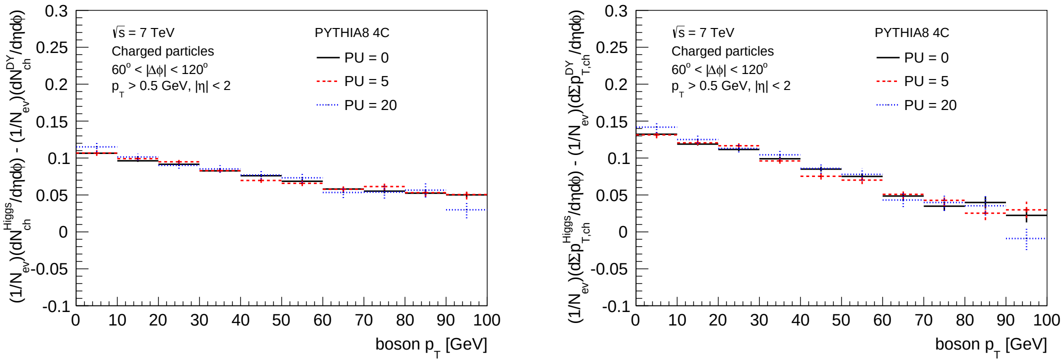

(a) (b)

Figure 2: The subtracted average charged particle multiplicity (a), and average scalar sum of transverse momenta (Σp_{T}) (b) in the transverse region of the azimuthal plane versus transverse momentum p_{T} of the produced boson. For PU = 0, PU = 5 and PU = 20 scenarios.

the transverse region. We constructed the subtracted underlying event observable (see eq. 1) and found that it is stable in high PU environments. Thus, by comparing Higgs to Drell-Yan production we can subtract the PU contributions, and directly measure the difference in gluon versus quark induced initial state radiation effects. Such that one can still access (small-p_{T}) QCD physics in high pile-up environments.

Acknowledgements

We are grateful to the organisers, convenors and participants of the PANIC conference for this opportunity to present and discuss our results in the poster session. The primary author is funded by the Research Foundation of Flanders (FWO).

References

[1] ATLAS Coll. (G. Aad et al.), Phys. Lett. **B716** (2012) 1; CMS Coll. (S. Chatrchyan et al.), Phys. Lett. **B716** (2012) 30.

[2] H. M. Georgi, S. L. Glashow, M. E. Machacek, and D. V. Nanopoulos, Phys. Rev. Lett. **40**, 692 (1978); J. Ellis, M.K. Gaillard and D. Nanopoulos, Nucl. Phys. **B106** (1976) 292; M.A. Shifman, A.I. Vainshtein, M.B. Voloshin and V.I. Zakharov, Sov. J. Nucl. Phys. **30** (1979) 711.

[3] ATLAS Coll., ATLAS note ATLAS-CONF-2013-072.

[4] P. Cipriano et al., Phys. Rev. D **88**, 097501 (2013).

[5] T. Sjöstrand, S. Mrenna, P. Skands, Comput.Phys.Commun.178:852-867 (2008).

[6] R. Corke and T. Sjöstrand, JHEP **1103** (2011) 032, [arXiv:1011.1759].

[7] M. Cacciari, G. P. Salam, G. Soyez, JHEP **0804** (2008) 063.

[8] R.D. Field, arXiv:1010.3558 [hep-ph].

[9] CMS Coll. (S. Chatrchyan et al.), JHEP **1109** (2011) 109.

List of Authors